Investigations on maar-diatreme volcanoes by inversion of magnetic and gravity data from the Eifel area, Germany

Thesis for the obtention of the degree of

"Doctor rerum naturalium"

at the Department of Chemistry, Pharmaceutics and Geosciences of the Johannes Gutenberg University of Mainz

Evariste Sebazungu

born in Ruhengeri/Rwanda

Mainz, October 2005

Abstract

A study of maar-diatreme volcanoes has been perfomed by inversion of gravity and magnetic data. The geophysical inverse problem has been solved by means of the damped nonlinear least-squares method. To ensure stability and convergence of the solution of the inverse problem, a mathematical tool, consisting in data weighting and model scaling, has been worked out. Theoretical gravity and magnetic modeling of maar-diatreme volcanoes has been conducted in order to get information, which is used for a simple rough qualitative and/or quantitative interpretation. The information also serves as a priori information to design models for the inversion and/or to assist the interpretation of inversion results.

The results of theoretical modeling have been used to roughly estimate the heights and the dip angles of the walls of eight Eifel maar-diatremes — each taken as a whole. Inverse modeling has been conducted for the Schönfeld Maar (magnetics) and the Hausten-Morswiesen Maar (gravity and magnetics). The geometrical parameters of these maars, as well as the density and magnetic properties of the rocks filling them, have been estimated. For a reliable interpretation of the inversion results, beside the knowledge from theoretical modeling, it was resorted to other tools such like field transformations and spectral analysis for complementary information. Geologic models, based on the synthesis of the respective interpretation results, are presented for the two maars mentioned above.

The results gave more insight into the genesis, physics and posteruptive development of the maar-diatreme volcanoes. A classification of the maar-diatreme volcanoes into three main types has been elaborated. Relatively high magnetic anomalies are indicative of scoria cones embeded within maar-diatremes if they are not caused by a strong remanent component of the magnetization. Smaller (weaker) secondary gravity and magnetic anomalies on the background of the main anomaly of a maar-diatreme — especially in the boundary areas — are indicative for subsidence processes, which probably occurred in the late sedimentation phase of the posteruptive development.

Contrary to postulates referring to kimberlite pipes, there exists no generalized systematics between diameter and height nor between geophysical anomaly and the dimensions of the maar-diatreme volcanoes. Although both maar-diatreme volcanoes and kimberlite pipes are products of phreatomagmatism, they probably formed in different thermodynamic and hydrogeological environments. In the case of kimberlite pipes, large amounts of magma and groundwater, certainly supplied by deep and large reservoirs, interacted under high pressure and temperature conditions. This led to a long period phreatomagmatic process and hence to the formation of large structures. Concerning the maar-diatreme and tuff-ring-diatreme volcanoes, the phreatomagmatic process takes place due to an interaction between magma from small and shallow magma chambers (probably segregated magmas) and small amounts of near-surface groundwater under low pressure and temperature conditions. This leads to shorter time eruptions and consequently to structures of smaller size in comparison with kimberlite pipes. Nevertheless, the results show that the diameter to height ratio for 50% of the studied maar-diatremes is around 1, whereby the dip angle of the diatreme walls is similar to that of the kimberlite pipes and lies between 70 and 85°. Note that these numerical characteristics, especially the dip angle, hold for the maars the diatremes of which — estimated by modeling — have the shape of a truncated cone. This indicates that the diatreme can not be completely resolved by inversion.

Zusammenfassung

Mittels Inversion von gravimetrischen und magnetischen Daten wird eine Studie an Maar-Diatrem-Vulkanen durchgeführt. Das geophysikalische Inversionsproblem wird durch eine gedämpfte nichtlineare Methode der kleinsten Quadraten gelöst. Um die Stabilität und die Konvergenz der Lösung des inversen Problems zu gewährleisten, wird ein mathematisches Verfahren ausgearbeitet, das eine Gewichtung von Daten und eine Skalierung von Modell zum Kern beinhaltet. Um Informationen für eine einfache grobe qualitative und/oder quantitative Interpretationzu erhalten, werden theoretische Schwere- und Magnetik-Modellierungen von Maar-Diatrem-Vulkanenerarbeitet. Die gewonnenen Resultate dienen weiterhin als a priori Information, um genauere Modelle für die Inversion zu konzipieren und/oder als Unterstützung für die Interpretation der Inversions-Ergebnisse.

Um die vertikale Ausdehnung von Maar-Diatrem-Vulkanen und die Einfallswinkeln ihrer Diatremwände abzuschätzen, werden die Ergebnisse theoretischer Modellierungen auf acht Objekte in der Eifel — jedes einzelne in seiner Gesamtheit — angewandt. Inversionsmodelle werden für das Schönfelder Maar (Magnetik) und das Hausten-Morswiesen Maar (Schwere und Magnetik) berechnet. Sowohl die geometrischen Parameter dieser Maare, als auch die Dichten und die magnetischen Eigenschaften der Gesteine ihrer Füllungen werden bestimmt. Neben der aus theoretischer Modellierung stammenden Information, werden für eine zuverlässige Interpretation der Ergebnisse zusätzliche Informationen einbezogen, die aus weiteren Operationen, wie Feldtransformationen und Spektral-Analyse, gewonnen wurden. Auf Basis der jeweiligen Gesamt-Ergebnisse werden geologische Modelle für die zwei oben erwähnten Maare dargestellt.

Die Ergebnisse geben tieferen Einblick in die Physik, die Genese und die posteruptive Entwicklung von Maar-Diatrem-Vulkanen. Maar-Diatrem-Vulkane werden in drei Haupt-Typen klassifiziert. Relativ starke magnetische Anomalien, die nicht durch eine starke remanente Komponente der Magnetisierung verursacht werden, weisen auf die in Maar-Diatremen eingebetteten Schlackenkegeln hin. Kleinere bzw. Schwächere sekundäre Schwere- und magnetische Anomalien innerhalb der Haupt-Anomalie eines bestimmten Maar-Diatrems — insbesondere in Randbereichen — weisen auf Subsidenzprozesse hin, die während der späteren Sedimentationsphase der posteruptiven Entwicklung stattfanden.

Im Gegensatz zu den Postulierungen, die sich auf Kimberlitschlote beziehen, gibt es keine allgemeine Systematik zwischen Durchmesser und Tiefe, noch zwischen der geophysikalischen Anomalie und den Dimensionen der Maar-Diatrem-Vulkane. Zwar sind sowohl Maar-Diatrem-Vulkane als auch Kimberlitschlote Produkte des Phreatomagmatismus, ihre Bildung aber findet unter verschiedenen thermodynamischen und hydrogeologischen Umgebungsbedingungen statt. Im Falle der Kimberlitschlote, sind große Mengen von Magma und Grundwasser, sicherlich aus tiefen und großen Reservoirs, unter Hochdruck- und Hochtemperatur-Bedingungen am phreatomagmatischen Prozess beteiligt. Dies führt zu einem langzeitigen Prozess und folglich auch zur Bildung von großen Strukturen. Die phreatomagmatische Entstehung von Maar-Diatrem- und Tuffring-Diatrem-Vulkanen hingegen, wird durch die Wechselwirkung zwischen Magma aus relativ kleinen, nicht tiefliegenden Magmakammern (wahrscheinlich Segregationsmagmen) und kleinen Mengen von oberflächennahem Grundwasser unter Niedrigdruck- und Niedrigtemperatur-Bedingungen verursacht. Der Bildungsprozess ist daher kürzer und demzufolge sind auch die Strukturen kleiner im Vergleich zu Kimberlitschloten.

Die Ergbnisse zeigen trotz allem, dass das Verhältnis von Durchmesser zu Tiefe für 50% der untersuchten Maar-Diatreme bei 1 liegt und der Einfallwinkel der Diatremwände dem der Kimberlitschlote gleicht und zwischen 70 und 85° liegt. Es ist zu bemerken, dass diese numerischen Charakteristiken, insbesondere der Einfallwinkel, für die Maare gelten, deren Diatreme durch Modellierung abgeschätzte Kegelstümpfe sind. Dies weist darauf hin, dass die Tiefe des Diatrems durch Inversion nicht genau bestimmt werden kann.

Table of contents

1. Introduction

The maar-diatreme volcanoes — being products of an unusual type of volcanism, namely of a phreatomagmatic one — have long attracted the interest of geoscientists in different countries. Till the present day, several geologic and geophysical investigations of maar-diatreme volcanoes have been conducted (e.g., Kopecký et al., 1966; Berger et al., 1968; Dawson, 1967, 1970, 1971; Camus, 1975; Lorenz, 1970, 1971, 1973, 1975, 1980, 1986; Lorenz and Büchel, 1980; Clement, 1982; Büchel, 1982 – 1984, etc.). Recent studies perfomed by diverse geoscientific institutions have outlined further maar structures of Tertiary age (Baruth, Saxony) or produced evidence of their phreatomagmatic origin (Messel, Hesse) in Germany. In order to better understand the nature of maar-diatreme volcanoes, their formation, the relationship between them and other structures such like scoria cones and tuff-rings, and their relevance to the formation of other geologic structures such as kimberlite-diatremes, further geologic and geophysical studies are required (Lorenz, 1986).

Geophysical methods have been widely used to investigate the Eifel volcanic area. Large scale geophysical surveys (refraction seismics, magnetotellurics, gravity) have been conducted in order to study the tectonic phenomena occuring in the Rhenish Massif (Fuchs et al., 1983). Small scale geophysical investigations carried out in this area were aimed either to assist geologic mapping or to outline volcanic features such like maars and related diatremes, tuff-rings or scoria cones (Büchel, 1978–1980; Henk, 1984; Hoover, 1987; Lepold, 1987; Bannert, 1989; Franzreb-Hertel, 1989 ; Stachel and Büchel, 1989; Hörrle, 1991; Smilde, 1997; Diele, 2000 and many others). Magnetic and gravity were the most common methods. The interpretation of the data has been mainly qualitative. Within some maars, geoelectrics, mainly vertical electrical sounding, has been conducted with the aim to study the geologic layering and the electrical properties of the upper part (Hunsche, 1973). Some important investigations have been conducted by students and staff members of Institut für Geowissenschaften of Mainz in the framework of annual geophysical fieldworks under the supervision of Prof. Dr. W. Jacoby. One of those contributions is a 44 km long gravity profile across the central part of the Kelberg High (Büchel et al., 1988). The negative gravity anomaly correlates well with the positive magnetic anomaly, observed on the map of the total geomagnetic field of the Federal Republic of Germany (BGR, 1976). By data processing and interpretation of all existing geophysical data assisted by geological mapping of the High Eifel Tertiary volcanic field of the Kelberg High area, Büchel (1990) showed that a series of near-surface acidic intrusive bodies — characterized by a negative gravity anomaly — overlie an anomalous magnetic body, which is located at 10–13 km depth and appears to be the top of an underlying magma chamber.

Paleomagnetic properties of the Eifel volcanics (lava flows and surface tuffs) have been studied by Cipa (1958), Böhnel et al. (1987) and Herzog et al. (1988). Haverkamp (1984) has done paleomagnetic measurements of the crater sediments of the Meerfeld Maar. The configuration and the parameters of the upper part (maar) of the structures under study are more or less known from geologic and shallow geophysical investigations. Attempts have been made to construct geological models of some of the maar-diatremes of the Eifel area in Germany (Stachel and Büchel, 1989; Hörrle, 1991; Pirrung, 1992), trying to find the best fit to observed gravity data by forward modeling. Franzreb-Hertel (1989) has done gravity investigations in the area of Kelberg. Using Fourier analysis of gravity data, she could

better outline some maar-diatremes and identify some fracture zones in the area. Bannert (1989) has presented a model for the Mosbruch Maar, derived from the inversion of gravity data using the method of vertical prisms worked out by Cordell and Henderson (1968). Further investigations on maar-diatremes by inverse 3-D modeling of gravity data were conducted by Smilde (1997) on the example of the Meerfeld Maar. Using a combination of different surveying and interpretation techniques (gravity, magnetic, electrical soundings and volume calculations), Diele (2000) gave an insight into the morphological, physical and tectonic nature of the Pulvermaar and its surroundings.

Although all the above studies were valuable contributions to understanding the nature of maar-diatreme volcanoes, it is still necessary to get more detailed answers to some pertinent questions related to their genesis, their morphology and their physics. One would like to know the type of the volcanic feature which is dealt with, its vertical and lateral extent, and the physical properties of the rocks it is made of. Two other important questions, directly connected to the above ones, are the evolution of the volcanic activity and the posteruptive development. Most of all these problems have also been geologically formulated and in some cases investigated.

While conducting a geophysical survey, one gets a set of records which are nothing but a given physical field expressed in digital or analog form. The character and the amplitude of the physical field observed either in the air or at the Earth's surface, at the sea or in a borehole, depends on the morphological aspect and the physical properties of the subsurface structure to be explored. The aim of every geophysical survey is to get as much information as possible about the geological structure under study with the aid of appropriate data processing and data analysis. Depending on the type of the survey and its aim or on the data to be analysed and on the way they are analysed, geophysical data interpretation can be qualitative and/or quantitative.

This work is aimed at making a quantitative analysis, i.e., estimating parameters of some of the Eifel maar-diatreme volcanoes from observed gravity and magnetic data. This enables to build up geological models which could supply with complementary information to the existing geological and geophysical knowledge about the maar-diatreme volcanoes. However, it should be noted that a qualitative step will precede the quantitative interpretation since it is always necessary to set up a strategy for given problems; and there is no totally automatic procedure conceivable. The procedure of estimating parameters of causative sources from observations is generally known as **inversion** or solving the inverse problem. The philosophy of this method, which has become the standard method for solving geophysical problems, is to try to match theoretical data with observations to get the best fit. This is usually achieved by means of the so-called **modeling**. Modeling is conducted in two operations dependent on each other: **forward** and **inverse** modeling. Theoretical data ($\mathbf{f}$), also called "model response", are computed by forward modeling for models ($\mathbf{m}$) estimated by inverse modeling and are compared with observations ($\mathbf{y}$). Under forward modeling one understands the solution of the forward problem. Given some source distribution (e.g., mass or magnetization distribution), geophysical fields (e.g., gravity, magnetic field) are calculated by means of mathematical relations which are derived from known physical laws and are uniquely determined. Inverse modeling is the reverse operation of the forward modeling, i.e., the solution of the inverse problem consists in the

evaluation of sources from observed data (**y**). In other words, by means of appropriate methods, one tries to build some quantitative models (**m**) which are described by defined parameters. It is obvious that solving an inverse problem can be thought of only if there exist mathematical means for relating the model parameters to the data. The feasibility of an inverse problem to be solved is fully conditioned by the possibility of the forward problem to be solved. Hence it would not be a mistake to state that the way how the forward problem is being solved (either analytically or numerically) will have a significant influence on the computations (e.g., speed, accuracy) and on the solution of the inverse problem. There are several different methods to solve geophysical inverse problems — simple conventional and computer aided ones. The choice of the method is defined by the type and the complexity of the problem to be solved. The whole set of mathematical techniques implemented to solve the inverse problem is referred to as the "inverse theory". A good description of the inverse theory can be found in several textbooks, e.g., Menke (1984) and Tarantola (1987).

In the inverse theory, there are two main groups of mathematical techniques used to solve inverse problems: matrix equations for problems in which physical properties can be described by discrete parameters or numerically approximated and integral equations techniques for problems in which physical properties must be described by continuous functions. In this work the discrete inverse problem will be dealt with. Moreover, the relationship between the gravity/magnetic field and most of involved parameters is nonlinear. Thus modeling will be carried out by means of iterative nonlinear inversion, using algorithms based on matrix equations. By this technique, geological models estimated by inverse modeling are adjusted by comparing physical effects computed by forward modeling with observed data. To enhance both data and model prediction, all available relevant information, referred to as **a priori information**, must be taken into account. A model, which best fits the observations and is in good agreement with existing information from different geoscientific sources, is then thought as to represent the investigated target. However, because of the problem of the nonuniqueness in most geophysical inverse problems (Treitel and Lines, 1988), especially in potential field problems (Al-Chalabi, 1971), the estimated model has to be considered as one of the various plausible candidate models. That is the reason, instead of selecting out one particular model for a given maar-diatreme volcano, a range of possible models will be defined beside the estimated one, i.e., a model will be presented with its probabilistic bounds. The method of matrix equations consists in solving a linear system, the coefficients of which — also called **Jacobian** or **data kernel** — are made of partial derivatives respective to given model parameters. The solution is computed by multiplying the inverse of the Jacobian by the observations. This procedure can encounter problems of slowness, instability, singularity and non-convergence due to errors from different sources (observations, model, computations, soft- and hardware). Thus, it is envisaged to work out a tehchnique which could enhance the solution of the inverse problem.

Further goals of this work are to find out whether there exists a certain systematics between the amplitude of the geophysical anomaly and the dimensions of the maar-diatremes and to make a classification of the latter into different types. Therefore theoretical modeling of maar-diatremes will be conducted to assist and complement the inverse modeling.

2. Geology and petrophysics of the Eifel maar-diatreme volcanoes

2.1. Brief geologic overview of the Eifel volcanic field

2.1.1. Crust and mantle structure

The upper part of the geologic structure of the Eifel area (Fig. 2.1) is made up of slightly metamorphosed, folded and faulted Devonian sedimentary rocks, mainly slates and sandstones (Schmincke et al., 1983). Their thickness is about 5–10 km. After analyses of crustal xenoliths, mainly from the Quaternary volcanic field of the East Eifel, the sediments are underlain by the crystalline basement composed of metamorphic rocks represented, with increasing depths, by metapelites of the greenschist facies, by metasediments and metagranitoids, migmatites of the amphibolite facies and finally above the Moho by mafic granulites, pyroxenites and hornblendites as well (Wörner et al., 1982; Voll, 1983). The Moho is estimated at 30–35 km depth (Meissner et al., 1987). Under the Moho, the material is made up of peridotites and other ultrabasic rocks. The lithosphere/asthenosphere interface lies approximately at 50 km depth (Mechie et al., 1983).

Large scale geological, geophysical and geodetic investigations within the Rhenish Massif have revealed the existence of an intracrustal shear zone characterized by high conductivities (100–200 mS/m) (Jödicke et al., 1983) and relatively low velocities (6.25 km/s) (Mechie et al., 1983). This zone, located at depths between 15 and 20 km, is assumed to be under stress connected with the overthrusting phenomenon considered as the main cause of the continuous thickening of the crust in its whole (Fuchs et al., 1983). After Mechie et al. (1983), in the crust of the Eifel area, seismic velocities of p-waves at depths below 3–5 km generally range from 5.6 to 6.7 km/s. In the mantle part of the lithosphere, velocities reach values of 8.5 km/s. As indicated by the results of the modeling of the rheological structure of the lithosphere, the lower crust of the Eifel area, like the neighbouring coal-mining region, is characterized by low viscosities due to high temperatures (Klein et al., 1997). In the asthenosphere, between depths of 50 and 200 km, there exists a body of low velocity, probably due to partial melts (Raikes and Bonjer, 1983). This might be considered as the cause of the lower Bouguer anomaly observed in the Rhenish Slate Mountains area to the left of the Rhine relative to the eastern side (Drisler and Jacoby, 1983).

2.1.2. The Paleozoic basement (bottom)

As can be seen on the schematic geological map of the Eifel area and its vicinity (Fig. 2.1), rocks of the Eifel — except some Tertiary and Quaternary volcanics and some Triassic rocks of small extent, are exclusively of Devonian age. At the present day, the oldest Devonian rocks occur within the big anticlinorium of the main East Eifel anticline. In the area of its maximal culmination in the East Eifel, Lower Siegenian rocks, up to 1000 m thick, are exposed (Meyer, 1958; Meyer and Pahl, 1960). The whole Siegenian series (Lower-, Middle-, and Upper Siegenian) with a maximal thickness of 5000 m in the Central Eifel, is made up of interlayered clay-, silt- and sandstones. Southwards, this so-called "sandy Siegenian normal facies" is taken over by the main Siegenian overthrust. In the South of the overthrust occur Siegenian thick schist layers, which, in analogy with the comparable schists series in Hunsrück and Taunus, are referred to as Hunsrück schists.

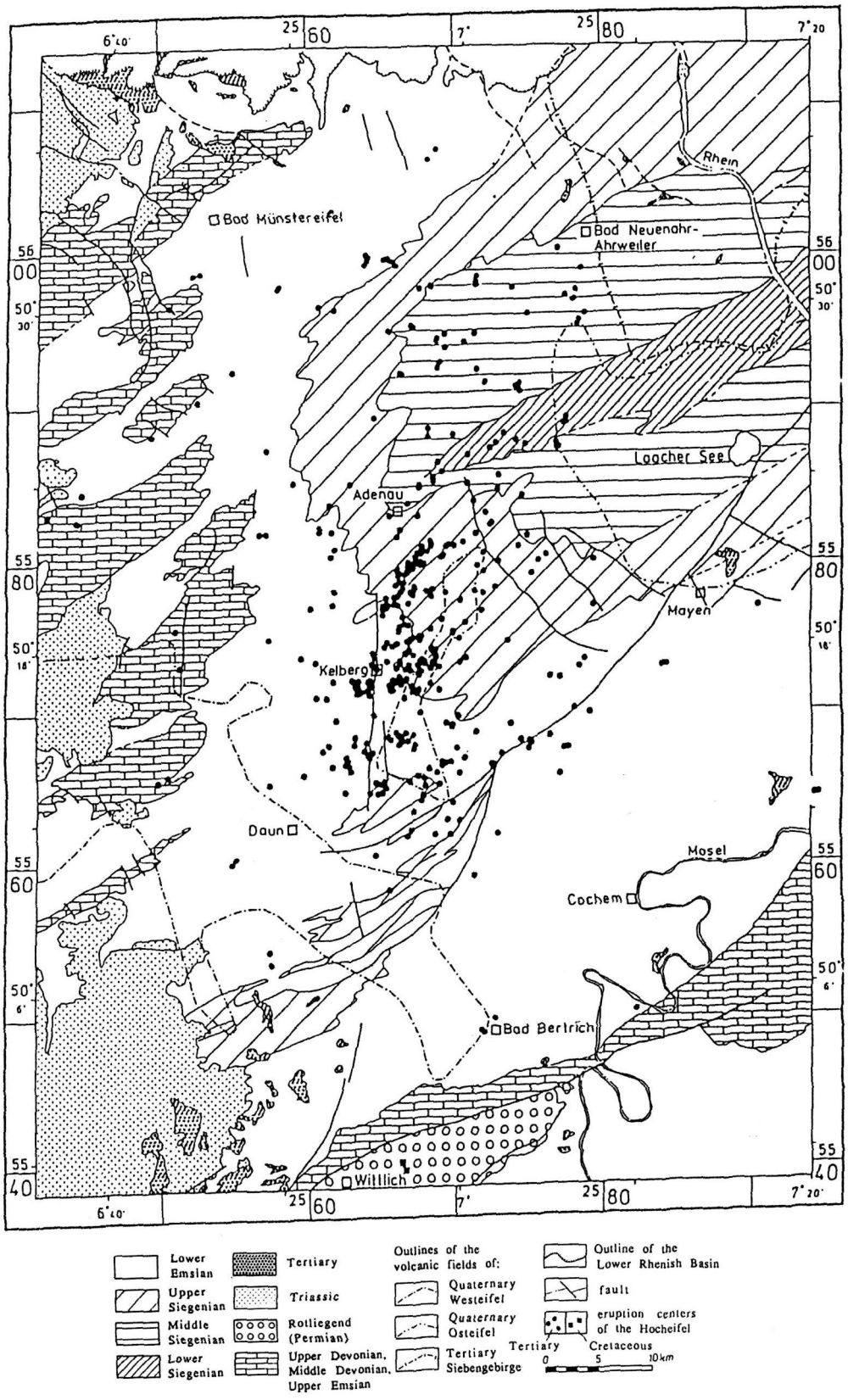

Fig. 2.1 Schematic geological map of the Eifel and the vicinity after geological maps of Ledoux (1987), Zitzmann and Grünig (1987) and Kuckelkorn and Vorster (1926); from Büchel, 1990).

The Lower-Emsian layers, with a maximal thickness of 5000 m as well, are subdivided into two parts: a lower part with abundant fossils and made up of grey sand-, silt- and claystones and an upper part with less fossil occurence, in which reddish, unsorted clastic sediments characterized by quick lateral variations are often prevailing (Klerf-Layers, "Schistes rouges de Clerveaux", Gosselet, 1885).

In the Upper-Emsian, due to regression, only small amounts of sediments have accumalated; in the East Eifel area a few tens of metres, in the West Eifel up to 300 m whereas in the Moselle-Trough fine clastic sediments reached a maximum thickness of 1000 m. After Meyer (1988), the Eifel North-South Zone, situated in the western Eifel Mountains, begins to develop. But after Murawski (1964), this zone has a pre-Variscan origin.

In the Middle and Upper Devonian, the sedimentation went on with a marl and limestone series with an increasing component of fine clastic sediments northwards. In some areas of the Eifel North-South Zone, the Middle and Upper Devonian sediments are preserved. Carboniferous sediments, if they ever existed in the Eifel, have been completely removed. They occur at the northern boundary of the Rhenish Slate Mountains.

The Permian was characterized by the tendency to form tectonic basins with northerly directions different from the NE-SW Variscan trend (Murawski, 1983). Such basins, as the Lower Permian Wittlich basin, located South of the Eifel, were filled up by clastic material eroded from the mountains, which formed isostatically at the same time. Due to arid climatic conditions, red coarse clastic fanglomerates, conglomerates and sandstones were formed mainly from the North. Rhyolithic clasts, up to a few decimetres thick in the lower part of the rock pile, indicate that the volcanic activity has taken place within these structures (Binot in Meyer, 1988). The uppermost series is composed of fine-grained sandstones and siltstones, which probably belong to the Upper Permian.

2.1.3 The Mesozoic cover

The structural development of the Permian time carried on in the Triassic and Lower Jurassic, leading to a continuous subsidence of the Eifel Depression (Murawski, 1983). In the Middle Lower Triassic, the Eifel North-South Zone was again filled up by fluvial sediments such like conglomerates and sandstones. In the Uppermost Lower Triassic, the sedimentation extended from this zone over the whole Eifel east of the former depression (Meyer, 1988). Sandstones, siltstones and schists are the prevailing rock types of this series. At the present day, Lower Triassic occurs only at the southern and northern boundaries of the Eifel N/S-Zone. In the central part of the Eifel N/S-Zone, it survived in the Oberbettingen graben-like structure and in Stadtkyll. The Lower Triassic has an average thickness of 200–300 m.

Above the Lower Triassic lay shallow marine sediments of the Middle and Upper Triassic, overlain, in turn, by Lower Jurassic rocks which conclude the Mesozoic sedimentation in the Eifel. The latter sediments are represented in the Trier-Bitburg Embayment and in a narrow zone at the northern boundary of the Mechernich Triassic Embayment. In the Central Eifel, relics of Middle Triassic sediments exist only in the Oberbettingen area (Büchel, 1990).

2.1.4 The Cenozoic cover

In the Tertiary, the central Eifel was subject to denudation. The changes of the surface of the Slate Mountains, which began in the late Mesozoic, continued till the end of the Oligocene. The alteration was characterized by a high degree kaolinitisation, leading to the formation of kaolinite minerals and of a brown ferrigeneous crust on the bottom of the layer. Under these conditions, the Eifel became a nearly flat deeply eroded peneplain in the Earlier Tertiary.

Layers resulting from the young Mesozoic and Tertiary alteration are present only at the boundaries of the Eifel area. The absence of such layers in the High Eifel area might be explained by the denudation, which at the latest began in the early Oligocene; this can be deduced from the condition of the Eocene/Oligocene volcanoes (Büchel, 1990).

Within the present-day Moselle valley, Tertiary sediments also accumulated in a wide subsiding zone extending eastwards toward the Neuwied Basin which was connected to the Paris Basin in the west. Such sediments are preserved in Eckfeld, at the southern boundary of the High Eifel volcanic field. Here, layers of Eocene sediments accumulated in a small lake and are underlain by basaltic tuffs. Therefore Negendank et al. (1982) consider this feature to be an Eocene maar. The tuffs might also have been ejected by the Tertiary volcanoes, located in the vicinity (Büchel, 1990). Geological and geophysical investigations conducted by Pirrung (1992, 1997) confirmed the hypothesis of Negendank.

To the south of the Eifel occur Tertiary sediments which correspond to the Upper-Eocene to Lower-Oligocene sand- and gravel layers of tributaries of the old Moselle river (Löhnertz, 1978).

In the Antweiler Graben, north of the High Eifel, Oligocene sands and gravels with clay and brown coal layers overlie Eocene clays (Knapp, 1978). In the North Eifel, beside Pliocene sediments, Oligocene-Miocene sediments occur only as relics of the erosion. These sandy-clayey rocks are referred to as Cologne layers (Ledoux, 1987).

From the beginning of the Tertiary till the end of the Mid-Oligocene, the Eifel had a very uniform topography. In the transition period between the Middle and Upper Oligocene, the Eifel was subject to vertical tectonics which particularly led to the formation of the Rhenish Embayment and the Neuwied Basin. In the Upper Eocene, the Eifel was briefly flooded by the sea (Sonne and Weiler, 1984). The filling of the Neuwied Basin — clay-, mergel and brown coal series — basically took place in the Oligocene and to a lesser degree in the Upper-Eocene.

In the Miocene, the Central Eifel was subject to denudation. Within the Low Rhenish Embayment gravels, sands and mainly clays and coal accumulated, which are preserved in small tectonic depressions between the Neuwied Basin and the Low Rhenish Embayment. In the Pliocene, the climate became cold and a fluviatile sedimentation takes place in the Rhine and Moselle valleys. In the Pleistocene, depressions were deeply eroded.

During the Pleistocene, the Eifel was a periglacial area. After the formation of the main terraces 0.6 Ma ago (Bibus and Semmel, 1977), the volcanic activity began in the West Eifel and a bit latter, 0.5 Ma, in the East Eifel (Büchel, 1990). In the beginning of the glacial period, antecedent deep and sloping valleys formed in connection with a strong uplift of the Rhenish Schield. In the Quaternary, those High Eifel volcanoes located in the valleys, suffered deep erosion, following strong denudation in the Tertiary.

2.1.5 The Eifel volcanism

The information about the oldest volcanic activity/rocks in the Eifel area is based on the results of the K-Ar dating conducted by Lippolt (1983). After him, the oldest volcanic rocks, melilite nephelinites, occuring at the southern boundary of the High Eifel volcanic field in the northern part of the Lower Permian Wittlich Basin, are more than 100 Ma old (Lippolt, 1983). Rocks of the same age have been identified also at the western boundary of the High Eifel volcanic field (Müller-Sohnius et al., 1989).

The main volcanic activity of the Eifel started in the Eocene (about 45 Ma ago) and kept on through the Oligocene until the Earlier Miocene. This Tertiary volcanism, spread in the High Eifel area, is represented by rocks of varied composition: trachytes, benmoreites, alkali olivine basalts (hawaiites, mugearites), nepheline basanites and hornblende bearing basalts (Huckenholz, 1983).

The Quaternary volcanic activity, which began about 0.6 Ma ago (Lippolt, 1983; Büchel and Lorenz, 1982, Mertes and Schmincke, 1983), is spread out in the West Eifel and East Eifel areas. The Laach Lake and the Ulmen Maar, with an approximate age of 11000 and 10000 years, respectively, are the youngest volcanic occurences of the Eifel (Büchel, 1990). The East and West Eifel volcanic fields strongly differ from one another concerning the number and the volume of volcanoes and as the relative fraction of intermediate and highly differentiated magmas. The length (50 km NW/SE), the area (600 km^2) and the number of volcanoes (250) of the West Eifel exceed those of the East Eifel (about 35 km NW/SE, 400 km^2, and 100). However, the volume of the erupted magma in the Laach Lake volcano (about 5 km^3) on its own is approximately twice that of all West Eifel volcanoes (about 3 km^3) (Frechen, 1976; Lorenz and Büchel, 1980; Büchel and Mertes, 1982; Schmincke et al., 1983; Lorenz, 1984; Büchel, 1990). In both the West and East Eifel, geological studies (Büchel and Lorenz, 1982; Büchel and Mertes, 1982; Mertes, 1983; Büchel, 1984) have shown that the youngest volcanoes are concentrated in the eastern and southeastern parts of the respective volcanic fields. That means that the centre of the volcanic activity has migrated from the Northwest to the Southeast. Nephelinites, leucite nephelinites, melilite nephelinites, nepheline leucitites, basanites and phonolites are the main rock types of the Eifel Quaternary volcanism (Mertes, 1983).

2.2 The West Eifel volcanic field

The West Eifel volcanic field (Fig. 2.2) is 50 km long and 20 km wide. The 600 km^2 big volcanic field extends in a NW-SE direction (130°) (Mertes, 1983; Büchel, 1984). The volcanic activity in this area began in the late Quaternary, probably in connection with stronger vertical tectonic movements of the Rhenish Massif and went on up to 10000 years ago. About 250 eruption centres have been identified to the present day. The oldest volcanic features, the majority, are concetrated in the central part while the youngest are in the South-East (Büchel and Mertes, 1982).

Depending on the origin and the form, the following types of volcanoes are known in the West Eifel (Büchel and Mertes, 1982):

- Scoria cones ($\approx$ 66%); they are on average 40 m high (max. 100 m) and 430 m wide (max. 1000 m); about 50% of them have lava flows (in some cases several kilometers long).
- Maars ($\approx$ 25%) with diameters from 70 m to 1700 m.
- Tuff-rings ($\approx$ 5%) with diameters from 70 m to 1400 m.
- Scoria rings ($\approx$ 2%): very small volcanoes with very gentle slopes.
- Diatremes ($\approx$ 2%): strongly eroded maars or tuff-rings, the crater of which is difficult to recognize.

Although erupted magmas generally are K-rich and SiO_2- undersaturated nephelinites, leucitites and basanites with a predominant mafic character, petrographic/geochemical analyses (Mertes, 1983) have shown that those volcanic rocks of phreatomagmatic origin (maars, tuff-rings, diatremes) contain melilite whereas the others (scoria cones, scoria rings) contain leucite and nepheline.

It is important to point out that the West Eifel volcanoes sometimes occur in complex groups with eruption centres forming areal clusters close to each other or lying in a line. These groups, usually referred to as volcanic or eruption systems (Lorenz and Büchel, 1980[b]), are believed to have erupted at about the same time each or within a very short period (Büchel, 1984). Moreover, taking into account that the volcanic activity in the West Eifel was highest within the last 100000 years (Mertes, 1983) and that tectonic processes such as vertical tectonic movements (Mälzer et al., 1983), crustal rifting and seismicity (Ahorner, 1983) are still occuring at the present day in the Rhenish Massif, it is not excluded that new eruptions might take place in this area (Büchel, 1984). These processes are obviously the continuation of the Quaternary tectonic phase that generated the Quaternary volcanism. Recent geophysical investigations showed that all the processes mentioned above, including the volcanism, are directly connected with the Eifel plume which derives from the upper mantle and the ascent of which is intermittent (Ritter et al., 2001).

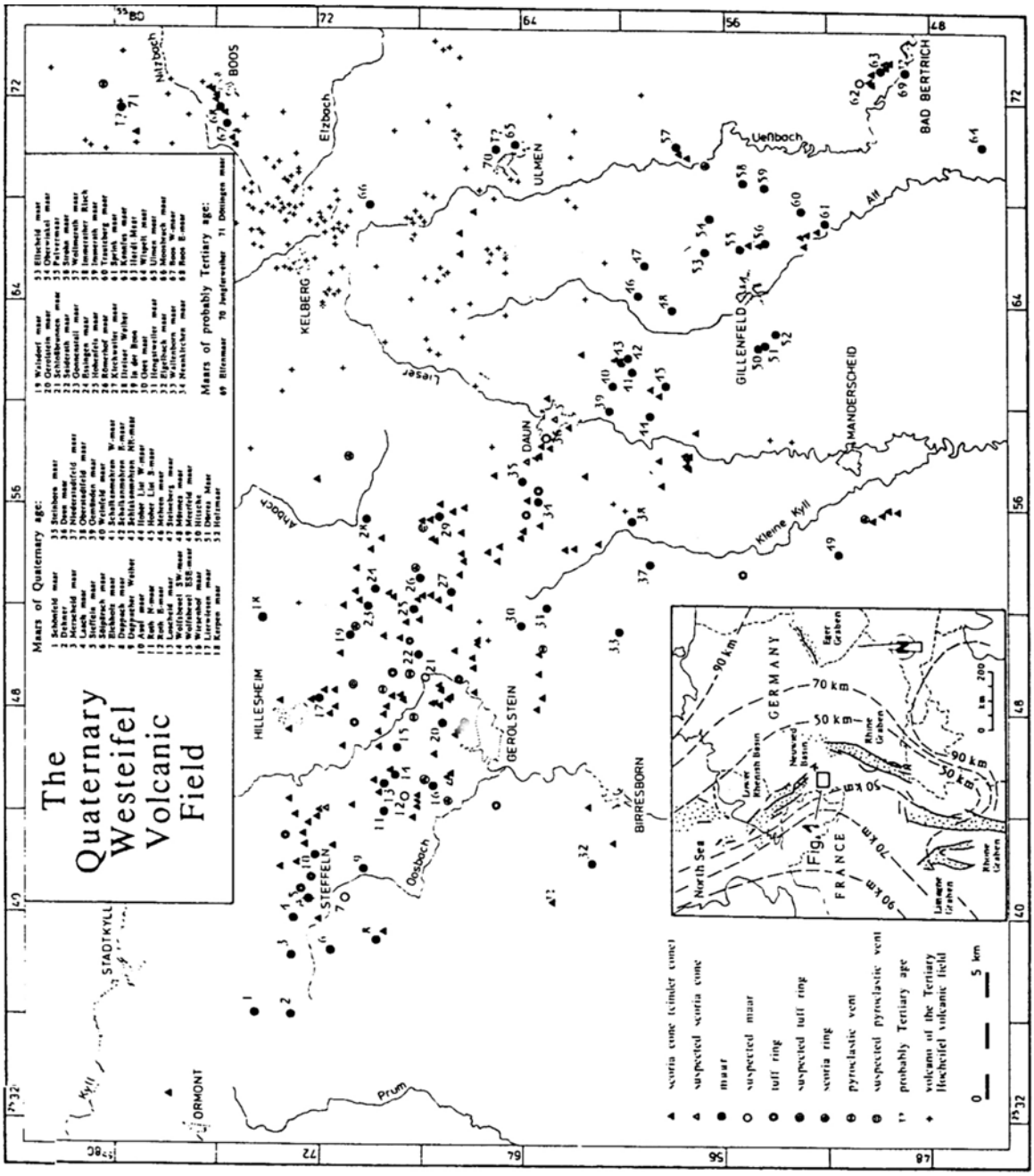

Fig. 2.2 Map of the eruption centres of the Quaternary Westeifel Volcanic Field (triangles and circles). Crosses mark the the volcanoes of the Tertiary Hocheifel Volcanic Field (after Büchel and Mertes, 1982).

2.3 Phreatomagmatic volcanism

Maar-diatreme volcanoes differ from ordinary volcanoes by the mechanism of their formation and their morphology. While the ordinary volcanism is driven by gases ejecting the upgoing magma to form volcanic edifices above the Earth's surface, the explosion volcanism which gives rise to the formation of maar-diatreme volcanoes is caused by magma/water interaction (Lorenz, 1985, 1986; Schmincke, 1986). The process, usually referred to as phreatomagmatism, depends on the magma/water ratio and the hydrostatic pressure. It results in the formation of complex structures ranging from maar-diatremes through scoria rings to tuff rings. The phreatomagmatic activity usually occurs along fracture or fissure zones, where surface and/or groundwater is available (Lorenz, 1973, 1986).

At the initial phase of the eruption, which normally occurs at shallow depth a maar is formed (Fig. 2.3, A). A maar is a volcanic crater cut into country rocks below the Earth's surface and surrounded by a low rim of ejecta, the thickness of which may reach a maximum of 40 m and decreases outwards (Lorenz, 1973 and 1986; Wood, 1974). Maars have diameters ranging from less than 100 m up to more than 1500 m and depths range from tens of metres to 200 m and more. The erupted material is mostly composed of country rock debris and a small proportion of juvenile pyroclasts. Subsequent eruptions associated with downward migration of the explosion centre (as confirmed by experiments, Woolsey et al., 1975) lead to the collapse of the walls of the former structure and to a continuous growth in depth and width. As a result, a diatreme is formed. A cone-shaped structure, also called pipe, is the subsurface feeder structure of the maar. At depth, the diatreme might extend into igneous dikes. While the diatreme is probably cut by a system of precursor dikes in its root zone (Clement, 1982; Lorenz, 1986), it is not excluded that a series of late dikes might intrude its body upwards. The diameters of diatremes are in the same range as those of maars but their depths may reach a maximum of 2000–2500 m. The filling of the diatreme is made of pyroclastic debris (tuff or lapilli tuff) and blocks of wall rocks. In the posteruptive phase a crater lake forms in the maar and its bottom is continuously filled by sediments (Fig. 2.3, B and C). As time goes on, the crater lake might dry up and the maar-diatreme is subject to erosion (Fig. 2.3, D and E).

It has been mentioned above that the magma/water ratio is the major controlling factor of the phreatomagmatic volcanism. Beside maar-diatremes, scoria cones, scoria rings or lava lakes may form within the maar if there is no more water to interact with the ascending magma. In contrast, instead of maars, tuff rings will form if large amounts of water are available. Being similar to maars in shape and size, tuff rings are large volcanic craters above the Earth's surface with shallow diatremes underneath (Fig. 2.4). The composition of their ejecta is predominantly made up of juvenile pyroclastic material with a small fraction of country rock clasts.

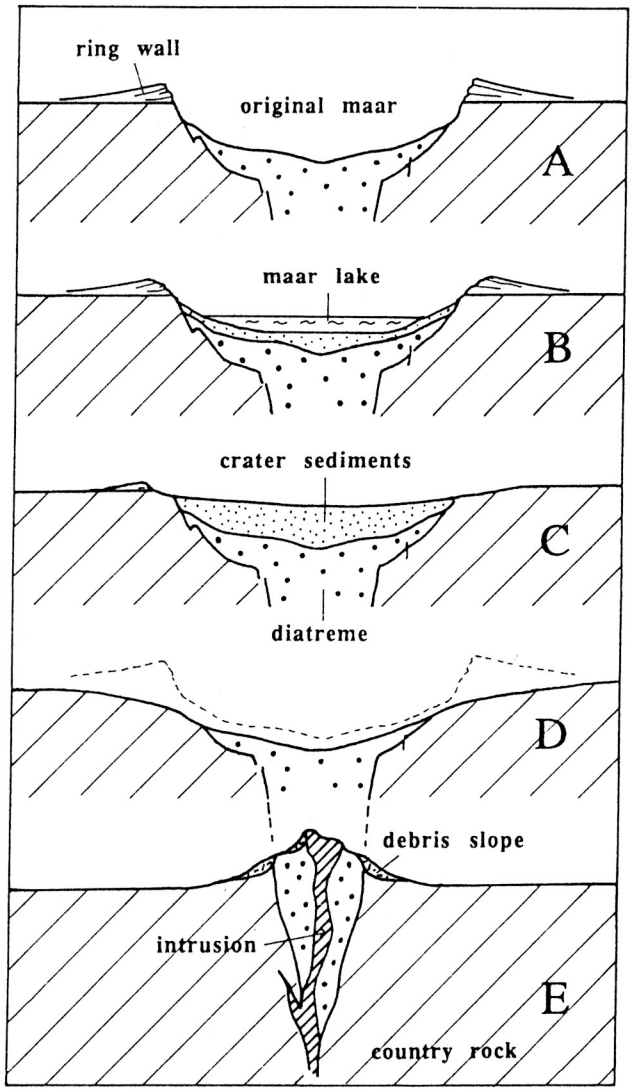

Fig. 2.3 Schematic plot of the post-eruptive evolution of a maar-volcano in four stages. A: initial stage, B: lake stage, C: post-lake stage, D and E : post-sedimentary erosion stages (from Büchel, 1984).

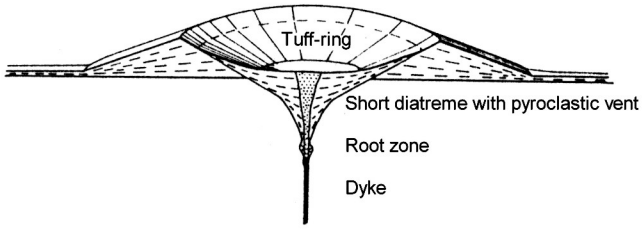

Fig. 2.4 Schematic representation of a tuff-ring and its supposed shallow diatreme · (after Lorenz, 1985)

2.4 The West Eifel maars

Owing to geophysical investigations and geological mapping, the number of recognized West Eifel maars has recently increased to more than 60. Most of them are located in fracture-controlled valleys (Lorenz, 1973; Lorenz and Büchel, 1980; Büchel and Mertes, 1982; Mertes, 1983; Schmincke et al., 1983; Büchel, 1984); the fractures are favourable pathways for circulating water and rising magma. The West Eifel maars have diameters between 70 and 1700 m; their depth varies between 10 and 180 m (Lorenz, 1982). Eight young maars have lakes in their craters and still preserve their tuff-rims. Older maars, whose tuff-rims and crater walls have been partially or completely eroded and denudated, are dry and filled up by sediments. Intermediate between the two types, some maars contain marshes. Petrographic studies (Negendank et al., 1982; Haverkamp, 1984) of drill cores and samples from different maars have shown that crater lake sediments are often made up of pyroclastics (bottom), sapropel deposits (diatomites, shales) and terrigenous material (clay, silt, clayey silt and silty clay).

Mostly, country rocks (Devonian clayey schists, sandstones, quartzites, graywackes, dolomites and limestones and Mesozoic sandstones as well) are exposed at the crater walls. The crater rims and walls consist of maar tuffs. The bottom of the maars is underlain by pipe structures (diatremes) filled with maar tuffs. Maar tuffs are composed of fragments of the erupted magmas (ashes with a grain size less than 2 mm of diameter, lapilli, between 2 and 64 mm, and bombs, larger than 64 mm) and of debris of the country rocks in the same grain size as the juvenile material: ashes, lapilli and blocks instead of bombs (Lorenz and Büchel, 1980; Lorenz, 1982).

After radiometric (^{14}C) dating, the maar volcanism and that of the scoria cones in the West Eifel have developed in the same time interval (Lorenz, 1973; Büchel and Lorenz, 1982). This means that there should exist old maars deeply eroded which geomorphologically can not be easily distinguished from the surrounding environment.

2.5 Physical rock properties

The Devonian sedimentary rocks of the West Eifel are represented by schists and sandy schists. As given by Telford et al. (1990), the average susceptibility and density of such rocks amounts to about 1500×10^{-6} SI and 2.64 g/cm^3, respectively. Kohnen et al. (1976) and Mertes (1983) gave a mean density of 2.5 g/cm^3 for the Devonian rocks of the West Eifel. As shown by density determinations conducted by Bannert (1989) for Devonian rocks in the Mosbruch Maar area, their density varies according to grain size: 2.51 g/cm^3 for massive rocks, 2.64 g/cm^3 for fine grained rocks and 2.76 g/cm^3 for coarse grained ones. Pirrung (1992) determined a value of 2.56 g/cm^3 for Lower Devonian rocks in the Eckfeld Maar area.

Magnetic properties of Quaternary West Eifel volcanics (lava flows and surface tuffs) have been studied by Cipa (1958), Böhnel et al. (1988) and Herzog et al. (1988). Values of the magnetic susceptibility of the tuffs given by Cipa lie betweeen 600 and 1800×10^{-6} SI while those determined by Böhnel et al. are about ten times higher ($\approx 10000\times10^{-6}$ SI). After Böhnel et al., the Königsberger ratio (Q-factor) of the tuffs is about 1.2, which means that the **N**ormal **R**emanent **M**agnetisation (NRM) component is about as strong as the induced one. Beside tuffs, other volcanic rocks have been sampled and investigated. The results have shown that the magnetic declinations vary in a broad range while the inclinations mainly vary in the range from 50 to 80°. Haverkamp (1984) has done paleomagnetic measurements of the Meerfeld Maar sediments. Both the intensity of the NRM

and the susceptibility of the sediments increase with depth. The susceptibility varies between 100 and 800×10^{-6} SI. The NRM reaches values of 0.1 A/m at 20 m depth. The inclination has a mean value of 52°, which is less than the expected one (67°) for the Eifel region. This means that the inclination is connected rather with the **D**epositional **R**emanent **M**agnetisation (DRM) than with the geomagnetic field.

In order to get more information about the density and magnetic properties of the tuffs and sediments of the West Eifel maars, I sampled eleven maars for laboratory measurements. For maar tuffs (single sample per maar), the results are shown in Table 2.1. The Quaternary West Eifel maar tuffs have densities ranging approximately between 1.7, for the brittle type with a little fraction of volcanic material, and 2.3 g/cm^3, for the compact type with more magmatic material (palagonite tuffs). Density values of samples from nine maars gave a mean of (1.98 ± 0.20) g/cm^3. This value is in good agreement with the value of 2.0 g/cm^3 given by Mertes (1983) for Quaternary maar tuffs and that of 2.07 g/cm^3 given by Bannert (1989).

The susceptibility and the remanent magnetization of the West Eifel maar tuffs vary in a wide range and are, as expected, controlled by the texture and the structure of the rock, by the magmatic fraction and probably by the time, since the sedimentation. Brittle and porous units with a small volcanic fraction are characterized by low values, massive compact tuffs by medium values, and palagonite tuffs by high values. As shown in Table 2.1, the susceptibility and the remanent magnetization have mean values of $(10190 \pm 3660) \times 10^{-6}$ SI and (1.17 ± 0.48) A/m, respectively. The Q-factor of the sampled maar tuffs, determined for an assumed present day Earth's magnetic field strength of about 48000 nT in the Eifel area, has a mean value of (2.8 ± 0.7). This again shows that a certain NRM, higher than twice the induced one, is present. While the values of the susceptibility are in good agreement with those determined by Böhnel et al., those of the Q-factor are relatively higher. This might result from different instrument precision or man made measurement errors. Note that Böhnel et al. have used only two samples, which might not be representative. It seems that Cipa mistook units of the susceptibility; the values given by him obviously are in CGS-units, which are greater than SI-units by a factor of 4π.

It should be noticed that the maar tuffs were sampled at the surface, where they likely are weathered. Thus, their density and their susceptibility might probably be higher at deeper levels. Moreover, other factors such like compaction and cementation might also contribute to the increasing effect.

Magnetic directions (declination and inclination) are of irregular character. Taking into account that the Quaternary Eifel maars were formed within a broad period — between about 600000 and 10000 years ago (Büchel and Lorenz, 1982) — which belongs to the first chron (0.0–0.73 Ma) of a normal polarity of the geomagnetic field (Cox and Hart, 1986), the elements of the latter might have been remarkably different due to secular variations. After Cox and Hart, at some localities the orientation of the geomagnetic vector has changed by 20° in a century. These secular variations can last 10 to 10^4 years.

Density and susceptibility determinations for maar sediments have been conducted using three samples from the Neunkirchen Maar and four samples from the Dehner Maar. As can be deduced from the results shown in Tab. 2.2, maar sediments are generally characterized by low densities and susceptibilities with mean values of (1.58 ± 0.15) g/cm^3 and $(205 \pm 130) \times 10^{-6}$ SI, respectively. Other densities for Cenozoic sediments ranging from 1.80 to 2.15 g/cm^3 have been reported (Schön, 1983). Density determinations conducted by Pirrung (1992) for the Eckfeld Maar sediments gave values of 1.6 to 2.0 g/cm^3. The

intensity of the remanent magnetization with a value of 0.04 A/m has been determined only for one sample of the Neunkirchen Maar. The values of both the susceptibility and the remanent magnetization are in the same range as those of the Meerfeld Maar determined by Haverkamp (1984, see above).

Table 2.1 Density and magnetic properties of the tuffs of the West Eifel maars.

Name	Description	Density ρ $[g/cm^3]$	Suscept. χ $[\times 10^{-6} SI]$	NRM [A/m]	Q-Factor	D [°]	I [°]
Schalken-mehren Maar	massive ash tuffs	1.82	14990	2.113	3.7	355	−29
Kirchweiler Maar	massive tuffs	1.86	10070	0.862	2.2	142	64
Pelm Maar	palagonite tuffs	2.35	26250	6.114	6.1	327	32
Roth Maar	massive tuffs	1.75	7800	0.573	1.9	132	−15
Lach Maar	massive palagonite tuffs	2.17	16223	1.273	2.0	241	−7
Schönfeld Maar	massive tuffs	1.92	11055	1.220	2.9	53	70
Essingen Pipe	porous tuffs	2.00	7026	1.035	3.9	96	72
Mosbruch Maar	massive tuffs	1.98	9511	1.122	3.0	5	−60
Pulver Maar	massive tuffs	1.85	4620	—	—	—	—
		$\bar{\rho} = 1.96$ $\sigma = 0.20$	$\bar{\chi} = 10160^*$ $\sigma = 3660$	$\bar{I} = 1.171^*$ $\sigma = 0.478$	$\bar{Q} = 2.8^*$ $\sigma = 0.70$	—	—

$\bar{\rho}$, $\bar{\chi}$, $\bar{I}$, $\bar{Q}$: mean values for tuffs' samples; * without consideration of the Pelm Maar; σ : standard deviation of the mean value.

Table 2.2 Density and magnetic properties of the crater lake sediments of the West Eifel maars.

Name	Description	Density ρ $[g/cm^3]$	Susceptibility χ $[\times 10^{-6} SI]$
Dehner Maar	crater sediments: 2.8 m depth black clayey lake sediments	1.58	160
Dehner Maar	crater sediments: 3.0 m depth dark-grey clayey lake sediments	1.50	130
Dehner Maar	crater sediments: 3.2 m depth bright-grey clayey lake sediments	1.59	120
Dehner Maar	crater sediments: 6.9 m depth yellowish lake sediments with magmatic fraction	1.88	185
Neunkirchen Maar	fine and layered sediments	1.43 1.58 1.50	432
		$\bar{\rho}_s = 1.58$ $\sigma = 0.15$	$\bar{\chi}_s = 205$ $\sigma = 130$

$\bar{\rho}_s$, $\bar{\chi}_s$ – mean density and susceptibility of the Dehner and Neunkirchen sediments
σ – standard deviation of the mean value

Extra density and susceptibility determinations have been done for the crater sediments and the scorias of the Schönfeld Maar (Table 2.3). Sediments sampled along a cobra drillhole within the maar crater up to 7.5 m depth are characterized by a mean density of (2.05 ± 0.10) g/cm^3 and a mean susceptibility of $(10000 \pm 300) \times 10^{-6}$ SI, values which are very similar to those of the maar tuffs. These sediments, which mainly are made of lapilli tuffs and lapilli- ash tuffs with a high content of magmatic fraction (scoria) are not lake sediments but probably redeposited maar tuffs, eroded from the crater rim or result from later eruptions, which took place with a less pronounced or without water-magma interaction. Some scorias have been observed at the north-eastern boundary of the Schönfeld Maar. Two samples of scorias have given density values of 1.90 and 2.65 g/cm^3 and susceptibilities of 15440×10^{-6} SI and 29415×10^{-6} SI.

Table 2.3 Density and magnetic properties of the crater sediments and scorias of the Schönfeld Maar.

Name	Description	Density ρ $[g/cm^3]$	Susceptibility χ $[\times 10^{-6} SI]$
Schönfeld Maar	dark and dense scorias with micas (NE boundary)	2.65	29415
Schönfeld Maar	brittle and light scorias with yellowish clayey material (NE boundary)	1.90	15440
Schönfeld Maar	crater sediments: 0.5-1.5 m depth sandy clay, debris of devonian rocks and basaltic scorias probably redeposited tuffs	2.18	14250
Schönfeld Maar	crater sediments: 1.5-2.5 m depth clayey sand, clay (ash tuffs) probably redeposited tuffs	2.10	10790
Schönfeld Maar	crater sediments: 2.5-3.5 m depth coarse grained silt, lapilli ash tuffs	2.10	10095
Schönfeld Maar	crater sediments: 3.5-4.5 m depth lapilli ash tuffs with augite grains and lapilli ash tuffs with clay matrix	2.00	11185
Schönfeld Maar	crater sediments: 3.5-4.5 m depth lapilli ash tuffs with augite grains and lapilli ash tuffs with clay matrix	2.00	11185
Schönfeld Maar	crater sediments: 4.5-5.5 m depth and lapilli ash tuffs with clay matrix lapilli ash tuffs with augite grains, country rocks debris and black scorias	2.10	14810
Schönfeld Maar	crater sediments: 5.5-6.5 m depth clayey-sandy silt with micas	1.85	10055
Schönfeld Maar	crater sediments: 6.5-7.5 m depth lapilli ash tuffs, clayey silt	2.15	10670

3. Brief theoretical review of geophysical inversion

3.1 The Geophysical Inverse Problem

As already mentioned, geophysical inversion consists in extracting parameters of a subsurface structure from a set of measurements of a definite physical field. This is done by trying to fit synthetic data computed for a set of parameters of the conceived model to actual observations. The whole procedure is also referred to as modeling. Modeling needs necessarily taking into account some a priori information. The estimated parameters can never be unique since observed data always contain effects which we are not able to explain in geologic terms. Thus, even the achieved solution which fits the observations within a prescribed error must be thought of as one of the candidate solutions and presented with probabilistic bounds.

3.1.1 Formulation and solution of the geophysical inverse problem

In most cases, the relationship between the geophysical model effects and the model parameters is nonlinear. However, all methods used to solve discrete geophysical problems are based on the solution of the linear inverse problem. This is well understandable since the mathematical techniques to be used have been developed on the basis of the solution of linear systems. The nonlinearity is dealt with by using linear approximation (linearization about a given model) and further proceeding with iterative techniques.

3.1.1.1 The Linear Inverse Problem

The simplest inverse problem is the linear problem. A problem is said to be linear if it is of the form:

$$Am = y \tag{3.1}$$

where

y is a set of, say, M observations; $\mathbf{y} = (y_1, y_2, y_3, \ldots y_M)^T$ †

m is a set of, say, N parameters; $\mathbf{m} = (m_1, m_2, m_3, \ldots m_N)^T$

A is a certain linear operator, also called data kernel, in the form of a $M \times N$ matrix.

In the matrix notation the linear problem can be formulated as follows:

$$\begin{bmatrix} A_{11} & A_{12} & \ldots & A_{1N} \\ A_{21} & A_{22} & \ldots & A_{2N} \\ A_{31} & A_{32} & \ldots & A_{3N} \\ A_{41} & A_{42} & \ldots & A_{4N} \\ \vdots & \vdots & \ddots & \vdots \\ A_{M1} & A_{M2} & \ldots & A_{MN} \end{bmatrix} \begin{bmatrix} m_1 \\ m_2 \\ \vdots \\ m_N \end{bmatrix} = \begin{bmatrix} y_1 \\ y_2 \\ y_3 \\ y_4 \\ \vdots \\ y_M \end{bmatrix}$$

where $A_{11}, A_{12} \ldots A_{MN}$ are the elements of the operator A.

† T denotes the transposed matrix

3.1.1.2 Methods for solving the Linear Inverse Problem

The method for solving a linear inverse problem is determined by the way how one wants to measure the size, or length, of the vector of the estimated model parameters m^{est} and that of the predicted data $f = Am^{est}$.

A measure of length or size is normally referred to as a norm. The mostly used norms are those based on the sum of some power of the components of a given vector. These norms are known as the L_n norms, where n is the power. Given a vector $\mathbf{V}$ with the components v_i $(i = 1, 2, \ldots p)$, its norm $\|V\|$ with respect to the power n $(n = 1, 2, \ldots \infty)$ can be expressed as follows:

$$L_1 norm : \|V\|_1 = \left[\sum_i |v_i|^1\right]$$

$$L_2 norm : \|V\|_2 = \left[\sum_i |v_i|^2\right]^{1/2}$$

$$\vdots$$

$$L_n norm : \|V\|_n = \left[\sum_i |v_i|^n\right]^{1/n}$$

When n tends to infinity $(n \to \infty)$ the L_∞ norm is equal to the greatest of all absolute values of the elements of the vector i.e.,

$$L_\infty norm : \|V\|_\infty = max_i |v_i|$$

The norm to be used for estimating a quantity is defined by the approach to weighting the data that fall far from the general trend (Fig. 3.1). For data which are believed to be accurate enough, the fact that a datum falls far from the trend is of importance. In this case a high order norm should be used to give more weight to that datum. On the other hand if the data are widely scattered, a more equal weight should be given to them by using a low order norm. We see that the statistics of the data (data distribution) is decisive for choosing the norm under which a quantity might be estimated.

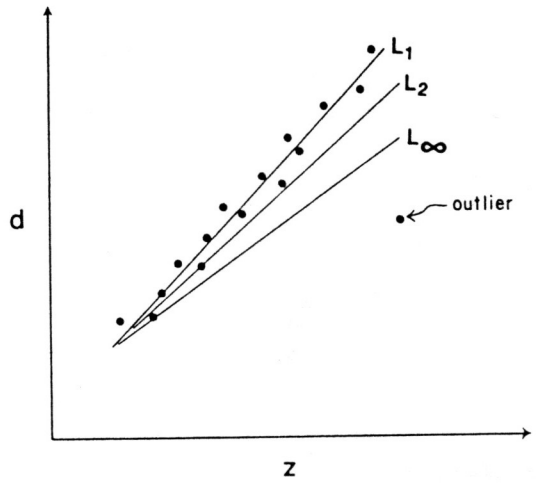

Fig. 3.1 Straight line fits to (z, d) pairs where the error is measured under the L_1, L_2 and L_∞ norms. The L_1 norm gives least weight to the one outlier; (from Menke, 1984).

Data with a wide scatter have a long-tailed distribution, whereas those with less scatter have a short-tailed distribution (Fig. 3.2). The most frequently encountered distribution is the short-tailed one which is classically known as the Gaussian or normal distribution. For data obeying this distribution a point falling far from the average will be given a considerable weight; hence the use of a high norm — usually — the L_2 norm. Moreover, as can be seen in Fig. 3.1, the L_2 norm can be considered as a compromise between the L_1 norm and the higher norms for measuring the length.

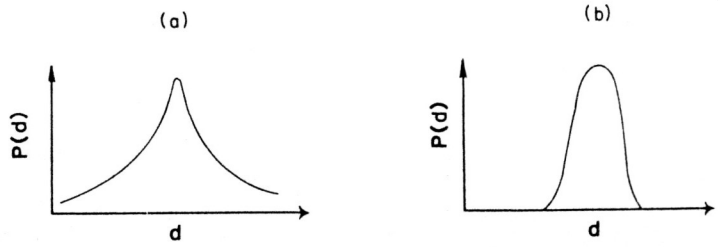

Fig. 3.2 (a) Long-tailed distribution; (b) Short-tailed distribution; (from Menke, 1984).

There are several methods based on the L_2 norm, but the most customary one is the so called "**Least-Squares**" method. This method has been widely and successfully used in applied geophysics for solving inverse problems. The method consists of solving an inverse problem by minimizing the predicted error or the solution length or the combination of both quantities measured under the L_2 norm.

Beside those methods based on the L_2 norm another group of methods based on the L_1 norm finds a common use for solving linear inverse problems. These methods are especially used to solve problems, where data obey a long-tailed distribution or problems in which data have Gaussian statistics but are of bad quality (data with saddles or outliers). The best known method is the one involving linear programming. Another successful and

robust method — the FIFO† method — has been worked out by J. Claerbout and F. Muir in 1973 and later, also well described by A.Tarantola (1987).

3.1.1.3 The Standard Least-Squares Method

The Least-Squares method consists in fitting the predicted data to observations by minimizing a misfit function (also called chi-squared function) which is the sum of squares of errors between the two sets of data. Let

y_i be a set of observations (i = 1, 2, ...M);

f_i be a set of predicted data (i = 1, 2,...M);

m_j be a set of model parameters (j = 1, 2, ...N);

If the problem is assumed to be linear, the predicted data f_i are related to the model parameters m_j by the following expression: $Am = f$, where A is a linear operator. We then define the error e_i as the difference between y_i and the corresponding f_i, i.e., $e_i = y_i - f_i$ or in vector form

$$e = y - Am \tag{3.2}$$

The misfit function which we refer to as **E** is the sum of the squares of all e_i (i = 1, 2, ...M)

$$E = \sum_{i=1}^{M} e_i^2$$

or in matrix notation $E = e^T e$. From (3.2)

$$E = e^T e = (y - Am)^T (y - Am)$$

Our aim is to determine those model parameters for which the misfit function **E** will assume its minimum value. From classical mathematics, we know that a function has a minimum when its first derivative with respect to a given variable is zero. Hence the minimization of the misfit function **E** with respect to the model **m** requires that $\partial E/\partial m$ be equal to zero.

$$\frac{\partial E}{\partial m} = 0 \Longrightarrow \frac{\partial}{\partial m}\Big[(y - Am)^T (y - Am)\Big] = 0$$

After some matrix and differentiation operations, we get

$$A^T Am - A^T y = 0$$

or

$$A^T Am = A^T y \tag{3.3}$$

The relation (3.3) is a linear system of the so-called normal equations. Assuming that the inverse of the square matrix $A^T A$ exists, m can be determined from (3.3)

$$m = [A^T A]^{-1} A^T y \tag{3.4}$$

† FIFO stands for first in, first out

which is the least-squares solution of the linear inverse problem, also called the Gauss-Newton solution.

3.1.1.4 Classification of inverse problems

Depending on how much information is contained in the equation Am = y for determining the model parameters, inverse problems can be classified into the three following groups:

a) underdetermined problems in which the information is insufficient. In such problems, one is faced with the task of determining model parameters using insufficient data. Classically, the underdeterminancy arises in problems, where there are more unkowns than data.

b) overdetermined problems for which the equation Am = y contains too much information capable of contributing to better approximating the solution. Such problems are characterized by a greater number of data than of the model parameters. Most problems in geophysics are formulated this way by the assumption of a sufficiently small number of model parameters.

c) even-determined problems which have just sufficient information for determining the unique existing solution.

3.1.1.5 The standard least-squares solution of the linear inverse problem

Having classified geophysical inverse problems, let us examine the relevance of the least-squares solution to them.

In problems which are assumed to be completely *overdetermined*, the solution is found by minimising the overall predicted error $E = e^T e$. This is done by using the **" Least-Squares Method "** to yield the solution

$$m^{est} = [A^T A]^{-1} A^T y \tag{3.5}$$

In purely *underdetermined* problems, where we have an infinite number of solutions with a zero prediction error, additional information (a prori information) is needed to help us to single out a suitable solution. One of the guiding characteristics while solving geophysical inverse problems is to yield a solution which is simple. The characteristics can be used as a priori information in solving problems of this type. A solution is said to be simple if its measure under a certain norm is small. This means that under the L_2 norm, a solution is expected to be simple if its Euclidean length $L = m^T m$ is small. The approach to solve the underdetermined linear problem is the same as that for the overdetermined one. Only in this case, we want to determine parameter estimates m^{est} which, while satisfying the equation Am = y (predicted error = 0), minimize the solution length $L = m^T m$ at the same time. Without going into mathematical details of this problem, its solution looks like

$$m^{est} = A^T [A A^T]^{-1} y \tag{3.6}$$

The relation (3.6) is the minimum length solution of the underdetermined problem.

Geophysical problems are often considered to be overdetermined. But this fact can never be proved. This is only an assumption. It might happen that some parameters are not introduced into the problem because we are not able to see them. The same holds for underdetermined problems. The underdeterminancy might occur just because of some superfluous parameters. Therefore, instead of solving a purely overdetermined or underdetermined problem, one solves rather the so called **" mixed-determined "** inverse problem.

The strategy consists in solving an overdetermined problem which is supposed to contain a slight indeterminancy. The problem could be well solved only if we were able to form a new model m' — a linear combination of the old one m — and then partition it into two parts: the overdetermined part $m^{o'}$ and the underdetermined one $m^{u'}$. Consequently, the data would be divided into two sets: one $y^{o'}$ and another $y^{u'}$ related to the overdetermined and underdetermined model parameters, respectively.

In terms of linear algebra, from the system Am = y a new system $A'm' = y'$ will be formed, which would be composed of two sets of linear equations:

$$\begin{bmatrix} A^{o'} & 0 \\ 0 & A^{u'} \end{bmatrix} \begin{bmatrix} m^{o'} \\ m^{u'} \end{bmatrix} = \begin{bmatrix} y^{o'} \\ y^{u'} \end{bmatrix}$$

Having this operation done the upper part of the system might be solved in the least-squares sense giving the overdetermined part of the model whereas the underdetermined part might be given by that solution of the lower part of the system which has the minimum L_2 length. The **S**ingular **V**alue **D**ecomposition (SVD) is the most popular technique used to carry out such a partitioning procedure.

Another alternative in common use — instead of dealing with the partitioning procedure which is time consuming — is to find the solution by minimizing a function Φ which is the combination of the prediction error E and the solution length L:

$$\Phi(m) = E + \epsilon^2 L$$

or in matrix notation

$$\Phi(m) = e^T e + \epsilon^2 m^T m$$

where ϵ^2 is a factor which weighs the relative importance of one or the other component of the function. If ϵ has a significantly large value, both the overdetermined and the underdetermined part will be minimized. Consequently, the solution will not minimize the prediction error E and the estimated parameters will not be good representatives of the real ones. On the other hand, if ϵ is too small ($\epsilon \to 0$), the weight of the component $\epsilon^2 m^T m$ will be negligible. Here the prediction error E will be minimized but we are not able to single out the underdetermined model parameters because of the lack of a priori information.

A better suitable value of ϵ^2 is that which would lead to a solution with the least prediction error E and the minimum length at the same time. In practice, this compromise value is determined by the **trial and error** method.

The approach for solving a mixed-determined problem is the same as the one for the least-squares solution. The minimization of the function $\Phi(m)$ with respect to the model parameters leads to the solution

$$m^{est} = \left[A^T A + \epsilon^2 I\right]^{-1} A^T y \tag{3.7}$$

(3.7) is known as the "**damped least-squares solution**" (Menke, 1984; Lines and Treitel, 1984), also called in the literature the solution of the constrained least-squares problem by the so-called Marquardt-Levenberg method (Levenberg, 1944; Marquardt, 1963) or by the ridge regression (Hoerl and Kennard, 1970; Marquardt, 1970; Inman, 1975). The concept of this method is to bound the solution in order to avoid large fluctuations; which leads to a smoothed solution. It has the advantage of considering not only the prediction error but also the solution error, hence damping the indeterminancy of the inverse problem.

3.1.2 Enhancing the solution of the linear inverse problem

In most of cases, geophysical inverse modeling involves a great amount of data (experimental, theoretical and model parameters) and a lot of computations. Each of the above elements has its particular influence on the behaviour of the solution and on the model parameter estimates. It is well known that observations may contain errors of statistical and/or systematical character. Computed data might contain uncertainties which depend on the assumptions for the model, on the algorithm used (analytical or numerical approximation), on the machine used (round-off errors), on errors in programs and software (Hatton, 1989), on the computation mode (single or double precision), etc. Similarly, model parameters are not error-free. This means simply that the model parameters are not absolutely fixed values but are varying in a certain acceptable range. Beside that, geophysical inverse problems are generally ill-posed, that is, the $M \times N$ Jacobian matrix $\mathbf{A}$ is usually not square and not of a full rank. Practically, there are always more observations than parameters, i.e., $M > N$. Inverse problems are also, in most cases, ill-conditionned, that is, the $M \times N$ Jacobian matrix $\mathbf{A}$ has a large condition number. The ill-conditionness is often caused by inaccuracies in the partial derivatives approximated by numerical differentiation. All these factors can lead to slow convergence, to instability of the inverse problem, to large fluctuations of the solution and, as it should be expected, to unreliable results. Therefore special devices should be built in to enhance the functioning of the algorithm used and to improve the solution. Valuable contributions in this direction have been made by many scientists, among others Marquardt (1963, 1970), Hoerl and Kennard (1970), Smith and Shanno (1971), Jackson (1972), Claerbout and Muir (1973), Lawson and Hanson (1974), Inman (1974), Lines and Treitel (1984), Menke (1984), Tarantola (1987), Lines, Schultz and Treitel (1988), etc.

One of the ways to improve the solution of an inverse problem is the use of some extra knowledge about the nature of the data and/or the model. This extra information, usually referred to as a priori information, while included in the solution, improves the latter considerably. The uncertainties mentioned above are just one type of a priori information which contributes successfully to the improvement of the solution of an inverse problem (Jackson, 1972). The relative degree of accuracy in the data and/or in the parameter sets can be introduced into the solution, for instance, by weighting. The more accurate the

data, the higher their weight (Menke, 1984). A different approach to take into account the uncertainties in the data and in the model is the use of the covariance matrices of the respective errors (Tarantola, 1987; Smilde, 1997).

Scaling is also an operation which often has a significant influence on the performance of optimization methods (Gill et al., 1981). Since convergence tolerances and other criteria are necessarily based on an implicit definition of "small" and "large", problems with unusual or unbalanced scaling may cause difficulties for some algorithms. For instance, in many geophysical problems one is faced with the determination of depths, thicknesses and physical properties of geological structures at the same time. The two first quantities are in length units while others might be in units of density, magnetization, electrical resistivity or conductivity, etc. It is clear that all these quantities are characterized by uncertainties of different nature which will lead to an unbalanced data kernel. There exists no commonly adopted scaling technique. Depending on the problem to be solved, it is up to the user to design a scaling technique, which best enhances the performance of the optimization algorithm in the sense of meeting the interests and expectations. One of the ways of scaling the data kernel is to use a scaling diagonal matrix $\mathbf{D(j)}$ equal to the reciprocal of the mean of the $\mathbf{M}$ components (M is the number of rows of the data kernel) of the $\mathbf{j^{th}}$ column vector's uncertainty (Lawson and Hanson, 1974). This type of scaling has the effect of making the uncertainty of every column the same magnitude in the scaled matrix.

Mostly, there is no knowledge about the errors and the covariances of the data and of the model parameters. In this case one has to guess them. Depending on how the guess has been made, one might introduce too small or too large errors, which could worsen the solution instead of improving it. Below, I propose a technique for the data weighting and the scaling of the data kernel using information contained in the latter.

3.1.3 Proposed weighting and scaling technique

Given the linear inverse problem $Am = y$, I find it reasonable to use the information contained in the Jacobian matrix A to define the diagonal matrices $\mathbf{W(i)}$ and $\mathbf{D(j)}$, for the data weighting and the scaling of the data kernel, respectively. The data weighting matrix $\mathbf{W(i)}$ will be designed using the information about both observed and computed data. The data, and the model parameters, might be correlated or uncorrelated. To simplify the problem, as is usually the case in practice of geophysical data inversion, I assume both data and model parameters to be uncorrelated and have each its independent error or standard deviation.

Let σ_y be a vector containing the standard deviations of M observations; $\sigma_y = \sigma_y(i), i = 1, M$. The standard deviations of observations can be evaluated by means of repeated field measurements. For the computed data, I propose to use what I would like to call the pseudo-standard deviations σ_f which are calculated from the rows of the matrix A. In fact, the elements A_{ij} of the i^{th} row of the matrix A represent each the sensitivity of the i^{th} computed value f(i) due to the respective j^{th} model parameter. In terms of vector algebra, this simply means that each element of the i^{th} row is the projection of the i^{th} component of the model response vector f onto the given j^{th} direction of the model parameter space. In other words, the elements of the i^{th} row of A can be considered as the compo-

nents of the gradient of the i^{th} datum. The variance of the mean value of this gradient will reflect how accurate the datum has been or could be theoretically observed. It is believed that the probability of an error, if not systematic, to occur in theoretical computations is higher for the datum with larger variance of the gradient. In terms of geophysics, it is more probable for points located in the anomalous area to be affected by errors than for those situated away from the sources. These considerations can be introduced into the linear inverse problem as weighting to take into account the degree of accuracy with which different theoretical data are computed. From a statistical point of view, the standard deviation of the mean value of the gradient of the i^{th} datum can be calculated from the elements of the i^{th} row of A. This standard deviation is believed to be the image of that of the i^{th} computed value f(i). Hence the name of pseudo-standard deviation because it is not a true one. The i^{th} pseudo-standard deviation $\sigma_f(i)$ is calculated as follows:

$$\sigma_f(i) = \sqrt{\frac{1}{N-1}\sum_{j=1}^{N}[A(i,j) - \bar{A}_i]^2} \tag{3.8}$$

where $\bar{A}_i = \frac{1}{N}\sum_{j=1}^{N} A(i,j)$

Having computed the pseudo-standard deviations which take into account the uncertainties in the theory, we combine them with those of the observations to finally design the weighting diagonal matrix $\mathbf{W(i)}$. To obtain the complex vector of standard deviations σ_d, we sum up the corresponding values of the two sets of the standard deviations σ_y and σ_f element by element. The i^{th} element of σ_d is: $\sigma_d(i) = \sigma_y(i) + \sigma_f(i)$. The vector $\sigma_d(M)$ is then used to compute the weighting matrix $\mathbf{W(i)}$ according to the principle: the smaller the complex standard deviation, the greater the weight. The i^{th} element of $\mathbf{W(i)}$ is defined as:

$$W(i) = \sigma_d max/\sigma_d(i) \tag{3.9}$$

where $\sigma_d max$ is the largest complex standard deviation.

The resolution of the model and consequently the variances/covariances of the model parameters depend upon the condition of the data kernel A. The relationship between the relative data error δy and the relative solution error δm is given by:

$$\frac{\|\delta m\|}{\|m\|} \leq \kappa(A)\frac{\|\delta y\|}{\|y\|} \tag{3.10}$$

(Tarantola, 1987), where $\kappa(A)$ is the condition number of the matrix A. The condition number of A is defined as the ratio of the largest singular value of A to the smallest non-zero singular value of A. The relation (3.10) shows that, if the condition number is large, the relative solution error will be large too. To reduce the data error which will be projected into the model error, it is necessary to enhance the condition of the data kernel A. This can be done by scaling.

Proceeding in the same way as for the data weighting, I propose to calculate the scaling diagonal matrix $\mathbf{D(j)}$ using the information contained in the columns of the linear operator A. The elements of the j^{th} column of A represent, each, the sensitivity of the i^{th} datum with respect to the given j^{th} model parameter. In other words, those elements can be considered

as projections of the M components of the theoretical data vector onto the j^{th} direction of the model parameter space. It is believed that the fluctuations of the mean value of those elements reflect how accurate the given j^{th} parameter contributes to theoretical data and consequently to the behaviour of the expected solution. The parameters with which large fluctuations are connected will lead to instability of the algorithm and to wide scattering of the solution. The measure of the fluctuations relative to the j^{th} parameter can be expressed in terms of the standard deviation of the mean of the M elements of the j^{th} column of the Jacobian matrix A. The standard deviations computed for all columns can be thought of as representing those of the model parameters and are therefore referred to as their pseudo-standard deviations.

Relying on all the ideas discussed above, I find it justified to use these pseudo-standard deviations for designing the scaling diagonal $\mathbf{D(j)}$. Let σ_m be the vector of the pseudo-standard deviations of the model, $\sigma_m = \sigma_m(j), j = 1, N$. The j^{th} element of this vector is given by:

$$\sigma_m(j) = \sqrt{\frac{1}{M-1}\sum_{i=1}^{M}[A(i,j) - \bar{A}_j]^2} \tag{3.11}$$

where $\bar{A}_j = \frac{1}{M}\sum_{i=1}^{M} A(i,j)$

To design the scaling diagonal matrix $\mathbf{D(j)}$ using the vector $\sigma_m(N)$ of pseudo-standard deviations, I want the parameters with small pseudo-standard deviations to have the prevailing contribution to the general solution and the influence of those parameters with large pseudo-standard deviations to be damped. Following this reasoning, each j^{th} element of the scaling diagonal matrix $\mathbf{D(j)}$ will be the reciprocal of the corresponding pseudo-standard deviation, i.e.,

$$D(j) = 1/\sigma_m(j) \tag{3.12}$$

Implementing the data weighting and the scaling of the data kernel by multiplying all elements of the i^{th} row of $\mathbf{A}$ and the i^{th} element of $\mathbf{y}$ by the i^{th} element of the diagonal matrix $\mathbf{W(i)}$ and by multiplying all elements of the j^{th} column of A by the j^{th} element of the diagonal matrix $\mathbf{D(j)}$, one gets the following modified system:

$$WADm = Wy \tag{3.13}$$

Since column scaling has been applied to the data kernel A, the solution of (3.13) should be descaled by multiplying it by the scaling matrix D to get the actual solution of the original linear inverse problem.

3.1.4 Mathematical aspects of the Least-Squares Problem (LSP)

3.1.4.1 Linearization of the problem

Depending on the character of the relationship between the model response and the model parameters, geophysical problems can be linear, linearizable, quasi-linear or nonlinear.

In most cases geophysical observations are not linear functions of all the model parameters and cannot be linearly mapped into the latter by a simple inversion. A general approach for solving a geophysical inverse problem is to guess an initial model m_o about which a linearization is then made. The linearization is generally achieved by first order Taylor's expansion:

$$f = f_o + A\delta \tag{3.14}$$

where

f_o is the model response of the initial model m_o;
f is the response of the slightly perturbed initial model;
A is the the Jacobian (matrix of partial derivatives of the function with respect to all parameters);
δ is the vector of the parameter changes.

Let $\mathbf{y}$ be a vector containing observed data. The error between $\mathbf{y}$ and $\mathbf{f}$ is: $y - f = e$. From (3.14), $y - f_o - A\delta = e$. By replacing $y - f_o$ by $\mathbf{b}$, we obtain

$$b - A\delta = e \tag{3.15}$$

where $\mathbf{b}$ is the discrepancy vector. The relation (3.15) is of the same form as equation (3.2) in 3.1.1.3. Hence, the concept of solving a linearized problem in the least-squares sense, based on (3.15), will analogically lead to the normal equations

$$A^T A\delta = A^T b \tag{3.16}$$

From (3.16), it is clear that the linearization has led to the linear inverse problem

$$A\delta = b \tag{3.17}$$

with δ as unkown.

3.1.4.2 Mathematical methods for solving the normal equations

There are diverse mathematical methods for solving a system of linear equations (3.16); among others, the Cholesky decomposition and the Gaussian elimination. Having solved (3.16) for the parameter change vector δ,

$$\delta = [A^T A]^{-1} A^T b$$

the parameter estimates are then defined as follows:

$$m^{est} = m_o + \delta \tag{3.18}$$

If the problem is assumed to be linear, a single iteration is required for the convergence and the relation (3.18) is considered as the estimate of the solution of the inverse problem. For a nonlinear case the process will be iterated until a preset convergence criterium is satisfied. At each stage, the system $A_n\delta_{n+1} = b$ is solved for δ and the model is updated to get the new guess:

$$m_{n+1}^{est} = m_n^{est} + \delta_{n+1} \tag{3.19}$$

3.1.4.3 The least-squares problem with the SVD

In order to avoid errors connected with matrix multiplication while solving the normal equations, Golub and Reinsch (1970) proposed to solve the system $A\delta = b$ by means of the SVD. Without going into details, if the M×N matrix A is decomposed in such a way that $A = U\Lambda V^T$, where

U is a M×M orthogonal matrix,

V is a N×N orthogonal matrix,

Λ is a M×N diagonal matrix (the diagonal elements of which are the singular values λ of A), the solution of (3.17) computed by the SVD is of the form:

$$\delta = V\Lambda^{-1}U^T b = V\frac{1}{\lambda}U^T b \tag{3.20}$$

The vector of the parameter estimates is then adjusted as:

$$m_{n+1}^{est} = m_n + \delta_{n+1}$$

The advantage of the SVD, though slower than the other methods mentioned, is its numerical stability (Stewart, 1973; Lawson and Hanson, 1974; Lines and Treitel, 1984). Beside that, the method of the SVD offers the possibility to look inside the nature of the inverse problem itself; that is especially important for poorly conditioned problems. This allows us to build up different candidate solutions, the analysis and comparison of which might lead to choosing the one with better characteristics.

Owing to this method, the so-called **generalized inverse** (A^{-g}) can be used to compute the solution (Marquardt, 1970; Menke, 1984). The expression of the generalized inverse is:

$$A^{-g} = [A^T A]^{-1} A^T \tag{3.21$_a$}$$

or from the SVD

$$A^{-g} = V\Lambda^{-1}U^T \tag{3.21$_b$}$$

If some of the eigenvalues are zeros (Fig. 3.3 a), the so-called natural solution is computed using (3.21$_b$). An estimate which is no longer natural can be built up with the help of (3.21$_b$), when some singular values are so small that they are excluded (the components of the solution in the null space are assumed to be zeros).

If the p^{th} singular value is the cut-off in the spectrum, the solution will be

$$\delta = V_p \frac{1}{\lambda_p} U_p^T b \tag{3.22}$$

The solution (3.22) will yield a better variance but a worse resolution. This is due to the trade-off between the variance and the resolution.

Sometimes it is not clear enough which singular value should be taken as the cut-off (Fig. 3.3 b). The simplest way to get rid of this problem is to include all singular values and to add to all of them a small value β which will damp the influence of the small eigenvalues (the estimates of the solution in the null space are considered but in a damped manner).

$$\delta = V \left(\frac{\lambda_j}{\lambda_j^2 + \beta} \right) U^T b \tag{3.23}$$

In this case the resolution will be enhanced and a worse variance will be expected. But the quality and the measure of both the resolution and the variance will be strongly influenced by the chosen value of the damping factor β. Large values of this factor might lead to small variances (Hoerl and Kennard, 1970) while simultaneously degrading the resolution due to the exclusion of some eigenvalues. As can be seen on Fig. 3.4, there are some values of the damped factor β for which a least-squares solution with a minimum mean-square error and quite acceptable values of the bias and of the variance can be achieved. There exists no method for determining the values of the suitable damping factors β in advance. They must be determined by trial and error. A better choice of the damping factor would be that, which is small enough to yield a good resolution and allow the evaluation of the variances of the parameter estimates at the same time (Crosson, 1976). For a linear problem, such a value is that which gives the minimum mean-square error as shown in Fig. 3.4 (value β^*). However, for a nonlinear problem several iterations must be performed before a solution is obtained, and each iteration may require a different value of β. Marquardt (1963) has worked out an algorithm which determines the value of β for each iteration as the solution converges. A small starting value of β, say, 10^{-3}, will be increased by a factor of 10 if the sum of squared errors at a given iteration is greater than the previous one. If the iteration has converged, i.e., if its squared error is less than that of the previous one, β is decreased by a factor of 0.1 and the inversion process goes further till a final convergence to a minimum is reached. It is important to point out that, apart from the damping role, the damping factor β speeds up the convergence of the solution and is a good tool for avoiding singularity problems (Lines and Treitel, 1984).

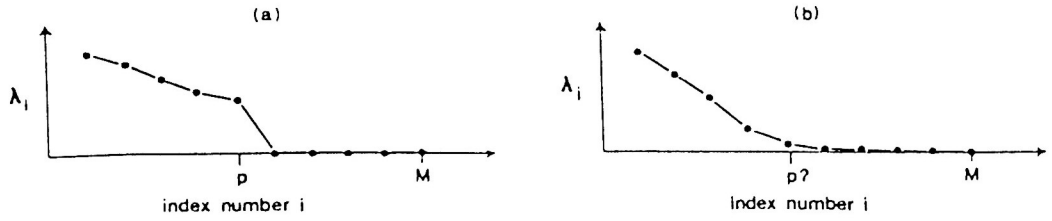

Fig. 3.3 (a) Singular values of a matrix with clearly identifiable p. (b) Singular values of a matrix where p must be chosen in a more arbitrary fashion (after Menke, 1984).

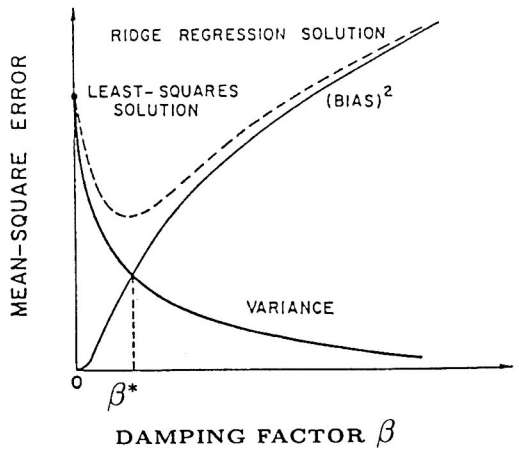

Fig. 3.4 Mean-square error functions for the ridge regression estimator (after Hoerl and Kennard, 1970a).

3.1.5 Assessment of the goodness and accuracy of the inversion

The quality of the inversion can be deduced from a statistical or a mathematical analysis of both predicted data and estimated model. The commonly used measure of how good the predicted model response fits the observations is the a posteriori data variance σ_p^2 or the related **R**oot **M**ean **S**quare error (RMS) σ_p, which is the standard deviation of the sample mean. The a posteriori variance σ_p^2 of the least-squares problem $Am = y$ is computed as

$$\sigma_p^2 = \frac{\|Am - y\|^2}{p - k} = E/\nu \tag{3.24}$$

(Stewart, 1973; Lawson and Hanson, 1974), where $E = e^T e$ is the least-squares error at convergence, ν is the number of the degrees of freedom of the Jacobian matrix $A_{m \times n}$, $p = max(m, n)$, $k = Rank(A) = min(m, n)$. In some cases, the Jacobian might be singular or rank deficient. Then, if the SVD is used, k is the number of non-zero singular values or of those singular values of the Jacobian, which are larger than a certain value (cut-off) given by the product of the smallest singular value and a very small preset number.

$$RMS = \sqrt{E/\nu} \tag{3.25}$$

The goodness of the fit between the predicted and observed data can also be measured by the so-called "Normalized Mean Square Error" **MSE**. It is given by the ratio of the sum of the squared errors divided by the sum of the squares of the observed data y(i).

$$MSE = \frac{E}{\sum_{i=1}^{M} [y(i)]^2} \tag{3.26}$$

However, the value of the a posteriori variance σ_p^2 should be assessed carefully. When σ_p^2 is greater than the variance σ_y^2 of the observations, the data have not been completely explained by the assumed model. This means that some elements of the data might be possibly well fitted if more parameters were used. But a greater value of σ_p^2 might also mean that σ_y^2 has been underestimated. Similarly a smaller value of σ_p^2 might also mean that σ_y^2 has been overestimated or that the data contain some noise which is fitted by the computed data.

Another mathematical tool to assess the goodness of the inversion with respect to the data is the **data resolution** matrix **N**. In terms of the generalized inverse, the data resolution matrix can be expressed as

$$N = AA^{-g} \tag{3.27}$$

Predicted data f are related to observations y as follows

$$f = Ny \tag{3.28}$$

If the data resolution matrix is an identity matrix **I**, the predicted error equals zero and the observed data can be considered as well resolved. If this even happens artificially, it is difficult to imagine it as corresponding to the true situation, especially in geophysical

problems which are in most cases overdetermined. Generally, predicted data are weighted averages of the observations through the resolution matrix N.

As in the case of the data, an analysis of the quality of the estimated model can be performed proceeding in the same way. The question of how well the estimated model is resolved can be answered by considering the **model resolution** matrix **R**. In terms of the generalized inverse, the model resolution matrix can be expressed as

$$R = A^{-g}A \tag{3.29}$$

R is a square $N \times N$ matrix. The model estimate is related to the true model as

$$m^{est} = Rm^{true} \tag{3.30}$$

If $\mathbf{R} = \mathbf{I}$, each model parameter is uniquely determined; otherwise the model parameter estimates cannot be independently determined and are weighted averages of the true model parameters. The goodness of the model resolution matrix **R** is partly assessed by the values of the diagonal elements. The resolution is good when the values of those elements are close to unity. The overall goodness is quantified by the spread of the off-diagonal elements, also called the Dirichlet spread function $\mu(R)$, which is measured under the L_2-norm of the differences between the resolution matrix R and an identity matrix I. It is given by:

$$\mu(R) = \|R - I\|_2^2 = \sum_{i=1}^{N}\sum_{j=1}^{N}[R_{ij} - I_{ij}]^2 \tag{3.31}$$

where R_{ij} are the elements of the resolution matrix, I_{ij} are the elements of the identity matrix. A concentration of the largest elements of the model resolution matrix around its main diagonal — the remaining off-diagonal elements being small — is an indication for a fairly good resolution.

The accuracy of the determined model parameter estimates can be evaluated by the a posteriori covariance matrix **COV [m]**

$$COV[m] = \sigma_p^2 A^{-g} A^{gT} \tag{3.32}$$

where σ_p^2 is the predicted variance of the data. The diagonal elements of the covariance matrix are considered as the variances of the estimated parameters; namely $\sigma_i^2(m) = cov_{ii}(m)$. Obviously, these variances are, or might be, different from those of the true parameters. The standard deviation of the given model parameter estimate is then evaluated as the square root of the respective variance. With the help of the standard deviations, we are able to define probabilistic bounds of the estimates (confidence intervals).

Sometimes, it is useful to analyze the correlation matrix of the estimated parameters. This analysis — rather qualitative than quantitative — can show us the interdependency of the estimates. The size of the correlation coefficients will show which estimates are linearly dependent and which are not (correlated or uncorrelated) and how strong is the dependency. This information has a double meaning:

– it shows the feasibility of an estimate to be determined independently or otherwise;

– it tells us whether our starting hypothesis of the model parameters being correlated or uncorrelated holds.

3.1.6 Convergence and nonuniqueness of the solution of the LSP

If the least-squares problem is purely linear, it will require one iteration to converge. But if it presents some nonlinearity, the convergence will be achieved only after a certain number of iterations have been performed. By convergence it has to be understood that a good match between the computed data and the observations has occured within a prespecified criterium. The whole procedure is controlled by the behaviour of the least-squares error E. The updating of the solution takes place if the value of E at the actual iteration is less than that of the previous iteration. The procedure will be stopped if a preset convergence criterium is satisfied. The inversion will be considered to have converged if the difference between two consecutive least-squares errors E_n and E_{n+1} is less than some suitably small positive number γ, say 10^{-5}, i.e.,

$$E_n - E_{n+1} < \gamma \tag{3.33}$$

However, it is important to recall that most geophysical inverse problems suffer from nonuniqueness (Al-Chalabi, 1971; Treitel and Lines, 1988). For several reasons the solution of the inverse problem can never be unique. For example, we are not able to see the inside of the model and to know exactly all geological factors that contribute to the observations. Moreover, geophysical observations contain always components that we cannot explain in geological terms. Another point is that, since the model optimization is based on the minimization of the chi-square function (sum of errors), the achieved convergence will be strongly connected with the behaviour of the latter. The function might have a single minimum — sharp or broad — or several minimum points. Thus the question whether the minimum reached is local or global can never be answered with absolute certainty. The optimized model is the one of all those plausible candidate solutions able to produce data which will fit the observations by satisfying the preset convergence criterium. Thus, it is not possible to single out one solution as the unique one. A reasonable approach is to solve the inverse problem with different starting models and/or a priori information in order to yield diverse solutions among which the one with better characteristics will be kept as the estimate of the model. Even for the retained solution, it is necessary to represent it with its confidence limits. The reliability of the solution can be enhanced by taking into account information from other sources, last but not least, the geophysicist's intuition!

3.1.7 Scheme of the nonlinear inversion

Since gravity and magnetic field measurements will be used to estimate the parameters of the maar-diatreme volcanoes, the inverse problem is discretely formulated. Thus, the problem will be solved by methods of matrix equations that are based on the fundamental relation (3.1). The problem to be dealt with is nonlinear, i.e., the physical field is not a linear function of all contributing parameters. The nonlinearity will be handled by an iterative procedure, i.e., by means of updating the solution of the linearized inverse problem until a preset convergence criterium is satisfied. Hence the linear inverse problem to be solved can be formulated as in (3.17), i.e.,

$$A\delta = b$$

where $\mathbf{A}$ is a $M \times N$ matrix of partial derivatives of the model response $\mathbf{f}$ with respect to model parameters, δ is the vector of the parameter changes, $\mathbf{b}$ is the vector of discrepancies between the observed and the computed data. Before the above linear system is solved, weighting and scaling are applied to it as described in 3.1.3.

Taking into consideration that more than one iteration are practically needed for the solution to converge and that linear systems of large dimensions will be dealt with, it is of great importance for solving the problem to choose a mathematical method which best reduces errors connected with matrix operations and machine dependent errors such like round-off errors. The method must also be stable enough in order to avoid wide scattering in the solution. That is the reason I will use the damped least-squares method combined with the SVD. The SVD method provides more stability than other known methods used to solve linear systems (Golub and Reinsch, 1970; Lawson and Hanson, 1974) and the use of the damping factor also known as the "Marquardt-Levenberg" factor enables us to avoid problems of matrix singularities (Lines and Treitel, 1984). The parameter change vector δ and the model parameter estimates will be computed by (3.23) and (3.19), respectively. At a current iteration, the estimate of the solution of the inverse problem will be accepted if it achieves a least-squares error $\mathbf{E}$ which is less than that of the previous one. The flow-chart presented on Fig. 3.5 shows the whole inversion procedure.

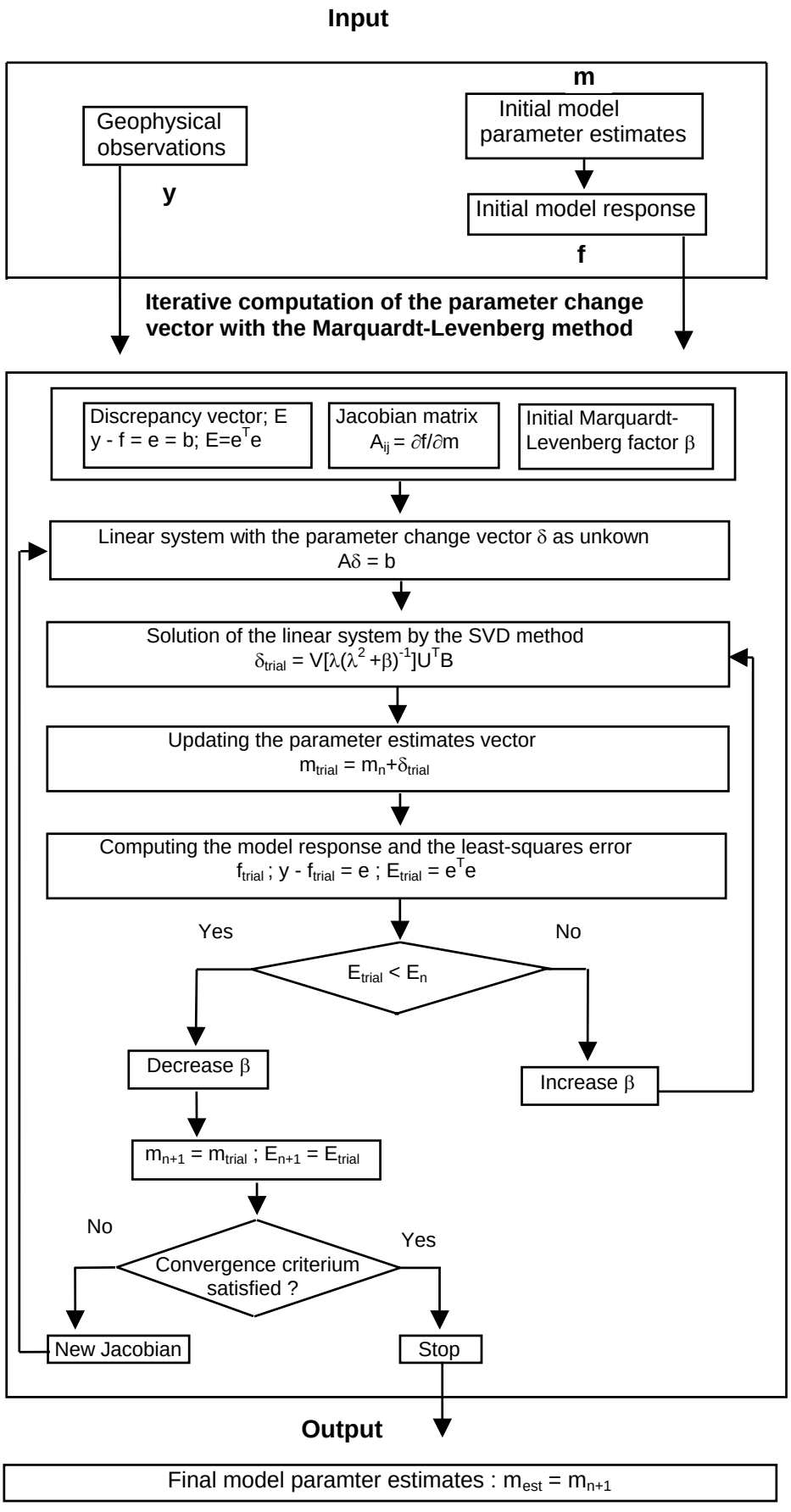

Fig. 3.5 Flow-chart of the nonlinear least-squares inversion.

3.2 Gravity and magnetic forward problems

3.2.1 Physical-mathematical fundamentals

3.2.1.1 The gravity forward problem

Mathematical expressions of the gravity field are based on the well-known Newton's law which describes the interaction force between two masses. From Newton's law, the acceleration of gravity **g** is expressed as

$$\vec{g} = -(\gamma m/r^2)\vec{r}_1 \tag{3.34}$$

where $\gamma = 6.67 \times 10^{-11} Nm^2/kg^2$ is the gravitational constant, m is the point mass attracting a unit mass situated at the distance r ($r = \sqrt{x^2+y^2+z^2}$) and $\vec{r}_1$ is a unit vector directed from the unit mass toward the point mass m along r.

Using the potential field theory, the acceleration **g** giving rise to the gravity field can be expressed as the gradient of a scalar potential function **V**(x,y,z), called Newtonian or three-dimensional potential (Telford et al., 1992). In cartesian coordinates, the relationship between **g** and **U** has the form:

$$\nabla V(x,y,z) = -\vec{g}(x,y,z) \tag{3.35}$$

Solving (3.35) for the gravitational potential, we get

$$V(\vec{r}) = -\int_{\infty}^{r} \vec{g}.d\vec{r} \tag{3.36}$$

By substituting g in (3.36) by its expression from (3.34) in the scalar form, the gravitational potential takes the following form:

$$V(\vec{r}) = -\gamma m/r \tag{3.37}$$

Considering a volume element dx, dy, dz of a body **B** (Fig. 3.6) with a uniform density ρ, the potential due to the corresponding elementary mass **dm** at the point **P1**(x,y,z) distant **r** from **P**(0,0,0) is

$$dV = -\gamma dm/r = -\gamma \rho dxdydz/r \tag{3.38}$$

By integrating (3.38), one gets the potential of the total mass.

$$V = -\gamma \int_x \int_y \int_z (\rho/r) dxdydz \tag{3.39}$$

In geophysical practice, the vertical component g_z of g (the acceleration of the gravity in the vertical direction) is dealt with. Using the relation (3.35), g_z can be expressed as follows:

$$g_z = -(\partial V/\partial z) \tag{3.40}$$

Substituting U by its expression from (3.39) and differentiating with respect to z, we get

$$g_z = -\gamma\rho \int_x \int_y \int_z (z/r^3) dx dy dz = -\gamma\rho \int_x \int_y \int_z (z/r^3) dv \tag{3.41}$$

The relation (3.41) is the fundamental 3-D expression of the gravity effect.

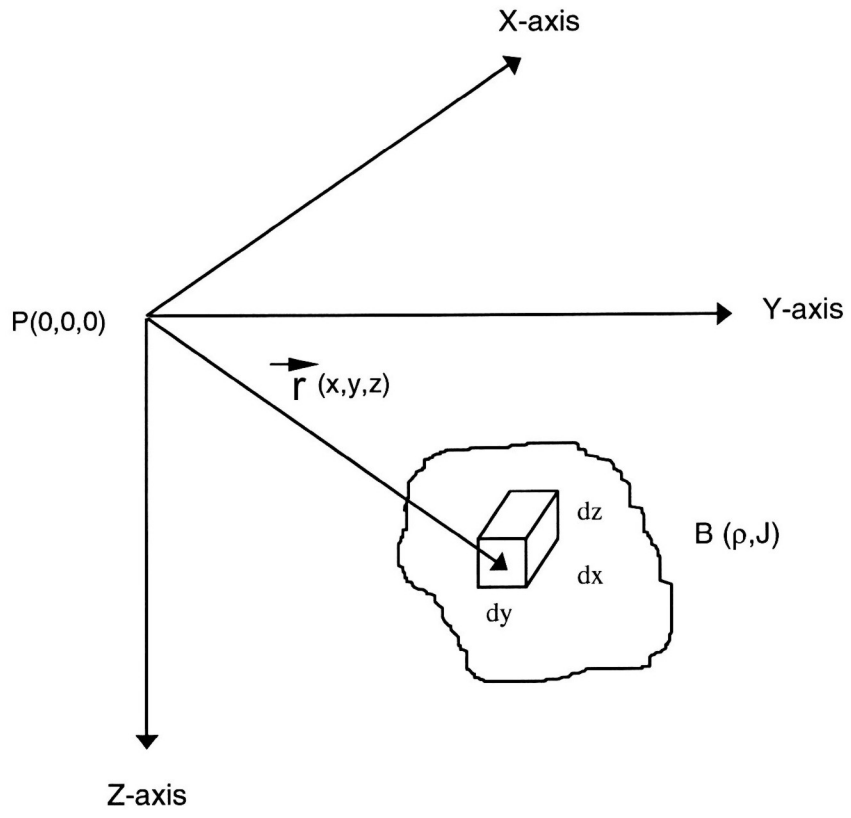

Fig. 3.6 Coordinates system and volume element dx, dy, dz of body B with uniform density ρ and magnetization J.

After Poisson's theorem, if a causative body is homogeneous in both density ρ and magnetisation J, its magnetic U and gravity V potential are related through the following formula:

$$U = -[1/(\gamma\rho)](J_x \frac{\partial V}{\partial x} + J_y \frac{\partial V}{\partial y} + J_z \frac{\partial V}{\partial z}) \tag{3.42}$$

where J_x, J_y and J_z are components of the magnetization. Consequently, the components of the magnetic field are obtained by differentiating the potential U relative to the respective directions. In geophysical practice, anomaly fields are usually dealt with. Thus, instead of the absolute values of ρ and J, the physical contrasts relative to a homogeneous earth, $\Delta\rho$ and ΔJ, are used for the calculations.

3.2.1.2 The magnetic forward problem

Classically, the expressions for the magnetic field are derived from Coulomb's law which defines the magnetic force between two magnetic poles. The magnetic field strength $\vec{H}$ of a pole of strength **p** acting on a unit pole located at a distance r from it is given by

$$\vec{H} = (p/\mu r^2)\vec{r}_1 \tag{3.42}$$

where μ is the magnetic permeability of the medium and $\vec{r}_1$ is a unit vector directed from the pole toward the unit pole along r.

The modern theory of the magnetic field is based on the laws of electromagnetism and uses a magnetic dipole as the basic unit. A magnetic dipole (Fig. 3.7) is considered as two poles of strength +p and −p separated by a distance 2l. The magnetic moment of the dipole is expressed as

$$\vec{M} = 2lp\vec{r}_1 \tag{3.43}$$

where $\vec{r}_1$ is a unit vector directed from the negative pole toward the positive.

After Ampère's law, also called Bio-Savart's law, an electrical current $\vec{I}$ flowing in a conductor of length Δl produces at a point P situated at a distance r (Fig. 3.8) a magnetizing field $\Delta\vec{H}$ expressed as

$$\Delta\vec{H} = \mu_0(\vec{I}\Delta l) \times \vec{r}_1/4\pi r^2 \tag{3.44}$$

where $\mu_0 = 4\pi \times 10^{-7} TmA^{-1}$ is the magnetic permeability of the vacuum and $\vec{r}_1$ is a unit vector directed from the length element Δl of the conductor toward the point P along r.

If the current is flowing in a circular loop, it acts as a magnetic dipole located at the centre of the loop. Electrons in materials, in addition to their orbital motions around the atomic nuclei, have rotational or spinning motions around their axes (Alonso and Finn, 1968). The orbital motions constitute circular currents which result in orbital magnetic dipoles with moments $\vec{M}_o$. The rotational motions result in spin magnetic dipoles with moments $\vec{M}_s$. The total magnetic dipole moment $\vec{M}$ of an orbiting and spinning electron is therefore

$$\vec{M} = \vec{M}_o + \vec{M}_s$$

and depends on both the magnitudes and the relative orientations of M_o and M_s. If a magnetizable body is placed in an external magnetic field H_o, it becomes magnetized by induction due to the internal reorientation of the dipoles. The sum effect of all dipoles in the body produces a magnetic field H_i which is added to the inducing field H_o to give the total magnetic field H which is measured. The degree to which a body is magnetized is measured by the *magnetization intensity* **J** or *magnetic dipole moment per unit volume*. If there is no **N**ormal **R**emanent **M**agnetization (NRM), the magnetization is only induced and can be expressed as

$$J = \chi F_o$$

where χ is the effective magnetic susceptibility of the body assumed to be magnetically homogeneous and F_o is the total intensity of the ambient Earth's field. The components of the magnetization are then calculated as follows:

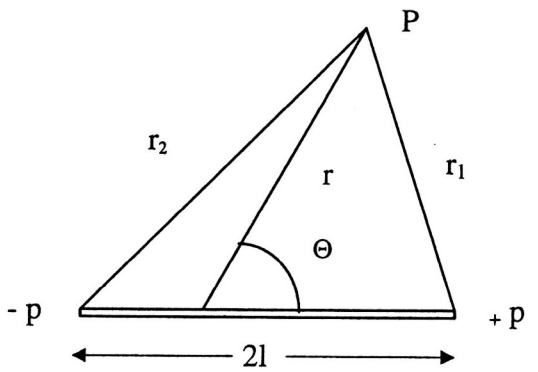

Fig. 3.7 Magnetic dipole and geometric elements involved in the calculation of its magnetic potential.

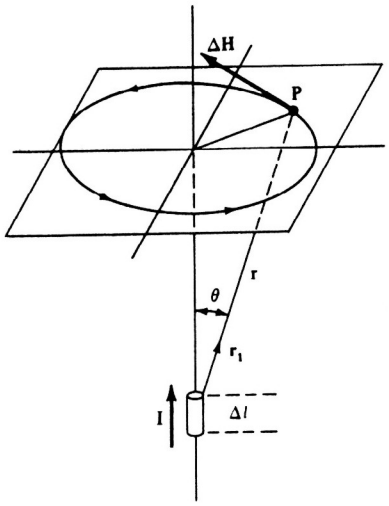

Fig. 3.8 Magnetic field $\Delta\vec{H}$ created at a point P by a current $\vec{I}$ flowing through a length of conductor Δl.

$$J_x = J \cos I \cos D$$

$$J_y = J \cos I \sin D$$

$$J_z = J \sin I \tag{3.45}$$

where I is the inclination and D the declination of the geomagnetic field. In case where a NRM is present, the total magnetization is the sum of both the induced ($\mathbf{J}_i$) and the remanent ($\mathbf{J}_r$) components. The ratio **Q** between the remanent and the induced components of the total magnetization is known as the Koenigsberger ratio and is given by the relation: $Q = J_r/J_i$. Let J_{xi}, J_{yi} and J_{zi} be the components of the induced magnetization and J_{xr}, J_{yr} and J_{zr} those of the NRM. The horizontal (J_x, J_y) and vertical (J_z) components of the total magnetization are then

$$J_x = J_{xr} + J_{xi}, \quad J_y = J_{yr} + J_{yi}, \quad J_z = J_{zr} + J_{zi} \tag{3.46}$$

In order to be able to judge whether the induced magnetization alone or both the induced and the remanent components are responsible for the magnetic anomalies, the components of the total magnetization will be parameterized for inversion purposes. Having the X-, Y- and Z-components of the total magnetization from the inversion and calculating the induced components by (3.45), it is then possible to get the components of the NRM by a simple subtraction using (3.46). The values of the geomagnetic field F_o, its inclination I and declination D are calculated by the **I**nternational **G**eomagnetic **R**eference **F**ield (IGRF) formula. The magnitude J_r, the horizontal component, the inclination I_r and the declination D_r of the NRM can be thereafter evaluated by

$$J_r = \sqrt{J_{xr}^2 + J_{yr}^2 + J_{zr}^2}$$

$$J_{hr} = \sqrt{J_{xr}^2 + J_{yr}^2}$$

$$I_r = \sin^{-1}(J_{zr}/J_r) = \tan^{-1}(J_{zr}/J_{hr})$$

$$D_r = \tan^{-1}(J_{yr}/J_{xr})$$

As in the case of the gravity field, the magnetic field strength $\vec{H}(\vec{r})$ can be expressed as a gradient of a scalar potential function $\mathbf{U}(\vec{r})$:

$$\vec{H}(\vec{r}) = -\nabla U(\vec{r}) \tag{3.47}$$

Solving (3.47) for the potential $\mathbf{U}(\vec{r})$, we get

$$U(\vec{r}) = -\int_{-\infty}^{r} \vec{H}(\vec{r}).d\vec{r} \tag{3.48}$$

Substituting $\vec{H}$ by its value from (3.42) in the scalar form and assuming $\mu = 1$, the potential is

$$U(\vec{r}) = p/r \tag{3.49}$$

For a magnetic dipole (Fig. 3.7), the potential will be the sum effect from both poles, i.e.,

$$U = \frac{p}{r_1} - \frac{p}{r_2} = p\Big\{\frac{1}{\sqrt{r^2 + l^2 - 2rl\cos\theta}} - \frac{1}{\sqrt{r^2 + l^2 + 2rl\cos\theta}}\Big\} \tag{3.50}$$

$$U \approx 2pl\cos\theta/r^2 \approx |M|\cos\theta/r^2 \tag{3.51}$$

where $\cos\theta$ is the direction cosine of the magnetic moment vector $\vec{M}$, i.e., the cosine of the angle θ between the positive directions of $\vec{M}$ and the radius vector r.

Taking into account that r has three components x, y, and z in x-, y- and z-direction, the respective cosines are defined as

$$\cos\theta_x = x/r, \quad \cos\theta_y = y/r, \quad \cos\theta_z = z/r \tag{3.52}$$

Using (3.51), we define the magnetic potential dU at the point $P(0,0,0)$ for the volume element dx, dy, dz (Fig. 3.6)

$$dU = dM\cos\theta/r^2 \tag{3.53}$$

where dM is the magnetic moment of the volume element dv, r is the distance from the volume element dv to the point P . dM, in turn, can be expressed as $dM = Jdv = Jdxdydz$, where J is the magnetization intensity or the dipole moment per unit volume, assumed uniform for the whole body. Decomposing the magnetization vector J in its three components J_x, J_y and J_z and using the expressions from (3.52), the relation (3.53) for the magnetic potential becomes

$$dU = \frac{J_x x + J_y y + J_z z}{r^3} dxdydz \tag{3.54}$$

By integrating (3.54), we get the magnetic potential of the entire body

$$U = \int_x \int_y \int_z \frac{J_x x + J_y y + J_z z}{r^3} dxdydz \tag{3.55}$$

The X-, Y- and Z-components of the magnetic intensity, which are referred to as the magnetic anomaly are given by the partial derivatives of the magnetic potential with respect to the corresponding directions.

$$\begin{aligned}
\triangle X &= \int_x \int_y \int_z -\frac{\partial U}{\partial x} dxdydz \\
\triangle Y &= \int_x \int_y \int_z -\frac{\partial U}{\partial y} dxdydz \\
\triangle Z &= \int_x \int_y \int_z -\frac{\partial U}{\partial z} dxdydz
\end{aligned} \tag{3.56}$$

Substituting U by its value from (3.55) and differentiating with respect to x, y and z, the three components are:

$$\begin{aligned}\triangle X &= J_x V_1 + J_y V_2 + J_z V_3 \\ \triangle Y &= J_x V_2 + J_y V_4 + J_z V_5 \\ \triangle Z &= J_x V_3 + J_y V_5 + J_z V_6 \end{aligned} \tag{3.57}$$

where

$$\begin{aligned} V_1 &= \int_x \int_y \int_z \frac{3x^2 - r^2}{r^5} dxdydz \\ V_2 &= \int_x \int_y \int_z \frac{3xy}{r^5} dxdydz \\ V_3 &= \int_x \int_y \int_z \frac{3xz}{r^5} dxdydz \\ V_4 &= \int_x \int_y \int_z \frac{3y^2 - r^2}{r^5} dxdydz \\ V_5 &= \int_x \int_y \int_z \frac{3yz}{r^5} dxdydz \\ V_6 &= \int_x \int_y \int_z \frac{3z^2 - r^2}{r^5} dxdydz \end{aligned} \tag{3.58}$$

The integrals V_1, V_2, ... V_6, represent integrations over the volume of the body.

In most magnetic surveys, the total intensity F of the magnetic field, i.e., the sum of the normal ambient field F_o and the anomalous field F_a, is measured (Fig. 3.9). The magnitude of the total intensity anomaly $\triangle F$ is given by

$$\triangle F = \sqrt{(F_{ox} + \triangle X)^2 + (F_{oy} + \triangle Y)^2 + (F_{oz} + \triangle Z)^2} - F_o \tag{3.59}$$

or

$$\triangle F = \sqrt{F_o^2 + F_a^2 + 2(F_{ox}\triangle X + F_{oy}\triangle Y + F_{oz}\triangle Z)} - F_o \tag{3.59'}$$

where F_{ox}, F_{oy} and F_{oz} are the components of the undisturbed total magnetic field F_o in the respective directions and $\triangle X$, $\triangle Y$ and $\triangle Z$ are the components of the anomaly F_a. If the anomaly F_a is small in comparison with the undisturbed field F_o ($F_a << F_o$), the expression (3.59′) for $\triangle F$ can be simplified. It is sufficient that F_a be $< 0.2\ F_o$, that is $F_a < 13000\ nT$ in zones close to poles and $F_a < 6000\ nT$ in zones near the equator for this condition to be satisfied. This condition is practically fullfilled since the anomalies are rarely higher than some thousand gammas in most magnetic surveys. Extracting F_o out of the root and neglecting the term F_a^2/F_o^2 in (3.59′), we get

$$\triangle F = F_o(\sqrt{1 + 2(F_{ox}\triangle X + F_{oy}\triangle Y + F_{oz}\triangle Z)/F_o^2} - 1)$$

or by replacing F_{ox}/F_o, F_{oy}/F_o and F_{oz}/F_o by the direction cosines of F_o,

$$\triangle F = F_o(\sqrt{1 + 2(\triangle X \cos I \cos D + \triangle Y \cos I \sin D + \triangle Z \sin I)/F_o} - 1) \qquad (3.59'')$$

Since $F_a << F_o$, its components $\triangle X$, $\triangle Y$ and $\triangle Z$ are a fortiori much less than F_o, hence the second term of the expression under the root in $(3.59'')$ is less than 1. Applying the known formula of the binomial series $\sqrt{1+x} \approx 1 + \frac{x}{2}$, the expression for $\triangle F$ becomes

$$\triangle F = \triangle X \cos I \cos D + \triangle Y \cos I \sin D + \triangle Z \sin I \qquad (3.60)$$

i.e, the total intensity anomaly $\triangle F$ is the projection of F_a onto the direction of F_o, i.e., $\triangle F = F_a \cos\theta$ which is the sum of the projections of the components $\triangle X$, $\triangle Y$ and $\triangle Z$ onto the direction of F_o (Fig.3.10).

The magnitude of the horizontal magnetic field anomaly is expressed as

$$\triangle H = \triangle X \cos D + \triangle Y \sin D \qquad (3.61)$$

Substituting $\triangle X$, $\triangle Y$ and $\triangle Z$ by their values from (3.57), $\triangle F$ and $\triangle H$ can be expressed in terms of the components of the magnetization J_x, J_y and J_z:

$$\triangle F = J_x(V_1 \cos I \cos D + V_2 \cos I \sin D + V_3 \sin I) +$$

$$J_y(V_2 \cos I \cos D + V_4 \cos I \sin D + V_5 \sin I) +$$

$$J_z(V_3 \cos I \cos D + V_5 \cos I \sin D + V_6 \sin I) \qquad (3.62)$$

and

$$\triangle H = J_x(V_1 \cos D + V_2 \sin D) + J_y(V_2 \cos D + V_4 \sin D) + J_z(V_3 \cos D + V_5 \sin D) \quad (3.63)$$

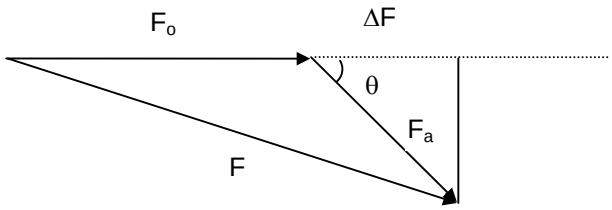

Fig. 3.9 Total intensity magnetic field, its components F_o and F_a and the total intensity anomaly ΔF.

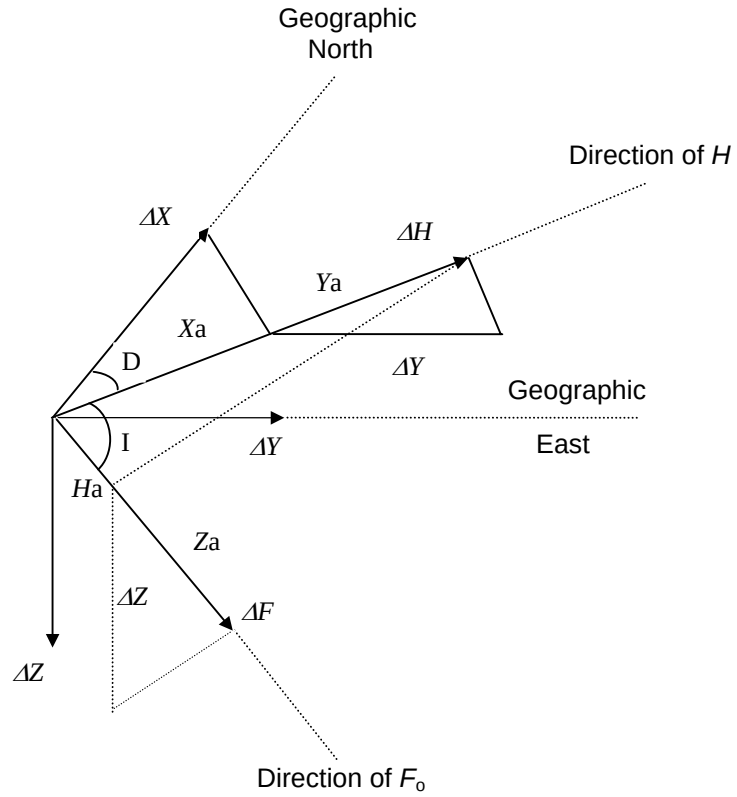

Fig. 3.10 The total intensity magnetic anomaly *ΔF* is the sum of the projections of the anomalies Δ*X*, Δ*Y* and Δ*Z* in the direction of F_o.
(redrawn from Talwani, 1965)

*X*a=*ΔX Cos D; Y*a=*ΔY Sin D; H*a=*ΔH Cos I; Z*a=*ΔZ Sin I*

3.2.2 Application to geological models

Taking into account that maar-diatremes are structures of small finite dimensions, a 3-D model will be used for the calculation of theoretical data. Moreover, maar-diatremes are not bodies of simple and regular geometric shape for which the anomalies can be calculated by analytical formulas. Therefore computations will be carried out by the method of Talwani (Talwani and Ewing, 1960; Talwani, 1965). The method consists in representing an irregularly shaped 3-D body by contours, which are then approximated by polygonal laminae (Fig. 3.11). In order to get gravity anomalies, the volume integral in (3.41) has to be solved. For magnetic anomalies, one has to solve first the volume integrals in (3.59) for V_1, V_2, V_3, V_4, V_5 and V_6. The volume integrals in (3.41) and (3.59) can be each split into two parts: the one (surface part) representing the integration over the contour and the other representing the integration over the depth. Thus the expressions (3.41) and (3.59) can be expressed as follows:

$$g_z = \gamma\rho \int_z S dz$$

$$V_1 = \int_z S_1 dz$$

$$V_2 = \int_z S_2 dz$$

$$\vdots$$

$$V_6 = \int_z S_6 dz$$

where

$$S = \int_x \int_y (z/r^3) dxdy$$

$$S_1 = \int_x \int_y \frac{3x^2 - r^2}{r^5} dxdy$$

$$S_2 = \int_x \int_y \frac{3xy}{r^5} dxdy$$

$$\vdots$$

$$S_6 = \int_x \int_y \frac{3z^2 - r^2}{r^5} dxdy$$

S and $S_1, S_2 \cdots S_6$ are the surface parts of the volume integrals in (3.41) and (3.59), respectively, and are referred to as surface integrals.

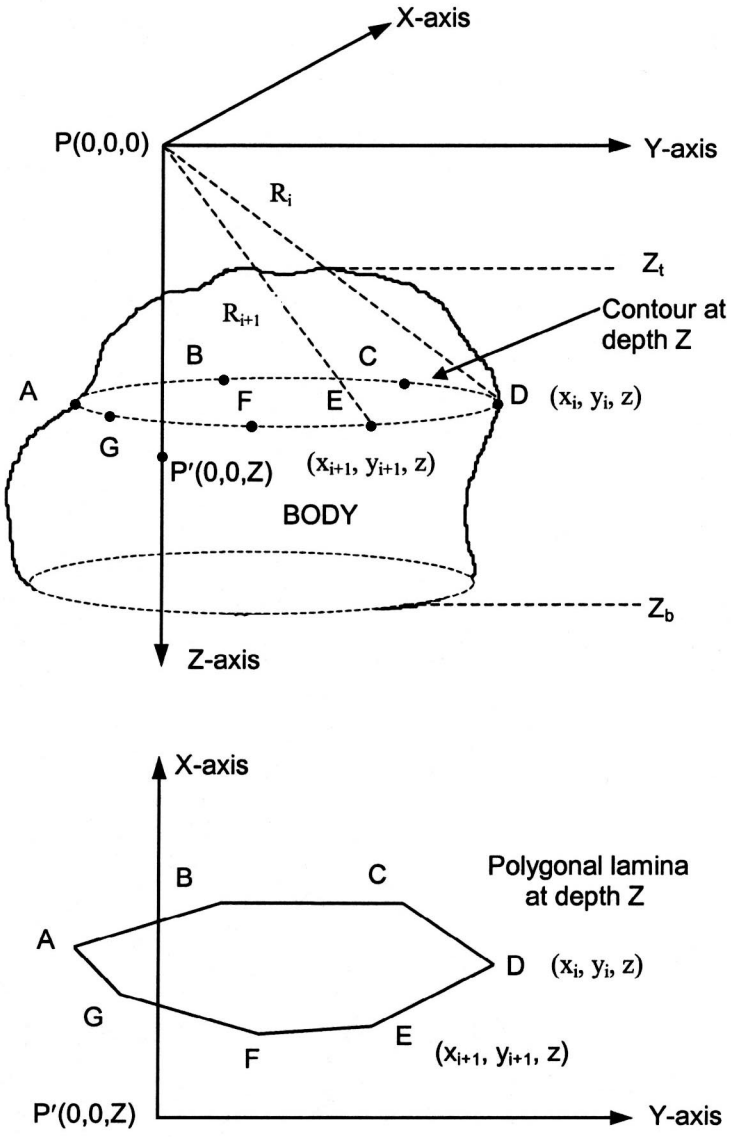

Fig. 3.11 Contour at depth z and its representation by a polygon.

The solution of the triple integrals in (3.41) and (3.59) is carried out in two stages. First, the surface integrals over the polygonal laminae are analytically evaluated. The values of the respective surface integrals are then summed up by numerical quadrature over the depth to get the total effects. Let $S_i, i = 1, n$ be the values of the surface integrals of the n polygonal laminae. The gravity anomaly $\triangle g_i$ caused by the i^{th} polygonal lamina of an infinitisimal thickness dz can be expressed as $\triangle g_i = u_i dz$, where u_i is the gravity anomaly per unit thickness. u_i, in turn, is expressed as $u_i = \gamma \triangle \rho S_i$, where $\triangle \rho$ is the density contrast of the body relative to the country rocks. To get the anomaly $\triangle g$ of the whole body, the gravity effects u_i per unit thickness of all polygonal laminae are numerically integrated over the depths, that is $\triangle g = \int_{z_t}^{z_b} u_i dz$, where z_t and z_b are the depths of the top and the bottom contours, respectively. For the magnetic anomalies, the surface integrals $S_1, S_2, \cdots S_6$ have to be evaluated each for all n polygonal laminae, i.e., $S_{1i}, S_{2i}, ..., S_{6i}, i = 1, n$. The respective integrals are then summed up by numerical integration over the vertical dimension Z to obtain the values of the volume integrals $V_1, V_2, \cdots V_6$; $V_1 = \int_{z_t}^{z_b} S_{1i} dz$, $V_2 = \int_{z_t}^{z_b} S_{2i} dz$ and so on. Using (3.62), the total intensity magnetic anomalies are then computed. If one is interested in the vertical and horizontal anomalies of the magnetic field, formulas given in (3.57), (3.61) and (3.63) may be used. More details about the computation of the surface integrals S, $S_1, S_2, \cdots S_6$ can be found in Talwani and Ewing (1960) and Talwani (1965).

3.3 Test inversion on synthetic 3-D gravity data

Before the described inversion technique is applied to real observed data, it is tested on synthetic 3-D gravity data. The test has two main objectives:

– to investigate the influence of the proposed weighting and scaling technique (3.1.3) on the behaviour of the inversion procedure, on the solution of the inverse problem and on different expected results such like the resolution of the model, the variances of the parameter estimates and the least-squares error.

– to verify the effectiveness of the presented damped least-squares method combined with the SVD for a nonlinear inverse problem.

For the first objective, data weighting and matrix scaling have been implemented in eight different combinations which are classified in two groups. The first group comprises the inversion procedures conducted without matrix scaling; to the second group belong the inversion procedures in which matrix scaling is applied. Depending on how data weighting is applied, four different cases are considered in each group:

– no data weighting is applied;

– only uncertainties in observed data are taken into account;

– only uncertainties in theoretical data are taken into account;

– uncertainties in both observed and theoretical data are taken into account.

Synthetic data (31 data points) computed for a known model are used as observed data. The related uncertainties were produced by a random number generator based on the normal probability distribution with a mean value of 0.2 mGal and a standard deviation of 0.02 mGal. For the uncertainties in theoretical data, pseudo-standard deviations calculated as described in 3.1.3 are used.

A cone shaped diatreme with regular circular contours (Fig. 3.12) was used as a synthetic model. Theoretical data have been computed using the Talwani's algorithm described in 3.2.2. For the parametcrization, five unknowns are used: H_d, the height of the body; $\Delta\rho$, the density contrast; Z_t, the depth to top; R_t $(D_t/2)$ and R_b $(D_b/2)$, radii of the top and the bottom, respectively. Following the scheme presented in 3.1.7, different inversion procedures have been conducted with the same initial parameter guess: $\Delta\rho = -450\ kg/m^3$, $Z_t = 30\ m$, $R_t = 800\ m$, $R_b = 120\ m$, $H_d = 1500\ m$. Confidence intervals of the parameter estimates were defined with a 98% probability based on the two-sided Student-distribution. The Student-distribution has the property to widen the probability intervals of the parameters in contrast to the normal distribution the probability of which is concentrated in the central part of the curve (Sachs, 1985). This is especially valid for small values of the degrees of freedom (ν) of the data kernel $A_{m\times n}$. The standard deviations of the parameters are multiplied by the significance limit, let be t, which depends on the value of ν; t can be approximated by the relation given by Sachs (1985): $t = \alpha + (\alpha^3 + \alpha)/4\nu$, where $\alpha = 2.326348$.

The results are discussed below. The results of inversion procedures conducted without and with matrix scaling have been compiled in Tab. 3.1–3.4 and Tab. 3.5–3.8, respectively. Tab. 3.9 contains some numerical characteristics which can be used to judge the condition of the Jacobian matrix and the goodness of the solution of the inverse problem.

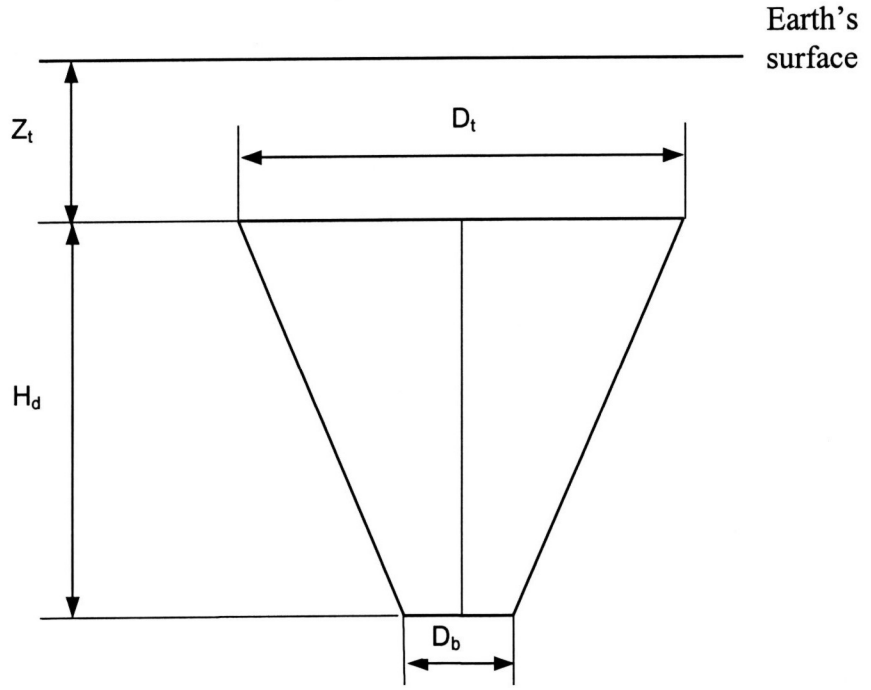

Fig. 3.12 Schematic conical model of a diatreme with circular contours.

Z_t – depth to top of the diatreme;
D_t – diameter of the top of the diatreme;
D_b – diameter of the bottom of the diatreme;
H_d – height of the diatreme.

3.3.1 Results of the test inversion and discussions

Meaning of some of the symbols used in Tables 3.1–11:

R_p – resolution of the parameter; σ_p – standard deviation of the estimate
σ_a – adjusted standard deviation; $\kappa(A)$ – condition number of the data kernel
LB – lower bound of the estimate; UB – upper bound of the estimate
Iter – number of iterations at convergence; T = Exact; F = Inexact

Before proceeding to discussions, I recall that data weighting plays the role of considering the uncertainties in data while matrix scaling takes into account the uncertainties in the model. Therefore it will be talked in the following rather about uncertainties than about weighting and scaling.

The results presented in Tab. 3.1 – 3.4 show that inversion procedures conducted without considering the uncertainties in the model, that is, assuming the model to be exact, yield parameter estimates characterized not only by a poor resolution but also by small variances/covariances and small standard deviations, respectively. This is also shown in Tab. 3.9 (cases 1 – 4) by the relatively large values of the spread of the resolution $\mu(R)$. Though the parameter estimates might be good in some cases, as this is shown in Tab. 3.1, 3.2, 3.3 and 3.9 (cases 1, 2 and 3) and despite large values of the condition number $\kappa(A)$ of the data kernel (Tab. 3.9, cases 1 – 4), we are not able to define confidence intervals of the parameters because of very small standard deviations. This can be well seen in Tab. 3.1 – 4, where the values of the lower and of the upper bounds of the respective parameter estimates don't differ from each other.

As can be seen in Tab. 3.5 – 3.8 and in Tab. 3.9 (cases 5 – 8), taking into account the uncertainties in the model has the major effect to yield large values of the standard deviations and a high resolution of the estimates. This is well understandable because the inversion with an inexact model allows the parameters to vary in a certain range defined by the respective standard deviations. The quality of the parameter estimates, which is generally good, depends on which data — observed, computed or both — the uncertainties have been considered for.

By examining all results shown in Tab. 3.1 – 3.9, it becomes evident that

– considering the uncertainties in the theory speeds up the inversion procedure as this is well shown by the results in Tab. 3.9. In fact,the number of iterations and the CPU (Central Processor Unit, DEC 8400 M 5/300) time at convergence are at smallest for those procedures conducted with the assumption of an inexact theory. But if the uncertainties in the observations and in the model are not additionnally considered, the estimated model might lie far from the true one. This is well demonstrated by the results shown in Tab. 3.4 and 3.6; the two last parameters R_b and H_d have been poorly estimated. The badness of the solution is also illustrated by the results presented in Tab. 3.9, cases 4 and 6, for which the values of the root mean (RMS) and normalized square (MSE) errors are at highest. The reason is that the pseudo-standard deviations used for taking account of the inaccuracies in the model response – being errors of another character and higher magnitude than those of the observations – are induced in the discrepancy vector b through the weighting matrix $\mathbf{W(i)}$, hence making the data too erratic. It is clear that inverting wrong data can only achieve erroneous parameter estimates. This fact is self-evidently an

indication that an inaccurate algorithm for the computation of theoretical data would lead to a model estimate, largely diverging from the true one.

– scaling has the effect to generally enhance the condition of the data kernel. As shown in Tab. 3.9, the values of the condition number $\kappa(A)$ in the 4 last cases are less than those in the 4 first ones. Though the matrix is still somewhat ill-conditioned, we do not have to worry much about this ill-condition because the possibility of yielding satisfactory results is not at all excluded (Jackson, 1972); which is confirmed by the results in Tab. 3.5, 3.7 and 3.8 and in Tab. 3.9 (cases 5, 7 and 8).

– taking into account the uncertainties in the observations plays the role of a regulator; it allows observed data to have some acceptable fluctuations caused by instrumental and/or man made errors, balances out errors in theoretical data and or in computations. This ensures the stability of the algorithm, what lets the solution smoothly converge (Tab. 3.5, 3.8).

– reliable estimates can be expected only if the algorithm to compute the model response is good enough.

Table 3.1 Results of inversion of synthetic 3-D gravity data without both data weighting and matrix scaling.

Param.	True	Estimate	R_p	σ_p	LB	UB
$\Delta\rho$	−500	−499.93	0.484	0.0030	−499.94	−499.93
Z_t	50	49.96	0.336	0.0031	49.95	49.96
R_t	1050	1049.98	0.335	0.0038	1049.97	1049.99
R_b	50	50.52	0.037	0.0010	50.52	50.53
H_d	1800	1799.43	0.011	0.0006	1799.43	1799.43

Table 3.2 Results of inversion of synthetic 3-D gravity data with data weighting (observed only) but without matrix scaling.

Param.	True	Estimate	R_p	σ_p	LB	UB
$\Delta\rho$	−500	−499.95	0.534	0.0030	−499.95	−499.94
Z_t	50	49.97	0.406	0.0034	49.96	49.97
R_t	1050	1049.98	0.429	0.0041	1049.97	1049.99
R_b	50	50.44	0.044	0.0011	50.44	50.44
H_d	1800	1799.52	0.013	0.0006	1799.52	1799.53

Table 3.3 Results of inversion of synthetic 3-D gravity data with data weighting (observed and computed) but without matrix scaling.

Param.	True	Estimate	R_p	σ_p	LB	UB
$\Delta\rho$	−500	−499.96	0.532	0.0031	−499.97	−499.95
Z_t	50	49.97	0.410	0.0036	49.96	49.98
R_t	1050	1049.98	0.428	0.0042	1049.97	1049.99
R_b	50	50.25	0.045	0.0012	50.25	50.26
H_d	1800	1799.82	0.013	0.0006	1799.82	1799.82

Table 3.4 Results of inversion of synthetic 3-D gravity data with data weighting (computed only) but without matrix scaling.

Param.	True	Estimate	R_p	σ_p	LB	UB
$\Delta\rho$	−500	−487.57	0.596	0.1595	−487.96	−487.17
Z_t	50	42.37	0.755	0.1823	41.92	42.82
R_t	1050	1049.71	0.482	0.2066	1049.19	1050.22
R_b	50	216.17	0.197	0.0968	215.93	216.41
H_d	1800	1553.15	0.077	0.0691	1552.98	1553.32

Table 3.5 Results of inversion of synthetic 3-D gravity data without data weighting but with matrix scaling.

Param.	True	Estimate	R_p	σ_p	LB	UB
$\Delta\rho$	−500	−499.94	0.995	0.0798	−500.13	−499.74
Z_t	50	49.96	0.997	0.0526	49.83	50.09
R_t	1050	1049.96	0.992	0.0899	1049.74	1050.18
R_b	50	50.41	0.642	1.4952	46.70	54.12
H_d	1800	1799.70	0.549	2.9828	1792.30	1807.09

Table 3.6 Results of inversion of synthetic 3-D gravity data with data weighting (computed only) and with matrix scaling.

Param.	True	Estimate	R_p	σ_p	LB	UB
$\Delta\rho$	−500	−484.51	0.921	10.3676	−510.21	−458.80
Z_t	50	40.60	0.981	5.9714	25.79	55.40
R_t	1050	1048.87	0.998	3.1648	1041.02	1056.71
R_b	50	247.88	0.550	105.4867	−13.63	509.38
H_d	1800	1512.11	0.756	134.4668	1178.77	1845.46

Table 3.7 Results of inversion of synthetic 3-D gravity data with data weighting (observed only) and with matrix scaling.

Param.	True	Estimate	R_p	σ_p	LB	UB
$\Delta\rho$	-500	-499.96	0.994	0.0706	-500.13	-499.78
Z_t	50	49.97	0.996	0.0529	49.84	50.10
R_t	1050	1049.96	0.994	0.0828	1049.76	1050.17
R_b	50	50.22	0.640	1.6174	46.21	54.23
H_d	1800	1799.94	0.572	3.1396	1792.15	1807.72

Table 3.8 Results of inversion of synthetic 3-D gravity data with both data weighting and matrix scaling.

Param.	True	Estimate	R_p	σ_p	LB	UB
$\Delta\rho$	-500	-499.97	0.984	0.0893	-500.23	-499.79
Z_t	50	49.98	0.991	0.0676	49.84	50.18
R_t	1050	1049.96	0.996	0.0758	1049.77	1050.15
R_b	50	49.98	0.598	1.6698	45.44	53.72
H_d	1800	1800.33	0.577	3.0506	1793.35	1808.48

Table 3.9 Numerical characteristics of inversion procedures conducted with different combinations of considering uncertainties in data (y), theory (f) and model (m).

Case	y	f	m	$\kappa(A)$ $\times 10^4$	RMS $\times 10^{-4}$	MSE $\times 10^{-6}$	$\mu(R)$	Iter	CPU-time [sec.]
1	T	T	T	0.41	2.89	0.294	3.39	10	2.1
2	F	T	T	0.45	2.90	0.299	3.11	10	2.1
3	F	F	T	0.48	3.01	0.320	3.10	10	2.1
4	T	F	T	0.82	161.9	926.7	2.45	6	1.2
5	T	T	F	0.18	2.94	0.305	0.67	7	1.4
6	T	F	F	0.30	197.9	1384.0	0.65	6	1.3
7	F	T	F	0.13	3.03	0.325	0.64	7	1.4
8	F	F	F	0.13	3.17	0.357	0.65	7	1.4

In order to verify the goodness and the consistency of the method, diverse inversion procedures with data weighting and matrix scaling (case 8) have been run for different initial guesses with strongly changed model parameters. One of such inversion procedures has been conducted with the following initial guess: $\Delta\rho = -350\ kg/m^3$, $Z_t = 150\ m$, $R_t = 500\ m$, $R_b = 90\ m$, $H_d = 1000\ m$. These values strongly differ from those of the previous initial guess (see above). The results are shown in Tab. 3.10. As can be seen, they almost do not differ from those presented in Tab. 3.8. This clearly demonstrates that the method exhibits high performances and stability.

Table 3.10 Results of inversion of synthetic 3-D gravity data with data weighting and matrix scaling.

Strongly changed parameters of the initial guess.

Param.	True	Estimate	R_p	σ_p	LB	UB
$\Delta\rho$	−500	−499.97	0.995	0.0731	−501.15	−499.78
Z_t	50	49.98	0.997	0.0526	49.85	50.11
R_t	1050	1049.96	0.994	0.0883	1049.74	1050.18
R_b	50	49.94	0.646	1.7139	45.73	54.22
H_d	1800	1800.41	0.571	3.3577	1792.02	1808.66

3.3.2 Adjustement of the standard deviations of the estimates

Till now it has been assumed that the model parameters are linearly independent, i.e., their covariances and their correlation coefficients are equal to zero. But the computed a posteriori covariance and correlation coefficient matrices (see below for case 8) show this assumption to be wrong.

Matrix of correlation coefficients for the case 8

$$r = \begin{bmatrix} 1.00 & -0.89 & -0.08 & 0.40 & -0.27 \\ -0.89 & 1.00 & -0.32 & -0.72 & 0.62 \\ -0.08 & -0.32 & 1.00 & 0.86 & -0.92 \\ 0.40 & -0.72 & 0.86 & 1.00 & -0.99 \\ -0.27 & 0.62 & -0.92 & -0.99 & 1.00 \end{bmatrix}$$

The correlation coefficient **r** between two variables can be positive, zero or negative. The values of **r** lie between −1 and +1, i.e., $-1 \leq r \leq 1$. A value of r close to either −1 or +1 indicates a strong linear relationship between two variables, whereas a value close to zero indicates a less definite relationship (Robinson, 1981). When the correlation coefficient r is positive, an increase or a decrease of one of the variables leads to a respective increase or decrease of the other. For a negative value of r, one of the variables tends to decrease as the other increases.

As it is known, the linearity coefficient of two variables is proportional to their correlation coefficient. As a matter of fact, the linear dependence of the parameters is reflected into their a posteriori standard deviations. Thus, I find it reasonable to take into account this linear dependence to adjust the a posteriori standard deviations of the estimates by using the matrix of the correlation coefficients.

Let σ_i be the standard deviation of the i^{th} parameter estimate and r_{ij} (j=1,N) be the values of the correlation coefficients. The adjusted standard deviation σ_{ai} is then defined as a weighted sum of products of the calculated value σ_i and the elements of the respective i^{th} row or column of the symmetric matrix of the correlation coefficients:

$$\sigma_{ai} = |s_i| * \sigma_i$$

where

$$s_i = \sum_{j=1}^{N} r_{ij}$$

In Tab. 3.11 are presented the lower and upper bounds of the parameter estimates defined with adjusted standard deviations for the case 8 with the same strongly changed initial guess as for results in Table 3.10.

Table 3.11 Results of inversion of synthetic 3-D gravity data with data weighting and matrix scaling.

Parameter bounds defined with adjusted standard deviations.

Param.	True	Estimate	R_p	σ_a	LB	UB
$\Delta\rho$	−500	−499.97	0.995	1.7359	−504.27	−495.66
Z_t	50	49.98	0.997	0.1492	49.61	50.35
R_t	1050	1049.96	0.994	2.1672	1044.59	10555.34
R_b	50	49.94	0.646	3.5505	41.18	58.78
H_d	1800	1800.41	0.571	9.2081	1777.51	1823.17

As can be seen, the confidence intervals in Tab. 3.11, defined with the adjusted standard deviations are somewhat wider than those in Tab. 3.10, defined with the non-adjusted standard deviations. The effect of the adjustement of the standard deviations, namely the enlargement of the confidence intervals of the estimates, is especially important for those estimates exhibiting poor resolution and consequently small variances.

Moreover, for large values of the degree of freedom (ν) of the Jacobian matrix $A_{m\times n}$— which usually is the case in most geophysical inverse problems in which the number of observations is much greater than that of involved model parameters — parameter limits based on the Student-distribution don't much differ from those defined by the normal distribution. Hence the adjustement of the standard deviations, using the correlation coefficients, is a good tool to ensure larger/better probability limits of the parameter estimates.

From all results discussed above, it is generally recommended to carry out the inversion with scaling of the data kernel in order to enhance the condition of the latter and to enable the determination of the significant confidence limits of the parameters. Even if the algorithm to compute theoretical data is accurate enough, the model response can not be error-free since errors coming from other algorithms involved in the computations such like that of calculating the partial derivatives and from other sources, e.g. round-off errors of the computing hardware, might corrupt it. Therefore uncertainties in observations should be taken into account in order to enhance the performance of the inversion algorithm and hence to provide with a more reliable solution of the inverse problem. To better define the confidence intervals of the model parameters, the computed a posteriori standard deviations of the estimates should be adjusted for the correlation between the parameters which are usually assumed to be uncorrelated.

4. Theoretical modeling of maar-diatreme volcanoes

In order to properly apply inversion techniques to geophysical data for the determination of the parameters of the maar-diatreme volcanoes, it is necessary to have a certain idea about the models to be used. The a priori knowledge about the physics, the geology and the geometry of the structures can help to conceive initial models which partly define the course of the inversion procedure and consequently the quality of the parameter estimates. In most cases, the a priori information is completely or partly missing. In such a situation, the a priori information can then be approximated or simply assumed with the help of any available source.

In this chapter, it will be dealt with theoretical modeling of the maar-diatreme volcanoes in order to show how observed gravity and magnetic fields can qualitatively and/or quantitatively be used to get a rough idea about the geology, the morphology and the physical properties of the maar-diatreme structures.

4.1 Magnetic modeling

Contrary to the gravity field which physically only depends on the density of the rocks, the magnetic field is defined by many parameters each of which has its particular influence on the shape and the amplitude of the magnetic signature. Therefore it is not easy, even not possible, to work out a simplified method which could enable us to determine the parameters of the maar-diatremes from magnetic anomalies.

The aim of the theoretical magnetic modeling presented here is to show how magnetic anomalies can be of first help while either conceiving models of the maar-diatremes and/or qualitatively interpreting data observed over those structures. In the following, it will not be investigated how every single parameter can influence the magnetic field. The investigation will be limited to only the influence of the morphology and the location depth of the body. A cone shaped body with circular contours (Fig. 3.12, chap. 3) has been used for the models. Theoretical magnetic anomalies have been computed for the cases indicated below:

a) a maar-diatreme buried at 30, 75 and 150 m depth, respectively;
b) a scoria cone buried at 30, 75 and 150 m depth, respectively;
c) a maar-diatreme buried at the same depth; constant diameter, different heights;
d) a maar-diatreme with a scoria cone located in it; the coordinates of the centres of both bodies coincide;
e) a maar-diatreme with a scoria cone located in it; the centres of the bodies have different coordinates.

The geometrical and physical parameters which have been involved in the computations are given in the captions of the figures showing the respective calculated magnetic anomalies. They are symbolized as: Z_t, the depth to top; D_t, the diameter of the top; D_b, the diameter of the bottom; H, the height of the body; X_c and Y_c, the coordinates of the centre; Fo, the strength of the magnetic field; I, the inclination; D, the declination and χ, the susceptibility. It has been assumed that the bodies are homogeneously magnetized by induction.

The computed magnetic anomalies are presented in form of profiles (S-N and W-E) and contour maps. The two forms, considered together, can give a better idea about the structure.

4.1.1 Conclusions from the magnetic modeling

Conclusions drawn from the magnetic modeling have been compiled in the following summary:

- For a nearly outcropping diatreme, the maximum of the magnetic anomaly is close to the southern boundary of the structure (Fig. 4.1a, c). The sharp extrema and high gradients of the anomaly approximately define the upper boundary of the structure (Fig. 4.1). As the burial depth increases, the maximum of the anomaly moves toward the centre of the structure and the shape of the contour lines passes gradually from a quasi elliptic to a circular one (Fig. 4.1c, 4.2c and 4.3c).
- For diatremes located at shallow depths, the magnetic anomaly is characterized by gradients stronger in the area southwards from the maximum than in the area northwards (Fig. 4.1a, c and Fig. 4.2a, c).
- For a scoria cone, independent of the burial depth, the maximum of the anomaly is located a bit away southwards from the centre of the structure and the shape of the contour lines is almost circular (Fig. 4.4, 4.5 and 4.6).
- Anomalies of scoria cones are generally narrower and sharper than those of diatremes. A comparison of the anomaly profiles shown on Fig. 4.1a, b and 4.2a, b with those on Fig. 4.4a, b and 4.5a, b lets this fact be well seen.
- Opposite to the case of diatremes, the gradients of the magnetic anomaly caused by scoria cones are stronger in the area northwards from the maximum than in the area southwards (Fig. 4.4a, c; Fig. 4.5a, c and Fig. 4.6a, c).
- Generally, the minima of the magnetic anomalies caused by diatremes are stronger and broader than those produced by scoria cones. This can be well seen if one compares Fig. 4.1c, 4.2c with Fig. 4.4c, 4.5c showing the contour maps of the magnetic anomaly caused by diatremes and scoria cones, respectively. For relatively great burial depths, the minima caused by scoria cones even become insignificant (Fig. 4.6).
- The anomalies caused by both the diatreme and the scoria cone get broader and smoother as the burial depth increases. For relatively great burial depths, the anomalies become rather similar and might be difficult to differentiate from each other (Fig. 4.3 and Fig. 4.6).

However, it should be noted that all the results and discussions presented here relate to ideal geometrical and homogeneous bodies. In reality, the behaviour and the amplitude of the magnetic fields might be influenced by other factors such like the irregular shape, the nature and the extension of the rocks filling the overlying part (maar crater), the talus slopes of the crater, the intrusions of magmatic bodies, lava flows coming from other nearby eruption centres, the degree of erosion, factors resulting from human activity etc.

Some maar-diatreme structures might even be complex, i.e., they might be built up of various bodies with different physical properties. The magnetic response will then be a resultant of the superposed fields. As just an example, I considered a scoria cone located within a maar-diatreme. A scheme showing a vertical cross-section of such a structure is shown on Fig. 4.7. While the susceptibilities of the diatreme (χ_4) and of the scoria cone

(χ_3) were assumed to be constant, that of the maar filling was thought of as to increase with the depth. Two susceptibility values, χ_1 and χ_2, were assigned to the portion of the crater filling above the scoria cone and to that between the scoria cone and the crater walls, respectively. Theoretical anomalies have been computed for two cases. In one case, it has been assumed that the centres of both the maar-diatreme and the scoria cone have the same coordinates; whereas in the other, the coordinates differ. The superposition of the fields is more stressed in the areas of the highs, where the scoria cone has more influence on the anomaly (Fig. 4.8). In fact, the effect of the scoria cone is especially remarkable in the central areas, where it leads to the sharpening of both the W-E and S-N anomaly profiles. The contour lines of the anomaly acquire a more or less oval shape. As already seen above, scoria cones produce very weak negative anomalies. Therefore the lows of the resultant magnetic anomaly are mainly due to the influence of the diatreme. The shape and the behaviour of the anomaly can also depend on the positions of the centres of the maar-diatreme and of the scoria cone relative to each other. This is well shown on Fig. 4.9, representing the profiles and the contour map of the magnetic anomaly resulting from a maar-diatreme and a scoria cone the centres of which are 100 m away from each other. In our example, the contour lines get an elongated shape northwards owing to the off-set centre of the scoria cone. The anomaly displays a general broadening in the central areas; while it flattens in the S-N direction, it remains sharp in the W-E one.

Another important factor which affects the behaviour of the magnetic anomaly of the maar-diatremes is the relationship between their vertical and horizontal dimensions. Figures 4.10, 4.11 and 4.12 show magnetic anomalies of diatremes — all buried at a same depth — the diameters and heights of which are in the proportion of 5:1, 2:1 and 1:1.5, respectively. The case of the 1:1 proportion has already been presented in Fig. 4.1. As can be seen on figures of contour maps, the effect of the relationship between the diameter and the height of the diatreme is clearly reflected in the behaviour of the magnetic anomaly in the southern areas. For heights much smaller than diameters, the area between the zero contour and the nearest contours of positive values of the magnetic anomaly is narrow; the zero contour runs close to the boundary of the body (Fig. 4.10c and 4.11c). This effect is also well noticeable in the magnetic profiles, especially in the W-E direction, where it is expressed by a sharpening of the curve (Fig. 4.10a, b and 4.11a, b). As the height gets larger and larger, the zero contour moves farther and farther away from the boundary southwards, south-south-westwards and south-south-eastwards (Fig. 4.1c and 4.12c).

The results discussed above indicate that both the burial depth and the diameter/height relationship are factors which control the amplitude and the shape of the magnetic anomaly. However, the effects caused by changes in the burial depth are stronger and more distinct than those due to changes in the diameter/height relationship. Theoretical computations show that for a 500 m wide and 250 m high diatreme buried at a depth of 30 m, the amplitude of the magnetic anomaly changes by a factor of 1.4 when the height is increased three times, whereas a tripling of the burial depth decreases the anomaly by a factor of 1.6.

The analysis of the effects of the physical properties (magnetization, inclination and declination) has been intentionally not discussed in this investigation. The results of this study hold for magnetic fields caused by bodies located in central Europe.

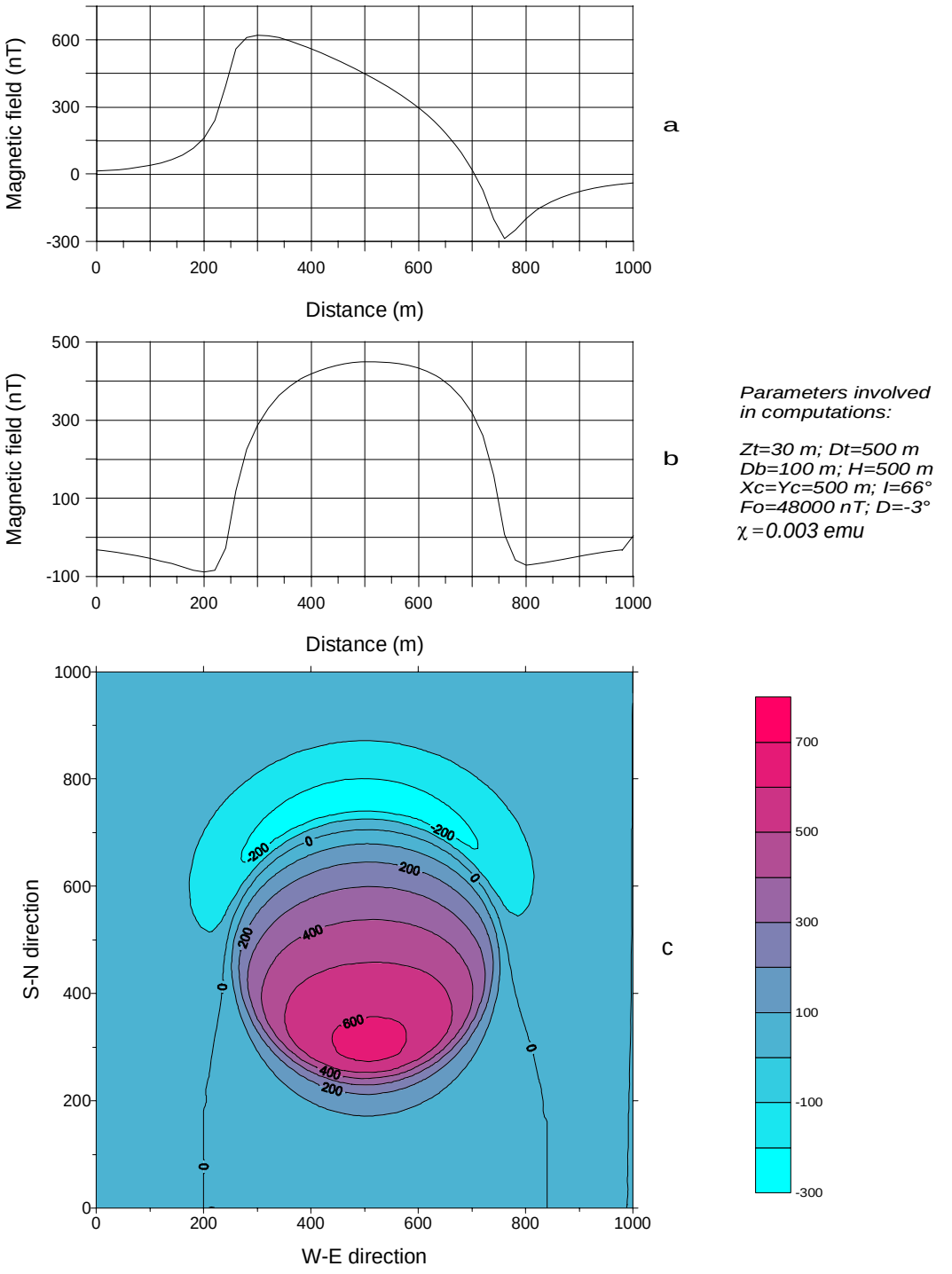

Fig. 4.1 Anomaly of the total magnetic field caused by a diatreme. a, b: S-N and W-E profiles, respectively; c: contour map.

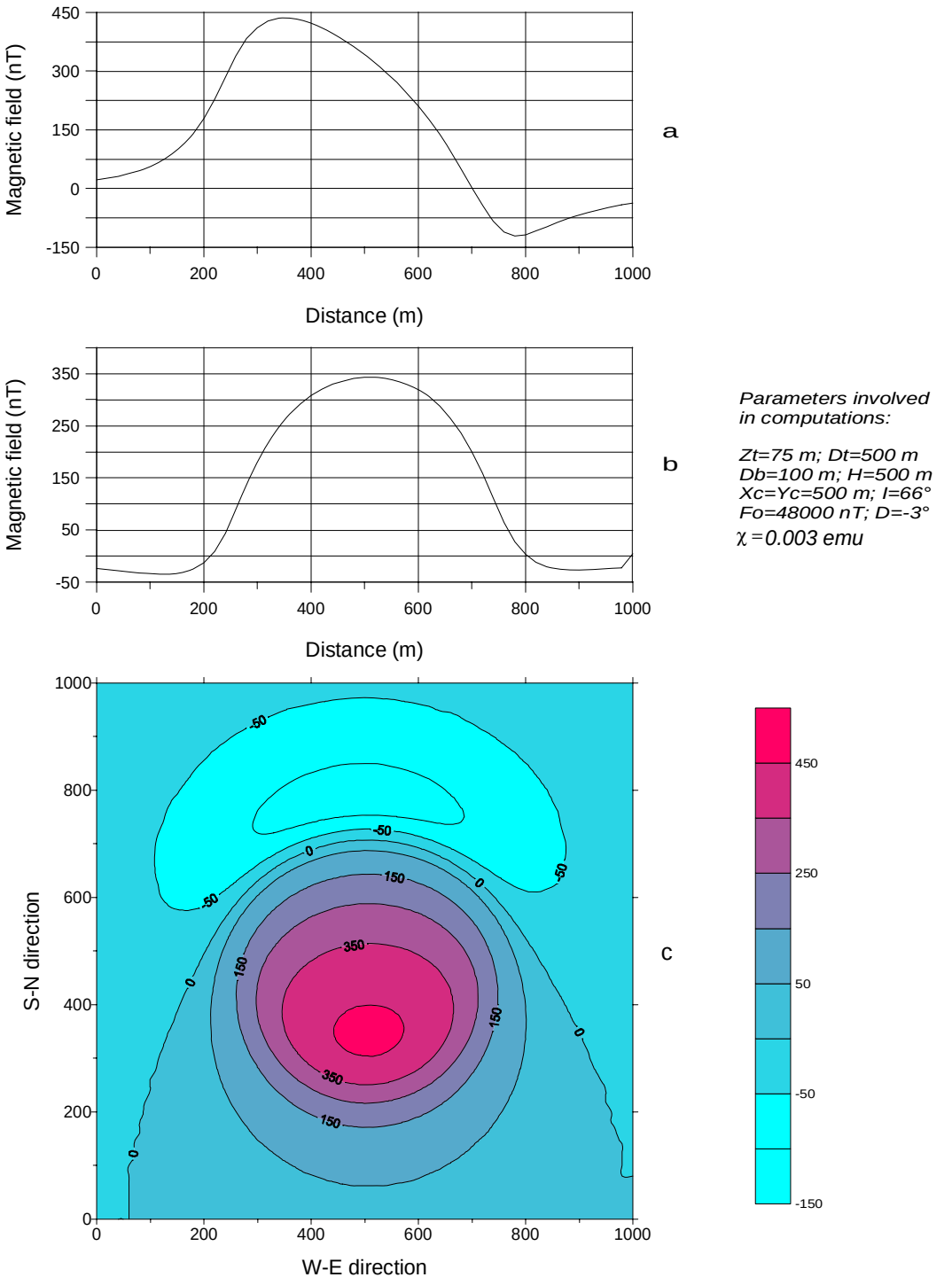

Fig. 4.2 Anomaly of the total magnetic field caused by a diatreme. a, b: S-N and W-E profiles, respectively; c: contour map.

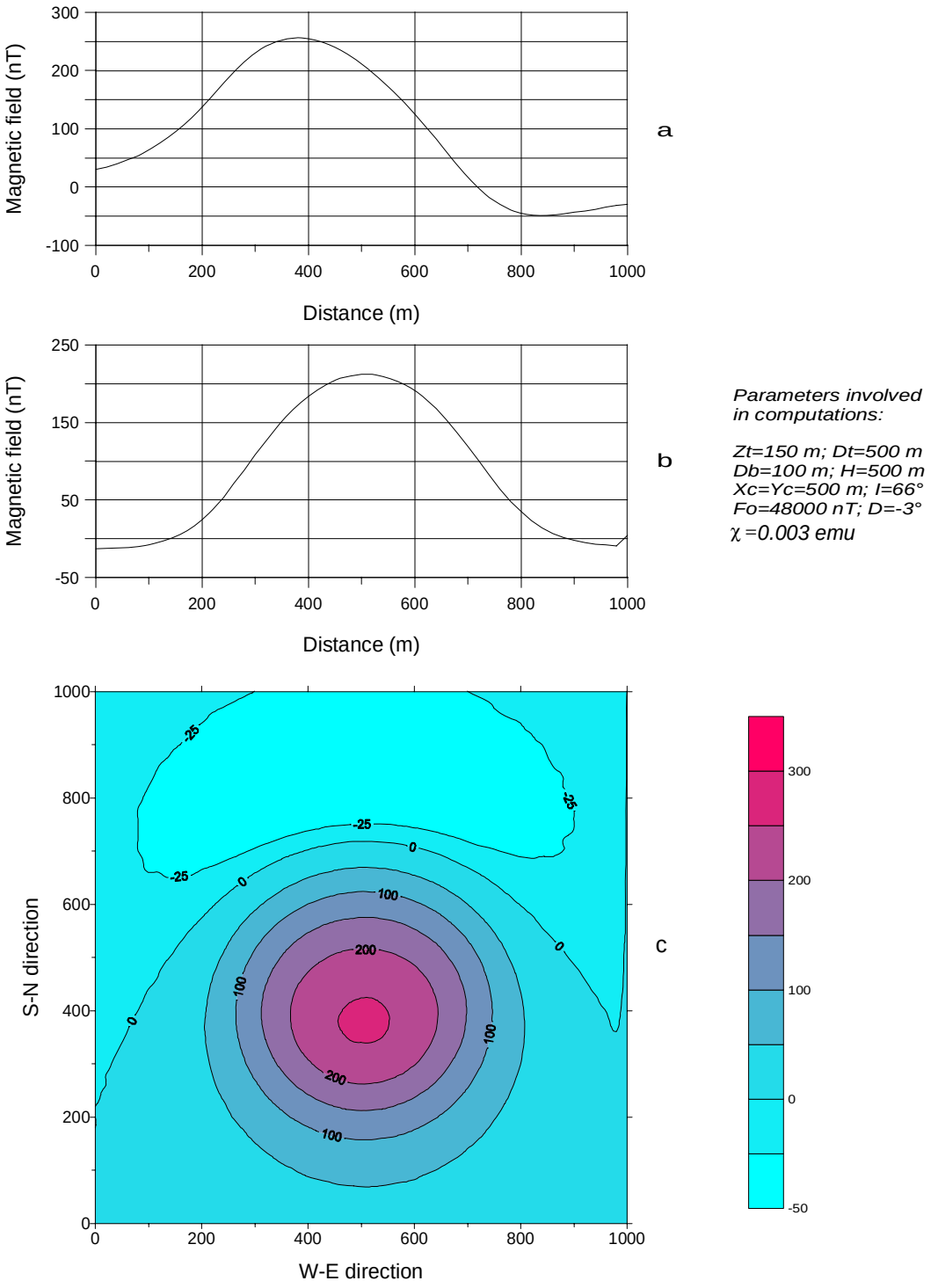

Fig. 4.3 Anomaly of the total magnetic field caused by a diatreme. a, b: S-N and W-E profiles, respectively; c: contour map.

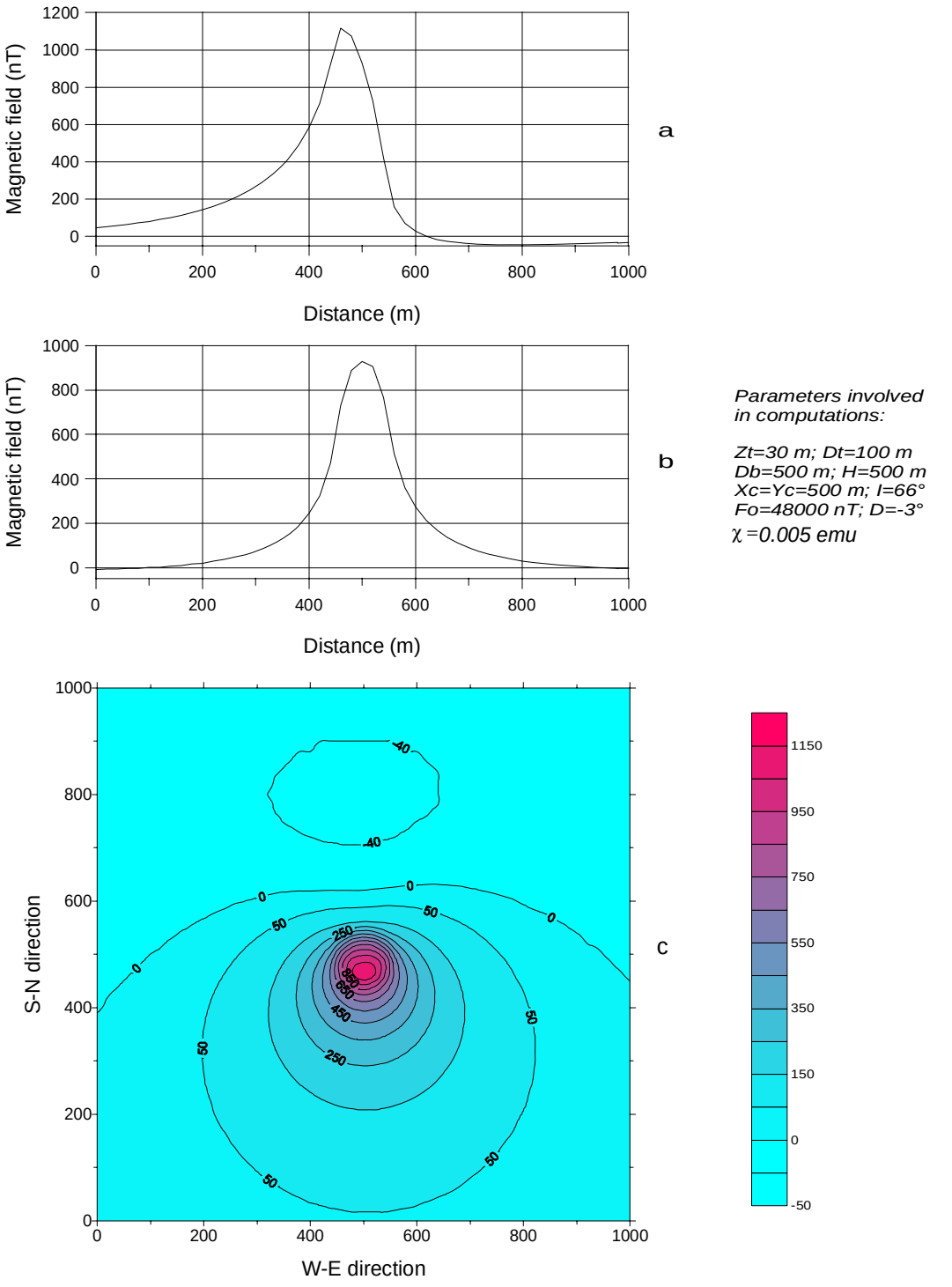

Fig. 4.4 Anomaly of the total magnetic field caused by a scoria cone. a, b: S-N and W-E profiles, respectively; c: contour map.

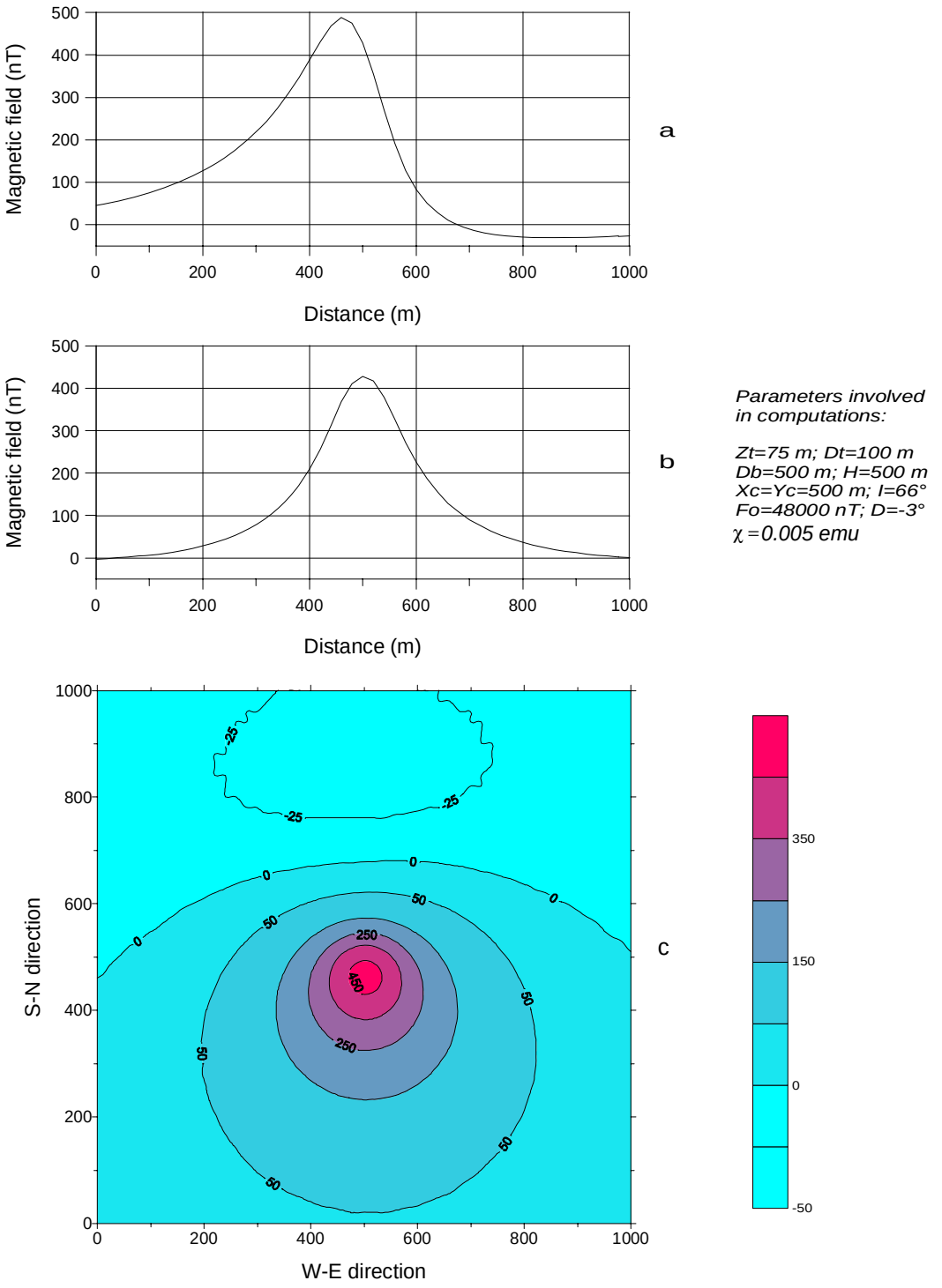

Fig. 4.5 Anomaly of the total magnetic field caused by a scoria cone. a, b: S-N and W-E profiles, respectively; c: contour map.

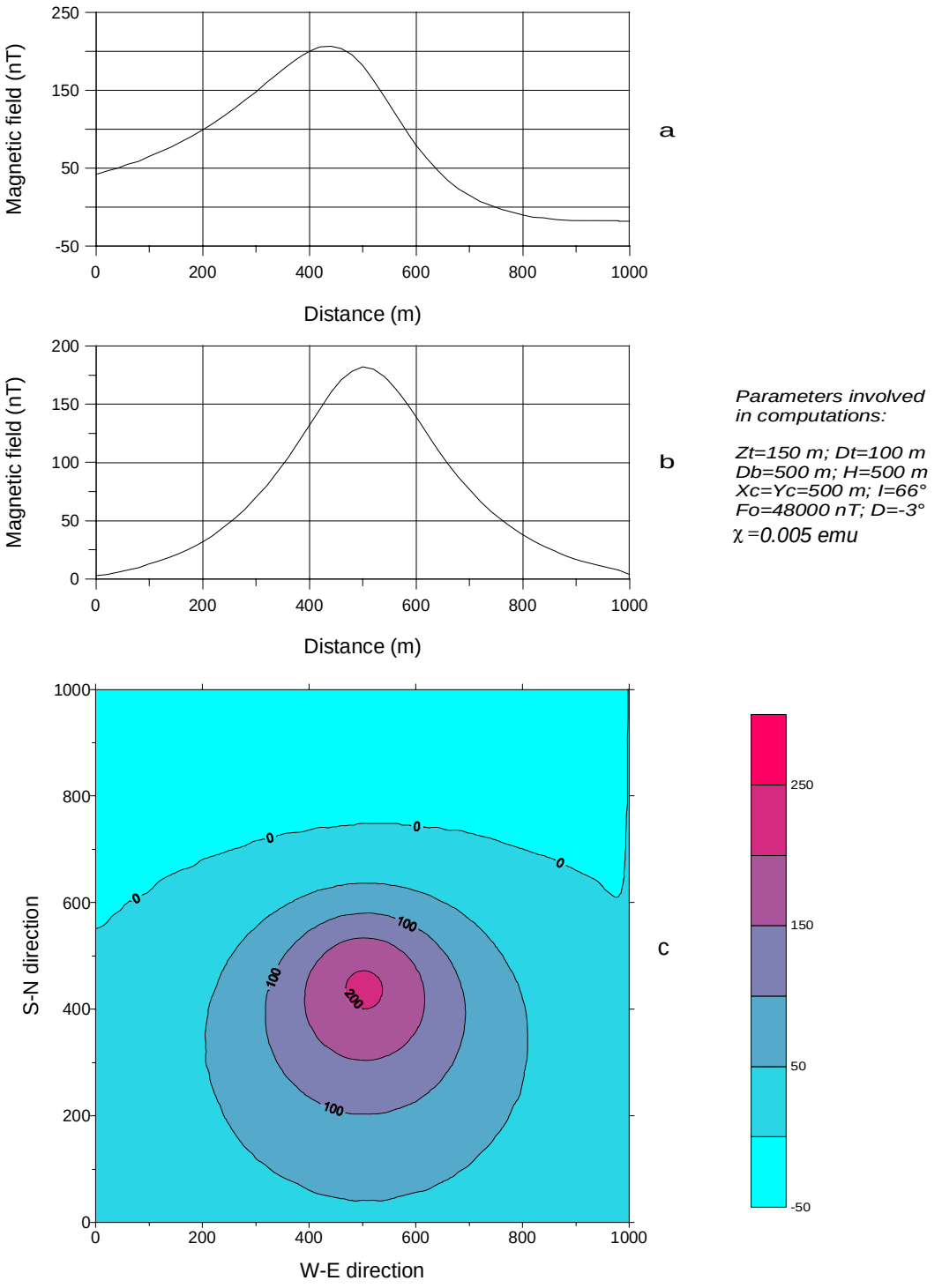

Fig. 4.6 Anomaly of the total magnetic field caused by a scoria cone. a, b: S-N and W-E profiles, respectively; c: contour map.

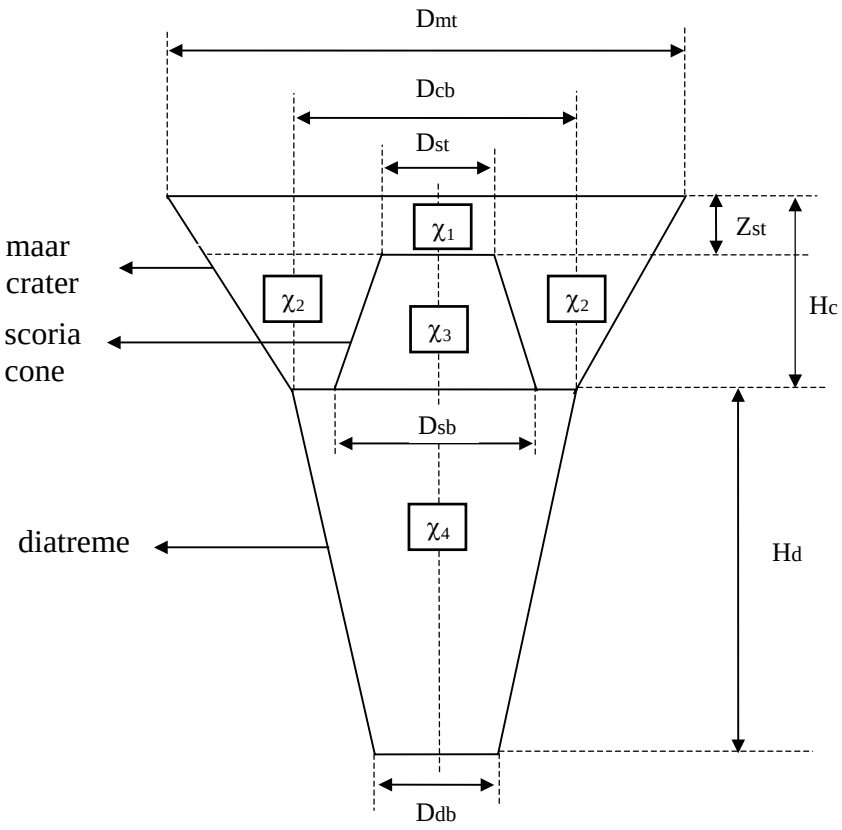

Fig. 4.7 Schematic cross-section of a complex maar structure: Maar-diatreme with a scoria cone located within the crater.

Dmt : diameter of the top of the maar
Dcb : diameter of the bottom of the maar crater
Hc : height of the maar crater
Dst : diameter of the top of the scoria cone
Dsb : diameter of the bottom of the scoria cone
Zst : depth to the top of the scoria cone
Hd : height of the diatreme
Ddb : diameter of the bottom of the diatreme
χ_1 : susceptibility of the rocks of the upper part of the maar
χ_2 : susceptibility of the rocks between the maar walls and the scoria cone
χ_3 : susceptibility of the rocks of the scoria cone
χ_4 : susceptibility of the rocks of the diatreme

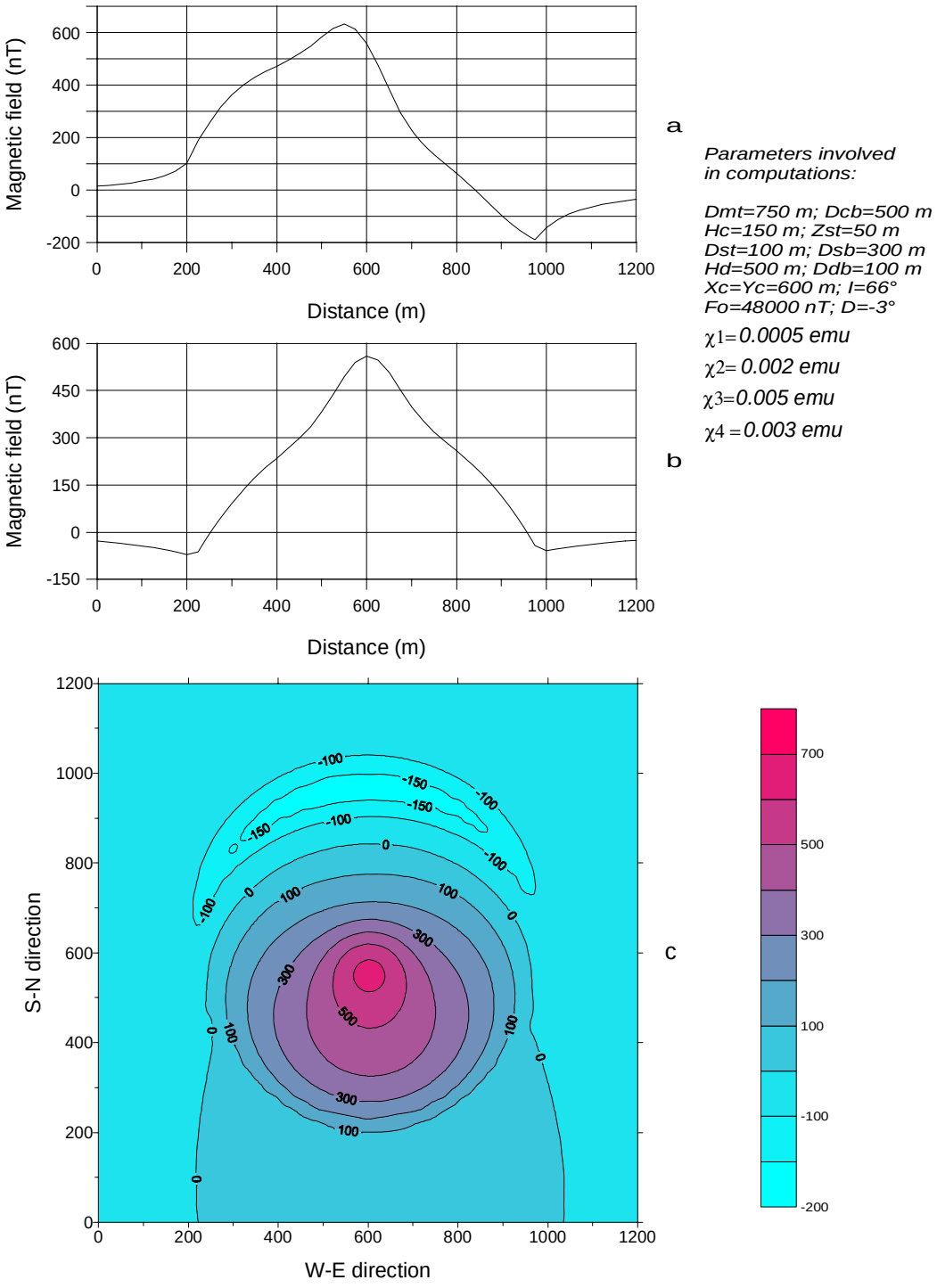

Fig. 4.8 Anomaly of the total magnetic field caused by a complex maar structure: maar-diatreme and a scoria cone located within the latter. The coordinates of the centres of both the maar-diatreme and the scoria cone coincide.
a, b: S-N and W-E profiles, respectively; c: contour map.

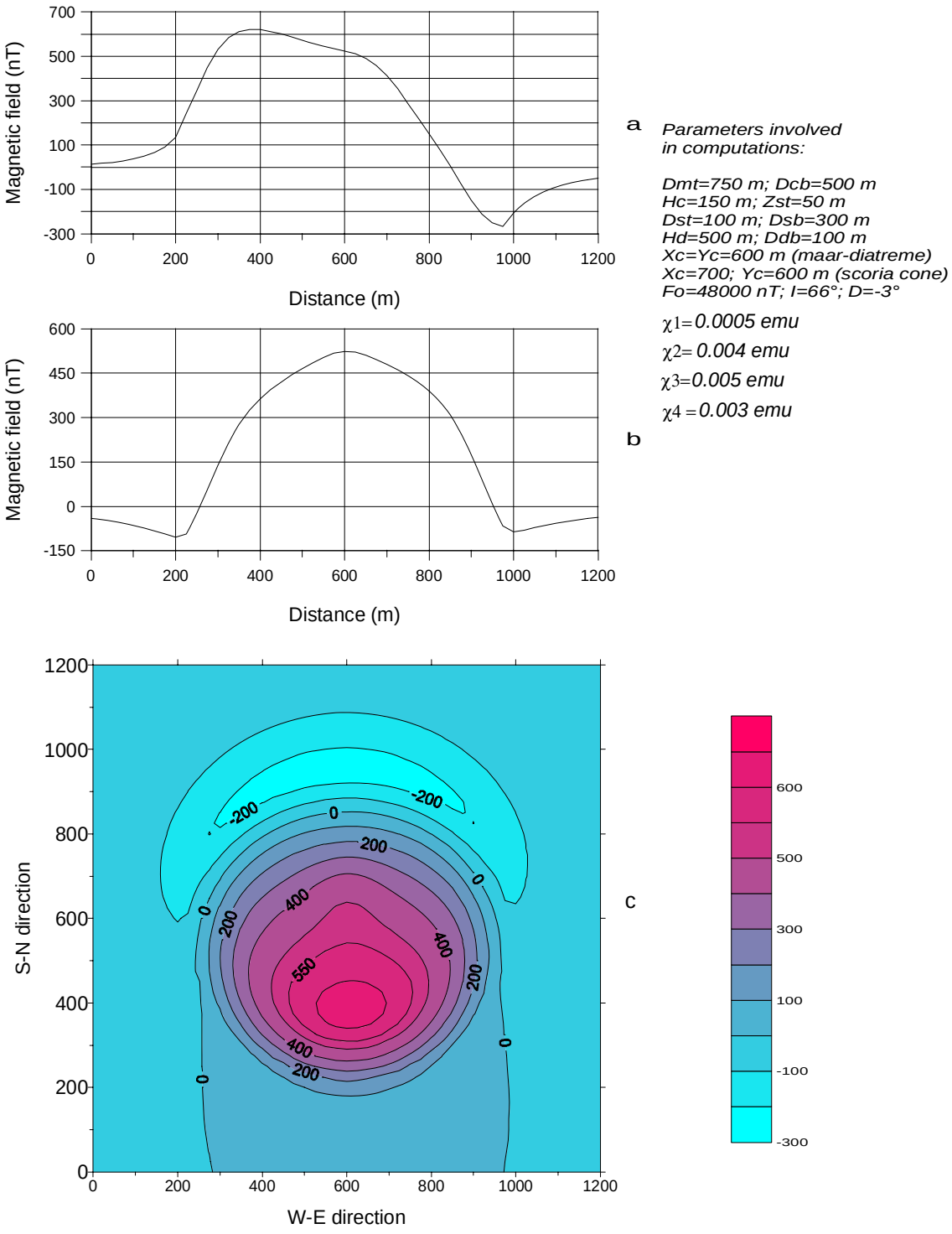

Fig. 4.9 Anomaly of the total magnetic field caused by a complex maar structure: a maar-diatreme and a scoria cone located within the latter. The centre of the scoria cone is located 100 m northwards from that of the maar-diatreme. a, b: S-N and W-E profiles, respectively; c: contour map.

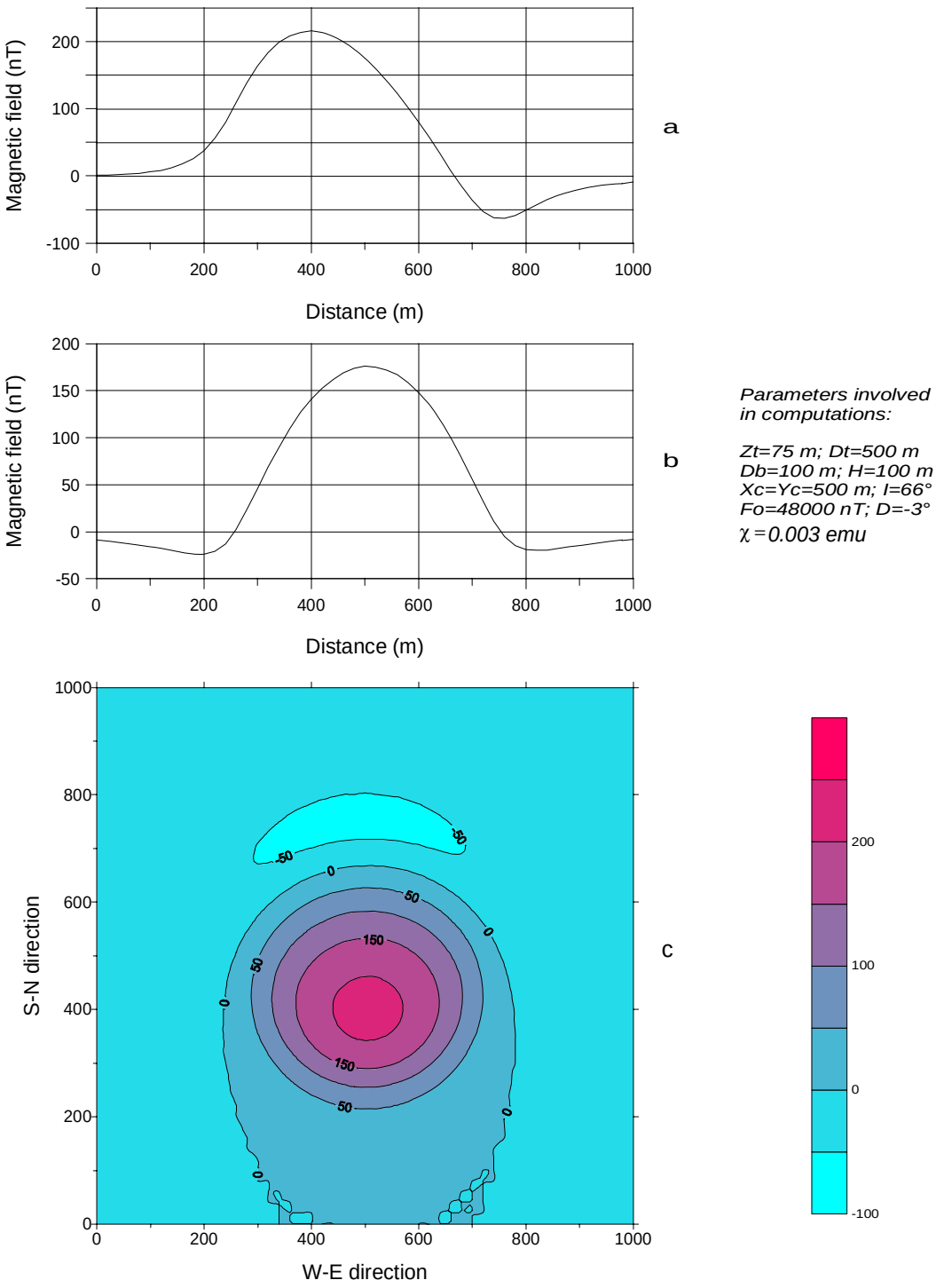

Fig. 4.10 Anomaly of the total magnetic field caused by a diatreme. a, b: S-N and W-E profiles, respectively; c: contour map.

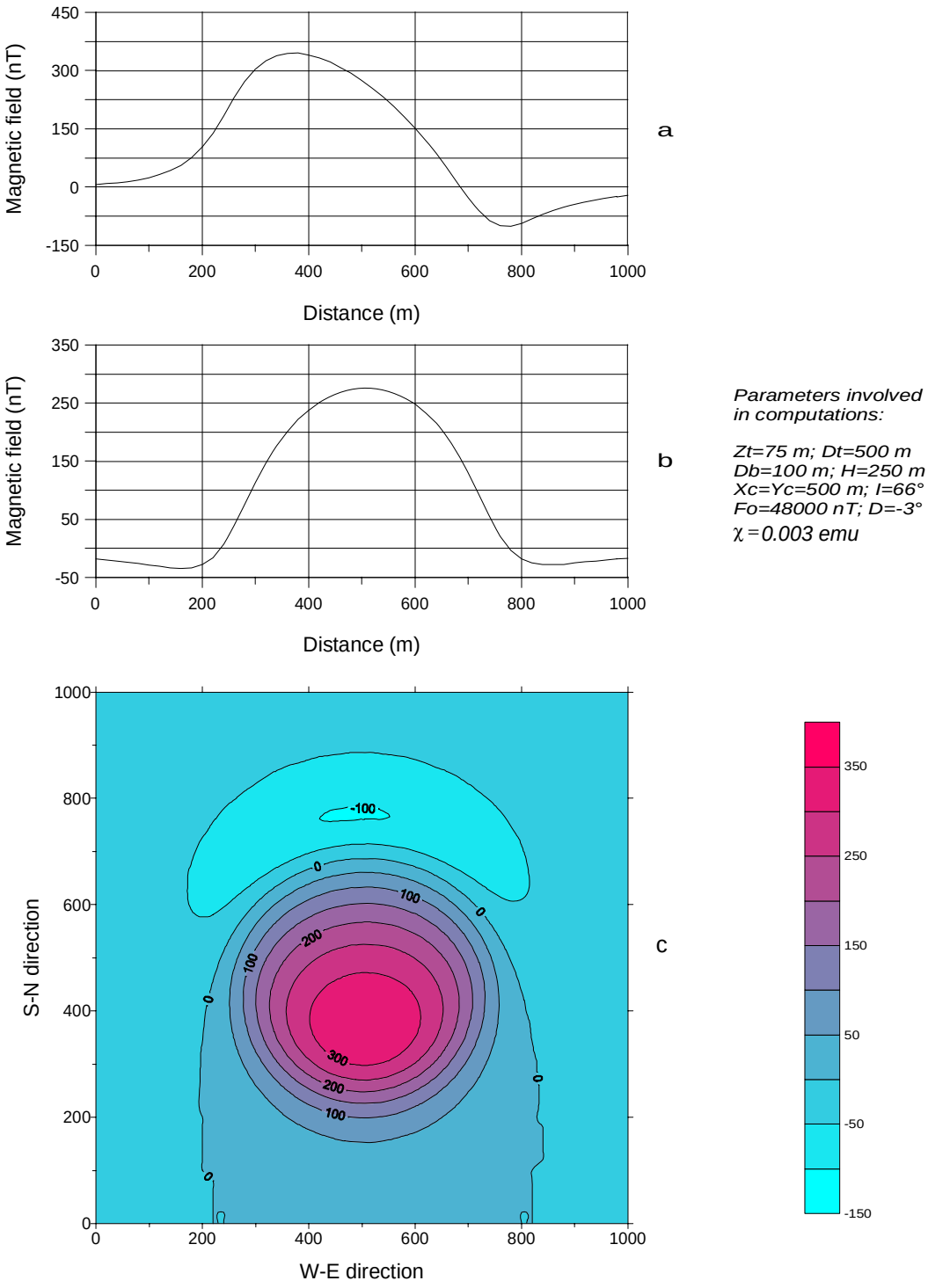

Fig. 4.11 Anomaly of the total magnetic field caused by a diatreme. a, b: S-N and W-E profiles, respectively; c: contour map.

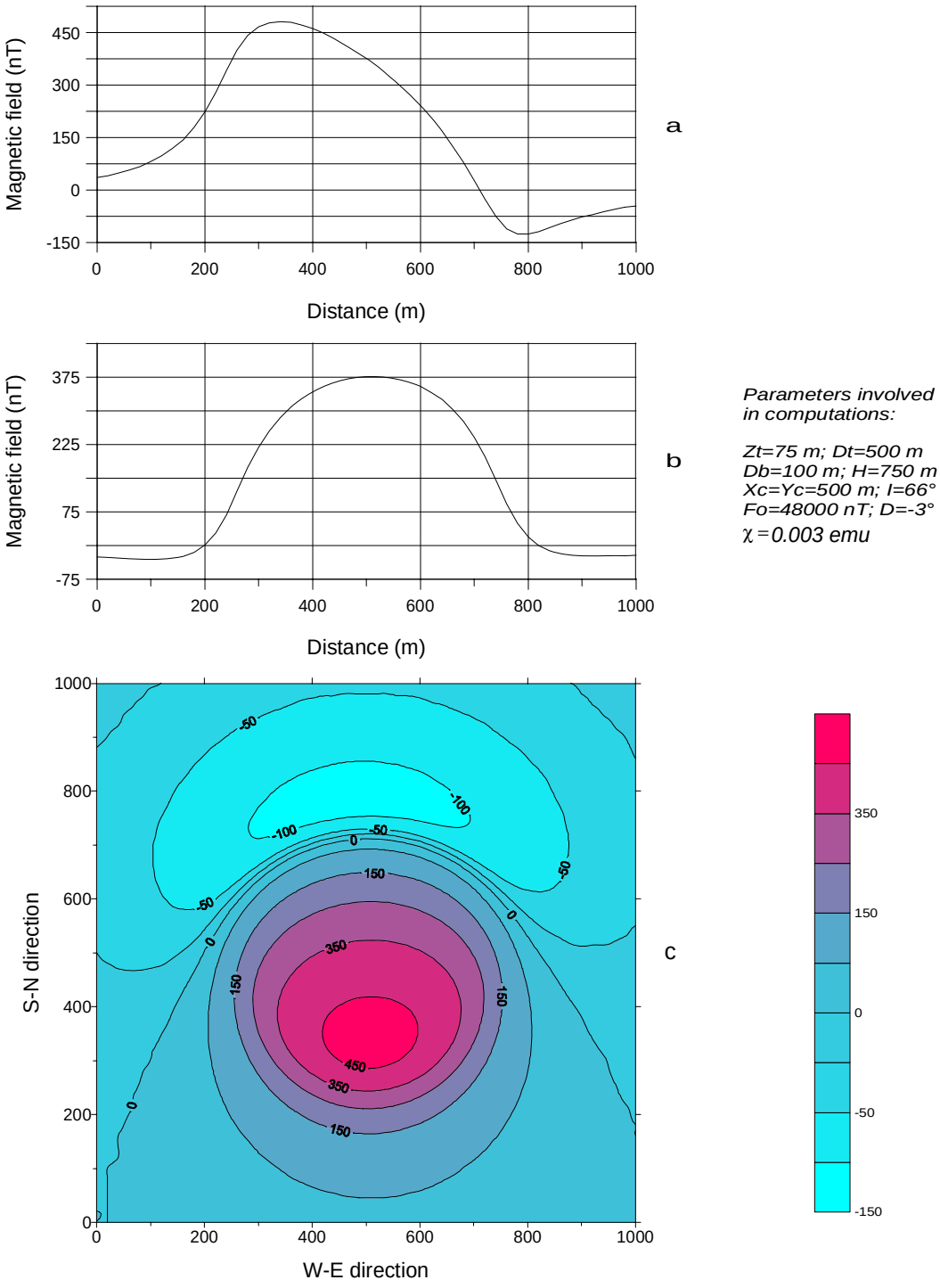

Fig. 4.12 Anomaly of the total magnetic field caused by a diatreme. a, b: S-N and W-E profiles, respectively; c: contour map.

4.2 Gravity modeling

4.2.1 Framework of the investigation

In addition to the general aim which was stated at the beginning of this chapter, gravity modeling is conducted in order to work out the diameter/depth systematics for the maar-diatremes. For this purpose, the relationship between the gravity response and the two mentioned parameters will be studied. I judged it reasonable to investigate that relationship on the basis of the amplitude of the gravity anomaly. This value seems to be more reliable than others which might be affected by noise, by surface inhomogeneities or by edge effects. For the envisaged investigation an inverted cone-shaped body with a base of diameter **d** and with a height **h** (Fig. 4.13 A) will serve as a model to represent the maar-diatreme structure in a simplified way. In the present study, it is assumed that the gravity anomaly is due to the effective density contrast characterizing the maar-diatreme structure in its whole. This implies that the body is outcroping, i.e., the depth to the top of the causative structure is zero. Litinsky (1989) has shown that even for narrow basin shaped structures, the error between the responses of the true model and the assumed homogeneous one with effective density contrast is so small that it can be ignored for practical purposes. In the following, the effective density contrast will be simply referred to as the density contrast. The effective density contrast can be expressed as

$$\Delta\rho = \frac{\sum \Delta\rho_i \Delta g_i}{\sum \Delta g_i} = \frac{\sum \Delta\rho_i \Delta g_i}{\Delta g} \tag{4.1}$$

where $\Delta\rho_i$ and Δg_i are respectively the density contrast and the gravity effect of a part (disk, layer, polygon etc.) at a given i^{th} depth.
The investigation will follow the approach below:

- first, computation of theoretical models;
- compilation of diagrams using results of theoretical models;
- application of the theory to actual field data (parameter determination from the field data using the diagrams);
- derivation of the diameter/depth systematics — if any exists — with the help of the results obtained.

4.2.2 Theoretical analysis

The major parameters which define the amplitude of the gravity anomaly Δg_a are the density contrast ($\Delta\rho$), the diameter (**d**) and the height (**h**) of a maar-diatreme structure, i.e.,

$$\Delta g_a = f(\Delta\rho, d, h) \tag{4.2}$$

If the diameter and the height are combined to one parameter h/d, which is the half-tangent of the inwards dip angle α of the maar-diatreme walls (Fig. 4.13), the expression (4.2) becomes

$$\Delta g_a = f(\Delta\rho, d, h/d) \tag{4.3}$$

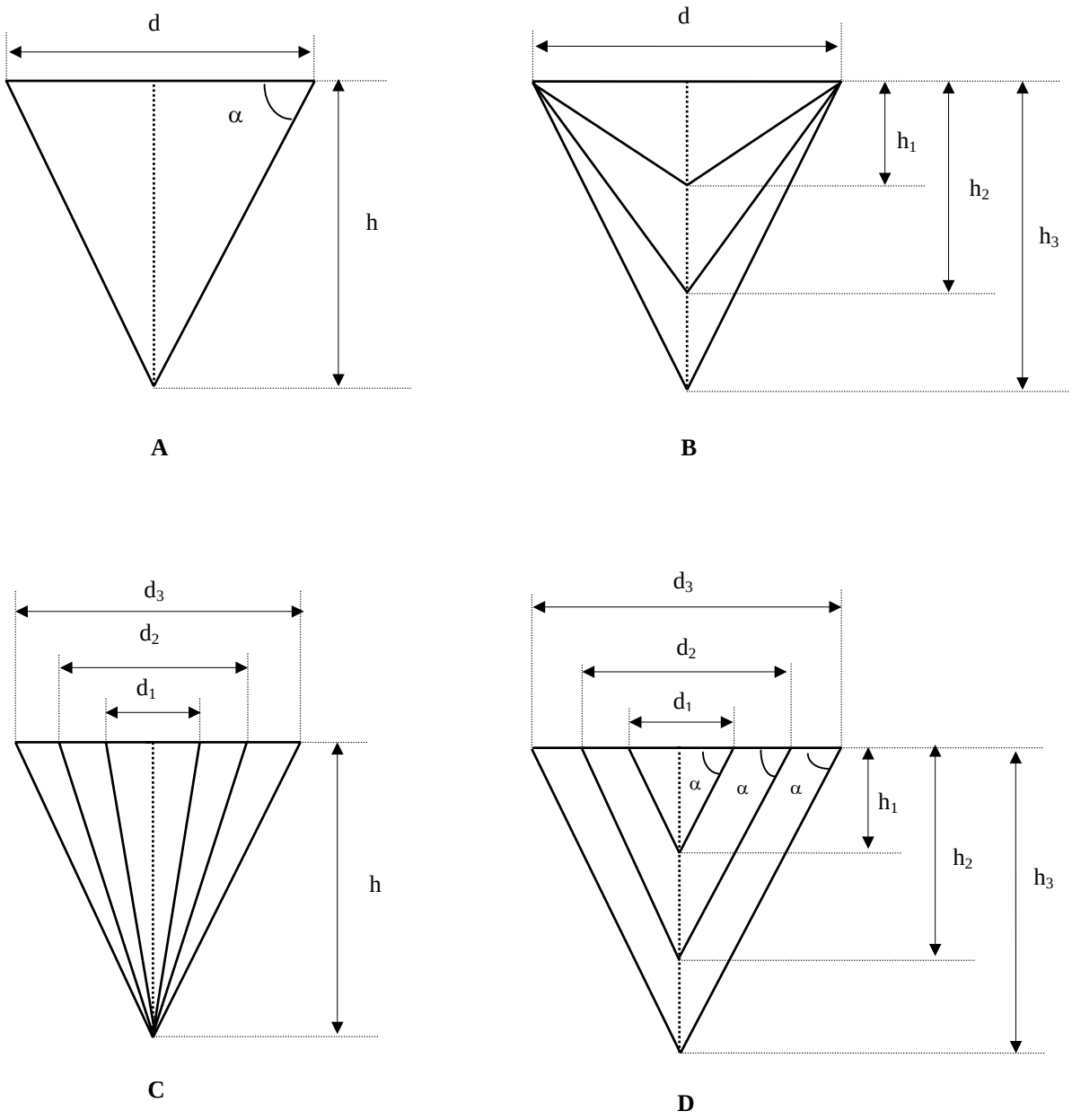

Fig. 4.13 Model configurations with parameterization. A: general case; B: constant diameter with varying height; C: constant height with varying diameter; D: diameter and height varying in a constant ratio.

Depending on how both parameters h and d vary relative to each other, three cases are to be considered, as illustrated in Fig. 4.13:

- a constant diameter with a varying height (Fig. 4.13 B);
- a constant height with a varying diameter (Fig. 4.13 C);
- both diameter and height vary but in a constant ratio, i.e., h/d (the angle α respectively) is constant (Fig. 4.13 D).

The gravity anomaly is a linear function of the density contrast. That is to say, for the same height and diameter, the gravity anomaly will increase or decrease as much as the density contrast does. For this reason, it is better not to consider the function $\Delta g_a = f(\Delta\rho, d, h/d)$ but a new one

$$\Delta g_a/\Delta\rho = f(d, h/d) \tag{4.4}$$

The advantage of doing this is that the value of the new function will remain the same for both the same diameter (d) and height (h) but for different density contrasts. This allows us to use the same diagram for the determination of parameters from gravity anomalies caused by bodies having different density contrasts. Hence the diagram will be of a general use. At this stage the new function is depending only on two parameters d and h. This means that if one of the parameters is known, the other can be determined. Fig. 4.14 shows two types of curves computed for a given density contrast ($0.5\ g/cm^3$) and for a combination of diverse diameters and heights. An analysis of the sets of the curves compiled in Fig. 4.14 lets us draw the following conclusions:

a) for constant heights (dashed curves), the gravity anomaly increases tending to a limit value as the value of h/d becomes smaller and smaller. In fact, it is clear that for very great values of the diameter tending to infinity, the body reduces to a semi-infinite horizontal slab (Bouguer slab), the response of which is expressed as

$$\Delta g_{bs} = 2\pi\gamma\Delta\rho h \approx 0.0419\Delta\rho h \tag{4.5}$$

where, Δg_{bs} is the gravity of the Bouguer slab in milligal, γ is the universal gravity constant, $\Delta\rho$ is the density contrast in g/cm^3, h is the thickness of the Bouguer slab in metres.

Let us consider the function ξ, which is the ratio of the amplitude of the gravity anomaly Δg_a to the gravity of the Bouguer slab Δg_{bs}

$$\xi = \Delta g_a/\Delta g_{bs} \tag{4.6}$$

As a matter of fact, the value of ξ is the same for all possible combinations of diameters and heights having the same value of h/d. The graph of the function ξ versus the height to diameter ratio h/d is shown in Fig. 4.15. Some of the respective values of ξ and h/d are also presented in Table 4.1. In the physico-mathematical sense, ξ can be considered as a transfer function through which the gravity effect of a Bouguer slab of thickness h is convolved in order to get the amplitude gravity of a maar-diatreme of the same height h and of a given diameter d.

b) for constant diameters (solid curves), the gravity anomaly increases continuously as the parameter h/d increases. If the height tends to infinity, the body reduces to a

semi-infinite vertical cylinder the amplitude of the gravity of which can be expressed by the relation of the maximum gravity on the axis of the cylinder:

$$\Delta g_{vc} = 2\pi\gamma\Delta\rho R \approx 0.0419\Delta\rho R \tag{4.7}$$

where, Δg_{vc} is the maximum gravity on the axis of the semi-infinite vertical cylinder in milligal, $\Delta\rho$ is the density contrast in g/cm^3, R is the radius of the semi-infinite vertical cylinder in metres.

Here also the ratio η of the amplitude gravity to the maximum axis gravity of a semi-infinite vertical cylinder is the same for a given value of h/d. It is expressed as

$$\eta = \Delta g_a / \Delta g_{vc} \tag{4.8}$$

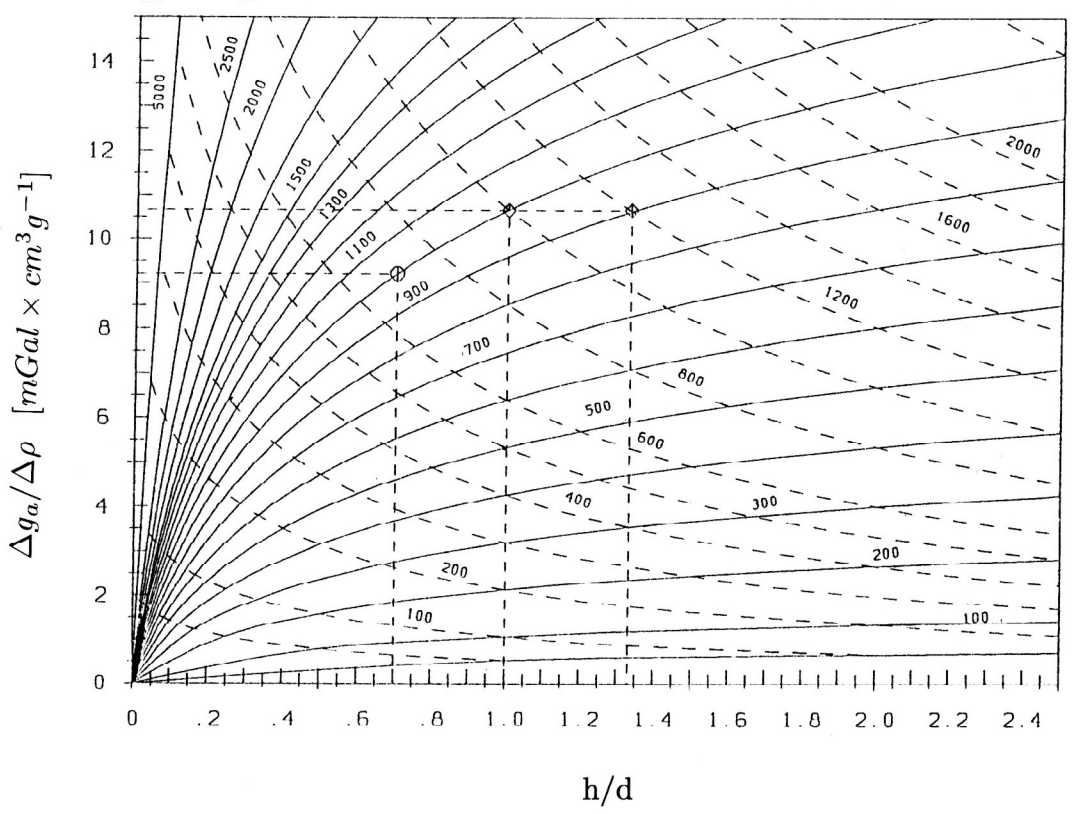

Fig. 4.14 Ratio of the amplitude gravity to the density contrast versus the height to diameter ratio. Solid line: d = const; dashed line: h = const.

Illustration of the determination of h/d and consequently of h for both known diameter and ratio of amplitude gravity to density contrast:

◇ case, where a curve for a given constant diameter exists;

○ case, where there is no curve for the given diameter and the intersection point doesn't lie on an existing straight line in Fig. 4.17; an auxilliary straight line (dashed) in Fig. 4.17 and an auxilliary diameter (1000 m) the curve of which exists in Fig. 4.14 are used to determine h/d and consequently h.

The graph and some values of the function η are presented in Fig. 4.15 and Table 4.1, respectively. As in the above case, the amplitude gravity of a maar-diatreme of a given height h and a diameter d can be obtained by convolution of the axis gravity of a semi-infinite vertical cylinder of the same diameter d through the transfer function η.

Expressed in other words, the functions ξ and η are the gravity amplitude of a maar-diatreme normalized with the gravity of the semi-infinite horizontal slab and the semi-infinite vertical cylinder, respectively.

Assuming that the diameter of the maar-diatreme is known, which in practice is often the case, the function $\Delta g_a/\Delta\rho$ in (4.4) can be normalized with it. This corresponds to the normalization of the amplitude gravity with the product of the density contrast and the diameter $\Delta\rho d$. The relation (4.4) becomes then

$$\Delta g_a/\Delta\rho d = f(d, h/d) \tag{4.9}$$

The graph of (4.9) is displayed in Fig. 4.16 and has the same shape as that of the relation (4.8). Actually (4.8) is the left part of (4.9) factored by $1/\pi\gamma$. Furthermore, the amplitude of gravity can be normalized with the product of the density contrast and the height $\Delta\rho h$. Since the height is normally unknown, the graph of this case is intentionally left out. By a similar approach, Jacoby (1970) has worked out a graphical method for gravity interpretation based on diagrams of the peak gravity effect normalized with dimensions (width, thickness) of bodies of different shape.

c) for a constant h/d (constant angle α), the function $\Delta g_a/\Delta\rho$ is, as expected, linear in diameter (d) and in height (h). This is shown in Fig. 4.17 and Fig. 4.18.

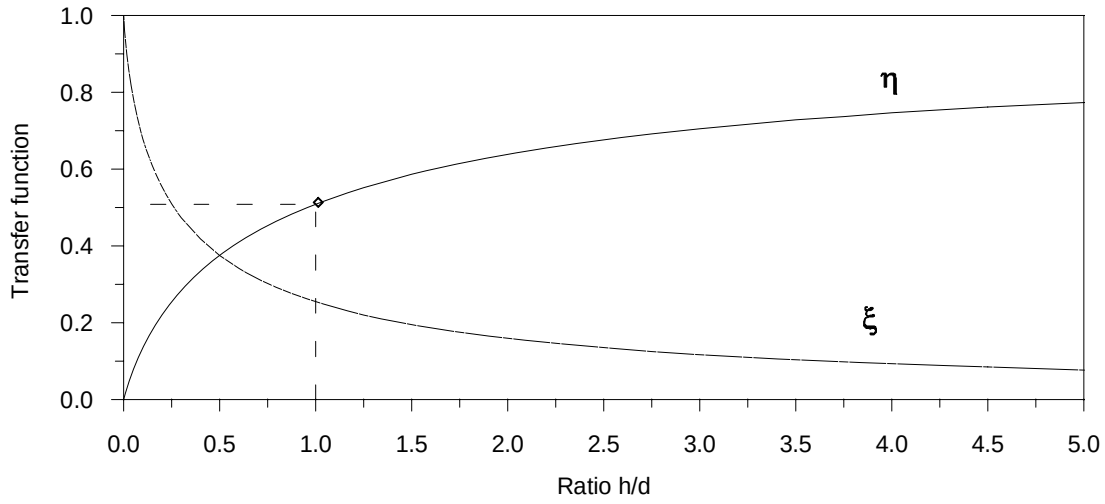

Fig. 4.15 Ratio of the gravity amplitude to the gravity of the infinite horizontal slab (ξ) and to the maximum axis gravity of the semi-infinite vertical cylinder (η) versus the height to diameter ratio (h/d). ◇ illustrates the determination of h/d and consequently of h.

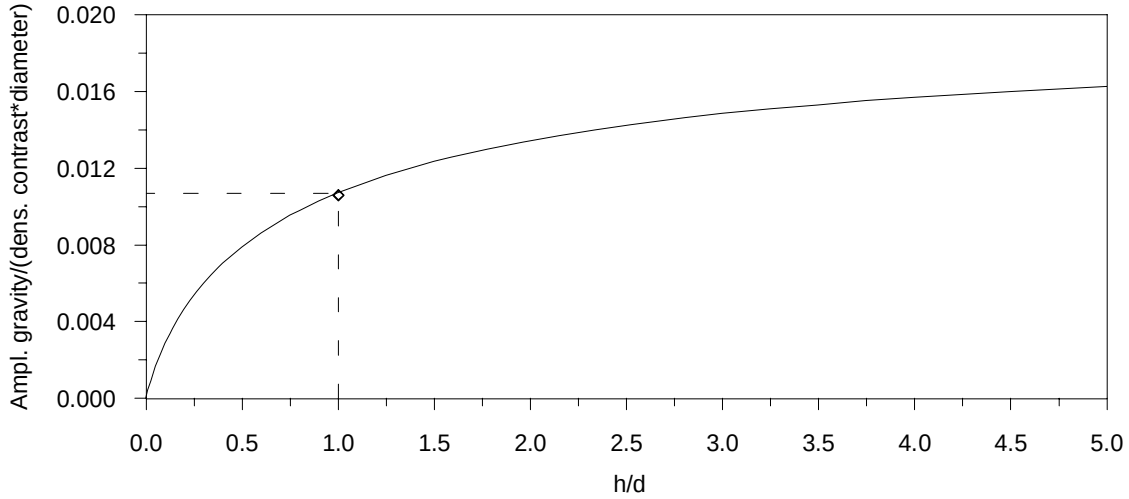

Fig. 4.16 Amplitude gravity normalised with the product of the density contrast and the diameter versus the height to diameter ratio (h/d).

Table 4.1 Values of the ratio of the height to diameter and their corresponding transfer functions.

h/d	ξ	η
0.0000	1.0000	0.0000
0.0100	0.9270	0.0200
0.0250	0.8630	0.0430
0.0500	0.7833	0.0783
0.0750	0.7250	0.1088
0.1000	0.6789	0.1358
0.1250	0.6404	0.1601
0.1500	0.6070	0.1822
0.1750	0.5790	0.2025
0.2000	0.5531	0.2212
0.2500	0.5098	0.2549
0.3000	0.4740	0.2844
0.4000	0.4179	0.3343
0.5000	0.3753	0.3753
0.6000	0.3415	0.4099
0.7500	0.3020	0.4530
0.8000	0.2910	0.4655
0.9000	0.2714	0.4885
1.0000	0.2545	0.5090
1.2500	0.2208	0.5520
1.5000	0.1955	0.5864
1.7500	0.1756	0.6148
2.0000	0.1596	0.6386
2.2500	0.1464	0.6590
2.5000	0.1353	0.6766
2.7500	0.1258	0.6920
3.0000	0.1176	0.7056
3.2500	0.1104	0.7176
3.5000	0.1040	0.7282
3.7500	0.0984	0.7378
4.0000	0.0933	0.7464
4.5000	0.0846	0.7613
5.0000	0.0774	0.7739
5.5000	0.0710	0.7849
6.0000	0.0662	0.7949
8.0000	0.0520	0.8320
10.000	0.0440	0.8731
12.000	0.0380	0.9223
14.000	0.0350	0.9791

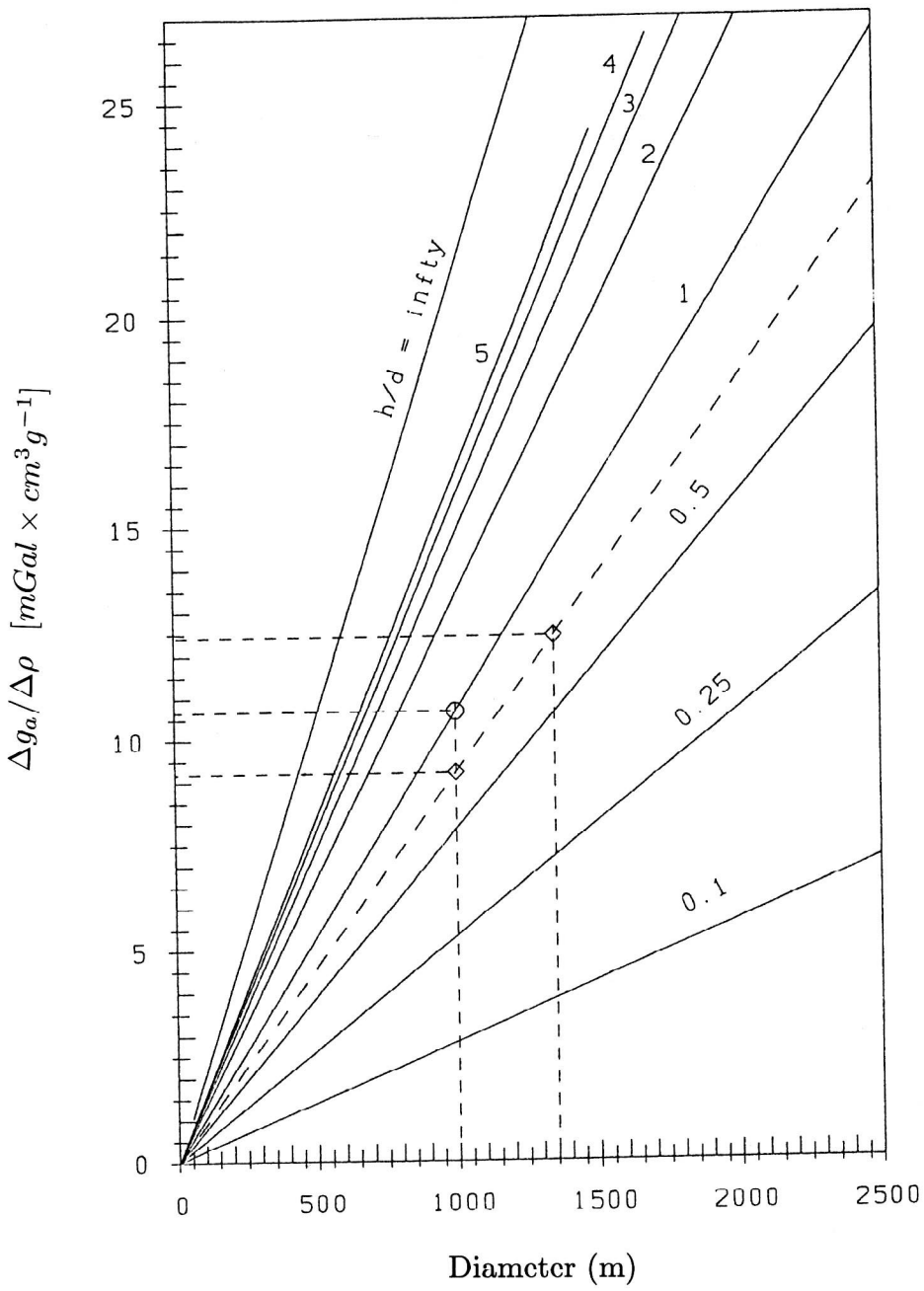

Fig. 4.17 Ratio of the amplitude gravity to the density contrast versus the diameter for a constant h/d.

Illustration of the determination of h/d and consequently h for both known diameter and ratio of amplitude gravity to density contrast:
o case, where the intersection point lies on an existing h/d straight line;
◇ case, where the intersection point doesn't lie on a h/d straight line: use of auxiliary h/d straight line, diameter and then Fig. 4.14.

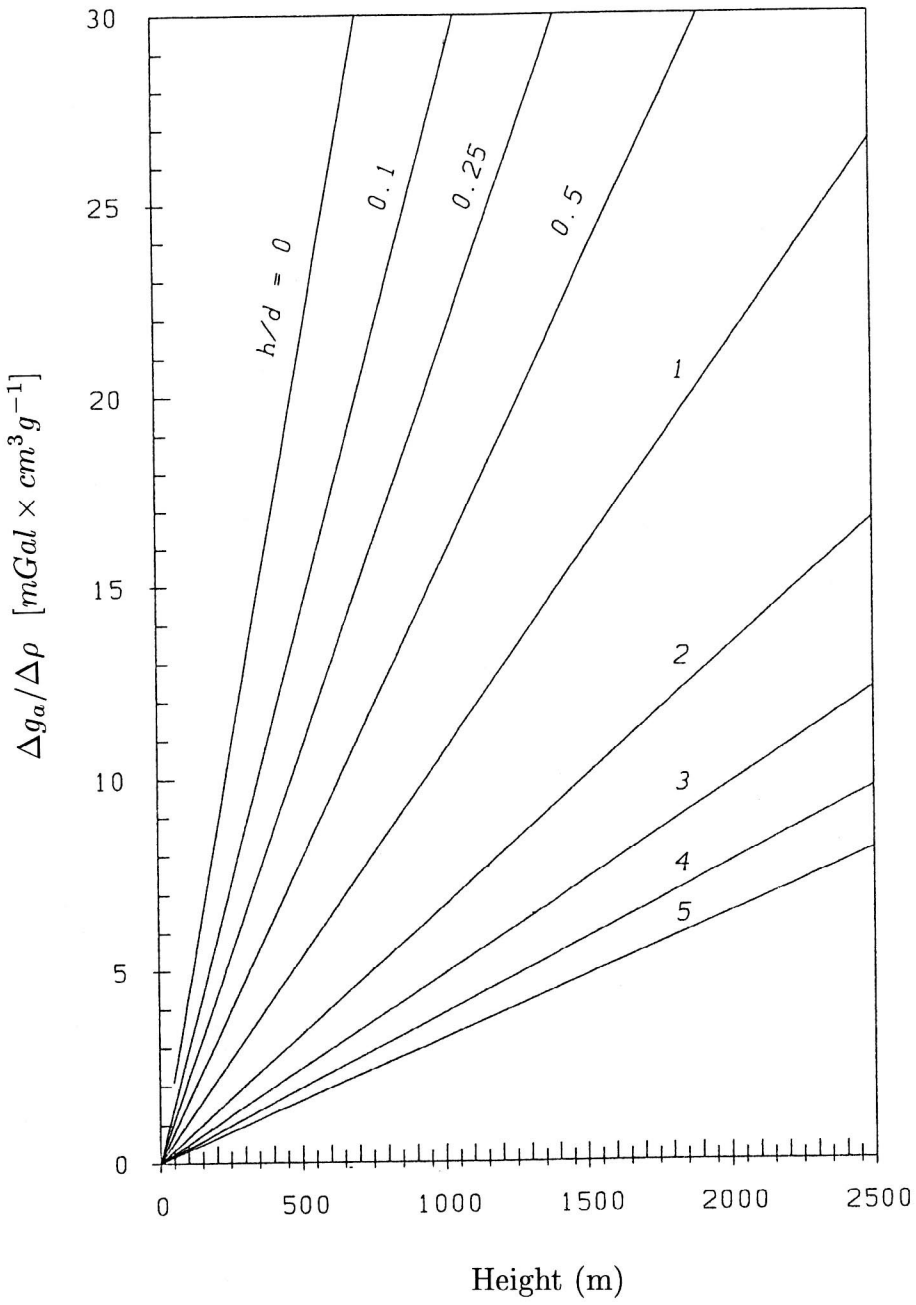

Fig. 4.18 Ratio of the amplitude gravity to the density contrast versus the height for a constant h/d.

For a clearer view, the graphs of the function Δg_a for the three cases discussed above have been presented together in Fig. 4.19 for only one diameter ($d = 500$ m), one height ($h = 500$ m) and consequently one height to diameter ratio ($h/d = 1$). As can be seen in Fig. 4.19, for both cases — constant diameter and constant height — the function Δg_a has a steep gradient for values of h/d, respectively of d/h, smaller than one; the slope becomes gentle with increasing values of h/d or d/h. However, as well seen on Fig. 4.19, there is a critical point, namely the intersection point of the three graphs, where the height to diameter ratio h/d equals 1. For values of h/d, d/h and d/do less than 1, the amplitude gravity is at highest for a constant diameter and at lowest for a constant height to diameter ratio h/d = 1. For values greater than 1, the situation is reverse. From this situation we can draw the following:

- For values of h/d or d/h less than 1, small changes either in the horizontal or in the vertical dimension of the maar-diatreme structure will cause strong changes in the amplitude of the gravity response.
- For values greater than 1, changes in the amplitude gravity due to the one or the other parameter are weak, even negligible for a constant diameter as the height increases. In fact, one sees on Fig. 4.19 that the function Δg_a rapidly tends to the asymptotic value of the maximum axis gravity of a semi-infinite vertical cylinder. Physically, this means that after a certain level the deepest masses of the body do not have anymore effect on the amplitude gravity of the maar-diatreme structure and can not be resolved by inversion.
- The effect of the diameter on the gravity amplitude is stronger than that of the height. Thus, an accurate determination of the surface diameter is very relevant for the inverse modeling of maar-diatremes.

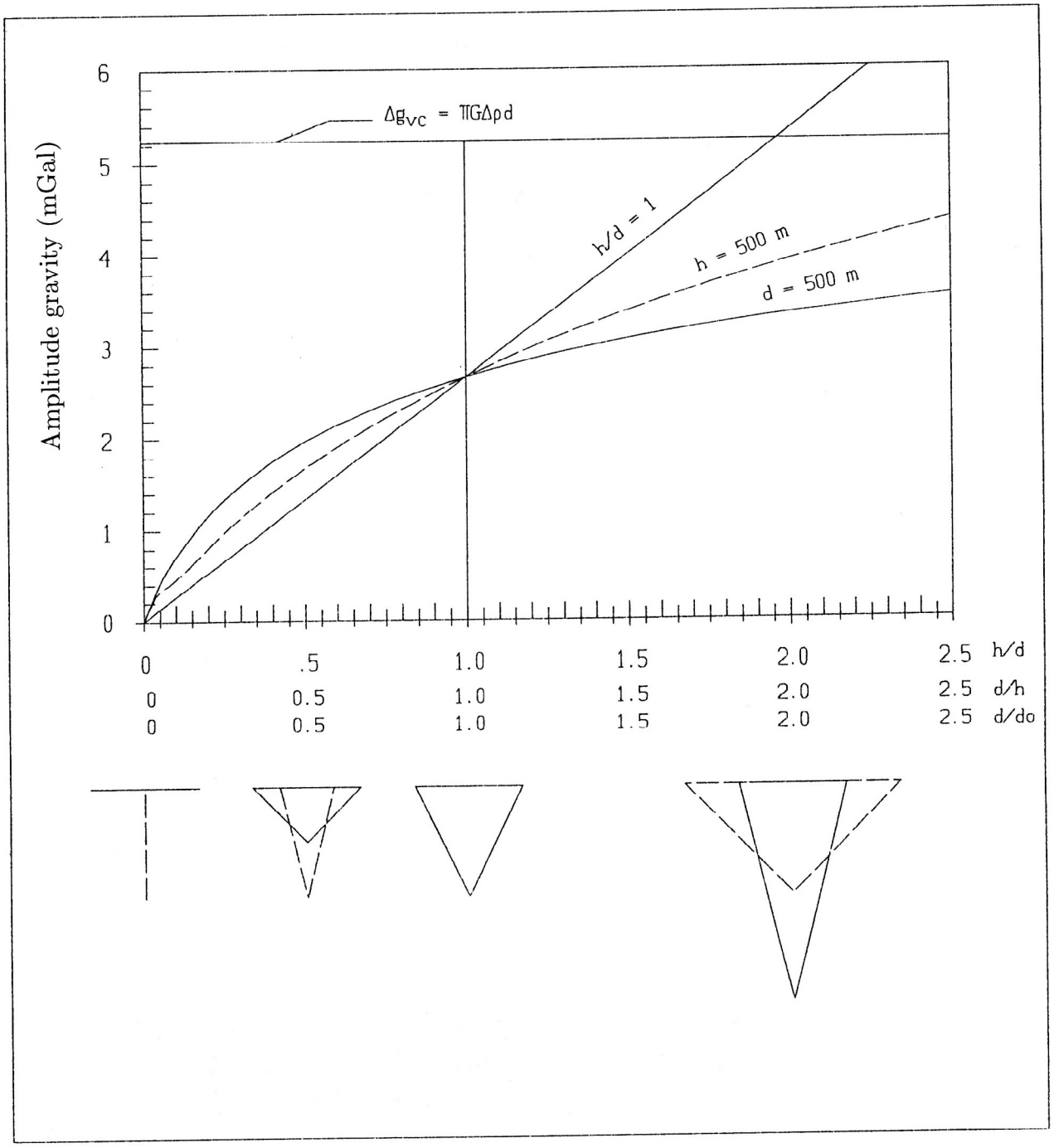

Fig. 4.19 Amplitude gravity versus: a) the height to diameter ratio, d = const = 500 m; b) the diameter to height ratio, h = const = 500 m; c) the normalized diameter, h/d = const = 1; $d_o = 500$ m.

4.2.3 Parameter determination

4.2.3.1 Feasibility of parameter determination

Let us examine the possibility of parameter determination using the diagrams shown in Fig. 4.14, 4.15 and 4.16. The attempt to extract one unknown parameter with the help of the presented diagrams supposes the knowledge of the two others in advance. Knowing the type of country rocks and that of the rocks filling the maar-diatreme, an approximate value of the density contrast can be evaluated. Laboratory measurements of the density can give more reliable values of the latter. Having the value of the density contrast, the value of the function $\Delta g_a/\Delta\rho$ can be calculated since the amplitude Δg_a of the gravity anomaly is known from the field data. Usually, the value of the diameter can easily be approximated from geomorphological, geological and/or geophysical field measurements and observations. Knowing both the values of the function $\Delta g_a/\Delta\rho$ and that of the diameter d, it becomes then possible to determine graphically the value of the parameter h/d, which in its turn allows to determine the height h.

4.2.3.2 Procedure of parameter determination

Let us first consider the use of diagrams in Fig. 4.14 and Fig. 4.17. For a known or assumed diameter the use of the plot in Fig. 4.17 is straightforward. The value of the diameter read on the horizontal axis is extrapolated vertically. Similarly the value of the calculated ratio $\Delta g_a/\Delta\rho$ located on the vertical axis is extrapolated horizontally. The intersection point defines the value of h/d from which the height is calculated. This is illustrated in Fig. 4.17 for a diameter value of 1000 m and $\Delta g_a/\Delta\rho$ equal to 10.64. In this case, the ratio h/d is one; which gives a height of 1000 m. This can be achieved by using Fig. 4.14 as well; especially if the intersection point does not lie on one of the existing lines of constant h/d in Fig. 4.17 but a curve of the given constant diameter is available in Fig. 4.14. The value of $\Delta g_a/\Delta\rho$ is extrapolated horizontally to intersect the curve of the given constant diameter. From this point on the curve, another extrapolation is made vertically over to the horizontal axis, on which the value of h/d is read. This is demonstrated in Fig. 4.14 for both cases: a value of $\Delta g_a/\Delta\rho$ of 10.64 for diameters of 1000 m ($h/d = 1$, h=1000 m) and 900 m ($h/d = 1.33$, h=1200 m). If the intersection point in Fig. 4.17 ($\Delta g_a/\Delta\rho = 12.4$ and d = 1350 m) does not lie on an existing line of constant h/d and there is no curve for the given diameter in Fig. 4.14, an auxilliary straight line must be drawn through that point and the origin (dashed line in Fig. 4.17). A diameter for which a curve exists in the diagram of Fig. 4.14 is then selected (in our case d = 1000 m). The vertical extrapolation of the value of the selected diameter intersects the auxilliary line at a point, whose projection onto the ordinate gives a new value of $\Delta g_a/\Delta\rho$ (in our example this value is 9.2). This new value of $\Delta g_a/\Delta\rho$ together with the selected diameter will allow us to get the value of h/d by using Fig. 4.14 as described above. In our example, as shown in Fig. 4.14, this value is 0.7. Having h/d, we use our initial diameter (1350 m) to calculate the height, which is 945 m.

For the parameter determination, the diagrams in Fig. 4.15 and Fig. 4.16 may also be used. For the use of the diagram in Fig. 4.15, the maximum gravity Δg_{vc} on the axis of a semi-infinite vertical cylinder is calculated by the formula (4.6). As demonstrated in Fig. 4.15, the ratio of the observed amplitude gravity Δg_a to the maximum gravity Δg_{vc}

of the semi-infinite vertical cylinder defines the value of the transfer function η, which enables us to find the value of h/d through a consecutive projection, first to the curve and then to the abscissa. Having calculated the ratio of the amplitude gravity Δg_a (in mGal) to the product $\Delta\rho d$ of the density contrast (in g/cm^3) and the diameter (in m), the diagram in Fig. 4.16 can be used as well. Proceeding the same way as in the previous case, the value of h/d is found. The use of the curve of ξ in Fig. 4.15 is less direct than in the two preceeding cases. It is a trial to match the observed amplitude gravity Δg_a with the convolved gravity effect of a Bouguer slab corresponding to an assumed height. To each assumed value of the height corresponds a value of h/d. The projection of h/d to the curve gives the intersection point, which is on its turn projected to the ordinates to give the value of the transfer function ξ. This value is then multiplied by the gravity effect of the Bouguer slab Δg_{bs}. If the result matches the observed amplitude gravity, the assumed height is kept as the correct one. If not, the procedure is repeated till a good fit is achieved. Instead of using the diagrams of Fig. 4.15, values of the parameter h/d and those of their corresponding transfer functions ξ and η can be taken or interpolated from Table 4.1.

However, it is important to point out that this study has been conducted for a causative body represented by an idealized model with a regular shape and a homogeneous density. But actually, the shape of the true body might deviate from that of the idealized one. Moreover, other small bodies such like dykes intruded through the pipe, dykes cutting the body at its root, magmatic sills, xenoliths etc. might be within the main body. Taking into account that all these considerations have been dropped for the theoretical computations, it is clear that the results based on the present analysis are approximate. Nevertheless these results might certainly be helpful in solving inverse problems since they provide with an idea about the influence of the major parameters on the gravity effect. As example, while modeling maar-diatreme structures, it is possible to keep one or more parameters — assumed as knowns — constant in order to avoid parameter redundance, a fact which leads to stability of the solution. Beside that, parameters determined by this simple method might be used as initial model for an iterative nonlinear inversion.

5. Application of theoretical modeling to observed data

The results of theoretical modeling have been applied to some of the Eifel maars for which gravity/magnetic observations are available. For this purpose, the Döttingen and the Jungferweiher Maars of Tertiary age and six other maars of the Quaternary volcanic field, namely the Schönfeld Maar, the Dehner Maar, the Roth Maar, the Pelm Maar, the Meerfeld Maar (West Eifel) and the Hausten-Morswiesen Maar (East Eifel) have been selected. The aim was to approximate some parameters (heights, dip angles) and to get an idea about the building and the physics of the maar-diatreme structures. The results could help to find out whether there exists a certain systematics between the diameter and the depth and/or between the geophysical anomaly and the dimensions of the maar-diatremes.

As mentioned in Chapter 4, the determination of one of the main parameters ($d, h, \Delta\rho$) responsible for the gravity anomaly of a maar-diatreme, taken as whole, requires the knowledge of the two others. The known parameters are, in this case, the diameter (d) and the density contrast ($\Delta\rho$). The values of the present day diameters of the maar-diatremes have been approximated from geological and geophysical observations (magnetics and gravity). The density contrasts were evaluated using known densities of the tuffs and of the Devonian country rocks, determined by laboratory measurements (cfr Chap. 2). It has then been possible to estimate the diameter to height ratio (d/h), the heights (h) of the maar structures and the dip angles (α) of their walls.

5.1 The Döttingen Maar

Stachel and Büchel (1989) have conducted a detailed geological and geophysical study of the Döttingen Maar. They proved that the Döttingen Maar should be of Tertiary age. They estimated the density of the Tertiary maar tuffs to be slightly higher than that of the Quaternary maar tuffs and to have a mean value of 2.2 g/cm^3. The gravity anomaly of the Döttingen Maar (Fig. 5.1a) has a size of about (-3.6 ± 0.2) mGal. The diameter, estimated from magnetic and gravity anomalies, is about 1100 m. Taking into account that the Döttingen Maar might have a layer of crater lake sediments in its upper central part, this could have a decreasing effect on the effective density of the maar-diatreme structure. But this effect could be compensated by a probable increase of the density of the tuffs with depth. From this consideration, I assume an effective density of 2.2 g/cm^3 — a density contrast of -0.3 g/cm^3, respectively — to be suitable for the parameter determination. Using the one or the other diagram in Fig. 4.14, 4.16, 4.17, we get an approximate value of 1.05 for the height to diameter ratio h/d, which gives a height h of 1150 m and a dip angle α of $\approx 65°$. Since the anomaly has an error of ± 0.2 mGal, the estimated height h varies in the range from 950 m till 1350 m. The dip angle α of the maar-diatreme walls varies between 60° and 68°, respectively. While modeling the Döttingen Maar, Stachel and Büchel (1989) achieved a best fit between the observed and the computed data using a model body which had a height of 1600 m. This higher value of the height can be explained by the fact that Stachel and Büchel assumed the tuffs to have a higher density of 2.3 g/cm^3 starting from the 500 m depth downwards. For a constant diameter, it is clear that the decreasing effect of the smaller density contrast should be compensated by a greater height in order to produce the same anomaly.

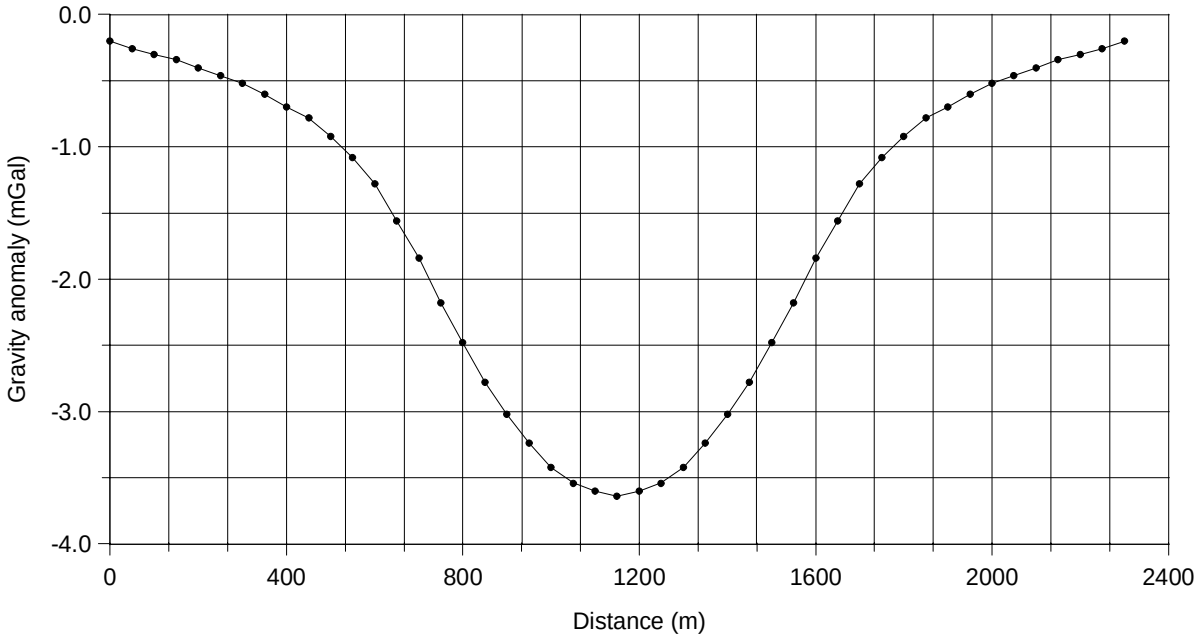

Fig. 5.1a S-N Gravity profile of the Döttingen Maar (after Stachel and Büchel, 1989) .

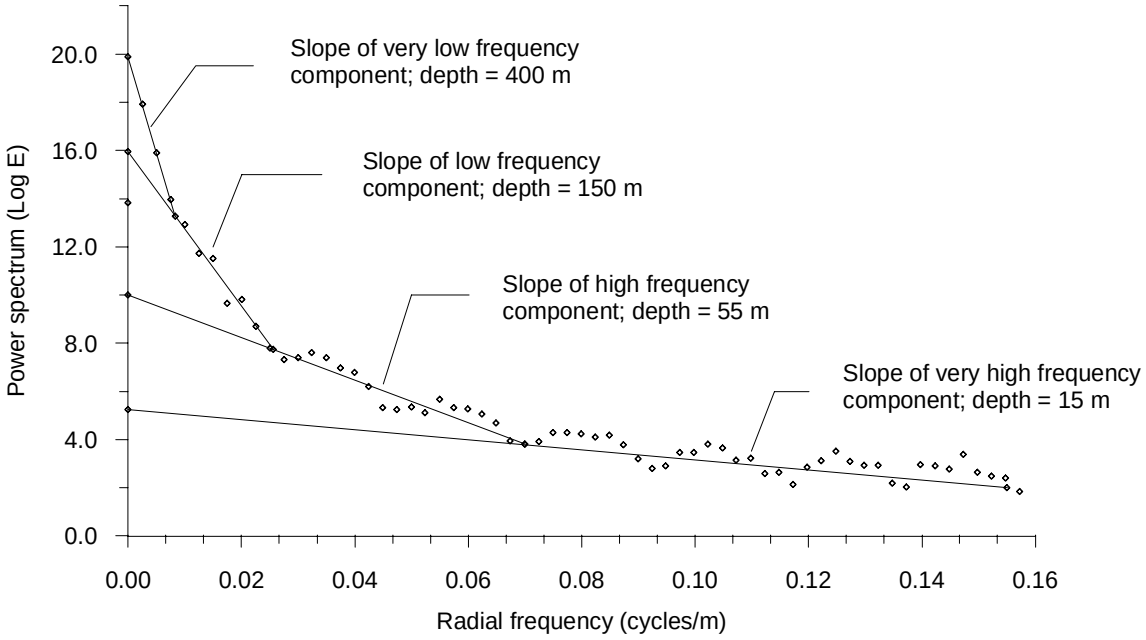

Fig. 5.1b Logarithmic power spectrum of the gravity anomaly of the Döttingen Maar.

The magnitude of the magnetic anomaly (400 nT) is in good agreement with the dimensions of the structure and the susceptibility of the tuffs.

In fact, a spectral analysis — will be discussed on later — of the gravity anomaly (Fig. 5.1b) shows that the Döttingen Maar is filled up by rocks the density properties of which change with depth. The power spectrum has two main components: the low and the high frequency components which are each differentiated on their turn. The high frequency components obviously correspond to crater sediments with a total thickness of about 150 m. The low frequency components correspond to maar-diatreme tuffs the density of which changes at 400 m depth. The change can be interpreted as an increase of the density of the tuffs due to compaction. As already mentioned above, the increase of the density will cause a decrease of the density contrast with respect to the Devonian country rocks, which in turn, will require an increase of the height of the maar-diatreme to produce the same gravity effect. From this point of view, the Döttingen Maar should have a height of at least 1500 m. These results confirm those of Stachel and Büchel (1989).

5.2 The Jungferweiher Maar

The diameter of the Jungferweiher Maar approximated from the magnetic profile (Fig. 5.2a) measured by Büchel (1984) is about 1500 m. Gravity measurements made by Lepold (1987) revealed a gravity anomaly of about -5.5 mGal. Using a density contrast of -0.5 g/cm^3, we get estimates of 800 m and 47° for the height and the dip angle of the walls of the maar-diatreme, respectively. The magnetic anomaly amounts to about 340 nT. The smoothness of the magnetic profile indicates that the source lies at a relatively great depth. This theoretically means that crater sediments of at least 250 m thickness overlay the diatreme tuffs.

In order to investigate the geometry of the structure, three theoretical magnetic models have been computed. For all models, it has been assumed that the crater height and the susceptibility of the crater filling have respective values of 250 m and 6300×10^{-6} SI. The geometrical parameters of the two first models were based on the estimates given above, i.e. taking the maar-diatreme as a whole. Assuming that the diatreme tuffs had a susceptibility of 12600×10^{-6} SI — mean susceptibility of the tuffs of the West Eifel Maars — and that the magnetization was only induced, the size of the magnetic anomaly (120 nT, Fig. 5.2a, curve with black stars) would be almost three times smaller than the observed one. Even a susceptibility of 38000×10^{-6} SI — value, which is too high for common tuffs — lets the size of the anomaly arise up to only 275 nT (Fig. 5.2a, curve with rhombuses). Since the susceptibility can not be anymore increased, it seems that the height of the Jungferweiher Maar is greater than the estimated one of 800 m, which implies a greater height of the diatreme.

As shown on Fig. 5.2a (curve with crosses), a more or less good fit between the computed and the observed data has been achieved for the model presented in Fig. 5.2b. The susceptibility value (32000×10^{-6} SI) is still higher than the mean susceptibility of the tuffs of the West Eifel Maars. This could be explained either by the increase of the susceptibility of deeper lying tuffs with more mafic content or by the contribution of a remanent magnetization, the intensity of which is approximately equal to that of the induced one (≈ 1.25 A/m). Actually, laboratory measurements showed that most of the West Eifel Maars exhibit a NRM ranging from 1 to 2 A/m. The misfit of the curves in the

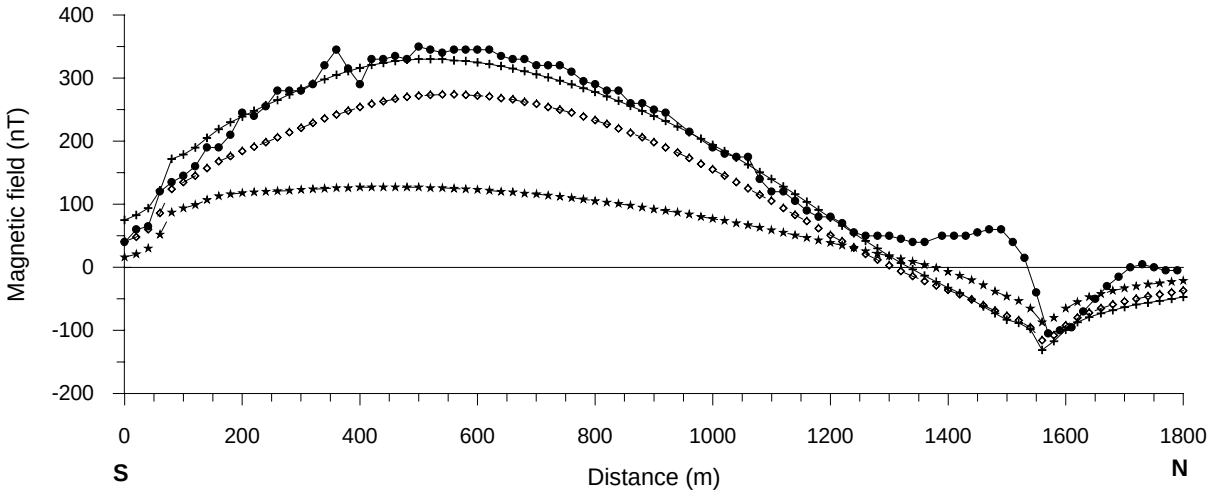

Fig. 5.2a Magnetic profiles of the Jungferweiher Maar.

observed — computed : χc = 0.0063 SI; χd = 0.032 SI; Hc = 250 m; Hd = 1250 m.

computed : χc = 0.0063 SI; χd = 0.038 SI; Hc = 250 m; Hd = 550 m.

computed : χc = 0.0063 SI; χd = 0.0126 SI; Hc = 250 m; Hd = 550 m.

Elements of the geomagnetic field : D = -2°; I = 66°; F_o = 48000 nT.

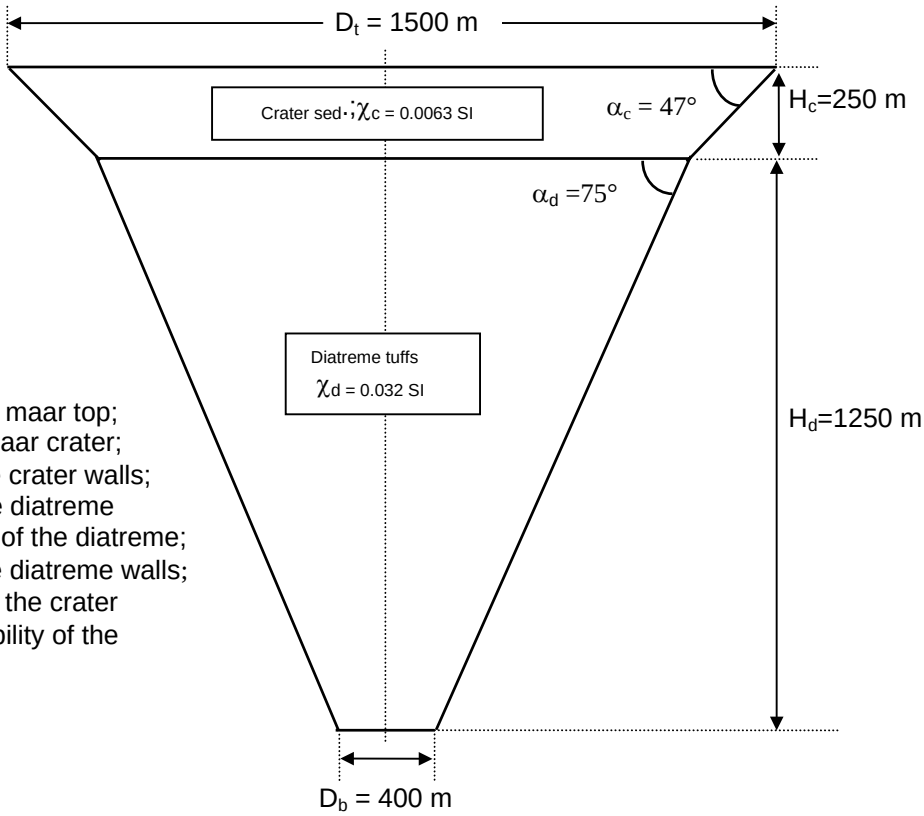

D_t = diameter of the maar top;
H_c = height of the maar crater;
α_c = dip angle of the crater walls;
D_b = diameter of the diatreme bottom; H_d = height of the diatreme;
α_d = dip angle of the diatreme walls;
χ_c = susceptibility of the crater filling; χ_d = susceptibility of the diatreme tuffs.

Fig. 5.2b Model of the Jungferweiher Maar.

centre, at the southern and northern boundaries of the maar is due to factors, which have not been considered in the theoretical model assumed isometrical. I assume that some tuffs eroded from the slopes accumulated in the central area of the crater and mixed up with sediments and country rocks, hence leading to an increase of the susceptibility of the crater filling. The misfit at the southern and northern boundaries is probably connected with the topography of the maar. Whereas the tuff slope in the south with low topography is covered by sediments, it is outcroping in the north with high topography.

As can be seen on Fig. 5.2b, the total height of the maar-diatreme amounts to 1500 m, the dip angles of the crater and the diatreme walls have values of 47° and 75°, respectively. Obviously, the Jungferweiher Maar is a classical maar type similar to the empirical model of a kimberlite pipe given by Hawthorne (1975).

5.3 The Meerfeld Maar

A gravity profile of the Meerfeld Maar is shown on Fig. 5.3a (Henk, 1984). The size of the anomaly is about −6.0 mGal. A later gravity survey, which was areally carried out in the framework of the geophysical field course of the Mainz University (1990, 1992) outlined a Bouguer anomaly (Fig. 5.3b) of about −4.5 mGal (Smilde, 1997). The diameter of the Meerfeld Maar, derived from the magnetic anomaly, is about 1100 m (Büchel and Stachel, 1989). After Büchel and Stachel (1989), a 150 m thick layer of crater lake sediments is supposed to overlay the diatreme tuffs. The crater and diatreme rocks are supposed to have a mean density of 2.0 g/cm^3 (Büchel, 1984), which can be taken as the effective density of the whole structure; hence a density contrast of −0.5 g/cm^3 with respect to the Devonian country rocks ($\rho = 2.5\ g/cm^3$). For the size of the Bouguer anomaly of −6.0 mGal, we get estimated values of 1100 m and 63° for the height (h) and the dip angle (α), respectively. For the anomaly size of −4.5 mGal, the respective estimates of h and α logically are smaller and amount to 600 m and 48°.

By inversion of the 1990 and 1992 gravity dataset, Smilde (1997) estimated the height of the Meerfeld Maar structure to 1000 m. Smilde used a larger density contrast (−0.62 g/cm^3) and a model body which more rapidly narrowed out as the depth increased. Considering that the model body used by Smilde probably better represents the natural shape of a maar-diatreme — contrary to the ideally assumed cone shaped one — a height greater than 600 m would be required to produce the anomaly of −4.5 mGal if the density contrast was −0.5 g/cm^3. Hence, a height estimate around 1000-1100 m seems to be plausible.

As outlined by investigations conducted by Büchel (1979, 1981) in addition to those previously carried out by Hunsche (1973), the magnetic anomaly of the Meerfeld Maar with a maximum of about 150 nT is relatively weak, probably due to the effect of the crater lake.

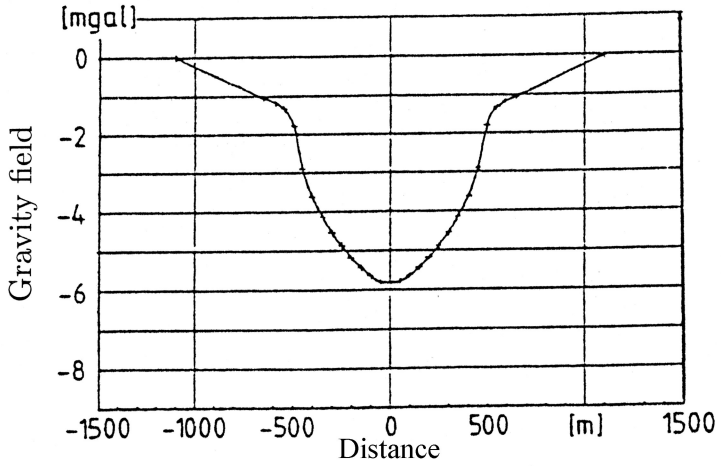

Fig. 5.3a Gravity profile of the Meerfeld Maar (after Schenk, 1984).

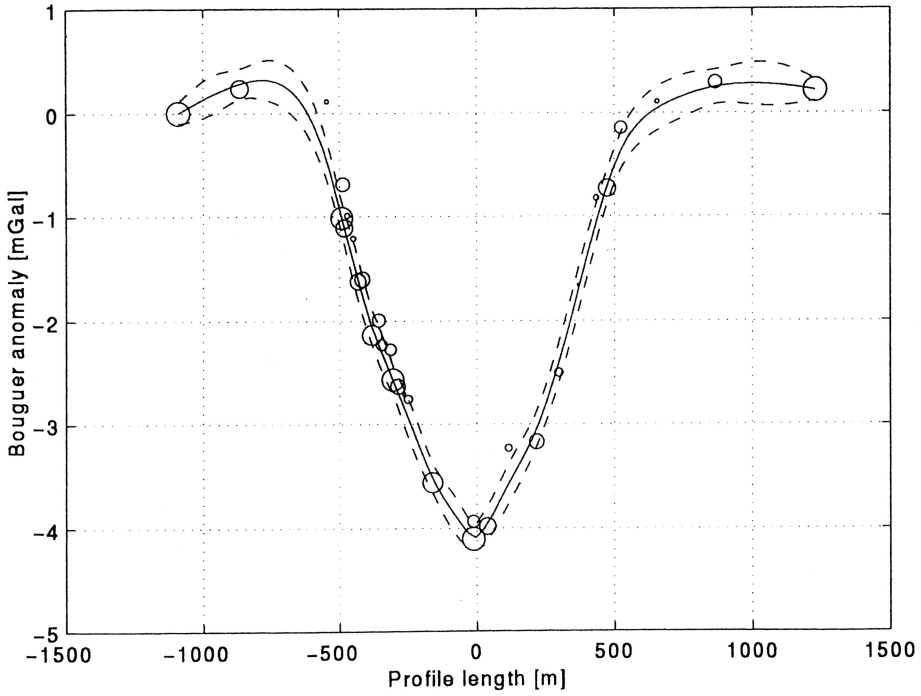

Fig. 5.3b Profile (SWW-NEE) of the Bouguer anomaly, observed over the Meerfeld Maar (after Smilde, 1997).

5.4 The Pelm Maar

A profile of the Bouguer anomaly of the Pelm Maar is shown on Fig. 5.4; the gravity minimum and the mean surface diameter of the maar are about -2.7 mGal and 800 m, respectively (Hörrle, 1991). Using the density of the palagonite tuffs (2.35 g/cm^3) sampled in the vicinity of the Pelm Maar, we get a density contrast of -0.15 g/cm^3 and a corresponding ratio $\Delta g_a/\Delta\rho$ of 18, a value which lies above the $h/d = \infty$ limit line in Fig. 4.18. This means that the density contrast is too small for the given values of the gravity anomaly and the diameter. Assuming a density value of 2.2 g/cm^3, that gives a contrast of -0.3 g/cm^3, we get a height of 900 m and a dip angle of 66°. However, the shape of the gravity anomaly suggests that the Pelm Maar is of a small vertical extent. This implies that a higher density contrast contributes to the gravity anomaly. If the mean density of the Quaternary West Eifel tuffs (2.0 g/cm^3) is used, the estimated height h and dip angle α are 330 m and 40°, respectively. These values seem to be more reliable. In fact, if we compare the observed anomaly (shape and size) of the Pelm Maar with the theoretical field (Fig. 5.4), computed for a body with a top diameter and a height of 800 m and 350 m, respectively, there is a relatively good agreement between both. The small discrepancies between the observed and the computed curves are probably due to the fact that the theoretical curve has been computed using an ideally cone shaped body with a constantly decreasing radius whereas the actual structure of the Pelm Maar might have the shape of a truncated cone with an irregularly decreasing radius. Moreover, the estimated dip angle lies in the range of the slope of the maar walls ($40 - 50°$), established by geological observations conducted by Hörrle. Hörrle (1991) tried to work out a model for the Pelm Maar using circular disks with an irregularly decreasing diameter downwards. Using a density contrast of -0.5 g/cm^3, she achieved a best fit between the observed and the computed data by modeling a structure the top diameter, the bottom diameter and the height of which were 900 m, 50 m and 230 m, respectively. Hörrle's model has a height smaller than the one estimated here because of larger disc diameters in the upper part.

From the above discussion, it can be drawn that the Pelm Maar should be of a small vertical extent, with a height not greater than 300 m and that the palagonite tuffs found in its vicinity belong to another volcanic eruption. From the genetic point of view, this means that the Pelm Maar formed during a short phreatomagmatic process/volcanic eruption. In case where the Pelm Maar was filled by palagonite tuffs or even by less dense tuffs with a density of more than 2.0 g/cm^3, the latter should be overlain by crater sediments of lower density. This would contribute to a low effective density of the maar-diatreme filling, hence to a high density contrast able to produce such a gravity anomaly for a small height.

5.5 The Roth Maar

A S-N gravity profile of the Roth Maar is presented on Fig. 5.5a. If the part of the curve in the North — where gravity increases probably due to another nearby geologic feature with higher density — is not considered, the size of the anomaly can be estimated to at most -2.0 mGal. The tuffs of the Roth Maar have a mean density of 1.8 g/cm^3. This gives a density contrast of -0.7 g/cm^3 with respect to the country rocks. For this density contrast and a surface diameter of ≈ 800 m, estimated from the magnetic anomaly (Fig. 5.5b), we get an estimated height of 105 m, which corresponds to a dip angle of 15°.

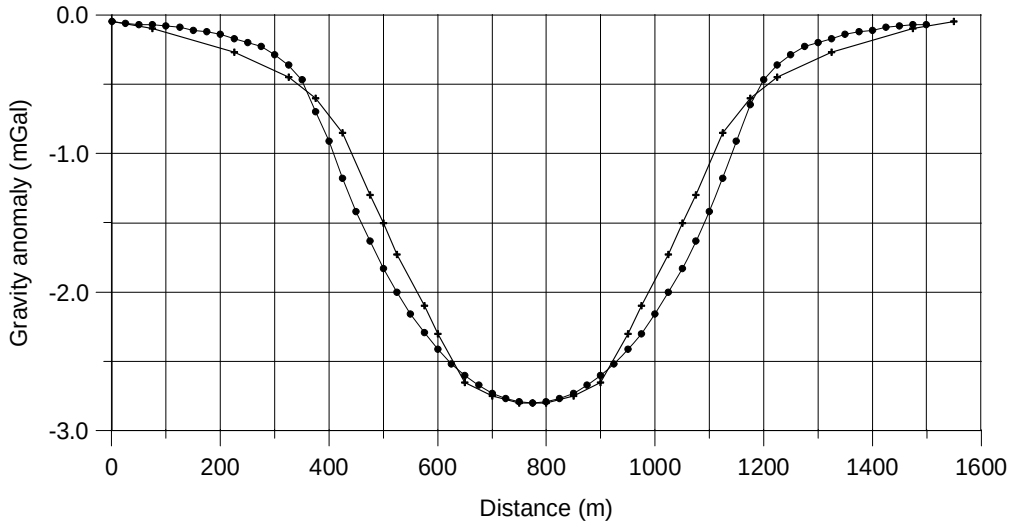

Fig. 5.4 Gravity profiles of the Pelm Maar.

observed (Hörrle, 1991) theoretical

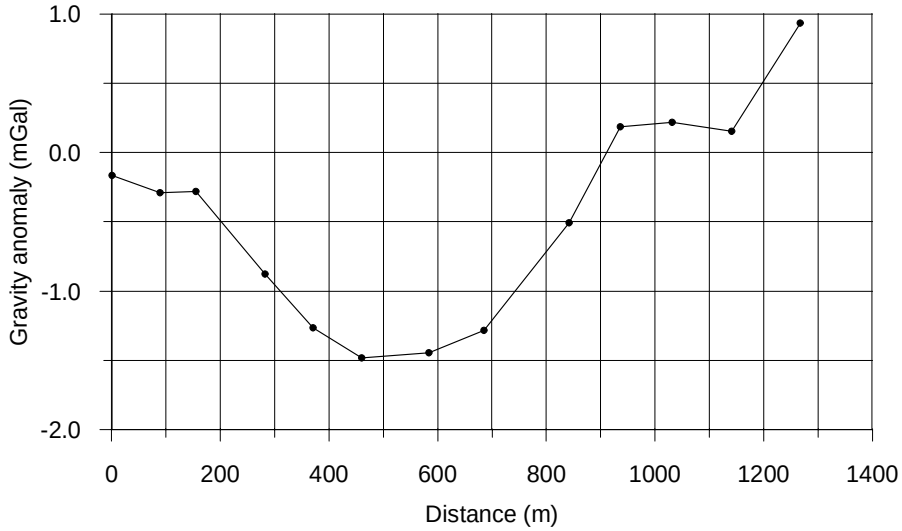

Fig. 5.5a S-N Gravity profile of the the Roth Maar.

Even using the mean density (2.0 g/cm^3) of the tuffs of the Eifel maars, we still get small estimates of the height of the structure and the dip angle of its walls: 175 m and 25°. The small size and the shape of the gravity anomaly would let think about the Roth maar-diatreme to be of a very small vertical extent. If this were true, how can then be explained the relatively high magnetic anomaly with a maximum of ≈ 800 nT?

Let us assume that the Roth maar-diatreme is filled up by rocks having a susceptibility of 8000×10^{-6} SI — susceptibility of the tuffs sampled at the southern boundary of the maar — and that the magnetization is only induced. Using the elements of the IGRF for the Roth Maar area ($F_o = 47750\ nT$, $I = 66°$, $D = -2.5°$), the computed magnetic anomaly caused by a diatreme (h = 105 m, d = 800 m) will have a maximum of 30 nT. Even if the contribution of the measured NRM (600 mA) was taken into account, the effect would still be much less than the observed anomaly. An increase of the susceptibility by ten times (80000×10^{-6} SI) will yield an anomaly maximum of 600 nT, which is still lower than the observed one. In order to explain the high magnetic anomaly of the Roth Maar, theoretical anomalies have been computed using different sets of parameters: the susceptibility, the height of the maar-diatreme and the depth to the top of the structure. The diameter of the maar-diatreme (800 m) has been kept constant. First, it has been assumed that the maar-diatreme has a greater height and is filled up by rocks with a susceptibility of 30000×10^{-6} SI, which is higher than the one determined by laboratory measurements. The height has been chosen to be ≈ 1000 m in order to nearly meet the assumed 1:1 diameter to height ratio. For a maar-diatreme located at 20 m depth, the anomaly maximum amounts to 500 nT. An increased susceptibility of 50000×10^{-6} SI raises the anomaly maximum to 1000 nT. Keeping the last value of the susceptibility and increasing the depth to top up to 50 m, the size of the anomaly maximum decreases and amounts to 800 nT, which nearly matches the observed one. This lets conclude that the Roth Maar is a structure of a large vertical extent and that some of the rocks filling it have a magnetization which, if it is assumed to be only induced, would be caused by a high susceptibility. Referring to the results of laboratory measurements of the physical properties of the rocks of the West Eifel Maars, high susceptibilities (30000×10^{-6} SI) and densities (2.65 g/cm^3) are exhibited by scorias. Taking into account that sampling was made at the surface, the susceptibility and the density of unweathered deeper lying scorias might be higher. From this point of view, the susceptibility of 50000×10^{-6} SI can be acceptable.

After having demonstrated that the Roth maar-diatreme is of a large vertical extent, one could ask why this structure, large in both horizontal and vertical dimensions, has such a small gravity anomaly. The answer is simple. If the assumption that the tuffs are overlain by dense scorias ($\rho = 2.65\ g/cm^3$) holds and taking into account that some Devonian rocks of the Eifel might have densities up to 2.65–2.7 g/cm^3 (Bannert, 1989) there will then be no density contrast and hence no contribution to the gravity anomaly from the scorias. From this point of view, the gravity anomaly would result almost entirely from the deeper lying tuffs, the density of which is probably higher than that of the weathered tuffs sampled at the surface. Another possibility is that the upper part of the maar might be underlain by a diatreme filled up by tuffs the susceptibility and the density of which are a little higher than those determined by laboratory measurements. In such a case a strong NRM should be present to contribute to the observed magnetic anomaly. Tuffs with high susceptibilities

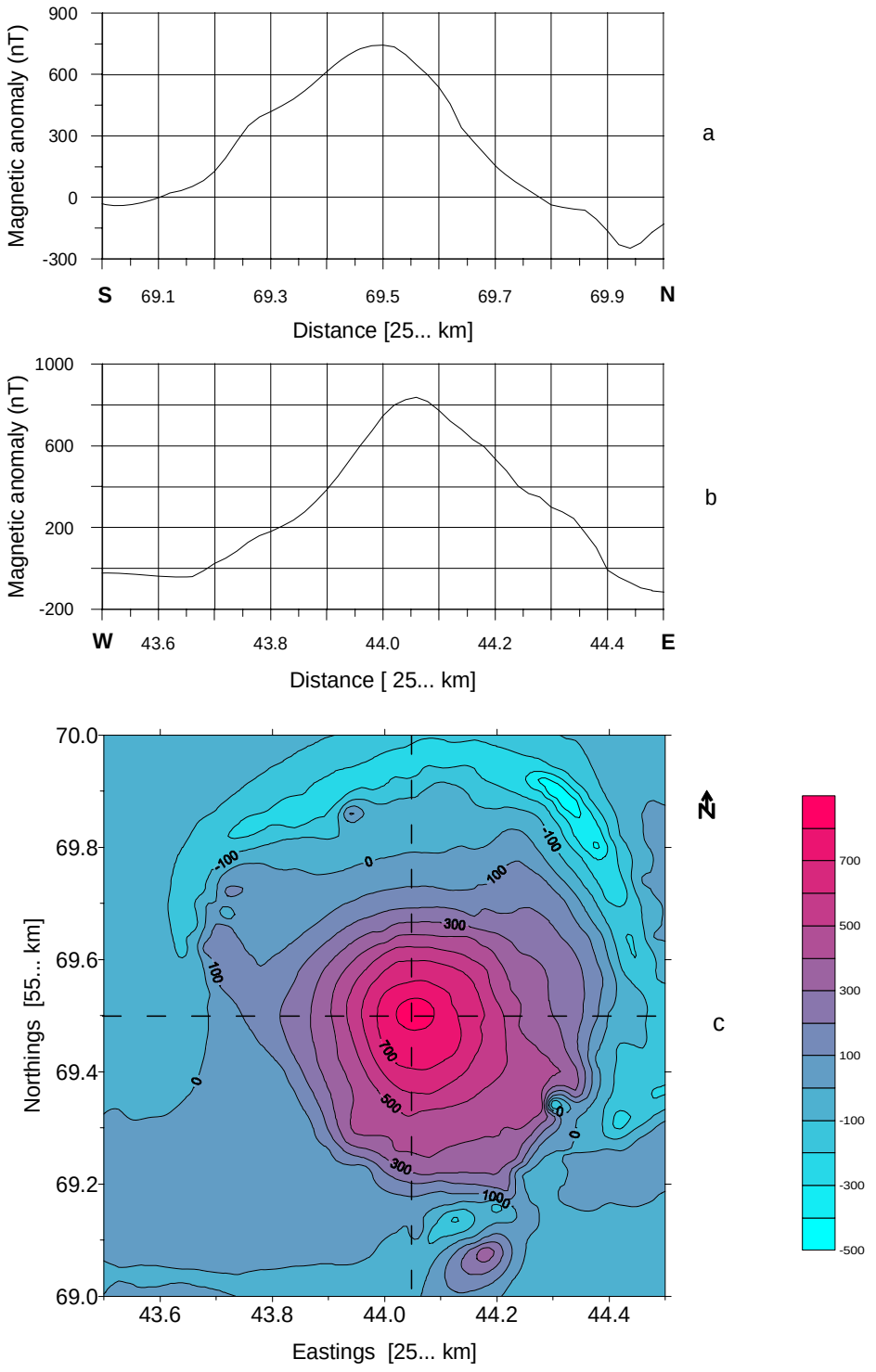

Fig. 5.5b Anomaly of the total magnetic field observed over the Roth Maar a, b: S-N and W-E profiles (dashed lines on contour map), respectively; c: contour map (redrawn from Büchel, 1987).

and densities have been reported (palagonite tuffs, Chap. 2). Using density values of 1.8 and 2.35 g/cm^3 for a 100 m thick upper layer and a 1000 m high underlying diatreme, respectively, an effective density contrast of -0.2 g/cm^3 is then calculated by the relation (4.1). For this density contrast, the gravity anomaly of -2.0 mGal and the height of 1100 m, we get a height to diameter ratio of 1.3 from the graphs presented on Fig. 4.18 and 4.14; the diameter is then estimated to about 845 m. Correspondingly, the walls of the maar-diatreme volcano, taken as a whole, would have a dip angle of about 70°.

Relying on the results of magnetic modeling (Chap. 4), the shape of the magnetic anomaly of the Roth Maar with a well expressed broad minimum (Fig. 5.5b) indicates that such an anomaly can not be caused by a scoria cone alone. A comparison of the magnetic profiles of the Roth Maar (Fig. 5.5b) with the theoretical profiles of a maar-diatreme-scoria cone structure (Fig. 4.8), lets think that a scoria cone is obviously located within the Roth maar-diatreme. From the genetic point of view, this means that at a late stage, the volcanic activity occured in a groundwater-poor environment, probably leading to the formation of a scoria cone.

The power spectrum presented on Fig. 5.5c shows that the magnetic field has three components corresponding to causative sources located, from higher to lower frequencies, at 15, 45 and 140 m depth, respectively. In terms of geology, a 60 m thick layer, made of differentiated sediments overlays a 80 m thick scoria cone, which is underlain by a diatreme filled by tuffs. According to the results of a borehole drilled at the northern boundary of the Roth Maar by the Geological Survey of Rhineland Palatinate in 1975, there is a 108 m thick layer made up of clayey sediments with juvenile lapilli and debris of Bundstein and of Devonian limestones. It is likely that the borehole did not hit the scoria cone located in the central part of the maar. Since the sedimentary layer is 108 m thick at the boundary of the maar, it is expected that the diatreme top is located at a greater depth in the central area. Hence, the estimated depth of about 140 m seems to be plausible.

A reconstruction of the posteruptive development of the Roth Maar (Fig. 5.5d) has been attempted. This has been done relying on Wood's theory (1974) according to which the initial crater diameter and crater depth of a maar are in the proportion of 5 to 1. The 5 to 1 ratio corresponds to a straight line which passes through the centre of the maar bottom and cuts the horizontal plane at an angle of 22°. The investigations conducted by Büchel (1984) showed that Wood's theory can be applied to the Eifel maars as well. According to the results of the spectral analysis, the maar bottom is at about 150 m depth. The present day crater bottom, maar-diatreme outcrop and surface of the vicinity have an altitude of 450, 470 and 490 m, respectively. From geological observations, the Roth Maar has an approximate diameter of 1000 m. Assuming that the original dip angle of the crater walls was 90°, the original crater diameter and crater depth would be in the ratio of 1000 to 200 m. The erosion would then amount to 10 m. For a dip angle of 35°, we get an original crater diameter of 1200 m and an original crater depth of 240 m. This means that the syneruptive surface of the vicinity has been eroded up to 50 m. For the estimated depth ($\approx$ 150 m) of the maar crater, the dip angle of the crater walls cannot be less than 25°. From this point of view, the initial crater diameter and crater depth would not have values larger than 2000 and 400 m, respectively, and the erosion should amount to between 0 and at most 200 m.

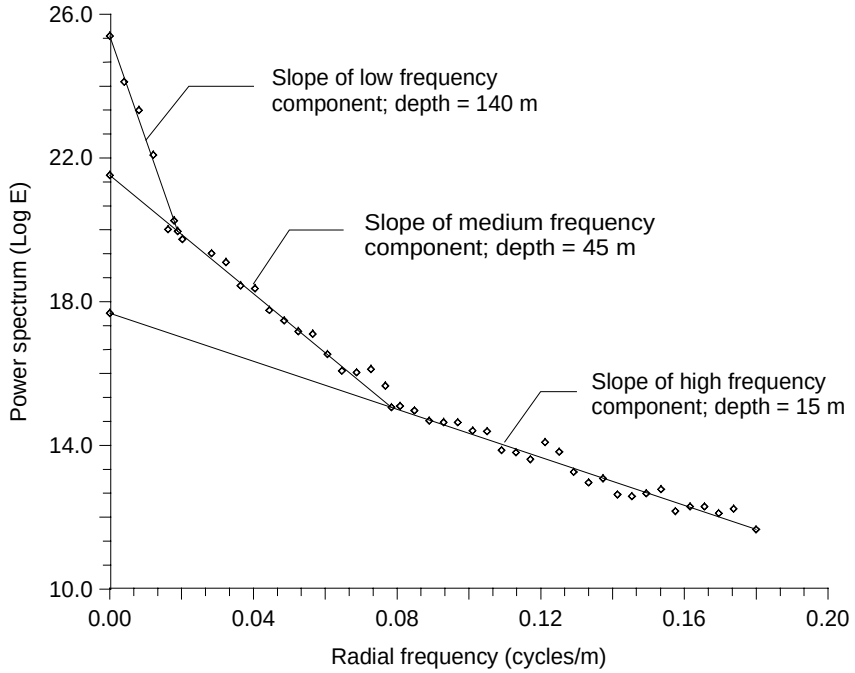

Fig. 5. 5c Logarithmic power spectrum of the magnetic field of the Roth Maar.

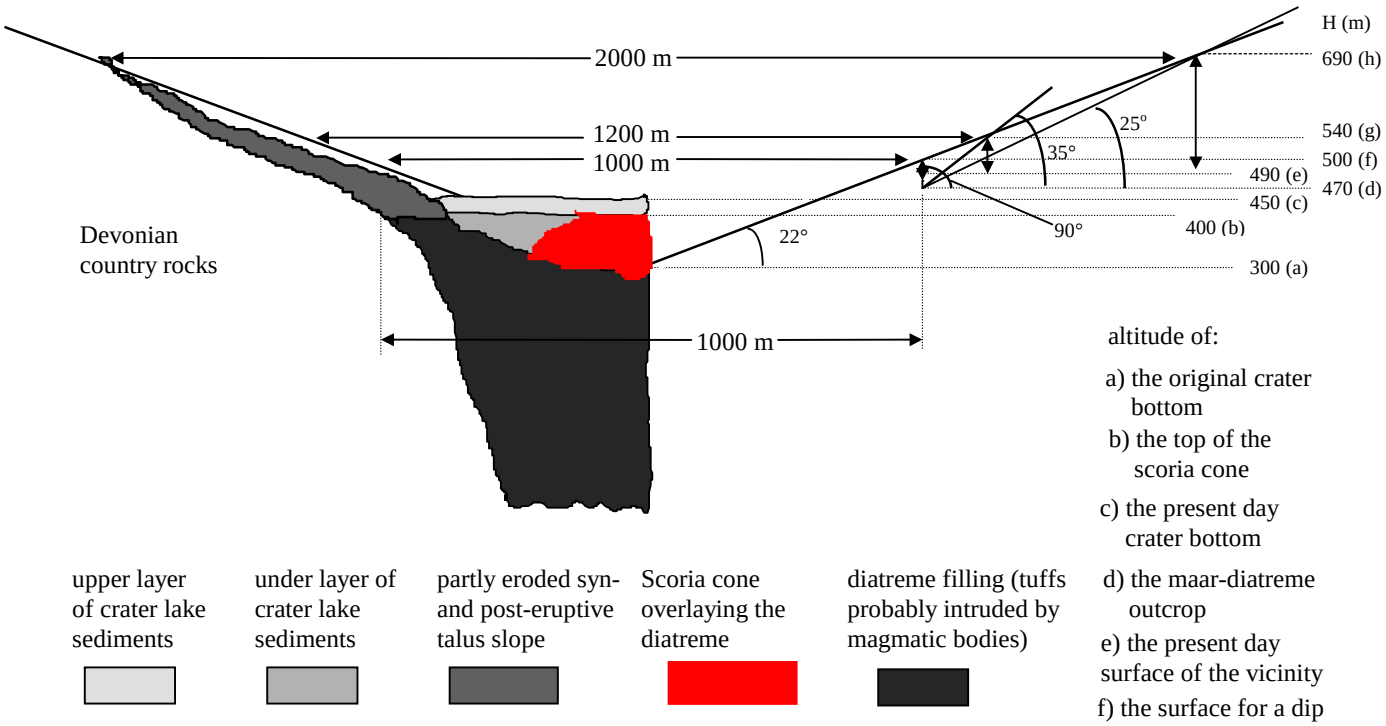

Fig. 5.5d Schematic reconstruction of the initial posteruptive crater shape of the Roth Maar, derived from geophysical and geological results.

5.6 The Dehner Maar

The gravity and magnetic profiles of the Dehner Maar, as well as their location, are shown on Fig. 5.6. The gravity anomaly has a size of -2.5 mGal. The diameter of the Dehner Maar, approximated from the magnetic anomaly, is about 750 m. Assuming that the rocks filling the Dehner Maar have an effective density of 2.0 g/cm^3 — mean density of the West Eifel maar tuffs — hence a density contrast of -0.5 g/cm^3 with respect to the Devonian country rocks, we get estimates of 310 m and 40° for the height and the dip angle of the walls, respectively. Taking into account that the crater sediments of the Dehner Maar have a mean density of 1.6 g/cm^3, which contributes to a decrease of the effective density of the whole structure, it should be expected that the height of the Dehner Maar would even be smaller than the estimated one. Actually, the character of the magnetic anomaly indicates that the latter is caused by a near-surface diatreme the height of which is much smaller than its top diameter and the walls of which dip at an angle greater than the estimated one of 40°. A height of 250 m and a mean dip angle of 55° were estimated by theoretical magnetic modeling. This means that the Dehner Maar, which counts to the oldest maar volcanoes of the West Eifel, has been deeply eroded. Sediments — obviously of a small horizontal and vertical extent — are only spread in the central (near-)surface part of the structure.

5.7 The Schönfeld Maar

The gravity and magnetic anomalies of the Schönfeld Maar are shown on Fig. 5.7. The size of the gravity anomaly amounts to -2.5 mGal. The surface diameter, approximated from the magnetic anomaly, is about 500 m. The tuffs of the Schönfeld Maar have a mean density of 2.0 g/cm^3, which gives a density contrast of -0.5 g/cm^3. The estimated height of the maar-diatreme is 440 m; this corresponds to a dip angle of 60°. Assuming that the magnetization is only induced — about 0.5 A/m for the mean tuff susceptibility of 12000×10^{-6} SI — the size of the magnetic anomaly seems to be too big for the estimated dimensions. To the strong anomaly contribute not only the tuffs, which, beside the induced magnetization, have a NRM of 1.2 A/m, but also the scorias and the crater sediments. The scorias found at the NE boundary of the maar have susceptibilities varying between 15000 and 30000×10^{-6} SI. It is likely that such scorias lie below and/or within the sediments above the tuffs. The susceptibility of the (near-)surface crater sediments is very similar to that of the tuffs. The scorias probably resulted from the late phase of the volcanic eruption when there was no more groundwater available, which led to a formation of a scoria cone. In fact, examining the profiles and the contour map of the magnetic anomaly (Fig. 5.7) and comparing them with those of the theoretical anomaly produced by a complex structure (maar-diatreme-scoria cone, Fig. 4.9), it is possible to establish a certain similarity between both. This indicates that a scoria cone, the centre of which is offset northwards, might be located within the maar-diatreme. Since the Schönfeld and Dehner Maars are very close to one another (Fig. 5.6a), they were formed in a common tectonic and hydrogeological environment and probably belong to a same eruption centre. From what discussed above, it is likely that the volcanic eruption occured by Dehner in its early phase and subsequently by Schönfeld.

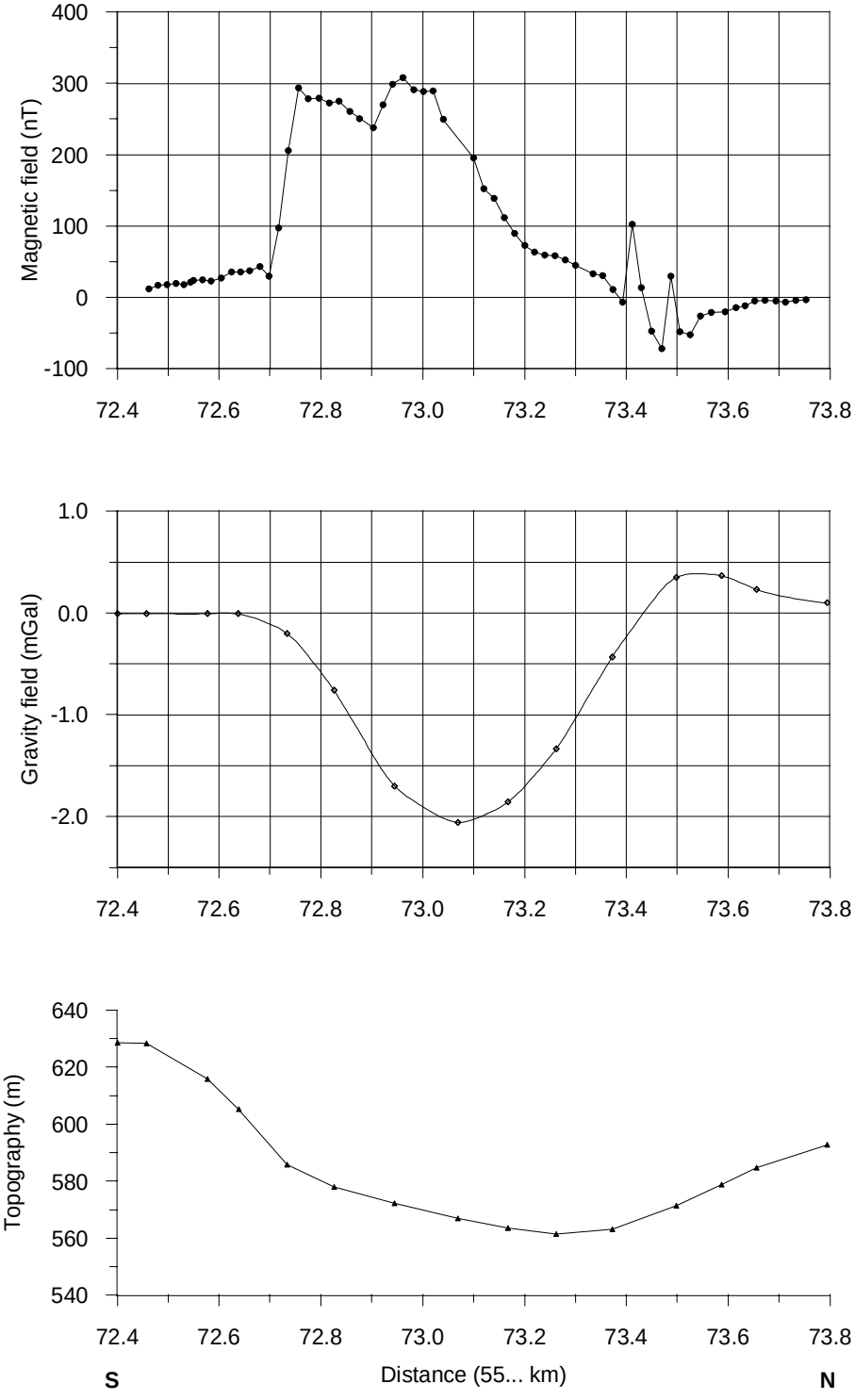

Fig. 5.6b Profiles over the Dehner Maar.

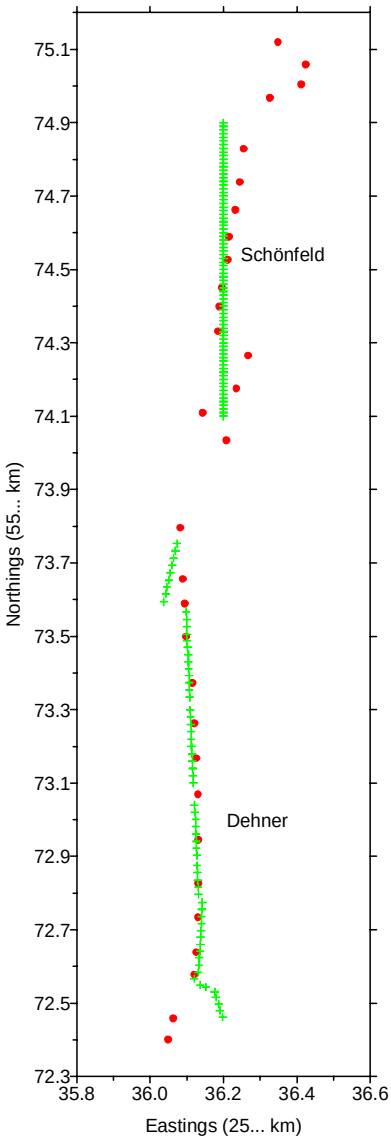

Fig. 5.6a Location of the gravity and magnetic profiles over the Dehner and Schönfeld Maars.

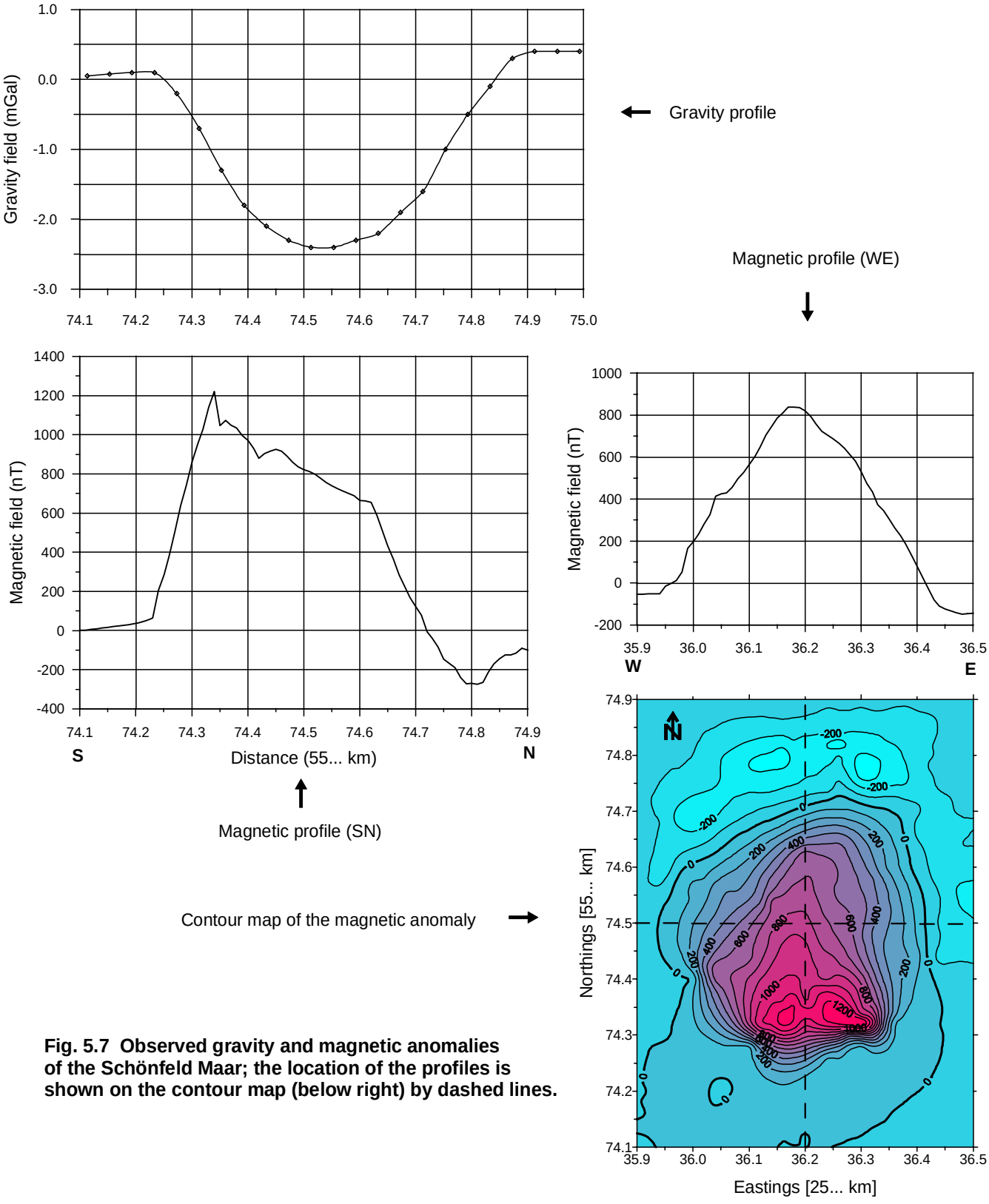

Fig. 5.7 Observed gravity and magnetic anomalies of the Schönfeld Maar; the location of the profiles is shown on the contour map (below right) by dashed lines.

5.8 The Hausten-Morswiesen Maar

According to Büchel (1991), the diameter of the Hausten-Morswiesen Maar varies between 1200 m in SW- and 1500 m in NNW-direction; thus a mean value of 1350 m. The size of the gravity anomaly is about −3.5 mGal (Fig. 5.8a). Assuming a density contrast of $-0.5\ g/cm^3$, we get estimates of about 320 m and 25° for the height and the dip angle, respectively. The surface diameter, approximated from geophysical observations, averages 1000 m, which gives respective estimates of 400 m and 40° for the height and the dip angle. Relying on Wood's theory about the relationship between the crater height and the top diameter of a maar (1:5 ratio), the crater height should be about 200–250 m, which implies that the height of the underlying diatreme would amount to a maximum value of 150 m. The magnetic anomaly has a maximum of about 380 nT (Fig. 5.8b). This value seems to be too high for a maar-diatreme of about 400 m height if the diatreme tuffs, covered by crater lake sediments of 200–250 m thickness had only an induced magnetization. Either the maar-diatreme rocks have a higher magnetization or the diatreme is simply larger/deeper. According to Pirrung (1997), basaltic deposits from a nearby eruption centre were put in a evidence within the crater sediments of the Hausten-Morswiesen Maar by a borehole drilled in 1990. The effect of these deposits obviously strengthens the magnetic anomaly on the one side and leads to a decrease of the overall density contrast of the structure on the other one. The latter implies that a larger/deeper diatreme should be expected. Gravity modeling of the Hausten-Morswiesen Maar conducted by Büchel (1991) gave a total height of 450–600 m. Contrary to the ideally cone shaped maar-diatreme, Büchel used a model body of a narrower diatreme overlain by a thinner layer of sediments to fit gravity data.

5.9 Concluding remarks

It should be noted that the dip angles and the heights which have been exclusively estimated by the method presented in Chapter 4 refer to a cone shaped maar-diatreme structure considered as a whole. In the reality, as the diatreme deepens, it narrows and almost grows vertically as the phreatomagmatic process continues. Thus, the height of the diatreme, the dip angle of its walls and consequently the actual heights of the maar-diatremes must be greater than the estimated ones.

Nevertheless, the results clearly show that there exists no generalized systematics of the maar-diatremes. This will be discussed later in details. It is first aimed to conduct inverse modeling of observed magnetic and gravity data of some maars. A combination of results from different methods can supply with more reliable information.

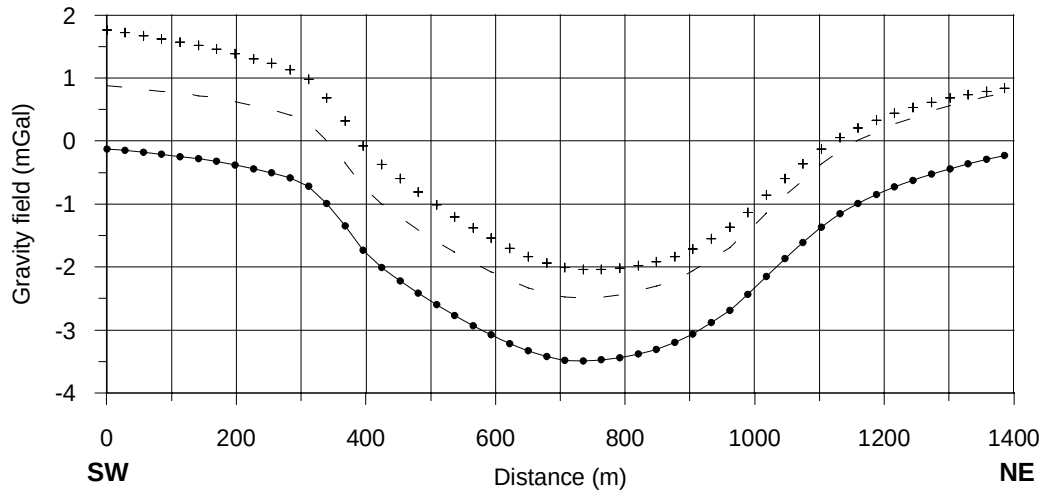

Fig. 5.8a Gravity profile of the Hausten-Morswiesen Maar.
End coordinates of the profile: (2579.0, 5584.4; 2580.0, 5585.4km).

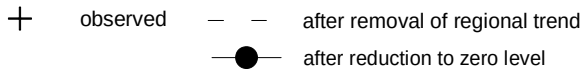

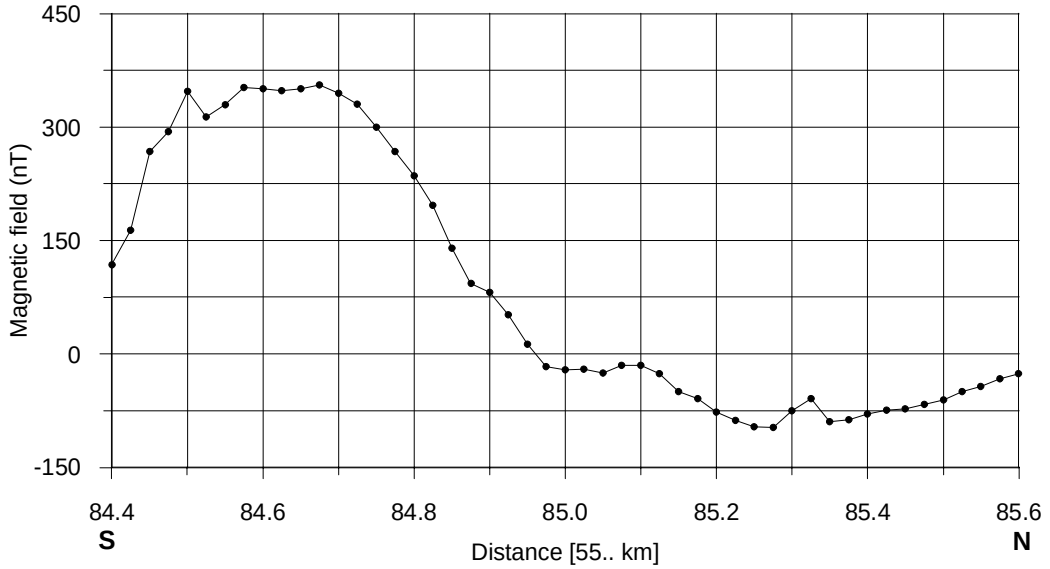

Fig. 5.8b Profile of the magnetic anomaly of the Hausten-Morswiesen Maar.

6. Inversion of magnetic data of the Schönfeld Maar

6.1 Description of the magnetic anomaly over the Schönfeld Maar

The Schönfeld Maar belongs to the Quaternary West Eifel volcanic field (No 1 on Fig. 2.2, Chap. 2). It is situated in the vicinity of the village Schönfeld and is drained by the small rivulet Wirft (Fig. 6.1a). Its diameter amounts to about 500 m and 440 m in the SN- and WE-direction, respectively. Like most maars in the Eifel area, the Schönfeld Maar is situated in a valley as can be seen on Fig. 6.1b showing, in a 3D-view, the topography and the magnetic field reduced to the pole, respectively. Actually, the reduction to the pole converts magnetic data which have been observed at whatever declinations and inclinations of both the induced and total magnetization vectors to what the data would have looked like at the pole, i.e. at vertical inclination of both the magnetization vectors (Sheriff, 1984). By pole reduction, the asymetry of the anomaly caused by the inclination disappears and the anomaly maximum is located above the centre of the causative source.

The original magnetic observations over the Schönfeld Maar were made by Büchel in 1984 during a geophysical campaign in the framework of his Ph.D. thesis. As can be seen on Fig. 6.1a, the anomaly is characterized by maxima and strong gradients of the magnetic field near the southern boundary of the maar. The zero contour of the magnetic anomaly converges inwards in the southern area. Relying on the results of theoretical magnetic modeling (Chap. 4), all these criteria indicate that the anomaly is caused by a near- surface, even quasi exposed structure, the surface diameter of which is larger than the vertical extent. The strong gradient of the anomaly in the South is probably due to the strongly eroded maar rim and to the nearly exposed tuffs and/or scorias of the maar boundary. In a late stage of erosion, a major part of these rocks is supposed to have slumped down into the maar crater, where it accumulated, hence partly contributing to the strong observed anomaly, which is northwards elongated. Results of laboratory measurements have shown that the near-surface rocks filling the Schönfeld Maar exhibit relatively high susceptibility values (Table 2.3, Chap. 2), contrary to what would be expected for crater lake sediments. The anomaly is somewhat SSW-NNE oriented, probably due to a slight positive declination of the magnetization vector.

The elements of the geomagnetic field of the Schönfeld locality computed by the 1985 **I**nternational **G**eomagnetic **R**eference **F**ield (IGRF) program (IAGA, 1987) provided by the World Data Centre C1 for Geomagnetism at the British Geological Survey are: $F_o = 47765\ nT$, $I = 66°$, $D = -3°$. For all computations to be done and all graphic presentations, the point with the Gauß-Krüger coordinates 2536.2 and 5574.5 has been chosen as origin of the coordinate system.

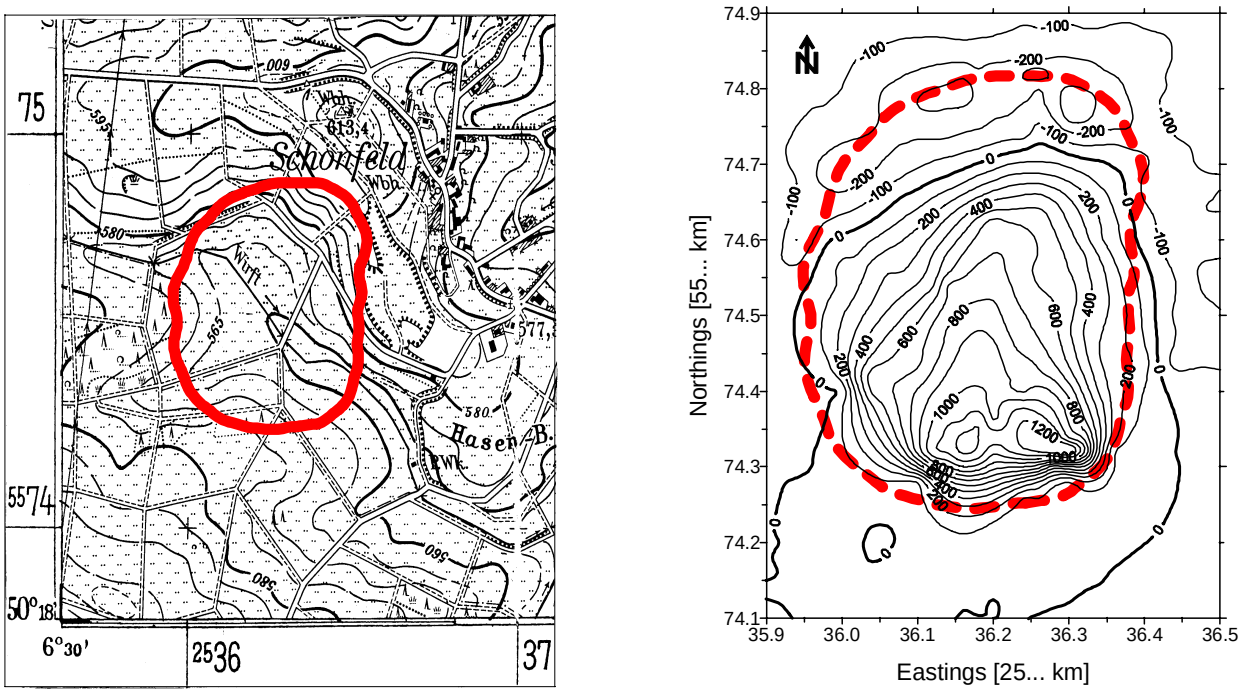

Fig. 6.1a Topography (left) and magnetic anomaly (right) of the Schönfeld Maar. The red solid and dashed contours respectively show the location and the boundary of the maar.

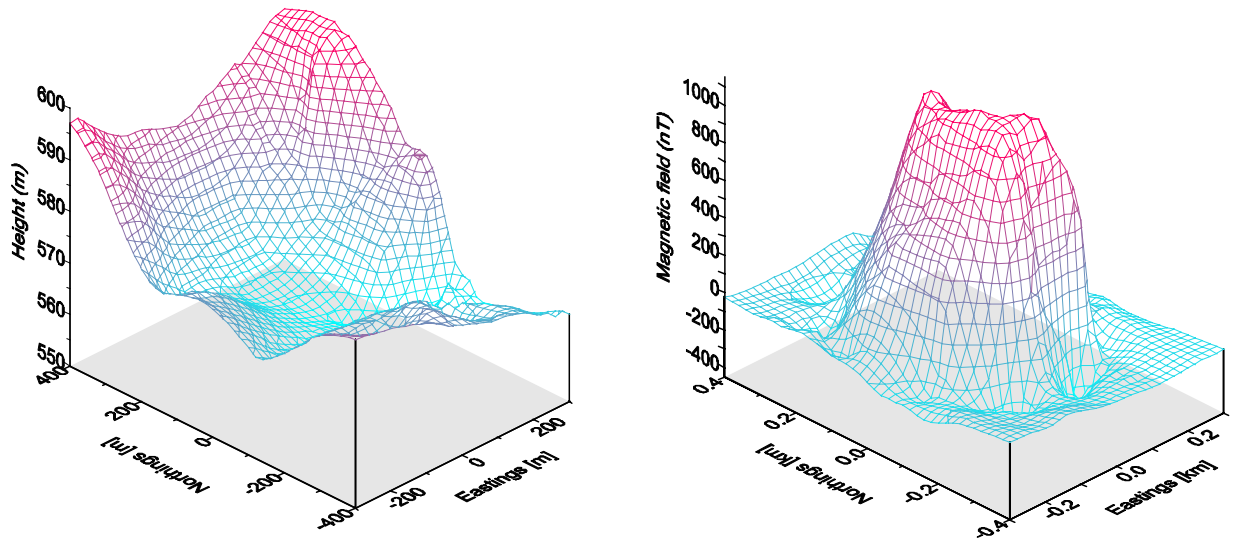

Fig. 6.1b 3-D view of the topography (left) and of the pole reduced magnetic field (right) of the Schönfeld Maar.

6.2 Geometric model

Before proceeding with the inversion, it has been necessary to design a geometric model which can easily be modified according to the parameterization. Maar-diatremes are almost circular in map view. But in reality, the true shape of the cross-section of each particular maar-diatreme differs from this assumption, depending on the geomorphological and tectonic conditions which controlled the maar formation. Therefore models should be individually designed for more accurate inversion procedures.

The shape of a maar-diatreme (at least of its upper part) can be deduced from its surface boundary, which can ─ as a priori information ─ serve as starting point for a model design. The top boundary of the maar was defined by means of the magnetic field reduced to the pole. Actually, the character and the shape of the pole reduced field are similar to those of the second vertical derivative of the gravity potential. The zero contour of the latter approximately outlines the edges of the anomalous structure. Thus, the zero contour of its analogous, the magnetic field reduced to the pole, roughly defines the top boundary of the maar-diatreme structure. The radii relative to the vertices of the uppermost polygonal contour were approximated from the top boundary of the maar and were kept constant. For the continuation of the model in depth, it was assumed that the radii were linearly decreasing, but differently for both the crater and the diatreme. Two different configurations are possible: a maar with a crater overlying a diatreme or a diatreme alone. On Figures 6.2a and 6.2b are respectively shown a prototype of the 3-D model and its schematic vertical cross-section.

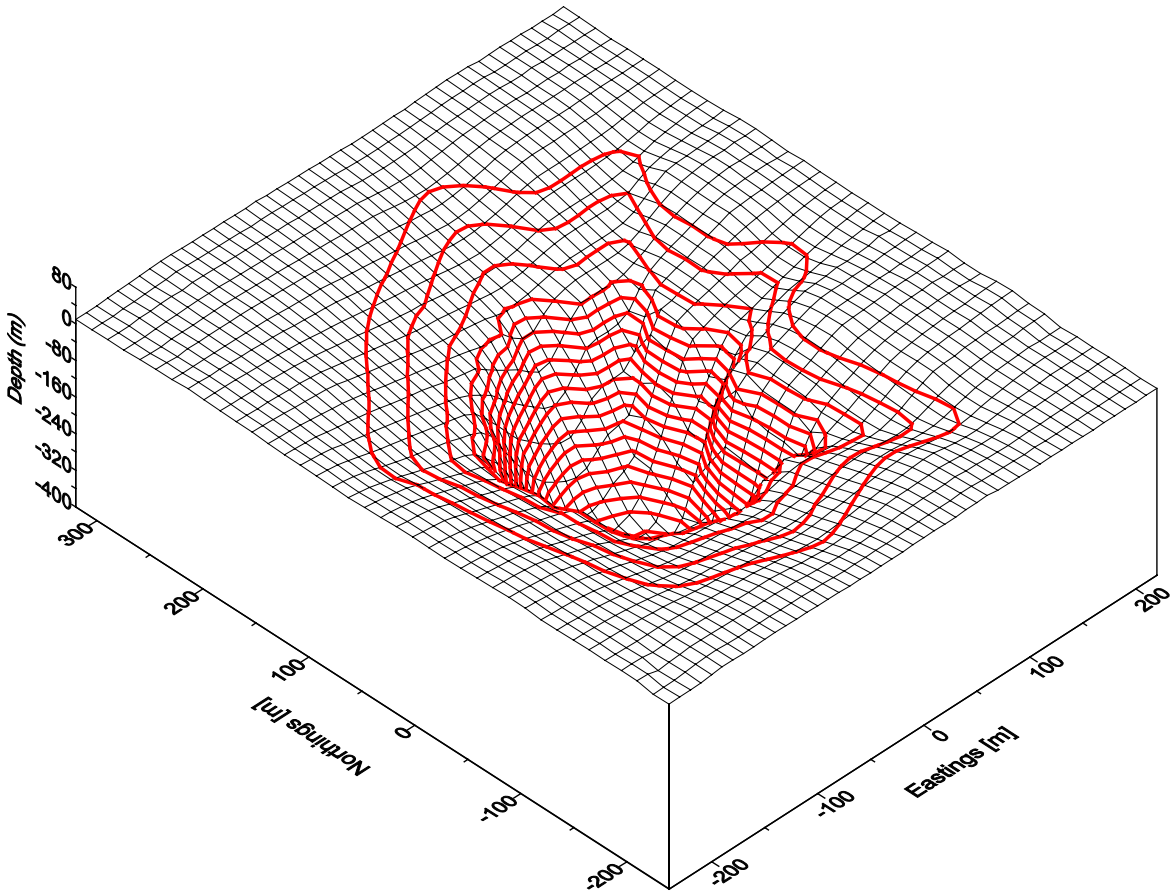

Fig. 6.2a A 3D-view of the geometrical model used for the inversion of magnetic data; the red lines represent the polygonal contours used for the computation of the surface integrals of the body(ies).

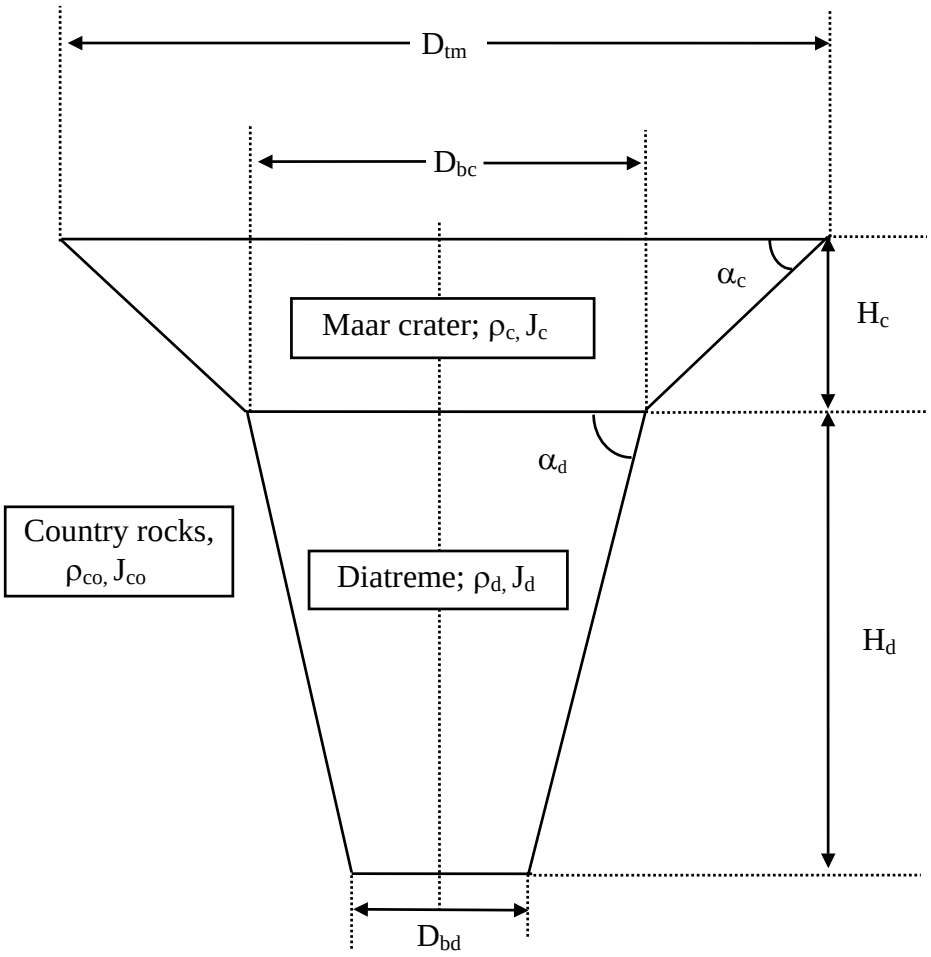

Fig. 6.2b Schematic vertical cross-section of a maar-diatreme with related parameters.

D_{tm} : diameter of the top of the maar
H_c : height of the maar crater
D_{bc} : diameter of the bottom of the crater
α_c : dip angle of the crater walls
H_d : height of the diatreme
α_d : dip angle of the diatreme walls
D_{bd} : diameter of the bottom of the diatreme
ρ_c , ρ_d , ρ_{co} : respective densities of the crater, diatreme and country rocks
J_c, J_d , J_{co} : magnetization of the crater, diatreme and country rocks, respectively

6.3 Estimation and derivation of parameters

A given model is defined by a set of physical and geometric parameters, some of which are known/assumed and others are not. Unknown parameters can be classified into two cathegories: primary and secondary. In our case, the primary cathegory includes those unknown parameters, such like the total magnetization, the dimensions of the body, which are used for the model optimization. These parameters will be estimated by means of nonlinear inversion, as described in Chapter 3. To the secondary cathegory belong unknown parameters, which are, directly or not, related to those of the first cathegory and can then be straightforward derived from the estimates or indirectly with the help of the known/assumed parameters using basic relationships given in Chapter 3 as well. This cathegory includes, for example, the dip angles of the walls of the maar-diatreme, the directions of the total magnetization, the elements of the remanent magnetization, the effective susceptibility — if the magnetization is assumed to be only induced — or the apparent susceptibility in the case, where a NRM is supposed to also be present, the Koenigsberger ratio, etc. The volume percentage, V, of magnetite in a rock can also be estimated from the susceptibility χ by the following empirical relationship (Balsley and Buddington, 1958):

$$V = 21.8\chi^{0.9}$$

where χ is in SI units. The estimated susceptibility and the corresponding volume percentage of magnetite are truely representative, if the magnetization is only induced or the NRM component is negligeable.

6.4 Inversion of profile data; model with 10 unknown parameters

A first attempt to model the Schönfeld Maar was made using 81 data points of the observed SN- profile and parameterizing the major elements supposed to have an effect on the model response. As unknown parameters were taken: the height of the maar crater (H_c), the diameter of the bottom of the maar crater (D_{bc}), the X-, Y- and Z-components of the magnetization of the crater rocks (J_{xc}, J_{yc} and J_{zc}), the height of the diatreme (H_d), the diameter of the bottom of the diatreme (D_{bd}), the horizontal and vertical components (J_{xd}, J_{yd} and J_{zd}) of the magnetization of the rocks filling the diatreme.

Inversion has been run with different initial models, which, as expected, led to different estimated models. No matter which directions of the magnetizations were obtained by the best fits between observations and model responses, all results generally show that the magnetic anomaly of the Schönfeld Maar is caused by sources having strong magnetizations. The results of one of the inversion procedures are presented in Tables 6.1a and 6.1b. Table 6.1a contains the estimates of the unknown parameters and some other parameters evaluated using the estimates. In Table 6.1b are only given the estimates, their bounds and their resolutions. LB and UB stand for lower and upper bound, respectively.

The magnetization of the crater rocks reaches values between 1.5 and 2.0 A/m. If it were assumed to be only induced, it would be caused by high susceptibilities of about 40000–50000$\times 10^{-6}$ SI corresponding to a volume content of magnetite of 1.2 to 1.5%. The susceptibility is much higher than those of crater sediments (10000–15000$\times 10^{-6}$ SI) and of tuffs (11000$\times 10^{-6}$ SI), determined by laboratory measurements.

Accordingly, the volume content of magnetite is also high compared to that in maar-diatreme rocks (0.4−0.65%). Probably, a remanent component (NRM) ─ as indicated by the values of the Koenigsberger ratio Q (2.5−4.0) ─ is mainly contributing to the strong magnetization. The values of the NRM are about 1.3−1.6 A/m. All this indicates that the rocks filling the maar crater are other than craterlake sediments, which ─ as known for some Eifel maars ─ have lower susceptibility and NRM values (100−800×10^{-6} SI, 0.05−0.2 A/m). The estimated height of the maar crater varies between 30 and 110 m, the average diameter of its bottom ─ between 300 and 430 m, which corresponds to dip angles of 60−80° for the crater walls.

The magnetization of the rocks filling the underlying diatreme is also high, whereby it gets higher as the overlaying maar crater gets shallower. Its estimates are around 3.0 A/m. Assuming that the magnetization was only induced, the causative rocks would have susceptibilities of about 85000×10^{-6} SI and a volume content of magnetite around 2.3%. Both latter values are much higher than those of tuffs and are characteristic for basalts. Here also, a NRM (2.5−3.0 A/m) is supposed to predominantly contribute to the strong magnetization. The Koenigsberger ratio amounts from 5 to 6. The computed values of the NRM and Q are higher than those respective measured ones of 1.2 A/m and 3.0 for the tuffs of the Schönfeld Maar. This means that either the magnetization of the diatreme rocks is higher than that of the tuffs sampled at the surface or the height of the diatreme has been underestimated. Actually, as shown in Table 6.2b, both the vertical component of the magnetization J_{zd} and the height of the diatreme H_d display a poor resolution. But this might also be caused by a bad estimation of the parameters of the maar crater. While the estimated height of the diatreme varies between 100 and 200, the diameter of its bottom ─ between 230 and 290 m, the dip angle of its walls lies between 50 and 85°.

Although, as shown by Fig. 6.3, good fits between computed and observed profiles could be achieved, some estimated parameters, particularly the directions of the magnetizations, are not in agreement with the observed anomaly. For instance, due to large negative or positive obtained declinations, the axis joining the extrema of the magnetic field should have a NW-SE or NE-SW orientation, different from the nearly NS-orientation characterizing the observed field (see Fig. 6.1a). As for the inclinations, they are varying between 60 and 70°, which is realistic.

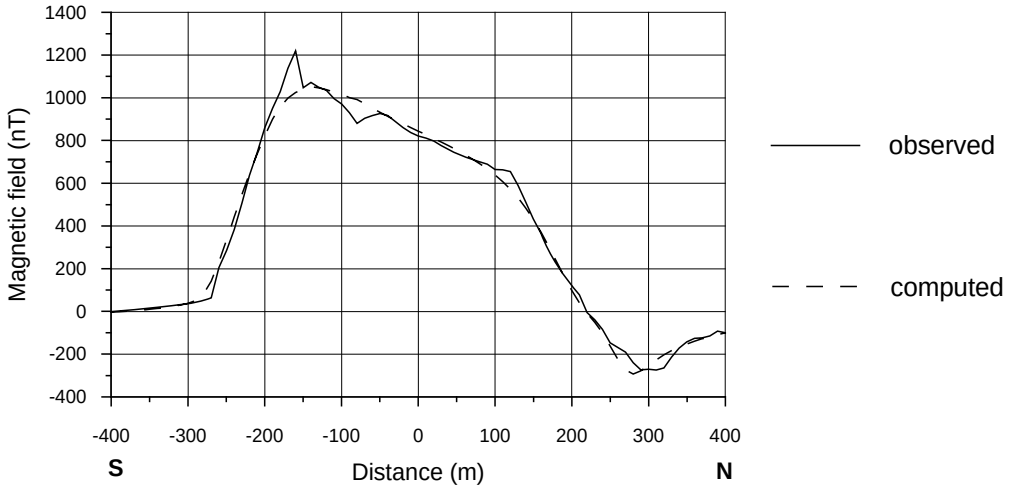

Fig. 6.3 Profile inversion of the magnetic anomaly of the Schönfeld Maar; model with 10 unknowns.

Table 6.1a Results of profile inversion; model with 10 unknown parameters.

Parameter	Value	Unit
Average diameter of the top boundary of the maar (D_{tm})	443.0	m
Average diameter of the crater bottom (D_{bc})	418.0	m
Average height of the maar crater (H_c)	42.0	m
Average slope of the crater walls (α_c)	73.0	°
Average diameter of the diatreme bottom (D_{bd})	288.0	m
Average height of the diatreme (H_d)	120.0	m
Average slope of the diatreme walls (α_d)	62.0	°
X-comp. of the magnetization of the crater rocks (J_{xc})	0.57	A/m
Y-comp. of the magnetization of the crater rocks (J_{yc})	0.53	A/m
Z-comp. of the magnetization of the crater rocks (J_{zc})	1.67	A/m
Total magnetization of the crater rocks	1.84	A/m
Inclination of the total magnetization of the crater rocks	65.0	°
Declination of the total magnetization of the crater rocks	43.0	°
Computed apparent susceptibility of the crater rocks	0.0483	SI
Remanent magnetization of the crater rocks	1.46	A/m
X-component of the NRM of the crater rocks	0.41	A/m
Y-component of the NRM of the crater rocks	0.54	A/m
Z-component of the NRM of the crater rocks	1.32	A/m
Inclination of the NRM of the crater rocks	62.0	°
Declination of the NRM of the crater rocks	52.0	°
Koenigsberger ratio for the crater rocks (Q)	3.8	–
Volume percentage of magnetite in crater rocks	1.4	%
X-comp. of the magnetization of the diatreme rocks (J_{xd})	1.1	A/m
Y-comp. of the magnetization of the diatreme rocks (J_{yd})	−0.18	A/m
Z-comp. of the magnetization of the diatreme rocks (J_{zd})	2.9	A/m
Total magnetization of the diatreme rocks	3.1	A/m
Inclination of the total magnetization of the diatreme rocks	69.0	°
Declination of the total magnetization of the diatreme rocks	−9.5	°
Computed apparent susceptibility of the diatreme rocks	0.081	SI
Remanent magnetization of the diatreme rocks	2.60	A/m
X-component of the NRM of the diatreme rocks	0.90	A/m
Y-component of the NRM of the diatreme rocks	−0.17	A/m
Z-component of the NRM of the diatreme rocks	2.45	A/m
Inclination of the NRM of the diatreme rocks	69.5	°
Declination of the NRM of the diatreme rocks	−11.0	°
Koenigsberger ratio for the diatreme rocks	4.0	–
Volume percentage of magnetite in the diatreme rocks	2.3	%
Root mean square error (RMS)	66.0	nT
Normalized mean square error (MSE)	1.0	%

Table 6.1b Confidence intervals and resolutions of the estimates from the inversion of profile data; model with 10 unknowns.

Parameter	LB	Estimate	UB	Resolution
J_{xc}	0.44	0.57	0.70	0.43
J_{yc}	0.12	0.53	0.94	0.60
J_{zc}	1.50	1.67	1.80	0.61
D_{bc}	407.0	416.0	425.0	0.56
H_c	37.0	42.0	48.0	0.53
J_{xd}	0.96	1.10	1.2	0.56
J_{yd}	−1.03	−0.18	−0.66	0.70
J_{zd}	2.80	2.88	2.96	0.40
H_d	113.0	120.0	125.0	0.48
D_{bd}	260.0	288.0	318.0	0.57

6.5 Inversion of areally distributed data; model with 10 unknown parameters

It is well known that inversion can be improved by using a priori information. Moreover, for overdetermined least squares problems, the more data the better the solution, of course provided that data are of good quality. This can be easily understood since the data themselves reflect the nature of the source, bearing de facto some kind of a priori information. Taking this into consideration, further inversion has been conducted using more data points (259) randomly distributed over the maar-diatreme. The model and the parameterization were kept the same as in the previous case. Tables 6.2a and 6.2b contain the results of the inversion.

The diameter of the maar crater has been estimated to 410 m at the bottom; the height — to 75 m. The slope of the crater walls is $\approx 78°$. A diatreme with a height ≈ 100 m and a bottom diameter ≈ 260 m underlies the crater; the dip angle of the diatreme walls varies between 40 and 70°. The results show that the high observed magnetic anomaly is a sum effect of two relatively high magnetizations, the intensities of which are 1.7 A/m and 3.3 A/m for the crater and diatreme rocks, respectively. If the magnetizations were only induced, they would correspond to respective susceptibilities of 45000×10^{-6} and 90000×10^{-6} SI, which are too high compared to those of the tuffs. Despite an improvement of the solution as shown by the resolutions of the parameters (see Table 6.2b), the estimates don't much differ from those of the profile inversion. This implies that all discussions and reflexions in 6.4 hold for this case as well. Figure 6.4 shows that the computed field doesn't well fit the observed one, especially in the central part northwards. This is probably due to a local (near-) surface feature which has not been modeled for.

Though the modeling results achieved in 6.4 and 6.5 seem to be unsatisfactory, they nevertheless contain some useful information about the physical character and the location of the causative source(s). First, they show that the maar-diatreme is filled up by rocks having strong magnetizations, responsible for the strong magnetic anomaly, whereby the remanent components are prevailing. Some of the rocks are located at/near the surface. Moreover, the walls of the maar crater are likely to be steep, which, considering the character of the anomaly, suggests that the maar is deeply eroded.

Table 6.2a Results of the inversion of random observed data; model with 10 unknown parameters.

Parameter	Value	Unit
Average diameter of the top boundary of the maar (D_{tm})	443.0	m
Average diameter of the crater bottom (D_{bc})	410.0	m
Average height of the maar crater (H_c)	76.0	m
Average slope of the crater walls (α_c)	78.0	°
Average height of the diatreme (H_d)	95.0	m
Average diameter of the diatreme bottom (D_{bd})	262.0	m
Average slope of the diatreme walls (α_d)	52.0	°
X-comp. of the magnetization of the crater rocks (J_{xc})	0.73	A/m
Y-comp. of the magnetization of the crater rocks (J_{yc})	−0.15	A/m
Z-comp. of the magnetization of the crater rocks (J_{zc})	1.57	A/m
Total magnetization of the crater rocks	1.74	A/m
Inclination of the total magnetization of the crater rocks	65.0	°
Declination of the total magnetization of the crater rocks	−12.0	°
Computed apparent susceptibility of the crater rocks	0.045	SI
Remanent magnetization of the crater rocks	1.26	A/m
X-component of the NRM of the crater rocks	0.53	A/m
Y-component of the NRM of the crater rocks	−0.14	A/m
Z-component of the NRM of the crater rocks	1.13	A/m
Inclination of the NRM of the crater rocks	64.0	°
Declination of the NRM of the crater rocks	−14.5	°
Koenigsberger ratio for the crater rocks	2.6	–
Volume percentage of magnetite in crater rocks	1.3	%
X-comp. of the magnetization of the diatreme rocks (J_{xd})	1.25	A/m
Y-comp. of the magnetization of the diatreme rocks (J_{yd})	0.55	A/m
Z-comp. of the magnetization of the diatreme rocks (J_{zd})	3.00	A/m
Total magnetization of the diatreme rocks	3.30	A/m
Inclination of the total magnetization of the diatreme rocks	66.0	°
Declination of the total magnetization of the diatreme rocks	24.0	°
Computed apparent susceptibility of the diatreme rocks	0.087	SI
Remanent magnetization of the diatreme rocks	2.88	A/m
X-component of the NRM of the diatreme rocks	1.06	A/m
Y-component of the NRM of the diatreme rocks	0.56	A/m
Z-component of the NRM of the diatreme rocks	2.60	A/m
Inclination of the NRM of the diatreme rocks	65.0	°
Declination of the NRM of the diatreme rocks	28.0	°
Koenigsberger ratio for the diatreme rocks	6.0	–
Volume percentage of magnetite in the diatreme rocks	2.4	%
Root mean square error (RMS)	118.0	nT
Normalized mean square error (MSE)	8.0	%

Table 6.2b Confidence intervals and resolutions of the estimates. Inversion of areally distributed data; model with 10 unknowns.

Parameter	LB	Estimate	UB	Resolution
J_{xc}	0.59	0.73	0.86	0.96
J_{yc}	− 0.33	− 0.15	0.03	0.92
J_{zc}	1.40	1.57	1.70	0.90
D_{bc}	395.0	410.0	425.0	0.93
H_c	60.0	76.0	92.0	0.86
J_{xd}	0.97	1.25	1.53	0.95
J_{yd}	0.26	0.55	0.85	0.70
J_{zd}	2.80	3.00	3.30	0.56
H_d	80.0	95.0	110.0	0.48
D_{bd}	185.0	262.0	340.0	0.57

6.6 Inversion of areally distributed data; model with 7 unknown parameters

Another well known tool to improve an inversion procedure and consequently the solution is to reduce the number of degrees of freedom of the model by constraining it. Constraints might be known and/or assumed parameters, their range, etc. Taking into account the results and discussions from 6.4 and 6.5, further modeling was attempted assuming that the whole structure had a homogeneous magnetization. Thus, the number of unknown parameters was reduced to 7. Inversion was conducted using both profile and areally distributed data. The results are not discussed each particularly, but are summarised in the following. As an example, results of one inversion procedure conducted using areally distributed data are presented in Tables 6.3a and 6.3b.

The results also show that the magnetic anomaly is caused by a high intensity of the magnetization (2.2–2.7 A/m), the inclination and declination of which vary between 66 and 71° and −2.5 and 5°, respectively. This direction does not much diverge from that of the ambient geomagnetic field and seems to be in good agreement with the observed field. While the inclination estimates were stable for all inversion procedures, some of the declination from profile data inversion did deviate from the range given above. This indicates that inversion of profile magnetic data can not guarantee reliable estimates of magnetic directions. Significant changes with respect to the results obtained in 6.5 are only for the parameters of the diatreme. While the magnetization of the diatreme has decreased, its height has increased and reached values between 150 and 200 m, giving an average dip angle of 75°. The overall remanent magnetization and the Koenigsberger ratio, relative to the induced magnetization of the tuffs, are about 2.2 A/m and 4.5, respectively. The maar crater has a height of about 75 m, its walls dip at an angle between 50 and 65°.

As shown on Fig. 6.5, due to the homogeneous high magnetization, an improvement in the fit between the observed and the computed fields can only be noticed in the intensity but not in the shape. Especially in the central areas, there still is a misfit, which, obviously, is due to a physically and areally non-uniform distribution of the causative masses at and near the surface. The misfit at the boundaries is probably caused by still badly optimized directions of the magnetization and geometry of the structure.

Table 6.3a Results of the inversion of random observed data; model with 7 unknown parameters.

Parameter	Value	Unit
Average diameter of the top boundary of the maar (D_{tm})	443.0	m
Average diameter of the crater bottom (D_{bc})	330.0	m
Average height of the maar crater (H_c)	77.0	m
Average slope of the crater walls (α_c)	51.0	°
Average height of the diatreme (H_d)	185.0	m
Average diameter of the diatreme bottom (D_{bd})	230.0	m
Average slope of the diatreme walls (α_d)	75.0	°
X-comp. of the magnetization of the diatreme rocks (J_x)	0.92	A/m
Y-comp. of the magnetization of the diatreme rocks (J_y)	−0.008	A/m
Z-comp. of the magnetization of the diatreme rocks (J_z)	2.50	A/m
Total magnetization of the diatreme rocks	2.6	A/m
Inclination of the magnetization of the diatreme rocks	70.0	°
Declination of the magnetization of the diatreme rocks	−0.5	°
Computed apparent susceptibility of the diatreme rocks	0.070	SI
Remanent magnetization of the diatreme rocks	2.20	A/m
X-component of the NRM of the diatreme rocks	0.70	A/m
Y-component of the NRM of the diatreme rocks	0.002	A/m
Z-component of the NRM of the diatreme rocks	2.00	A/m
Inclination of the NRM of the diatreme rocks	71.0	°
Declination of the NRM of the diatreme rocks	0.2	°
Koenigsberger ratio for the diatreme rocks	4.5	–
Volume percentage of magnetite in diatreme rocks	2.0	%
Root mean square error (RMS)	180.0	nT
Normalized mean square error (MSE)	19.0	%

Table 6.3b Confidence intervals and resolutions of the estimates. Inversion of areally distributed data; model with 7 unknowns.

Parameter	LB	Estimate	UB	Resolution
J_x	0.80	0.90	1.00	0.90
J_y	− 0.09	− 0.08	0.07	0.98
J_z	2.40	2.50	2.70	0.95
D_{bc}	310.0	330.0	355.0	0.55
H_c	65.0	77.0	90.0	0.54
H_d	135.0	185.0	230.0	0.67
D_{bd}	150.0	230.0	310.0	0.55

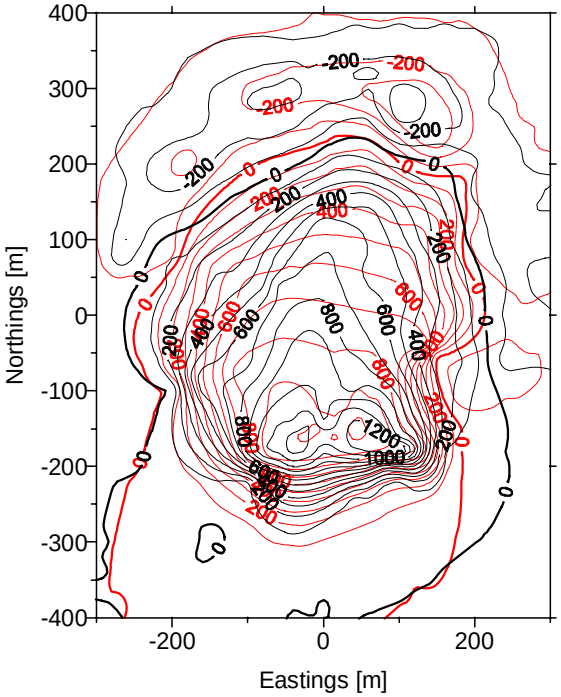

Fig. 6.4 Inversion of the magnetic field of the Schönfeld Maar; areally distributed data; model with 10 unknown parameters; black and red contours represent the observed and computed fields, respectively.

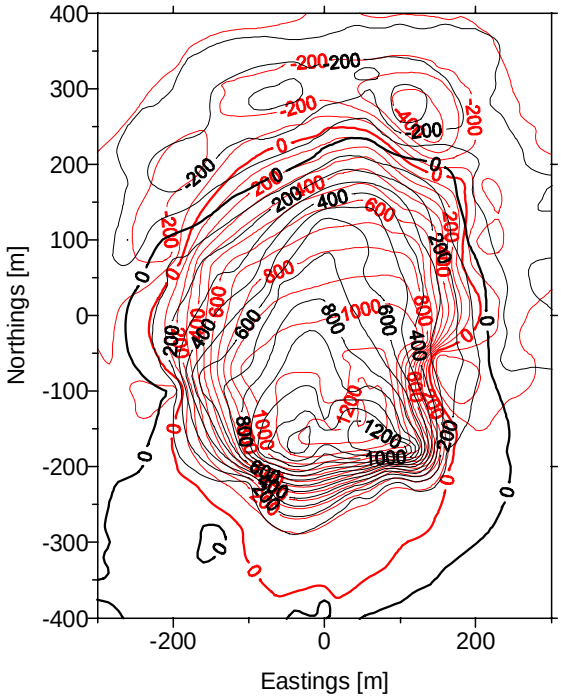

Fig. 6.5 Inversion of the magnetic field of the Schönfeld Maar; areally distributed data; model with 7 unknown parameters; black and red contours represent the observed and computed fields, respectively.

6.7 Inversion of areally distributed data; model with 5 unknown parameters

Taking into account the results of all the previous inversion procedures, the maar-diatreme structure has been assumed to be a deeply eroded maar. Considered as a whole, it then has been modeled as a diatreme, parameterizing only the magnetization, the height and the bottom diameter. The results are shown in Tables 6.4a and 6.4b.

The magnetization has been estimated to a value of 1.93 A/m with an inclination of 68° and a declination of 4°. The direction is in a very good agreement with the observed magnetic field. The elements of the remanent magnetization, calculated relative to the induced magnetization of the tuffs are 1.45 A/m, 69°, 7°, respectively the intensity, the inclination and the declination. This direction, which is nearly the same as that of the total magnetization, together with a Koenigsberger ratio amounting to 3.0 show that the NRM is the main contributing component to the anomaly. It is interesting to point out that the values of both the intensity of the NRM and the Koenigsberger ratio are very close to those defined by laboratory measurements (1.22 A/m and 2.9). The estimated effective susceptibility, in case of an induced magnetization alone, amounts to 50600×10^{-6} SI, which is four times higher than that of the tuffs of the Schönfeld Maar. The height and the bottom diameter of the diatreme have been estimated to 205 and 345 m, respectively; correspondingly, the diatreme walls have an average slope of 77°.

Although the results obtained by this model seem to be more or less satisfactory, there still exists a remarkable discrepancy between the computed and the observed field as can be seen on Fig. 6.6, showing the SN- and WE-profiles and the contour maps.

6.8 Inversion of areally distributed data; model with 3 unknown parameters

In order to verify the existing hypothesis about some of geometrical parameters of maar-diatreme volcanoes, among others the 1:1 ratio between the height and the surface diameter of the maar and the dip angle of about 80°of the diatreme walls, an inversion with only 3 unknowns has been carried out. The height and the diameter of the bottom of the diatreme have been assigned values of 400 and 350 m, respectively. Both values, giving a dip angle of 83°, have been kept constant. Only the magnetization (its 3 components) was parameterized. The estimated elements of the magnetization (J = 1.8 A/m, I = 69.6°, D = 4.1°) are similar to those given by the preceding inversion with 5 parameters in 6.7. But, as can be seen on Fig. 6.7, while the greater height has enhanced the fit in the size of the anomaly, it has worsened it in shape. The computed anomaly is wider than the observed one and its zero contourline diverges outwards in the southern areas, which indicates that the assumed value of the height (400 m) is too large.

These results together with those from the previous inversion in 6.7 again show that the mismatch in size and the misfit in shape are more noticeable in the central part of the maar structure. It is likely that the anomaly of the Schönfeld Maar is a result of superposed magnetic effects caused by two different features: the diatreme (main) and a narrower near-surface feature, both with relatively high magnetizations. While the magnetic effect of the near-surface feature adds to that of the diatreme, its geometry contributes to the stretching out of the shape of the anomaly in the central area.

Table 6.4a Inversion results of random observed data; model with 5 unknown parameters.

Parameter	Value	Unit
Average diameter of the top boundary of the maar (D_{tm})	443.0	m
Average height of the diatreme (H_d)	205.0	m
Average diameter of the bottom of the diatreme (D_{bd})	345.0	m
Average slope of the diatreme walls (α_d)	77.0	°
X-comp. of the magnetization of the diatreme rocks (J_x)	0.71	A/m
Y-comp. of the magnetization of the diatreme rocks (J_y)	0.05	A/m
Z-comp. of the magnetization of the diatreme rocks (J_z)	1.80	A/m
Total magnetization of the diatreme rocks	1.93	A/m
Inclination of the total magnetization of the diatreme rocks	68.0	°
Declination of the total magnetization of the diatreme rocks	4.0	°
Computed apparent susceptibility of the diatreme rocks	0.050	SI
Remanent magnetization of the diatreme rocks	1.45	A/m
X-component of the NRM of the diatreme rocks	0.52	A/m
Y-component of the NRM of the diatreme rocks	0.06	A/m
Z-component of the NRM of the diatreme rocks	1.35	A/m
Inclination of the NRM of the diatreme rocks	69.0	°
Declination of the NRM of the diatreme rocks	7.0	°
Koenigsberger ratio for the diatreme rocks	3.0	–
Volume percentage of magnetite in diatreme rocks	1.5	%
Root mean square error (RMS)	120	nT
Normalized mean square error (MSE)	8.5	%

Table 6.4b Confidence intervals and resolutions of the estimates from the inversion of areally distributed data with 5 unknowns.

Parameter	LB	Estimate	UB	Resolution
J_x	0.65	0.72	0.78	0.99
J_y	0.02	0.05	0.08	0.99
J_z	1.75	1.80	1.85	0.99
H_d	184.0	205.0	226.0	0.98
D_{bd}	316.0	346.0	375.0	0.55

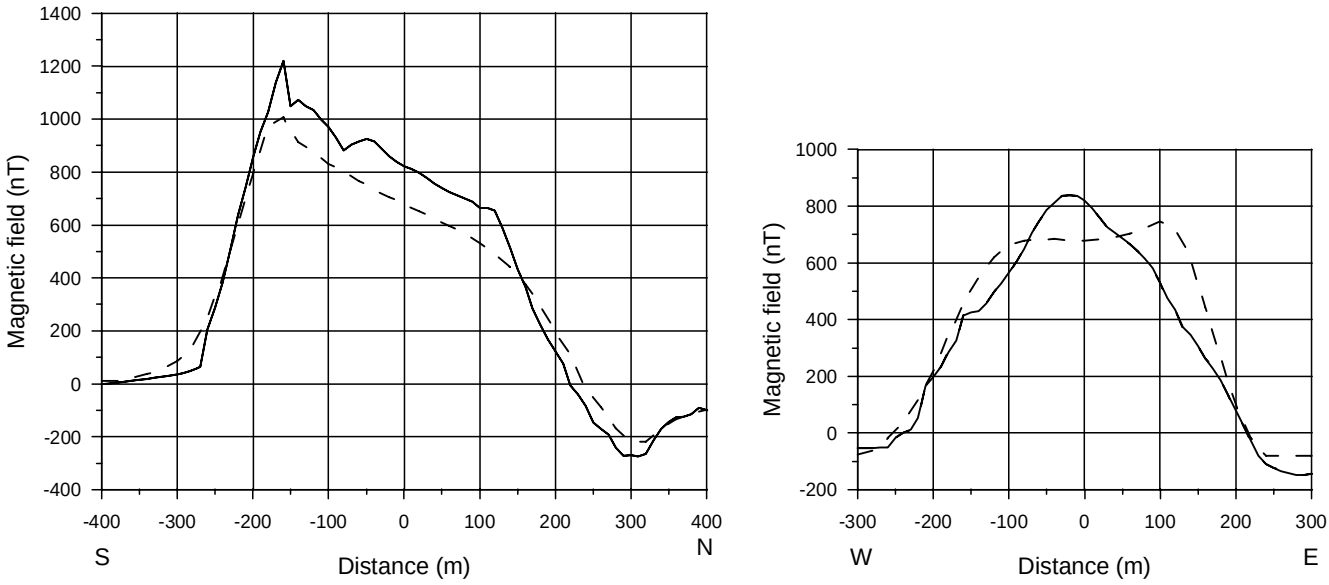

Fig. 6.6a SN- and WE-profiles of the magnetic anomaly of the Schönfeld Maar; solid lines : observed; dashed : computed. The profiles pass through the points (0,-400; 0,400) and (-300,0; 300,0), respectively (see figure below).

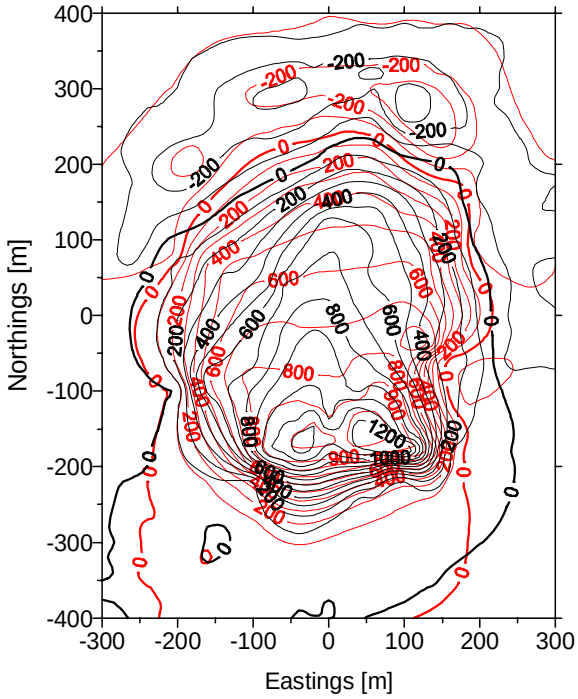

Fig. 6.6b Contour maps of the observed (black) and computed (red) magnetic fields of the Schönfeld Maar; the computed field results from the inversion of areally distributed data using a model with 5 unknown parameters.

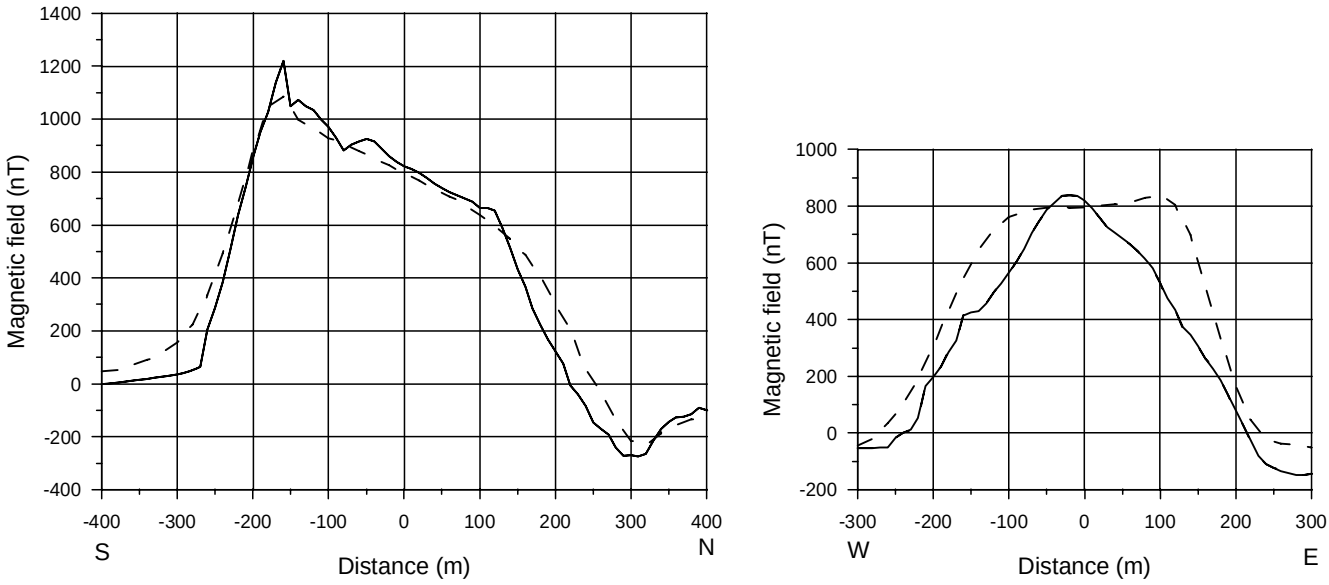

Fig. 6.7a SN- and WE-profiles of the magnetic anomaly of the Schönfeld Maar; solid lines : observed; dashed : computed. The location of the profiles is the same as in Fig. 6.6.

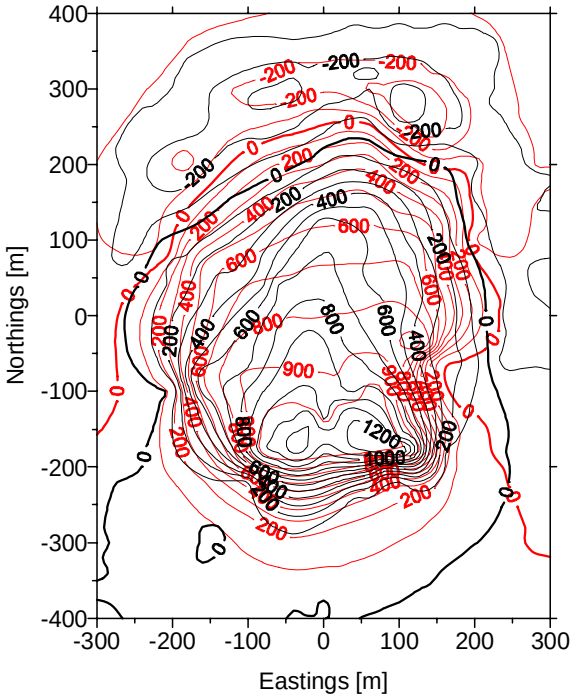

Fig. 6.7b Observed (black) and computed (red) magnetic fields of the Schönfeld Maar; the computed field results from the inversion of areally distributed data using a model with 3 unknown parameters (components of the magnetization).

6.9 Spectral analysis and data transformations

Although good and reasonable results were obtained by inversions with areally distributed data and fewer parameters, it is not yet clear whether the high observed anomaly is really caused by two superposed sources with different magnetizations/susceptibilities or only by one source, having a high magnetization/susceptibility. The nature of the magnetization itsself and its direction still have to be well investigated. Beside that, results from all previous inversions could be erroneous due to the following factors: the (near)-surface natural and man-made inhomogeneities which introduce a noise into the useful signal and are difficult to be considered while modeling, the uncertain position of the centre(s) of the polygonal laminae and eventual errors in digitized coordinates of data points. Moreover, it is well known that short wavelength elements especially are more sensitive to location errors, to aliasing, to sensor height etc.

In order to handle all these problems and to get complementary information which can be used to enhance the inversion and/or the interpretation of results, a spectral analysis and some transformations of the observed magnetic field have been done using Fourier techniques. Fourier techniques have been and are still being widely used in geophysical data analysis and interpretation (Odegard and Berg, 1965; Clarke, 1969; Ku et al., 1971; Spector and Parker, 1979). The use of the Fourier Transform requires data to be gridded. Therefore the data have been first gridded at a 10 m mesh before any operations could be undertaken. Such a small interval was chosen so that possibly useful near-surface signals would not be filtered out. As shown on Fig. 6.8, the energy spectrum of the field has two main components, the long and short wave components and a third one which is simply a pink noise.

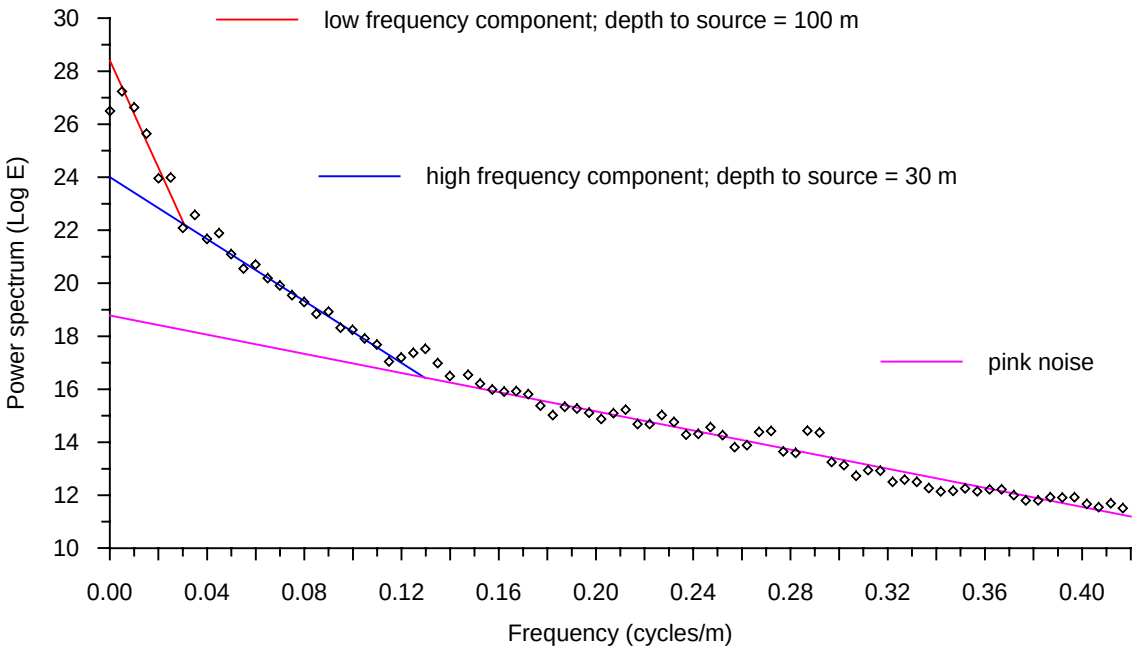

Fig. 6.8 Logarithmic power spectrum of the magnetic field of the Schönfeld Maar.

The interpretation of the power spectrum indicates that the high and low frequency sources are located at about 30 and 100 m depth, respectively. In terms of geology, the high frequency component would correspond to the rocks of the maar crater and the low frequency one, to the rocks of the underlying diatreme. These depths, of course, have to be considered with caution, because of the small dimensions (600×800 m) of the survey area. Interpretation made using the Fourier Transform might be highly unreliable, if the profile length is less than 8 times the depth of the source (Collins et al., 1974).

Using parameters of the power spectrum, matched filtering has been applied to the data in order to separate out the high frequency components. The low- and high-pass filtered fields are shown on Fig. 6.9. On Fig. 6.9b can be seen that the high frequency component consists of two zones: one in the South, which probably is the outcrop of the eroded maar rim, another in the central-northern part, where products of erosion (tuffs, clastic debris, scorias?), have accumulated. These two (near-) surface features cause the reinforcement and the elongation of the magnetic anomaly northwards.

The problems of the nature of the magnetization and the centre of the structure have been dealt with by means of the analytic signal of the magnetic field and the horizontal derivative of the pseudo-gravity as suggested by Roest, et al. (1993). The magnitude of the analytic signal of the field **F** is given by the expression:

$$|A(x,y)| = \sqrt{(\partial F/\partial x)^2 + (\partial F/\partial y)^2 + (\partial F/\partial z)^2} \tag{6.1}$$

where $\partial F/\partial x$, $\partial F/\partial y$, $\partial F/\partial z$ are first partial derivatives of the field. The derivatives have been calculated using the Fourier Transform. The use of the two functionals is based on their property to exhibit maxima over lateral contrasts in magnetization. Vertical or near-vertical contacts can be considered as 2-D or linear features. Roest et al. (1992b), Qin (1994) have shown that the magnitude of the analytic signal over such features is independent of the direction of the magnetization of the causative bodies. The shape of the analytic signal over 3-D bodies is also independent (Qin, 1994). Hence it can be used for the correlation of magnetic anomalies with the location of causative bodies. In this analysis, only the real part of the analytic signal, i.e. its horizontal derivative has been used.

Pseudo-gravity is the gravity field calculated from the magnetic field measurements using Poisson's theorem. To get pseudo-gravity using Fourier techniques, the magnetic field is first reduced to the pole and then convolved using the corresponding operator containing the factor $G\rho/J$. As can be seen in the expression (6.2), the operator of the reduction to the pole $W(r,\theta)$ is a function of the directions of both the ambient magnetic field and the total magnetization vector.

$$W(r,\theta) = \{[sinI_o + icosI_o cos(D_o - \theta)][sinI + icosI cos(D - \theta)]\}^{-1} \tag{6.2}$$

where r is the radial frequency, $r = 2\pi\sqrt{f_y^2 + f_x^2}$, f_x, f_y being the frequency in x- and y-direction, respectively (X-axis towards the North), θ is the azimuth, $\theta = tan^{-1}(f_y/f_x)$; I_o, D_o, I, D are the inclinations and declinations of the geomagnetic field and the magnetization vector, respectively. Since the pseudo-gravity is computed from the magnetic field reduced to the pole, it is then understandable why the behaviour and the magnitude of its horizontal derivative depend on the values of the declinations and of the inclinations used for the pole reduction. In case where a remanent magnetization is present, there is a shift

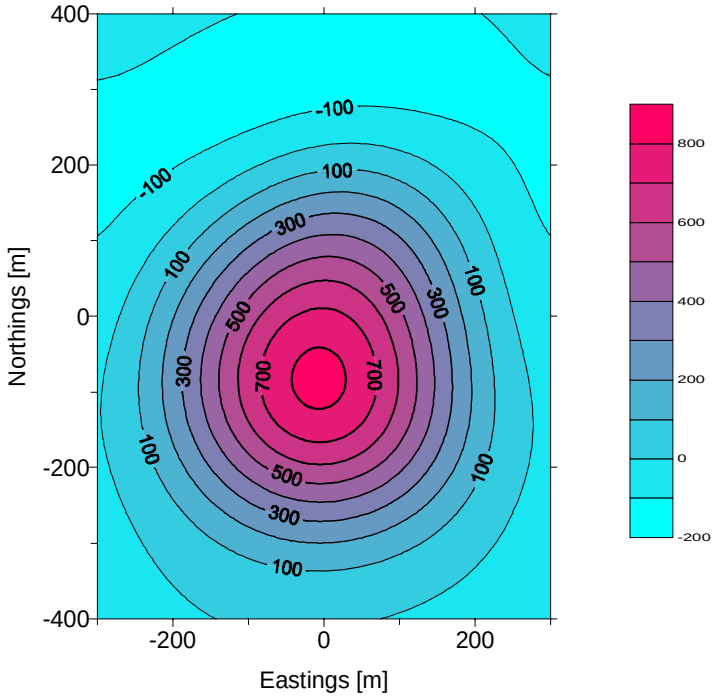

Fig. 6.9a Contour map of the low-frequency component of the magnetic anomaly of the Schönfeld Maar.

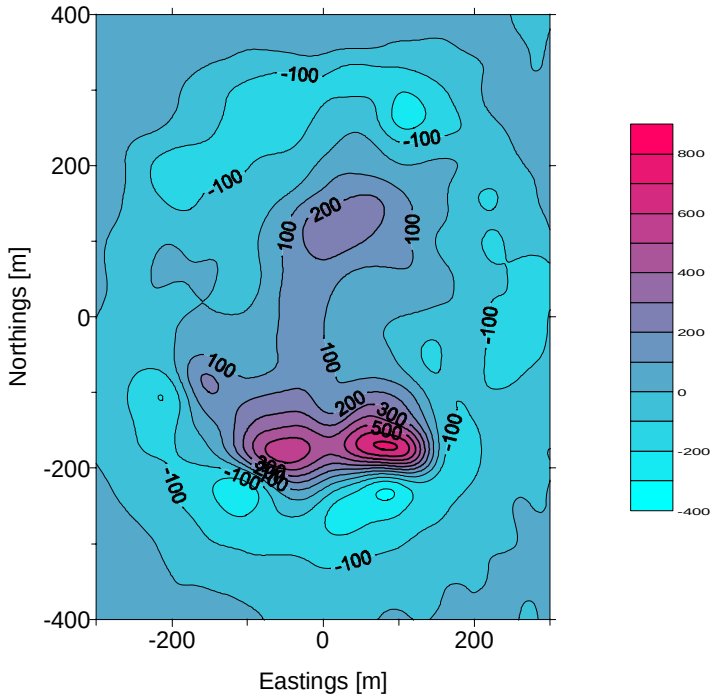

Fig. 6.9b Contour map of the high-frequency component of the magnetic anomaly of the Schönfeld Maar.

between the graphs of the analytic signal and those of the horizontal derivative of the pseudo-gravity. Looking at Figures 6.10a and 6.10b showing the graphs of the two functionals, we see that their respective extrema correlate well. This means that, either there is no significant remanent magnetization or, if any exists, it has a direction which is almost the same as that of the geomagnetic field. For the pole reduction of the magnetic field it has been assumed that both the total magnetization and the ambient geomagnetic field had the same direction (I = 66°; D = −3°). Pseudo-gravity has been computed using a magnetization of 0.48 A/m and a density contrast of −500 kg/m^3 — values based on measured physical properties of the tuffs of the Schönfeld Maar. The graphs on Figures 6.10a and 6.10b can also be used to determine the position of the centre of the structure; it corresponds to the minima of the functionals. The centre of the structure is supposed to nearly be at the point with the coordinates (−10,15) or (2536.19,5574.515) in Gauß-Krüger coordinates. The discrepancies in amplitudes of the SN-graphs are probably due to different dips of the crater walls, which are steeper in the South than in the North.

Further investigations have been conducted in order to determine the direction of the total magnetization vector. The method used is based on the distortion analysis of the magnetic field reduced to the pole as proposed by Fedi, et al. (1991). At the pole, magnetic anomalies have a broad area of highs (for a positive magnetization contrast) centred above the source and surrounded by a small area of lows. However, if reduction to the pole is done with incorrect values of the inclination and the declination, the transformed field is not really reduced to the pole but simply distorted. The distortion analysis consists in computing the pole reduced anomaly for different sets of inclinations and declinations of the total magnetization vector and studying the behaviour of the extrema of the field. From the so-called "distortion curves" for declination and inclination (Fig. 6.11), the actual value of the given direction can be approximated. This value corresponds to the abscissa for which peaks of the extrema of the curves (minima, maxima or their ratios) consistently correlate. After Fedi et al. (1991), minimum curves offer a better resolution of the peaks sought for. As can be deduced from Fig. 6.11, the actual value of the declination lies between 0 and 10° with clearly most of peaks concetrated around the value of 5°. Although the curves for the inclination less clearly show the best suitable value, one can see that most of peaks lie in the range between 64 and 70° with the highest amplitude at 66°. This result indicates that a relatively significant discrepancy between the directions of both the total magnetization vector and the geomagnetic field is only to be identified in the declinations. Though the discrepancy in declinations ($\approx 10°$) is not large, it nevertheless is an indication of the existence of a NRM component, which, together with the induced component, contributes to the total magnetization vector.

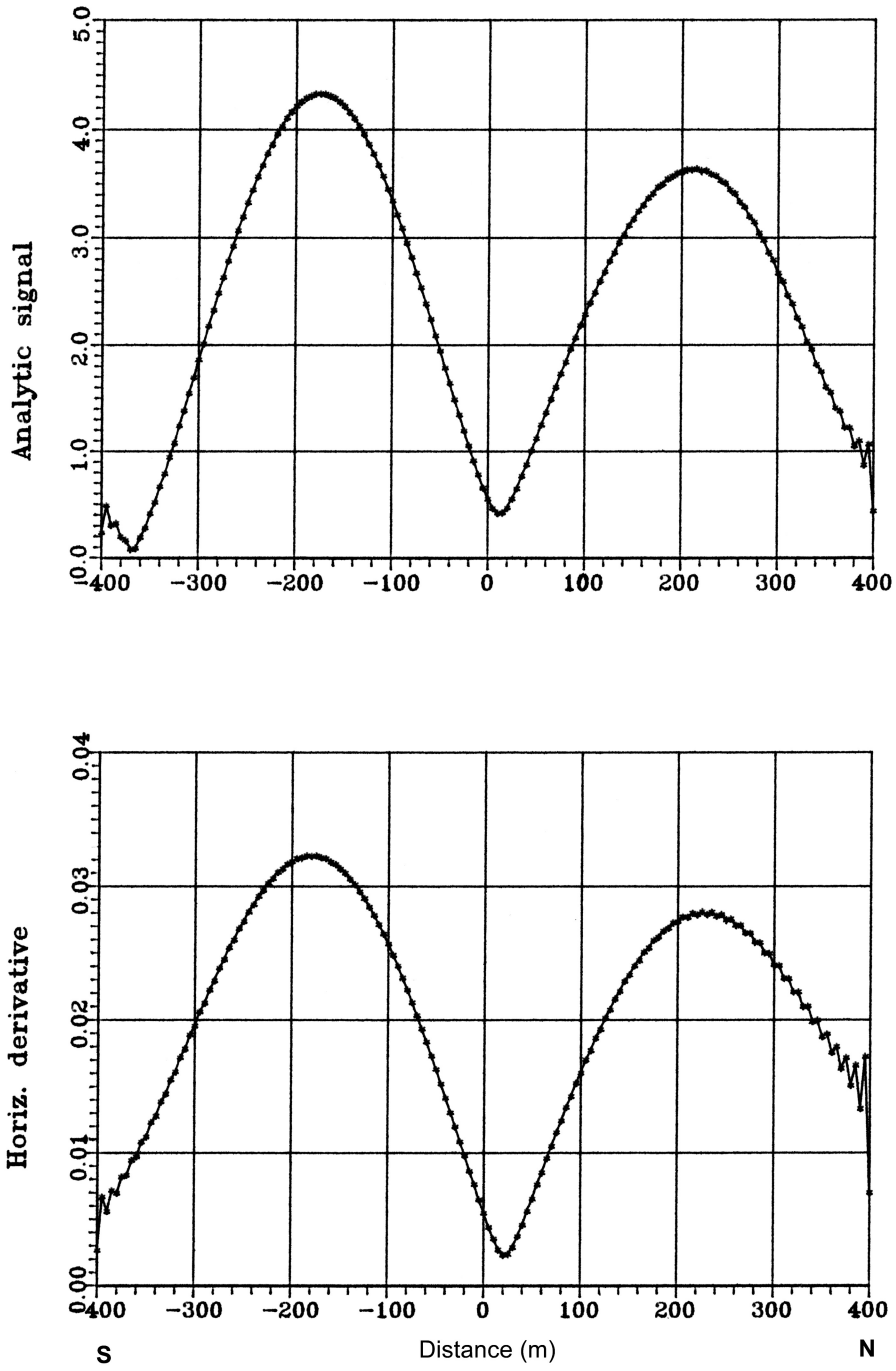

Fig. 6.10a Investigation of the nature of the magnetisation causing the magnetic anomaly of the Schönfeld Maar; SN-profiles: Analytic signal of the magnetic field (up) and horizontal derivative of pseudo-gravity (down).

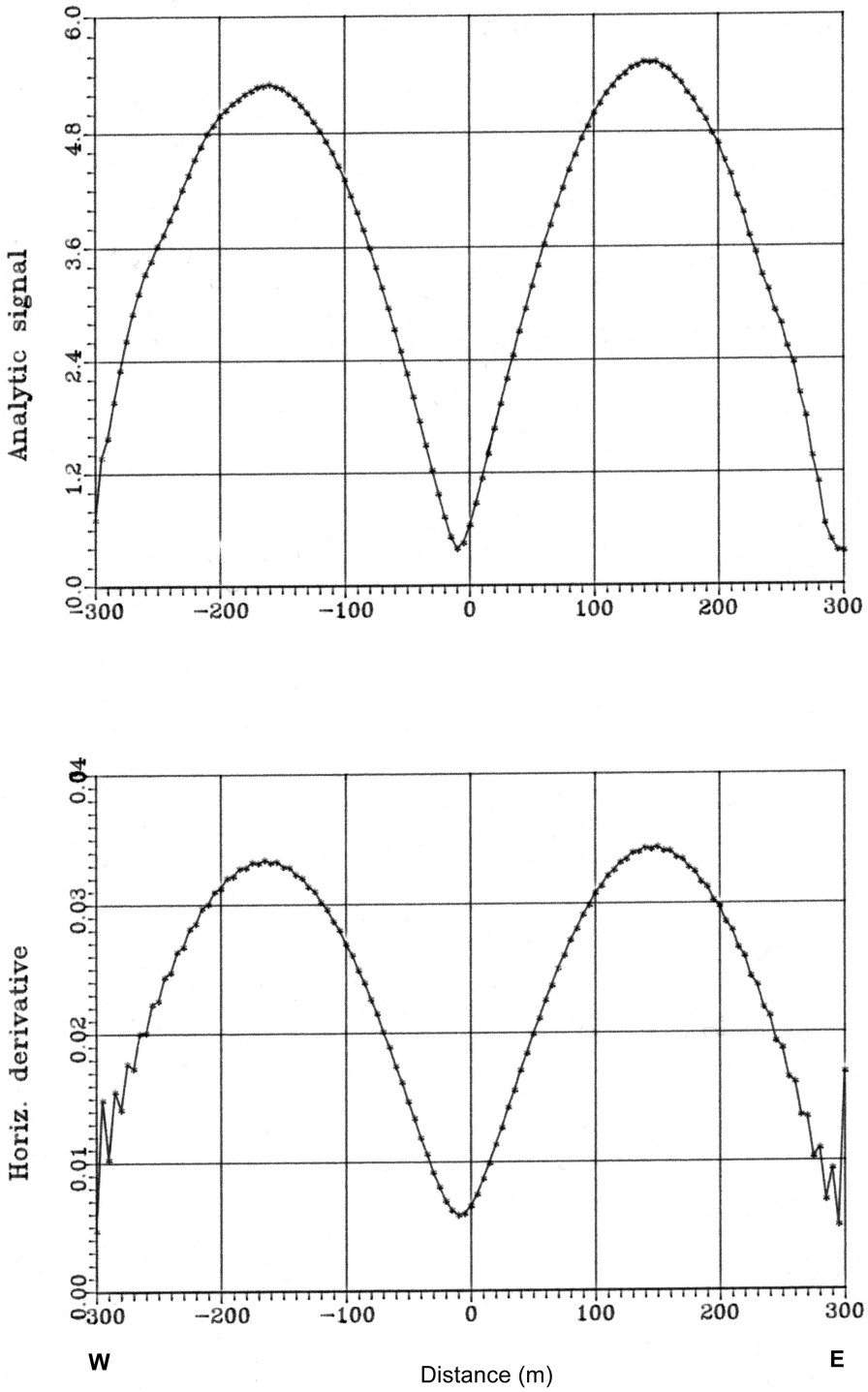

Fig. 6.10b Investigation of the nature of the magnetisation causing the magnetic anomaly of the Schönfeld Maar; WE-profiles: Analytic signal of the magnetic field (up) and horizontal derivative of pseudo-gravity (down).

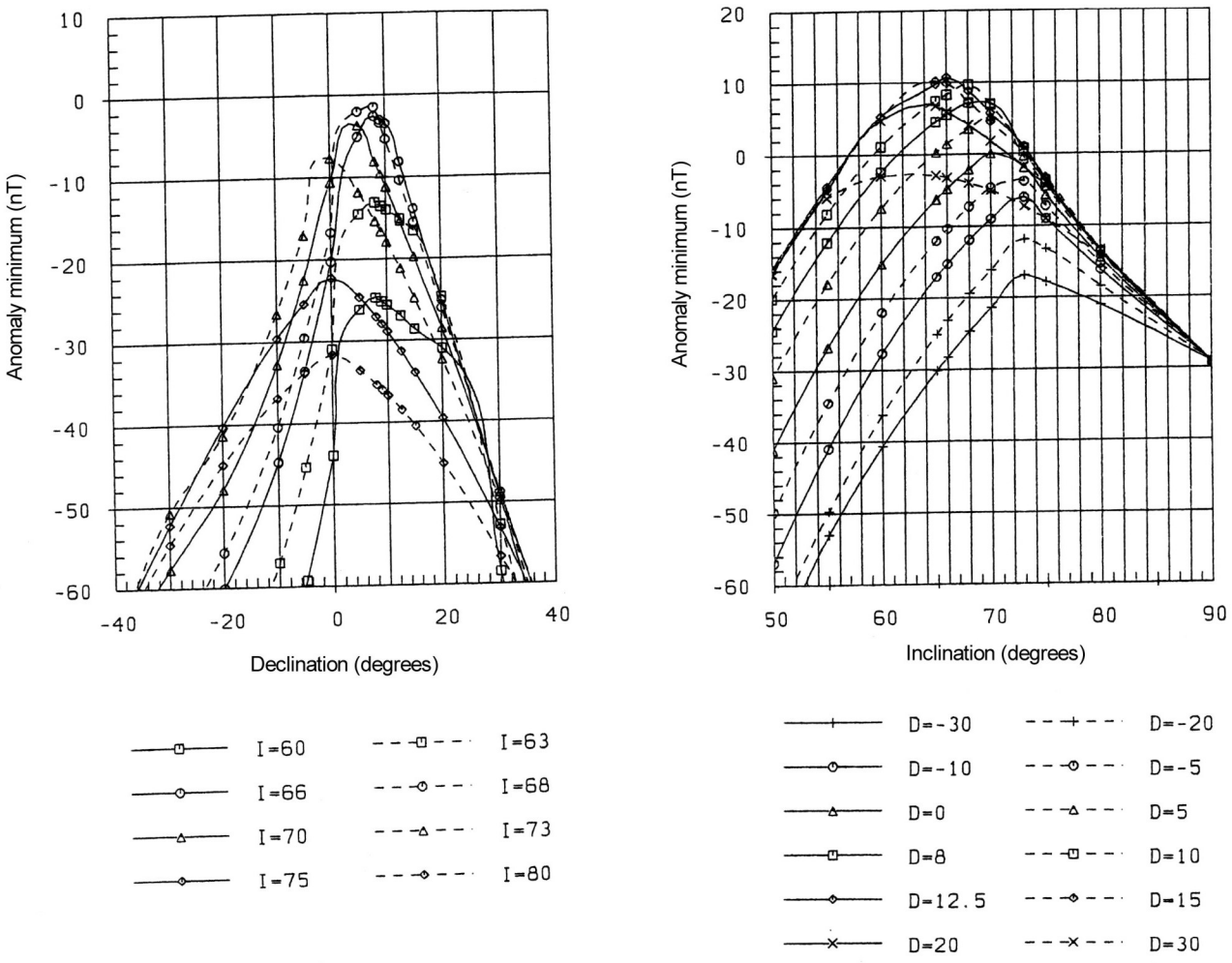

Fig. 6.11 Investigation of the direction of the magnetization causing the magnetic anomaly of the Schönfeld Maar; distorsion curves for the declination (left) and inclination (right).

Pseudo-gravity can give further information about the size of the magnetization. As can be seen on Fig. 6.12, the pseudo-gravity field has a size of about –10 mGal, value which is too high compared with the usually known gravity anomalies of maar diatreme structures. Gravity anomalies of some larger maar diatremes, such as the Döttingen and the Meerfeld Maars, have considerably smaller sizes of –3.5 (Stachel and Büchel, 1989) and –5.8 mGal (Henk, 1984), respectively. According to Smilde (1997), the size of the gravity anomaly of the Meerfeld Maar is even smaller and amounts to –4.5 mGal. Therefore a higher intensity of the magnetization should be required to produce a pseudo-gravity field which lies in an acceptable range. As can be seen on Fig. 5.7 (Chap. 5) showing the measured SN-gravity profile, the size of the gravity anomaly is about –2.5 mGal. This implies that a magnetization about four times the one used above for the pseudo-gravity transformation should be present in order to produce a gravity effect the size of which would match that of the observed field. Such a high intensity of the magnetization (2.0 A/m) might be due either to a high susceptibility ($50000*10^{-6}$ SI), in the case, where an induced magnetization alone is causative or to a resultant magnetization vector of both the induced and the remanent components.

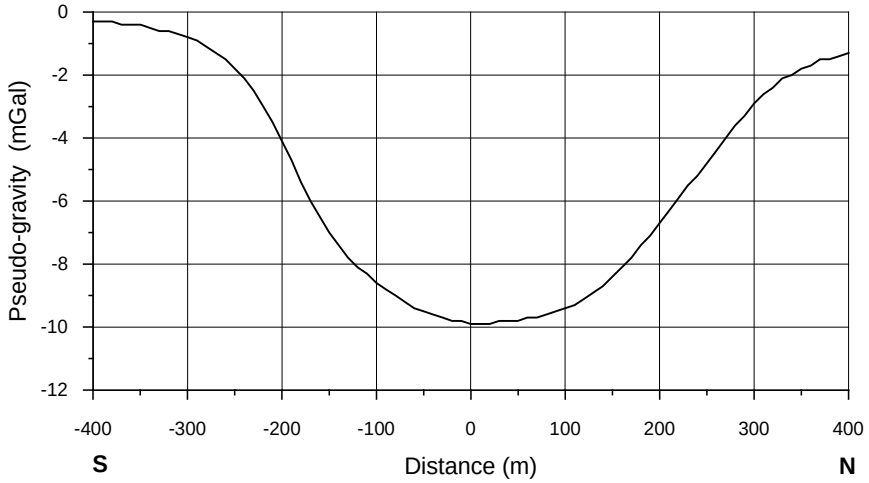

Fig. 6.12 SN-profile of pseudo-gravity of the Schönfeld Maar.

6.10 Inversion of low-pass filtered data

Having separated out the high frequency components thought of to correspond to (near-) surface features, a new attempt of inversion has been carried out using the low-pass filtered field (1271 points), considered to be the effect of the diatreme alone. The top polygonal boundary of the diatreme has been redefined using low-pass filter data. Its average diameter amounts to 430 m. Further, the model has been designed using the same approach as in the previous inversions. The diatreme was supposed to be located at 100 m depth as determined by the interpretation of the logarithmic power spectrum of the observed magnetic anomaly. Modeling has been done with five parameters : the components of the magnetization of the diatreme rocks, the height and the bottom diameter of the diatreme. The computed diatreme model has a height of 200 m, an average bottom diameter of 240 m, hence an average wall dip of 65°. The magnetization of 4.0 A/m — if it was only induced, would correspond to a high effective susceptibility of 0.10 SI, value which is extremely high for tuffs and even higher than the average susceptibility (0.06 SI) of basalts (Telford et al., 1990). The large estimate of the magnetization obviously is to compensate the weakening effect of the great location depth, which probably has been overestimated by the spectral analysis. Though the direction of the magnetization ($D = 1.2°$, $I = 67°$) does not much differ from those determined by some of previous inversion procedures conducted with fewer unknowns and by the distortion analysis, its intensity seems to be too high. Therefore other inversion procedures have been run with different starting model parameters, different number of model parameters and/or different damping factors to enable the choice of the one model with the most reliable results. Below will be given and discussed results of such a model (see Tables 6.5a and 6.5b).

Modeling was done assuming a variable depth to the top of the diatreme, which together with the cross-section of the diatreme bottom, the diatreme height and the components of the magnetization, were parameterized. The results of this inversion with 6 unknowns are presented in Tables 6.5a and 6.5b. The estimated diatreme is located at a shallower depth of 70 m, which consequently leads to a decrease of the magnetization. The latter has an intensity of 2.2 A/m and a direction of 66° (I), 2° (D). The computed susceptibility (0.06 SI) and the related volume percentage of magnetite (1.7%) are about 4–5 times those of the tuffs. This is an indication of a presence of a NRM, which with a Koenigsberger ratio of 3.6 amounts to 1.7 A/m and has the same direction as the total magnetization. The height of the diatreme has been estimated to about 243 m, while the average diameter of its bottom to nearly 290 m, giving an average dip of 72° for its walls. As shown on Fig. 6.13, a relatively good fit between the observed and the computed fields has been achieved. This is confirmed by the relatively small measures of the RMS (32 nT) and of the MSE (1.1%).

These results do not much differ from those of the inversion procedures in 6.6 with 7 parameters and in 6.7 with 5 parameters. Moreover, the magnetization and its direction also are in a good agreement with those derived from the distortion and pseudo-gravity analysis.

Table 6.5a Inversion results of low-pass filtered data; model with 6 unknown parameters.

Parameter	Value	Unit
Average location depth of the diatreme (H_c)	70.0	m
Average diameter of the top boundary of the diatreme (D_{td})	430.0	m
Average diameter of the bottom of the diatreme (D_{bd})	290.0	m
Average height of the diatreme (H_d)	243.0	m
Average slope of the diatreme walls (α_d)	72.0	°
X-comp. of the magnetization of the diatreme rocks (J_{xd})	0.91	A/m
Y-comp. of the magnetization of the diatreme rocks (J_{yd})	0.025	A/m
Z-comp. of the magnetization of the diatreme rocks (J_{zd})	2.03	A/m
Total magnetization of the diatreme rocks	2.20	A/m
Inclination of the total magnetization of the diatreme rocks	66.0	°
Declination of the total magnetization of the diatreme rocks	2.0	°
Computed apparent susceptibility of the diatreme rocks	0.06	SI
Remanent magnetization of the diatreme rocks	1.70	A/m
X-component of the NRM of the diatreme rocks	0.72	A/m
Y-component of the NRM of the diatreme rocks	0.035	A/m
Z-component of the NRM of the diatreme rocks	1.60	A/m
Inclination of the NRM of the diatreme rocks	66.0	°
Declination of the NRM of the diatreme rocks	3.0	°
Koenigsberger ratio for the diatreme rocks	3.6	–
Volume percentage of magnetite in diatreme rocks	1.7	%
Root mean square error (RMS)	32	nT
Normalized mean square error (MSE)	1.1	%

Table 6.5b Confidence intervals and resolutions of the estimates from the inversion of low-pass filtered data with 6 unknowns.

Parameter	LB	Estimate	UB	Resolution
H_c	65.0	70.0	75.0	0.85
J_{xd}	0.85	0.91	0.95	0.99
J_{yd}	0.01	0.025	0.04	0.99
J_{zd}	1.90	2.03	2.15	0.96
H_d	230.0	243.0	260.0	0.75
D_{bd}	275.0	290.0	315.0	0.75
α_d	65.0	72.0	76.0	

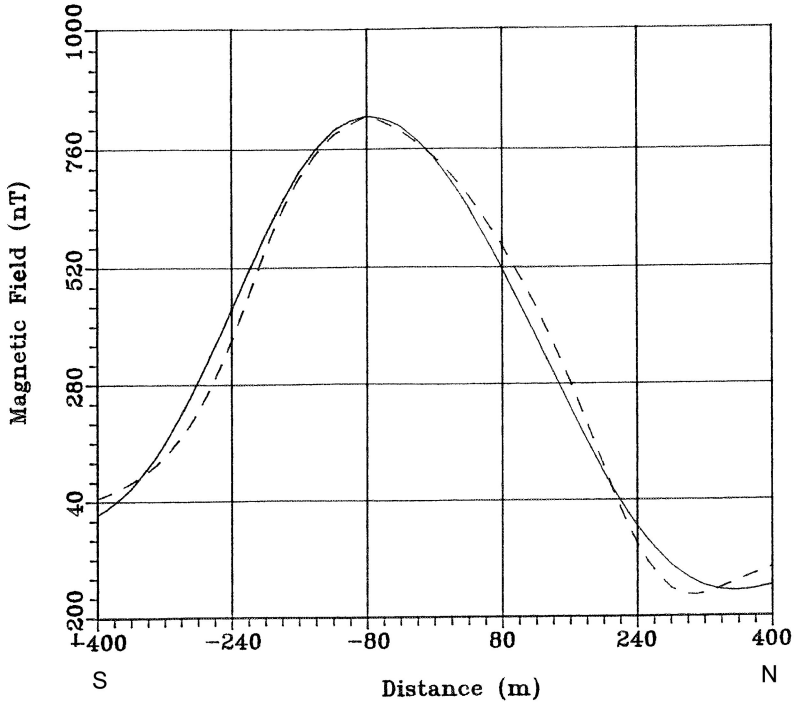

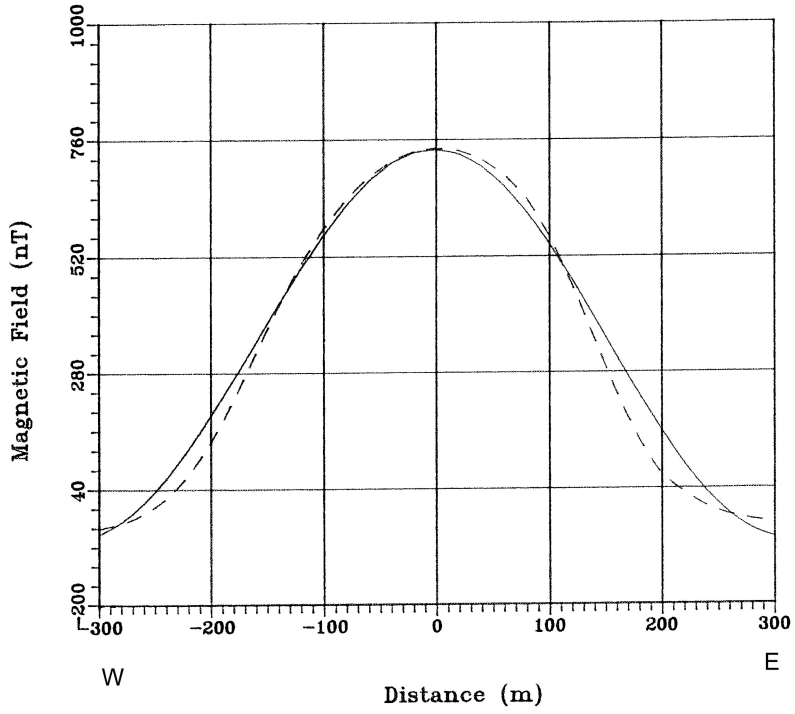

Fig. 6.13 Magnetic profiles of the Schönfeld Maar; solid lines: observed; dashed: computed. Inversion of low-pass filtered data; model with 6 unknowns.

6.11 Synthesis and interpretation of results

Analyzing the results of all inversion procedures conducted with different data sets and models and taking into account the results of theoretical modeling which have been discussed in Chap. 4 and those of the spectral analysis, the following conclusions can be drawn:

It is more likely that the relatively high magnetic anomaly of the Schönfeld Maar is caused by a source, having a relatively high magnetization of about 2.0 A/m. If the magnetization were supposed to be only induced, it would correspond to a high susceptibility of nearly 50000×10^{-6} SI, which is four times that measured susceptibility of the tuffs. The high magnetization, which can not be related to the induced component alone if the maar diatreme was supposed to be only made up of tuffs, is probably due to a strong total magnetization vector resulting from both induced and remanent components, whereas the NRM ($\approx$ 1.5 A/m) is prevailing. The Koenigsberger ratio Q amounts to a value around 3.5. The direction of the total magnetization vector ($I \approx 68°$, $D \approx 5°$) does not much differ from that of the ambient geomagnetic field ($I = 66°$, $D = -3°$). However, the discrepancy in declinations indicates that the geomagnetic pole has moved from the NNE to the NNW by about 10°.

The high magnetization might be explained by the fact that young effusive rocks, mainly mafic volcanics, and rocks of pyroclastic facies and of extrusive bodies as well, exhibit a strong magnetization with a Koenigsberger ratio Q varying between 1 and 20, generally due to the NRM component (Palmer and Carmichael, 1973; Dortman and Ishchanyan, 1992). Actually, eruptive rocks of the West Eifel are mainly represented by basanites and olivine nephelinites, rocks which are very mafic with a high content of Cr-, Ni-, Co-, Ti- and Fe-oxides (Schmincke et al., 1983). The high NRM might be caused by a thermoremanent magnetization (TRM) resulting from a quick cooling process.

Another explanation of such a high magnetization could be related to contributions of different magnetic sources having different susceptibilities and magnetizations. In this case, I suppose that one or more later eruptions took place and produced rocks with a higher magmatic fraction (probably mafic). These rocks, which have a higher susceptibility/magnetization than the former diatreme tuffs, overlay the latter. Indeed, some scorias have been observed at the NE boundary of the Schönfeld Maar. Since some of these scorias sampled at the surface — supposed to be weathered — have susceptibilities of about 30000×10^{-6} SI, corresponding to an induced magnetization of 1.2 A/m, those lying deeper would have a higher susceptibiltity/magnetization. It is not excluded that such scorias lie within the maar crater overlaying the diatreme tuffs. This would mean that the late eruption(s) took place with a smaller amount of interacting surface and/or groundwater or without it at all, hence leading to the formation of rocks with a predominantly magmatic fraction and a higher content of ferrimagnetic minerals. The presence of scorias and the shape of the anomaly indicate that a scoria cone might be located within the maar crater, with an offset northwards from the centre of the maar-diatreme structure. But taking into account that the Schönfeld Maar is one of the oldest maars (0.6–0.7 Ma) of the Westeifel volcanic field, the scoria cone probably has been strongly eroded. Alternatively, the scoria cone might have been destroyed by a later eruption of a reactivated phreatomagmatic process which led to its breakdown. In either case, the debris from the scoria cone should

have mixed with the rocks (lake sediments, tuffs, clastic debris) filling the upper part of the maar-diatreme, thus also contributing to the relatively high susceptibilities of the rocks of the maar crater. As determined by laboratory measurements, susceptibilities of rocks sampled in the maar crater up to 6 m depth are of the same order as those of the tuffs.

As shown by the results of the spectral analysis and of the inversion, a 70 to 100 m thick crater fill overlays a diatreme of 200 to 250 m height. The maar-diatreme structure has a height of about 300–350 m, which is smaller than the average diameter (450 m) of the top boundary and, as supported by results of theoretical modeling, is in a good agreement with the observed anomaly. While the dip angle of the crater walls averages to about 50°, that of the diatreme walls varies between 70 and 80°.

On Figure 6.14 is shown a vertical cross-section of the geologic-geophysical model of the Schönfeld Maar, as derived from the results of the inversion and of the spectral analysis. The related parameters, as well those known as those estimated and derived, are given in Table 6.6.

Table 6.6 Parameters of the model of the Schönfeld Maar.

Name	Rock type	Thickness/ height [m]	Density ρ $[g/cm^3]$	Magnetization J [A/m]	Dip angle of walls [°]
maar crater upper part	lake sediments mixed with tuffs, devonian clasts	≤ 30	1.95–2.15	0.4–0.5	45–55
maar crater lower part	lake sediments mixed with tuffs, devonian clasts and scorias	40–70	2.10–2.20	0.6–1.0	45–55
scoria cone	scorias	40–70	1.90–2.65	1.5–2.0	
diatreme	tuffs	200–250	2.0–2.3	2.0–2.5	70–80

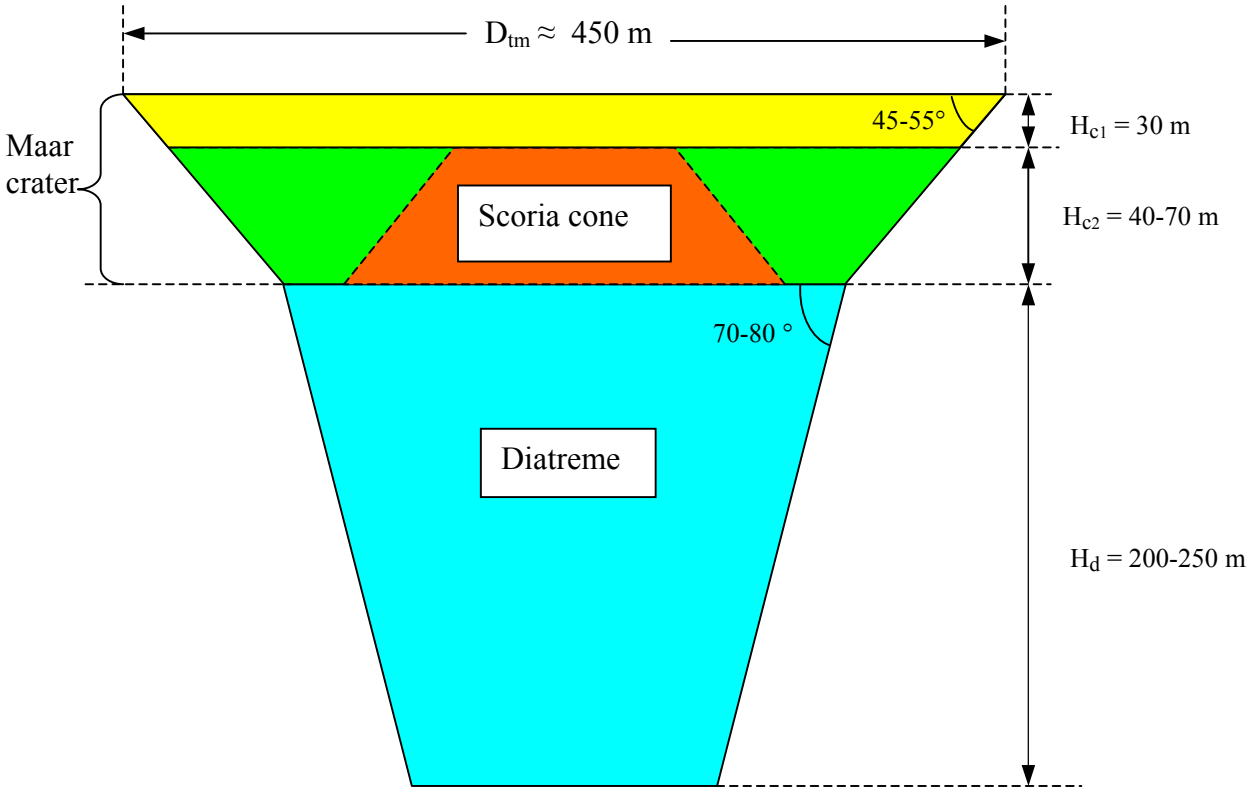

Fig. 6.14 Vertical cross-section of the model of the Schönfeld Maar, derived from the results of the inversion and of the spectral analysis.

Crater sediments: clay, sand, silt mixed with tuffs and debris of devonian rocks; J = 0.4−0.5 A/m.

Crater sediments: clay, sand, silt mixed with tuffs, debris of devonian rocks and scorias; J = 0.5−1.0 A/m.

Scorias; J = 1.5−2.0 A/m.

Tuffs; J = 2.0−2.5A/m.

7. Inversion of gravity and magnetic data of the Hausten-Morswiesen Maar

7.1 The Hausten-Morswiesen Maar, its gravity and magnetic fields

The Hausten-Morswiesen Maar belongs to the Quaternary East Eifel volcanic field. It is located in a valley between the villages Hausten in the Northwest and Morswiesen in the Southeast (Fig. 7.1). Its diameter, approximated from the surface boundary defined by the first vertical derivative of the gravity field, amounts to 1250 and 850 m, respectively in NNW- and SW-direction. These values diverge from those of 1500 and 1200 m given by Büchel (1991). The gravity and magnetic anomalies of the Hausten-Morswiesen Maar and its vicinity, measured by Büchel (1991), are presented on Fig. 7.2a and 7.2b. Beside the main gravity anomaly, there are two other small anomalies ─ one in the Northeast and another in the Southeast by the village Morswiesen. It is not known whether the causative structures of these small anomalies are also maars or not. The main gravity anomaly is somewhat distorted ─ elongated ─ at both the southeastern and north-north-western boundaries. The character of the magnetic anomaly with a maximum in the area close to the southern boundary is an indicattion for a relatively shallow source (s). Moreover, the magnetic anomaly is very disturbed, probably due to effects of small near-surface sources located within the maar and/or at its boundary.

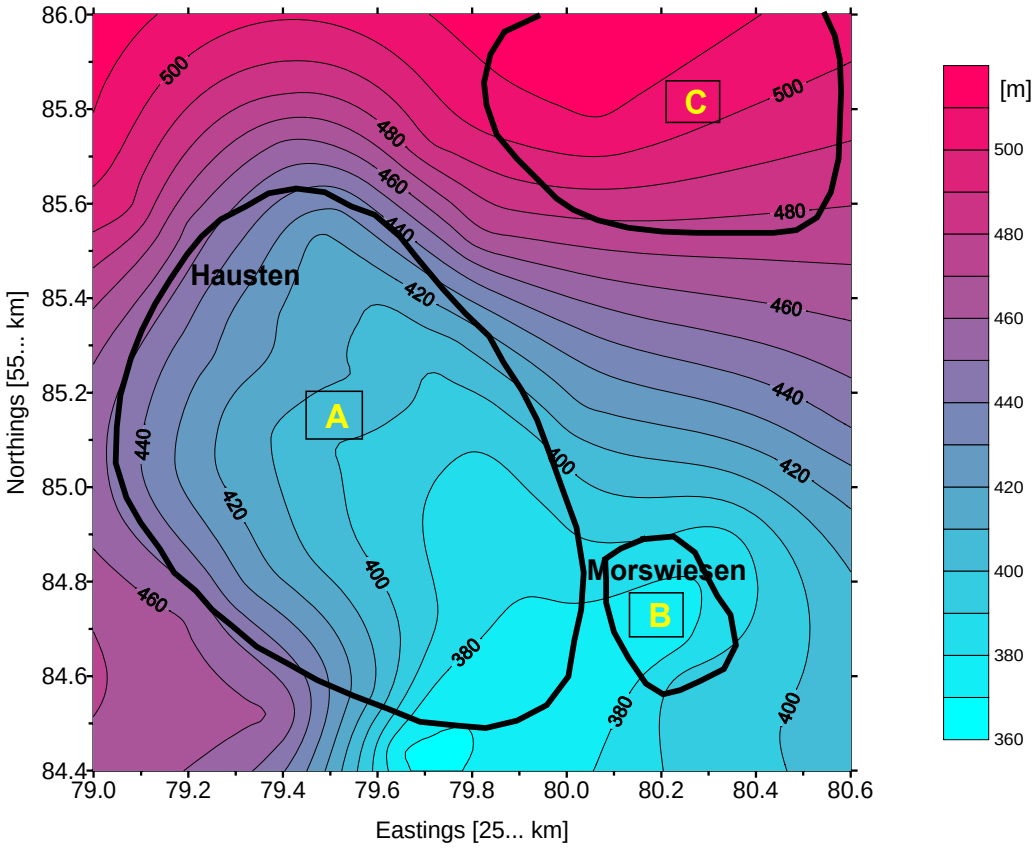

Fig. 7.1 Topography of the area of the Hausten-Morswiesen Maar; the thick lines ─ the zero contour of the first vertical derivative of the gravity field ─ approximately show the surface boundaries of the maar (A) and two other structures B and C.

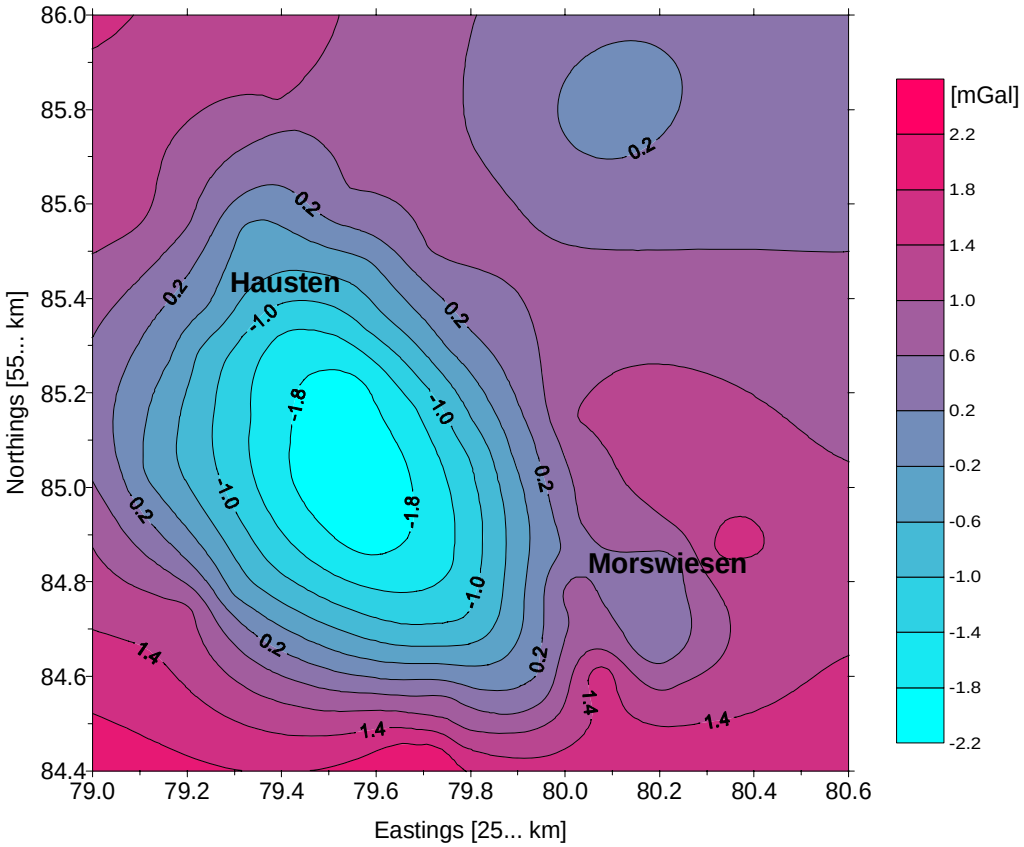

Fig. 7.2a Observed gravity anomaly of the Hausten-Morswiesen Maar.

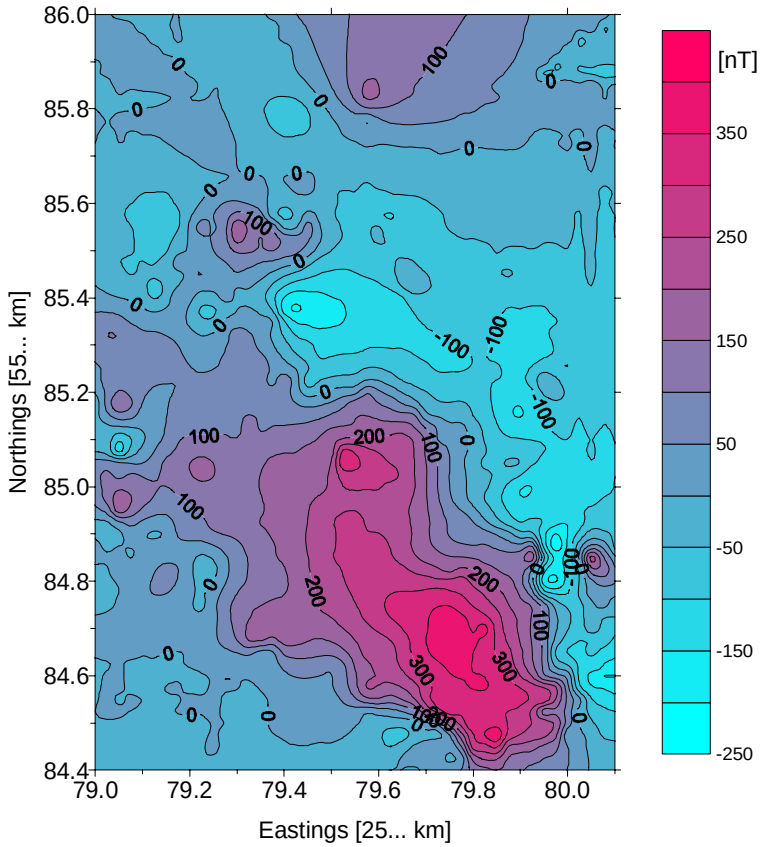

Fig. 7.2b Observed magnetic anomaly of the Hausten-Morswiesen Maar.

7.2 Inversion of observed gravity data

For the inversion of gravity data, only the main anomaly has been considered; the observations lying within the areas of the small anomalies in the Southeast and in the Northeast have been omitted. Before proceeding to inversion, the data have been first reduced to the zero level after a removal of a regional trend which decreases in the SW-NE direction. The philosophy of model designing and handling is the same as in the previous chapter. For computations, the point with the Gauß-Krüger coordinates (2579540.0,5585000.0) — approximately corresponding to the observed gravity minimum — has been chosen as origin. For the derivation of densities from the estimates, a density value of 2.65 g/cm^3, which was used by Büchel for data reduction, will serve as a reference throughout.

For the modeling of the Hausten-Morswiesen Maar, beside the known top boundary of the maar with an average diameter D_{tm}, the model was defined by the following unknown parameters: $\Delta\rho_c$ and $\Delta\rho_d$, the respective density contrast of the crater and the diatreme rocks, h_c and h_d, respectively, the height of the crater and the diatreme; the polygonal contour of the crater bottom was obtained by multiplying the radii of the top boundary by a factor — the fifth unknown parameter. Similarly, the radii of the bottom contour of the diatreme were obtained by multiplying the respective bottom radii of the crater by another factor (sixth unknown parameter), which has been so chosen to approximately meet the assumption of a quasi vertical diatreme in depth. Several inversion procedures have been conducted using different starting models. Among the estimated models only five cases have been considered. The results are presented in Tables 7.1a, 7.1b till 7.5, and discussed below. Instead of the multplication factors, the dip angles of the crater and diatreme walls (α_c, α_d), indirectly related, are displayed in the tables. The bottom diameter of the diatreme (D_{bd}) has also been derived.

In model A (Tab. 7.1a, 7.1b), the respective estimates are 100 and 930 m for the crater and diatreme heights, 1.97 and 2.08 g/cm^3 for the densities of the crater and diatreme rocks, 24 and 80° for the dip angles of the crater (α_c) and diatreme (α_d) walls. Compared to the estimates of model A, the dip angle of the crater walls (31°) and the diatreme height (1050 m) of model B (Tab. 7.2) are larger, the dip angle of the diatreme walls is the same. As effect, the crater height (91 m) and the density contrasts of the maar-diatreme rocks are smaller. Accordingly, the densities of the crater and diatreme rocks are larger; they respectively amount to 2.07 and 2.18 g/cm^3. The diatreme of model C (Tab. 7.3), with a dip angle of 85.5°, is steeper than that of the two previous models. The extent of the crater is larger too. The height of the crater and the dip angle of its walls are 115 m and 36°, respectively. Consequently, the height of the diatreme (830 m) and the density contrasts of the maar-diatreme rocks are smaller. Correspondingly, the crater and diatreme rocks have large densities of 2.25 g/cm^3 and 2.34 g/cm^3, respectively. Model D (Tab. 7.4) differs from the previous ones mainly by a larger extent of the crater. The height of the latter and the dip angle of its walls are respectively about 180 m and 44°. Compared to model C the density of the crater rocks (2.24 g/cm^3) and the height of the diatreme (880 m) do not much differ. The density of the diatreme rocks (2.14 g/cm^3) and the dip angle of the diatreme walls (79°) are similar to those of model B.

As can be seen on Fig. 7.3(a), the fit between the computed and observed data is better for models B, C, and D than for model A. This is due to a larger dip angle of

the crater walls on the one side and to smaller density contrasts, respectively to larger densities of the maar-diatreme rocks on the other. In the southern areas the fit is better for model B than for the other models; and reversely in the northern areas. This indicates that the dip angle of the crater walls is not constant. This asymmetry of the maar crater has been further confirmed by results of diverse computed models which are not discussed here. The crater walls are steeper in the northern areas than in the southern areas. The behaviour of the curve of model D is somewhat different from that of the other curves, especially in the southern areas. This might also be an indication of the asymmetry of the diatreme. It seems that the dip angle of the diatreme walls has been a bit underestimated in the southern areas and slightly overestimated in the northern areas. This means that the diatreme is steeper in the southern areas than in the northern areas. Note that none of the models achieves a satisfying fit in the W-E-profiles (Fig. 7.3(b)). Hence, the strong misfit can not only be explained by the geometric irregularities of the maar-diatreme.

As described by Pirrung (1997) using borehole data (Hausten, VB1, 1990, Fig. 7.4), the crater sediments of the Hausten-Morswiesen Maar are represented by clays, silts, sands and gravels. These rocks — if wet — have densities varying between 1.93 and 2.21 g/cm^3 (Telford et al., 1990). The densities of the tuffs of the Eifel maars are in the range of 1.8–2.3 g/cm^3. Thus, model B can be thought of being more plausible since most of its estimates match the expected/known parameters. But the crater height of about 100 m seems to be too small for such a maar with an average surface diameter of 1000 m. Theoretically, an estimate of about 200 m should be expected. For a comparison and a verification of the reliability of the estimates, other inversion procedures have been conducted using the same model concept but keeping the height of the crater — set to 200 m — constant. The results of one of the computed models are presented in Tab. 7.5. The parameter estimates do not much differ from those of model C, except the height of the crater which is larger. As can be seen on Fig. 7.3(a), the computed curve (E) almost coincides with that of model B. But here also, the asymmetry of the crater can be noticed. In the southern areas, the dip angle of the crater walls should be a bit smaller than the estimated value of 38° and in the northern areas — somewhat larger. It is thought of to have respective values of about 35 and 40°. Though model E fairly fits the observations too, the estimated densities of the crater (2.25 g/cm^3) and diatreme (2.36 g/cm^3) rocks are relatively too large and lie out of the known range. Therefore, model B is considered to be more reliable. Considering that the density of the crater sediments might be a little bit higher due to the content of juvenile components, Model D could be an alternative.

Judging all the results above, the following can be drawn about the geometry and the density properties of the Hausten-Morswiesen Maar. Concerning the crater height, it is not yet clear whether its estimate of about 100 m really corresponds to the depth to the crater floor or simply to a change in lithology and/or in physical properties of the crater rocks. In case of a shallow crater ($\approx$ 100 m), the dip angle of the crater walls should be around 30°; for a crater of a relatively larger height, α_c should lie in the range of 35–50°. The height of the diatreme and the dip angle of its walls should respectively be in the range of (1000 ± 200) m and $(80 \pm 10)°$. As to the densities of the crater and diatreme rocks, they should respectively amount to (2.10 ± 0.15) g/cm^3 and (2.20 ± 0.10) g/cm^3.

Table 7.1a Results of inverse modeling of random gravity observations; model with 6 unknown parameters; *model A.*

Parameter	Value	Unit
Average diameter of the top boundary of the maar (D_{tm})	1020.0	m
Average diameter of the crater bottom (D_{bc})	563.0	m
Average height of the maar crater (H_c)	101.0	m
Average slope of the crater walls (α_c)	24.0	$^\circ$
Average height of the diatreme (H_d)	928.0	m
Average diameter of the diatreme bottom (D_{bd})	225.0	m
Average slope of the diatreme walls (α_d)	79.7	$^\circ$
Average density of crater rocks (sediments) ρ_c	1.9689	g/cm^3
Average density of diatreme rocks (tuffs) ρ_d	2.0787	g/cm^3
Root mean square error (RMS)	0.340	g/cm^3
Normalized mean square error (MSE)	3.045	%

Table 7.1b Confidence intervals and resolutions of the estimates; model with 6 unknown parameters; *model A.*

Parameter	LB	Estimate	UB	Resolution
ρ_c	1.9135	1.9689	2.0243	0.76
ρ_d	1.8680	2.0787	2.2895	0.76
H_c	92.0	101.3	110.0	0.93
H_d	643.0	928.0	1210.0	0.95
α_c	21.0	24.0	28.0	0.88
α_d	75.0	80.0	82.4	0.87
D_{bd}	210.0	225.0	235.0	

Table 7.2 Confidence intervals and resolutions of the estimates; model with 6 unknown parameters; *model B.*

Parameter	LB	Estimate	UB	Resolution
ρ_c	2.0270	2.0765	2.1260	0.72
ρ_d	2.0750	2.1830	2.300	0.74
H_c	84.0	94.5	105.0	0.84
H_d	796.0	1042.0	1290.0	0.90
α_c	27.0	30.7	35.3	0.85
α_d	76.5	79.9	82.1	0.86
D_{bd}	316.0	330.0	339.0	

Table 7.3 Confidence intervals and resolutions of the estimates; model with 6 unknown parameters; *model C.*

Parameter	LB	Estimate	UB	Resolution
ρ_c	2.230	2.256	2.283	0.66
ρ_d	2.280	2.340	2.400	0.72
H_c	93.0	115.0	136.0	0.72
H_d	660.0	830.0	1000.0	0.96
α_c	28.0	36.4	44.5	0.65
α_d	84.0	85.4	86.4	0.65
D_{bd}	531.0	540.0	546.0	

Table 7.4 Confidence intervals and resolutions of the estimates; model with 6 unknown parameters; *model D.*

Parameter	LB	Estimate	UB	Resolution
ρ_c	2.20	2.2443	2.288	0.60
ρ_d	1.88	2.140	2.400	0.50
H_c	161.0	187.0	213.0	0.80
H_d	515.0	883.0	1250.0	0.78
α_c	36.0	45.0	51.0	0.55
α_d	70.0	78.8	82.5	0.55
D_{bd}	257.0	290.0	304.0	

Table 7.5 Confidence intervals and resolutions of the estimates; model with 5 unknown parameters; constant h_c = 200 m; *model E.*

Parameter	LB	Estimate	UB	Resolution
ρ_c	2.235	2.249	2.263	0.65
ρ_d	2.256	2.357	2.458	0.62
H_d	690.0	1040.0	1390.0	0.97
α_c	34.0	36.0	39.0	0.80
α_d	86.0	87.4	88.0	
D_{bd}	374.0	380.0	383.0	

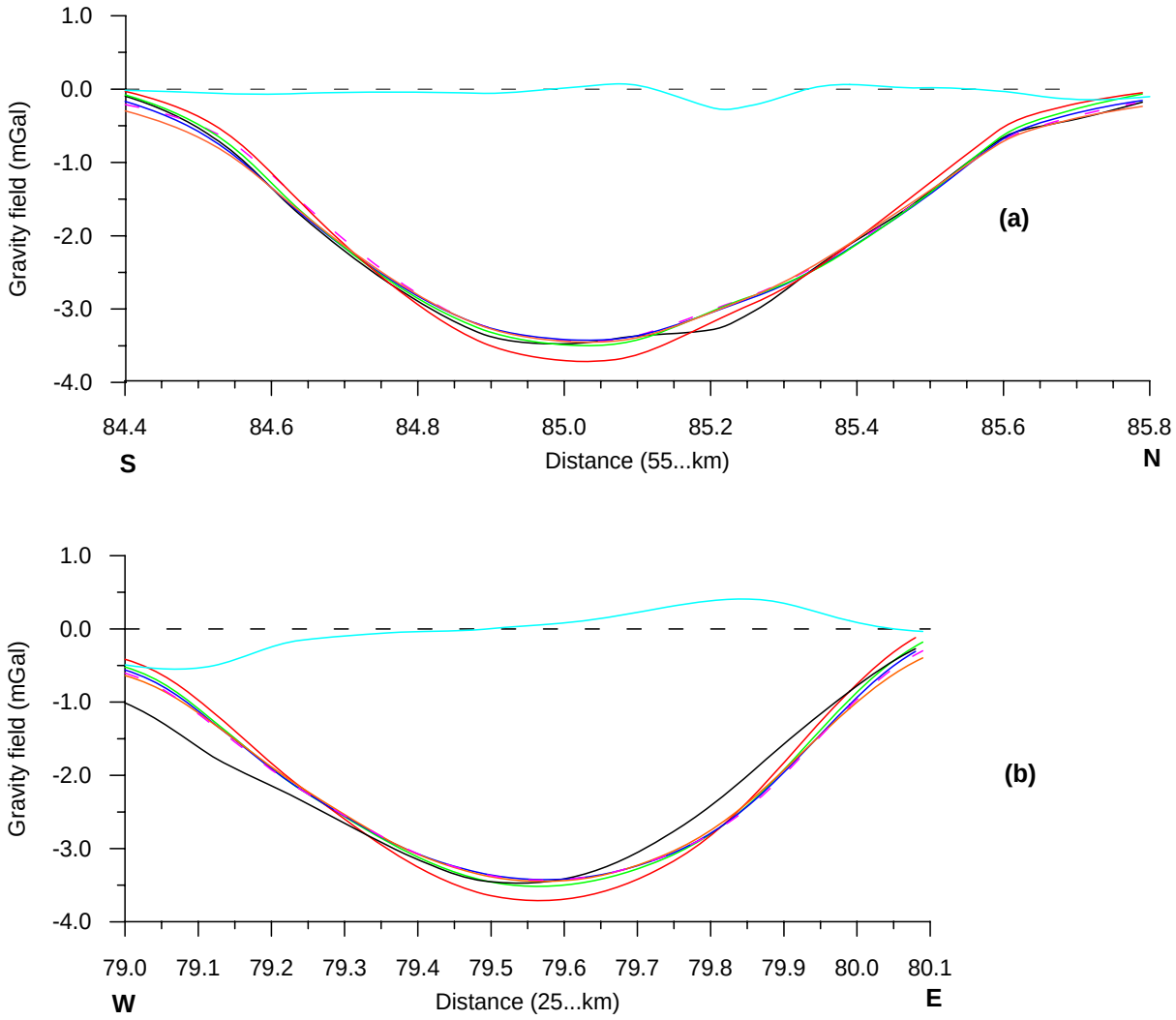

Fig. 7.3 Gravity profiles; coordinates of extremal points are (2579.54,5584.4; 2579.54,5585.8) for (a) and (2579.0,5580.0; 2580.1,5580.0 km) for (b), respectively. For the model represented by the blue curve, the height of the crater has been set to a constant value of 200 m contrarly to other cases where it was parameterized and estimated.

observed — residual between observed and computed for model B

A — computed : $H_c = 101$ m, $\rho_c = 1.97$ g/cm^3, $\alpha_c = 24°$, $H_d = 930$ m, $\rho_d = 2.08$ g/cm^3, $\alpha_d = 80°$

B — computed : $H_c = 95$ m, $\rho_c = 2.07$ g/cm^3, $\alpha_c = 31°$, $H_d = 1042$ m, $\rho_d = 2.18$ g/cm^3, $\alpha_d = 80°$

C — computed : $H_c = 115$ m, $\rho_c = 2.25$ g/cm^3, $\alpha_c = 36°$, $H_d = 830$ m, $\rho_d = 2.34$ g/cm^3, $\alpha_d = 85°$

D — computed : $H_c = 190$ m, $\rho_c = 2.24$ g/cm^3, $\alpha_c = 45°$, $H_d = 880$ m, $\rho_d = 2.14$ g/cm^3, $\alpha_d = 79°$

E — computed : $H_c = 200$ m, $\rho_c = 2.25$ g/cm^3, $\alpha_c = 36°$, $H_d = 1040$ m, $\rho_d = 2.36$ g/cm^3, $\alpha_d = 87°$

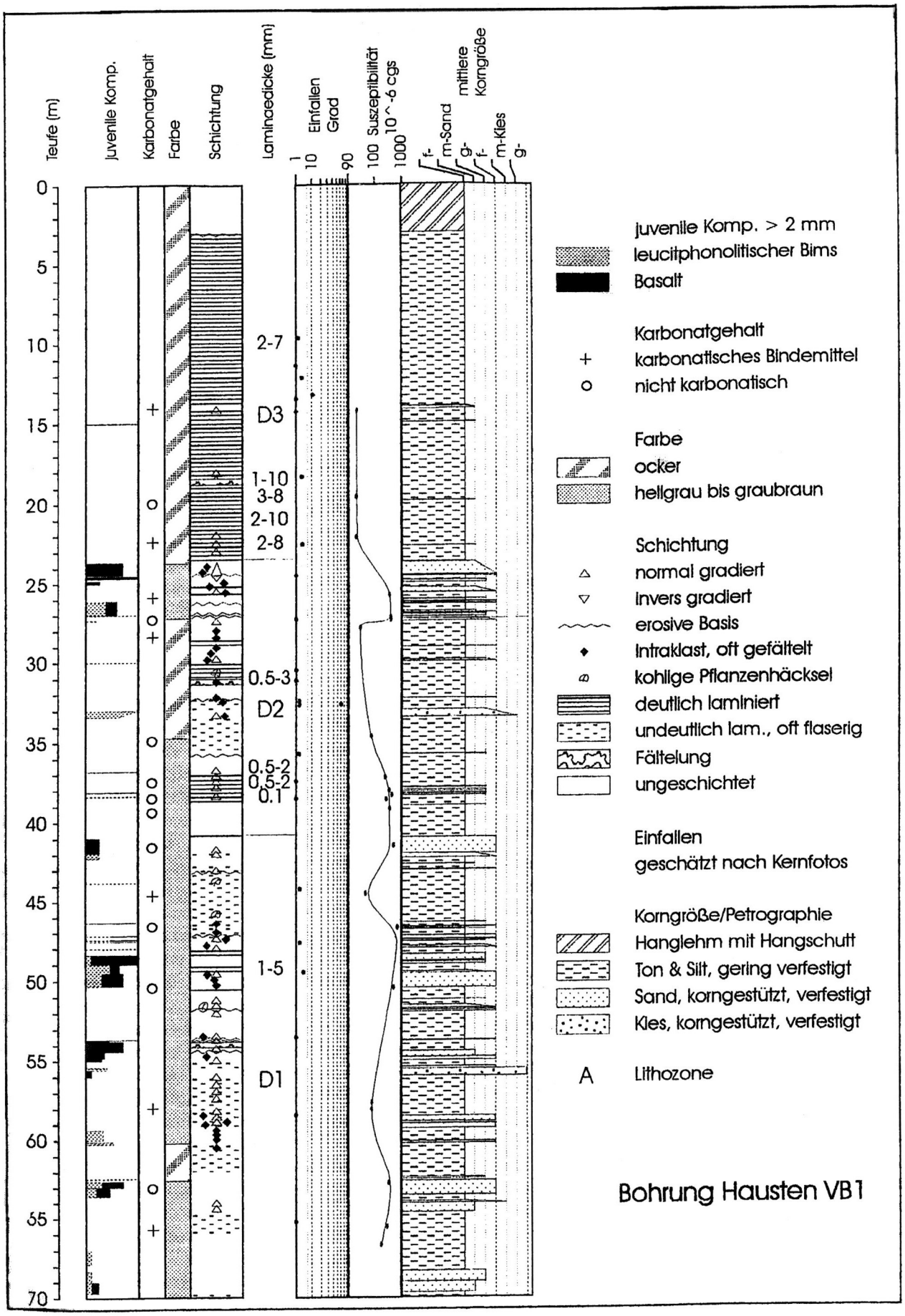

Fig. 7.4 Profile of the borehole Hausten VB1 (from Pirrung, 1997).

On Fig. 7.5 is shown a contour map of the residuals between the observed and computed gravity data for model B. Some small negative anomalies, more or less circular in shape, occur at the maar boundary. Another such anomalous zone is to be seen in the central-northern area, where the contour lines are distorted (see also Fig. 7.3(a) between the points 85.1 and 85.3). All these residuals occur in the areas where the observed gravity anomaly is distorted and/or where the magnetic anomaly manifests local disturbances. The negative character of the anomalies indicates that, in the corresponding areas, there are causative masses with negative density contrasts which have not been accounted for in the models. Whereas the anomaly in the East is certainly attributed to the influence of the small structure B, the nature of the causative sources for the four other negative anomalies is still unclear. The positive anomalies in the central- and south-eastern areas are probably due to topographic effects.

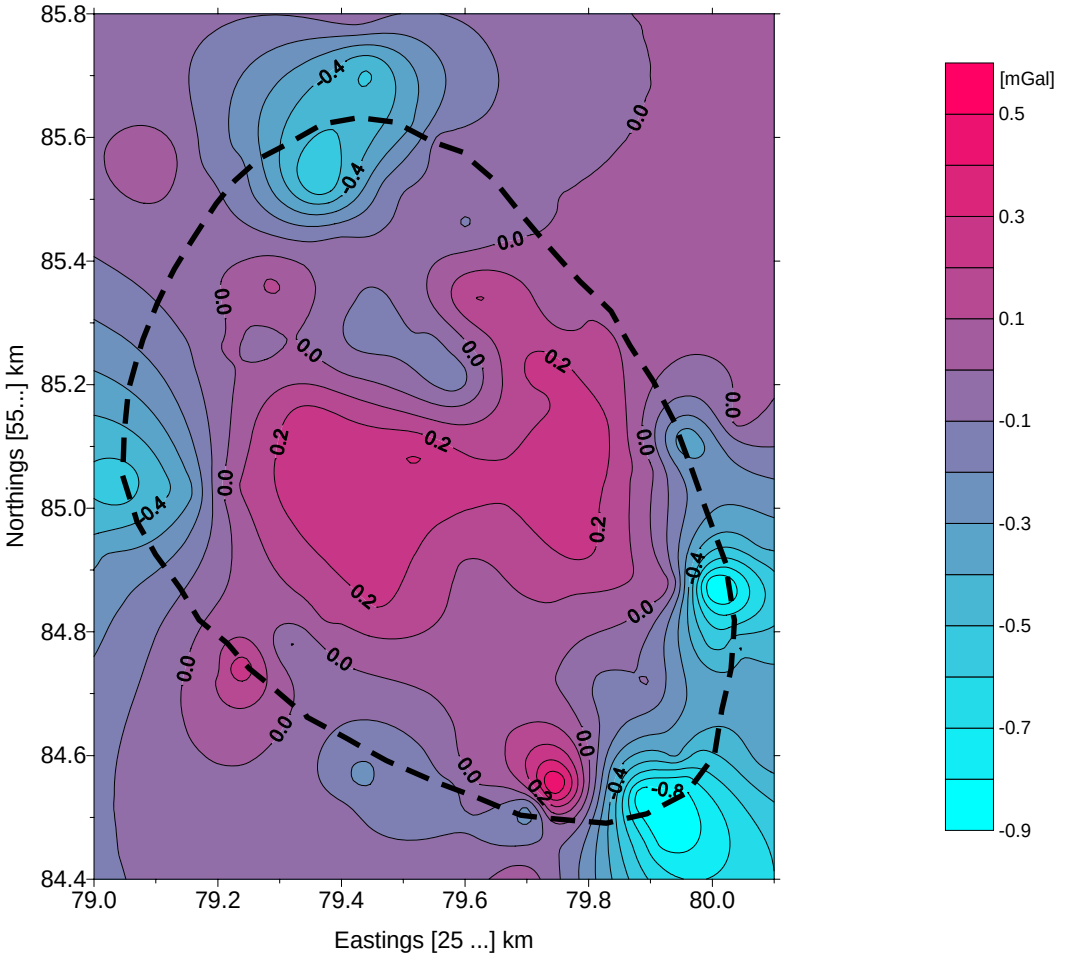

Fig. 7.5 Contour map of the residuals between the observed and computed gravity data; the residuals are relative to model B (Hausten-Morswiesen Maar). The dashed line shows the uppermost contour of the model body; this contour is assumed to correspond to the surface boundary of the maar-diatreme.

7.3 Qualitative and spectral analysis of the gravity and magnetic fields

In order to get a deeper insight into the structure of the Hausten-Morswiesen Maar, further investigations have been conducted by means of the spectral analysis and the first horizontal derivative of the field. These tools, based on Fourier techniques, provide with information about physical/lithological contacts, respectively in the vertical and horizontal dimensions. First, a rather qualitative analysis of the observed gravity and magnetic fields was carried out. For this purpose, the fields are again presented on Figures 7.6a and 7.7. The analysis was supported by the first horizontal derivative of the gravity field (7.6b, 7.6c), which, owing to its high sensitivity, can supply with complementary and detailed information.

7.3.1 Qualitative analysis

On Figures 7.8 up to 7.14 are presented some profiles of the gravity anomaly, its first horizontal derivative and of the magnetic anomaly as well. On Fig. 7.6b, 7.8, 7.9 and 7.10, it can be well seen that there is a main maar structure **(A)** at the northwestern and southeastern boundaries of which two other small structures **(A1)** and **(A2)** occur; the effects of the latter cause the distortion of the gravity anomaly. On Fig. 7.11(a) and 7.11(b), a flattening/widening of the gravity minimum and two minima of the lows of the first horizontal derivative are respectively to be seen in the central area. This is an indication of the existence of another small structure **(A3)** within the main maar-diatreme. As deduced from Fig. 7.6b, 7.11(b) and 7.12(b), the two minima are approximately located at the points (2579550.0, 5585020.0) and (2579530.0, 5585130.0). The first minimum suits the global observed gravity minimum, the second one — the local gravity minimum caused by the small strucutre A3. Due to the effect of the small structure A3, the actual gravity minimum of the main maar-diatreme A has been disturbed and therefore can not be well defined. But examining the SN-profile of the first horizontal derivative of the gravity field on Fig. 7.11(b), it is obvious that the actual gravity minmum and consequently the centre of the maar-diatreme structure nearly lies 50-60 m away from the location point of the global gravity minimum northwards, namely at the point (2579.550,5585.075).

The complex nature of the Hausten-Morswiesen Maar is reflected more in the magnetic anomaly than in gravity. This can be seen as well on the contour map (Fig. 7.7) as in some profiles of the magnetic field in different directions (Fig. 7.8 to Fig. 7.14). In the SE-NW profile (Fig. 7.10(c)), three sharp peaks are to be seen. The two peaks at the ends of the profile correspond to the small structures A1 and A2, which have been outlined by the first horizontal derivative of the gravity anomaly. The peak in the central area, also to be seen in the SN-profile (Fig. 7.11(c), confirms the existence of the small structure (A3), already indicated by the first derivative of the gravity field. The effect of this small structure is noticeable as well in the change of the pattern of the contours as in the highened intensity of the magnetic anomaly in the central area. Due to the effect of the small structure A2 at the SE-boundary, the magnetic anomaly has been somewhat extended southeastwards. Another small anomaly, which seems to be caused by a dipole source, is to be seen at the western boundary of the structure (Fig. 7.7 and 7.13(c), between the points 84.9 and 85.1). Moreover, as shown on Fig. 7.6b, 7.6c, 7.7 and Fig. 7.12(b), 7.12(c), there is a considerable distortion of the contour lines of both the horizontal derivative of the gravity

and the magnetic field in the central-western areas. Both effects — the small anomaly and the distortion — are probably caused by a further small structure (**A4**) at the western boundary of the main structure. The sharpness of the magnetic anomalies caused by the four small structures is clearly indicative for shallow sources.

Another characteristic of the magnetic anomaly is the stretching northwestwards (Fig. 7.7). This seems to be the effect of a (near)-surface source other than the diatreme tuffs. Indeed, according to Pirrung (1997), some juvenile components (basalts and leucite phonolite bims), which originated from one or more nearby eruption centres, occur within the crater sediments at different depths (Fig. 7.4). The stretching of the anomaly suggests that the ejected volcanic material came from the northwestern side into the maar crater, whereby a portion of it deposited at the northwestern boundary, where it causes the anomaly displayed between the points 85.15 and 85.45 of the profile M5-M5′ (Fig. 7.13(c)). Relying on the results of the core analysis conducted by Pirrung (1997) and assuming an average sedimentation rate of 0.75 mm/a (pers. comm. F. Sirocko), it can be deduced that the nearby volcanic eruptions occurred with an interval ranging from 1 to 9 Ka during the posteruptive development of the maar. The last eruption probably took place about 30 Ka ago.

The results of this analysis confirm those of gravity inversion, namely the existence of secondary small structures in the area of the Hausten-Morswiesen Maar. However, due to undersampling of the gravity field (see Fig. 7.6a) and to disturbing effects of the small structures, the boundary of the main structure cannot be clearly defined by the first horizontal derivative. Two plausible hypotheses are schematically shown on Fig. 7.6b: the surface boundary of the maar corresponds either to the dashed green contour (maximum of the first horizontal derivative of the gravity field) or to the solid one, which fits that defined by the first vertical derivative. In the first case, the main maar-diatreme structure would have an approximate surface diameter of 930 and 640 m in NNW and SW-direction, respectively. In the second case, the diameter would respectively amount to 1250 and 830 m. Accordingly, the small structures A1, A2, A4 would have formed outside the main one, in the outer boundary areas or within it, in the inner boundary areas. It is planned later to conduct gravity inversion again using the inner boundary as known top contour of the maar, in order to compare the results and know more about the horizontal extent.

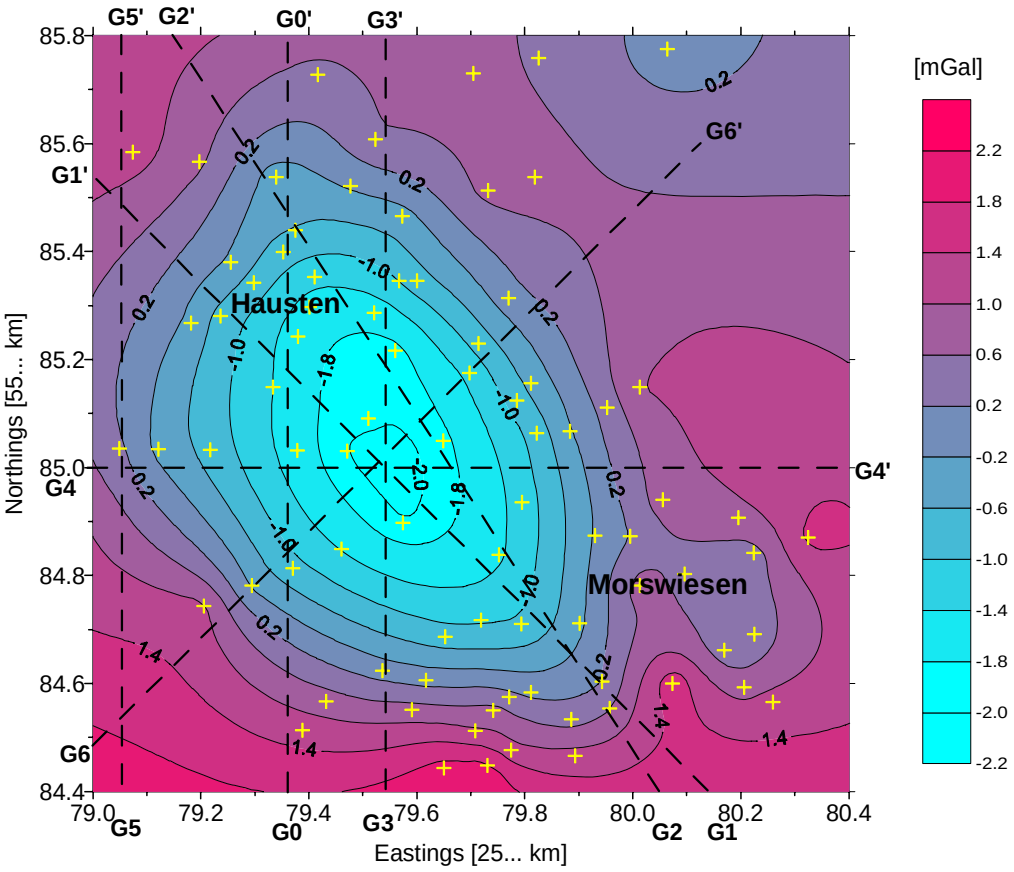

Fig. 7.6a Observed gravity anomaly of the Hausten-Morswiesen Maar. The yellow crosses correspond to observation points; the dashed lines show the directions of the profiles (gravity and its first horizontal derivative), considered in the analysis.

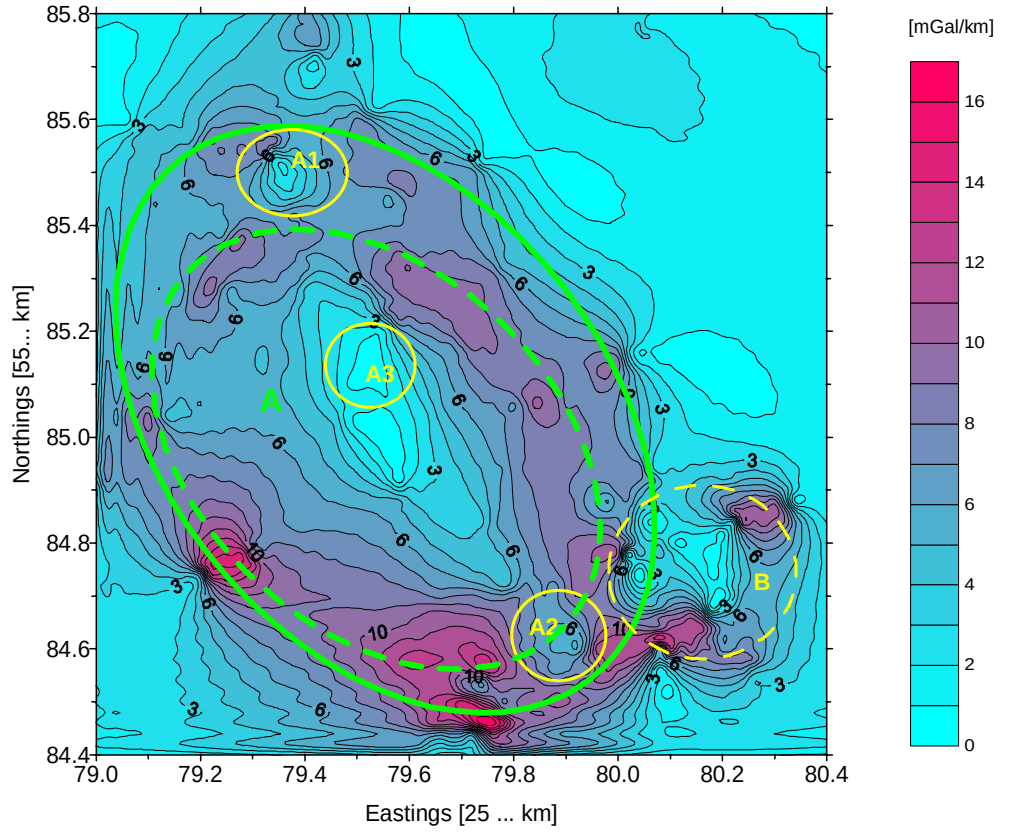

7.6b First horizontal derivative, computed from the gravity field. Anomalous zones corresponding to different causative features are roughly outlined. Green (either solid or dashed) : main maar-diatreme A; solid yellow : small structures A1, A2, and A3 related to A; dashed yellow : another small (maar?) structure B.

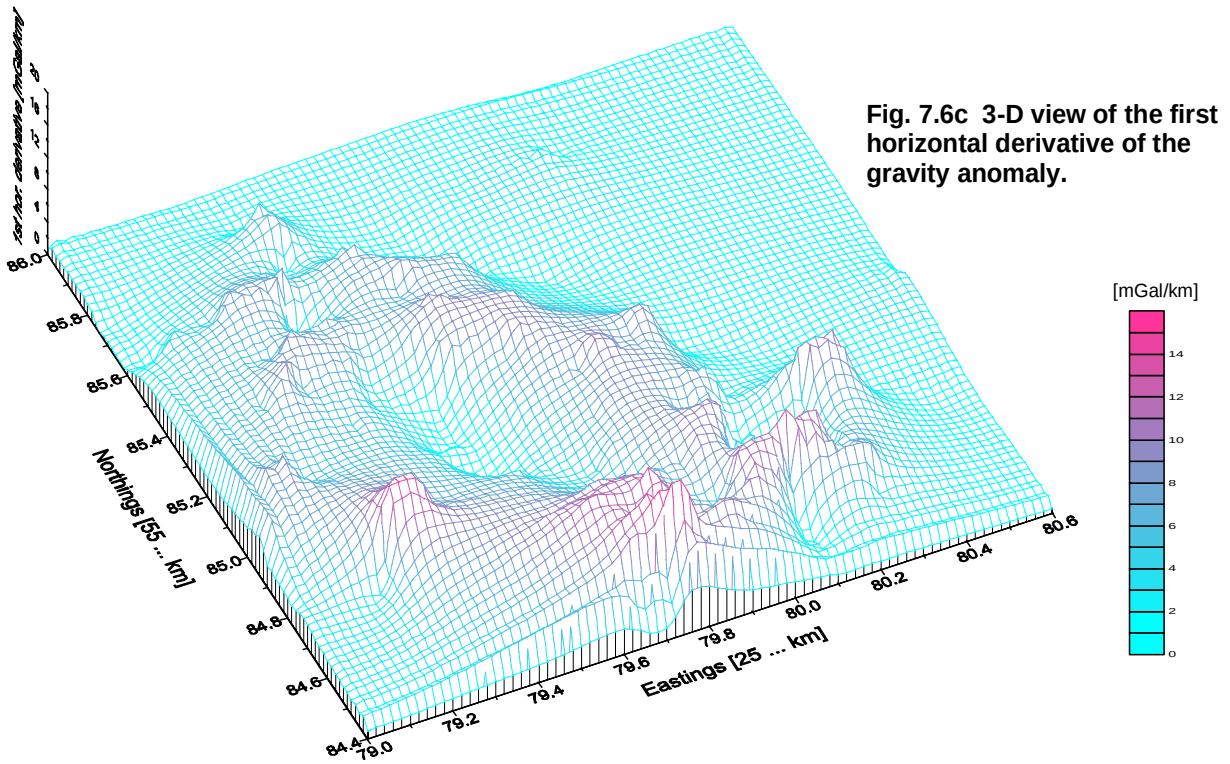

Fig. 7.6c 3-D view of the first horizontal derivative of the gravity anomaly.

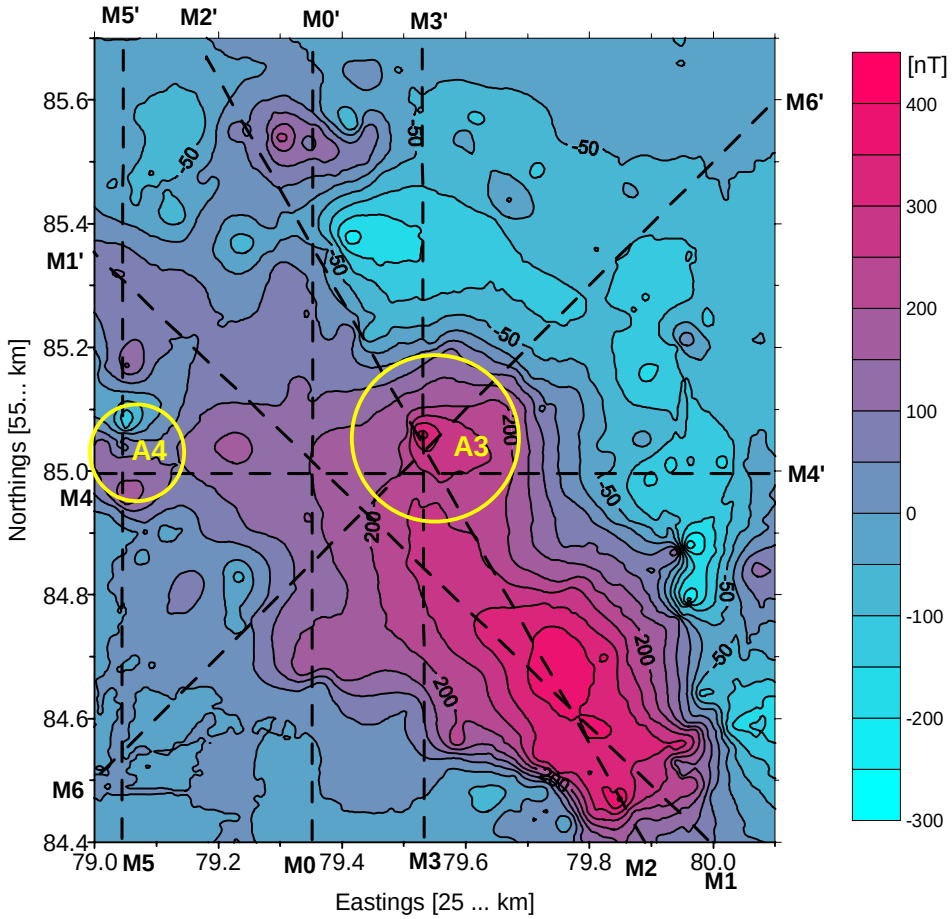

Fig. 7.7 Observed magnetic anomaly of the Hausten-Morswiesen Maar. The dashed lines show the directions of the profiles, considred in the analysis. The yellow circular contours show anomalous zones, which are not well or at all outlined by the gravity field and its first horizontal derivative; they correspond to the small structures A3 and A4.

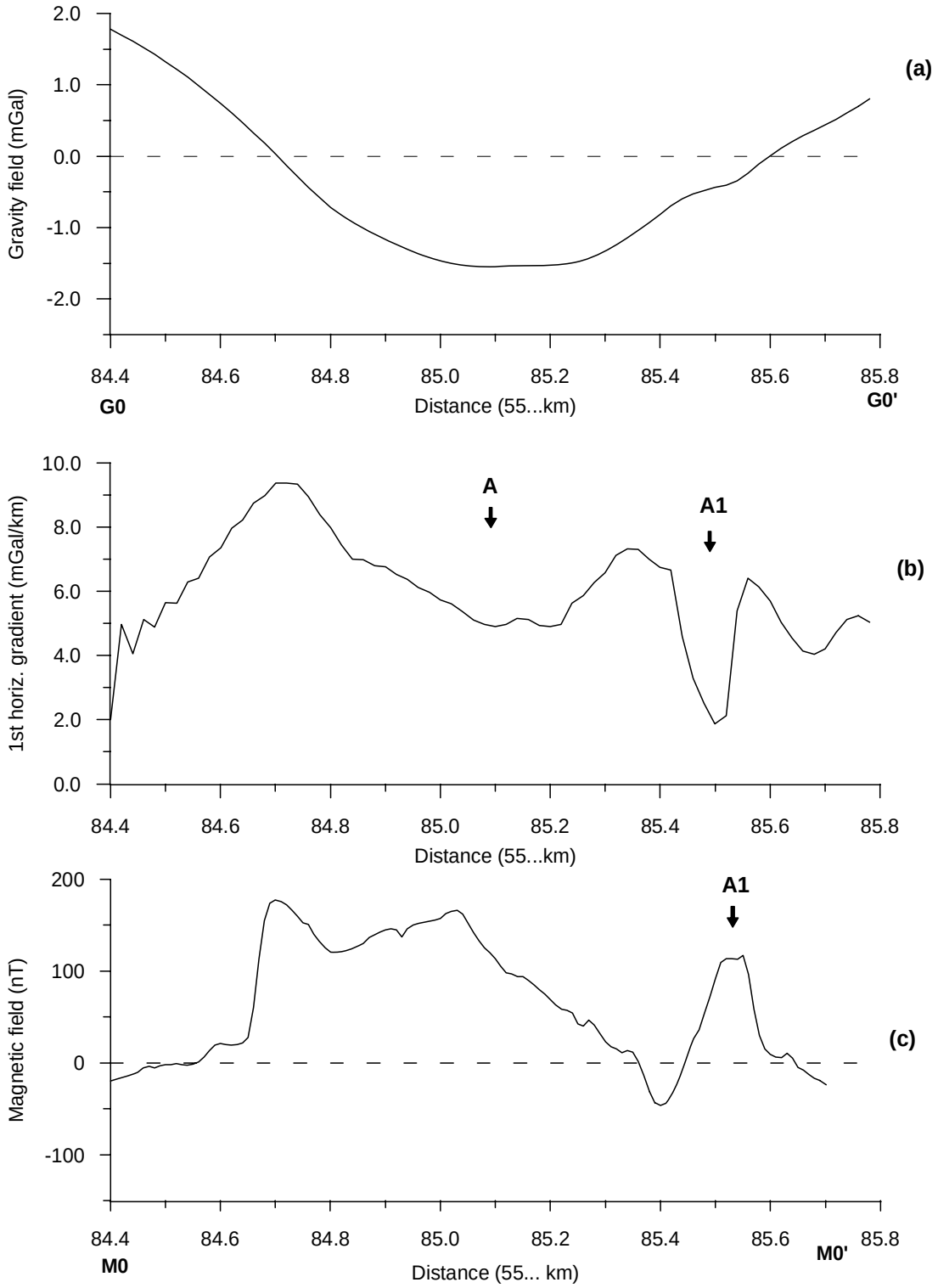

Fig. 7.8 SN-profiles of the observed gravity field (a), its first horizontal derivative (b) and of the magnetic field (c). Coordinates of extremal points are (2579.36,5584.4; 2579.36,5585.8), (2579.36,5584.4; 2579.36,5585.7 km) for G0-G0' and M0-M0', respectively.

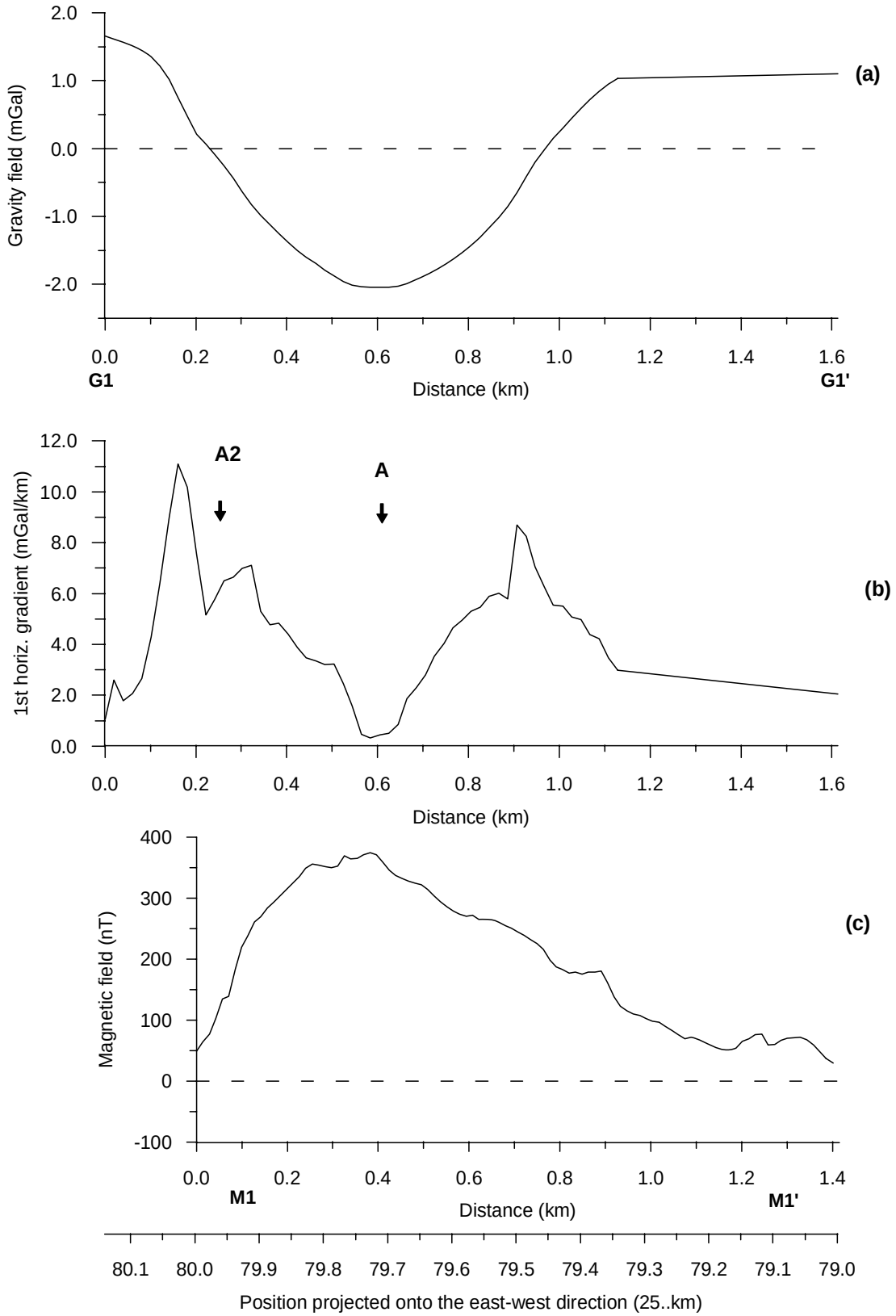

Fig. 7.9 SENW-profiles of the gravity field (a), its first horizontal derivative (b) and of the magnetic field (c). Coordinates of extremal points are (2580.14,5584.4; 2579.0,5585.54), (2580.0,5584.4; 2579.0,5585.4 km) for G1-G1' and M1-M1', respectively.

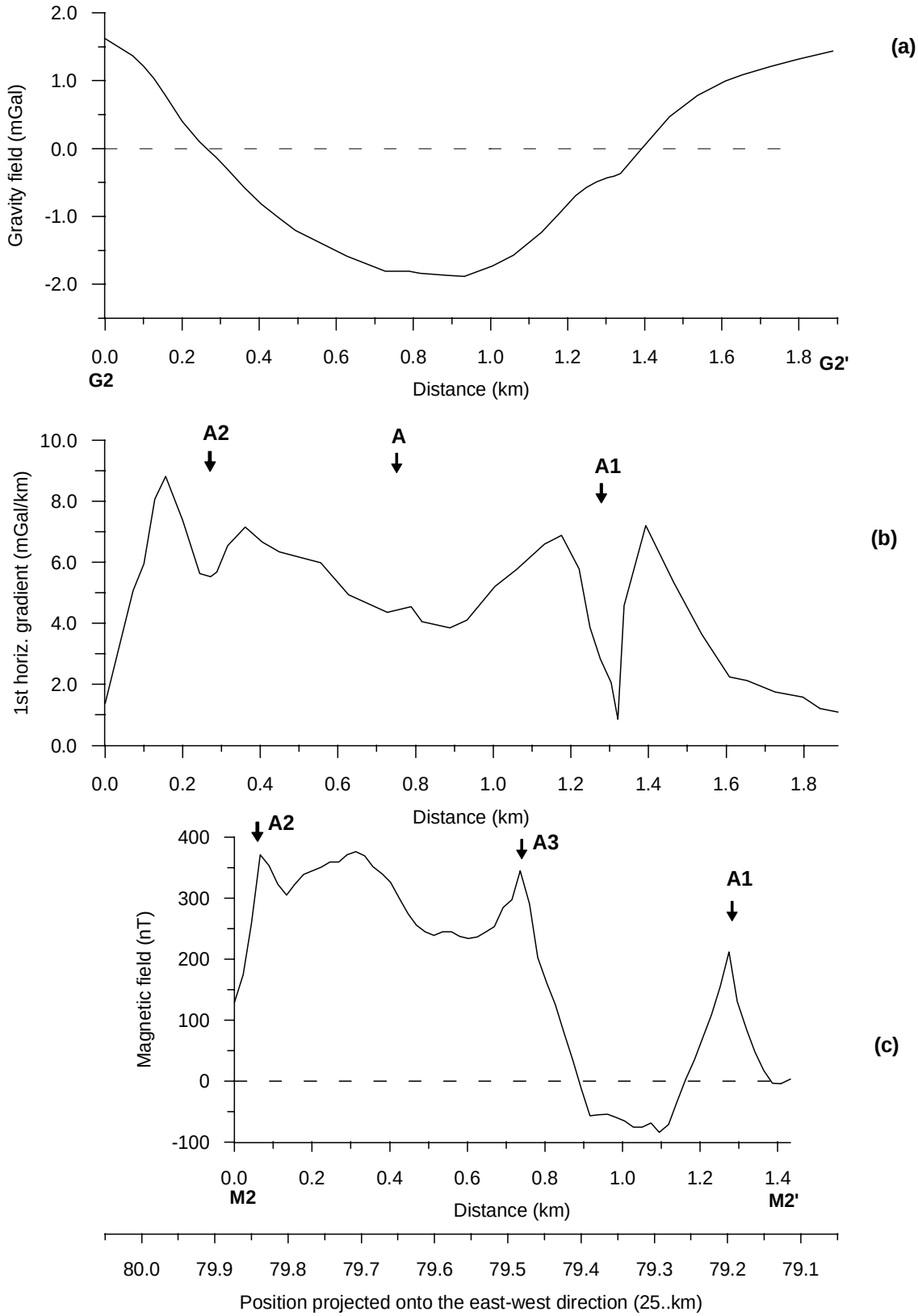

Fig. 7.10 SENW-profiles of the gravity field (a), its first horizontal derivative (b) and of the magnetic field (c). Coordinates of extremal points are (2580.05,5584.4; 2579.15,5585.8), (2579.87,5584.4; 2579.22,5585.7 km) for G2-G2' and M2-M2', respectively.

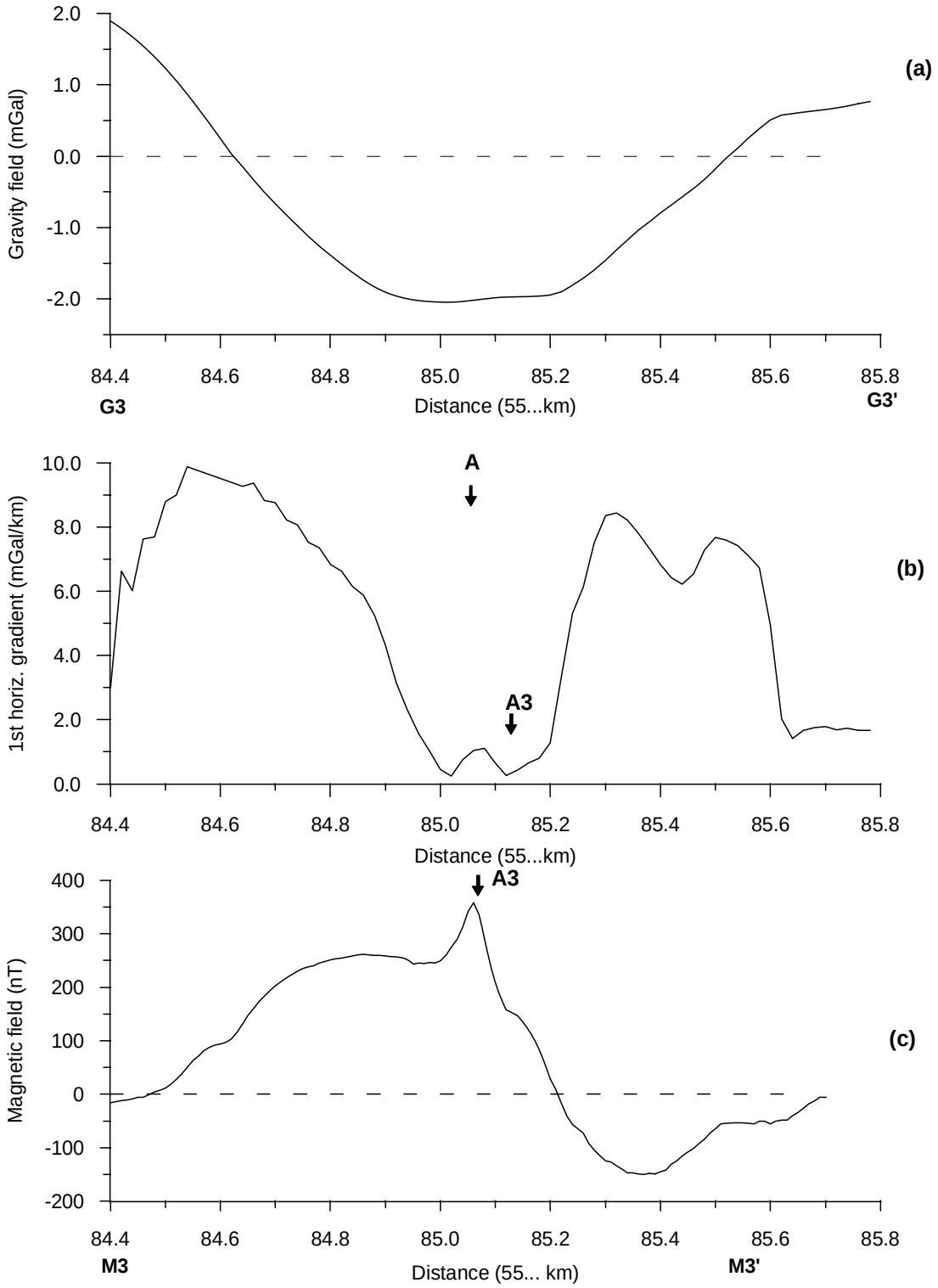

Fig. 7.11 SN-profiles of the observed gravity field (a), its first horizontal derivative (b) and of the magnetic field (c). Coordinates of extremal points are (2579.53,5584.4; 2579.53,5586.0), (2579.53,5584.4; 2579.53,5585.7 km) for G3-G3' and M3-M3', respectively.

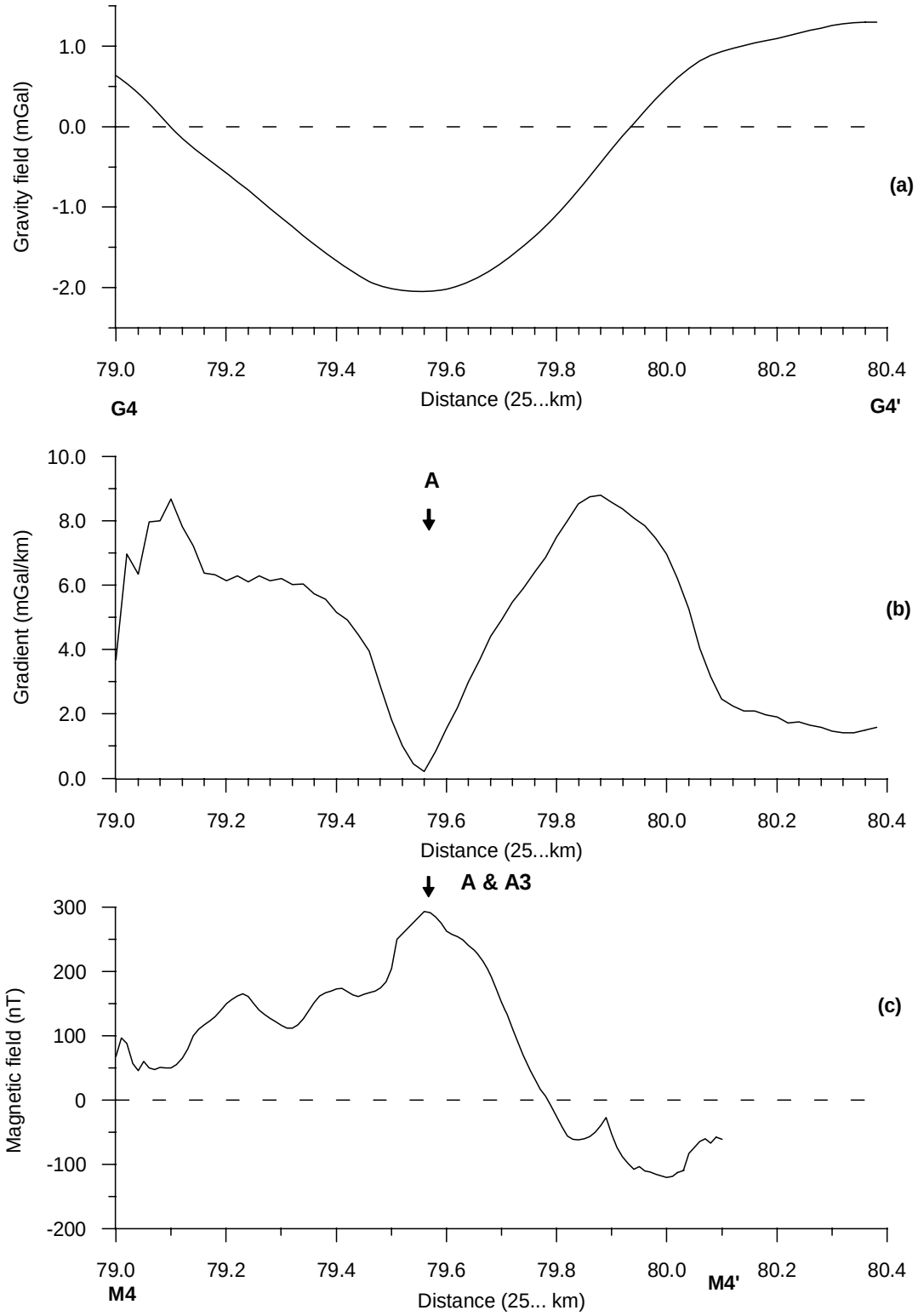

Fig. 7.12 WE-profile of the observed gravity anomaly (a), its first horizontal derivative (b) and of the magnetic anomaly (c). Coordinates of extremal points are (2579.0,5585.0; 2580.4,5585.0), (2579.0,5585.0; 2580.1,5585.0) km for G4-G4' and M4-M4', respectively.

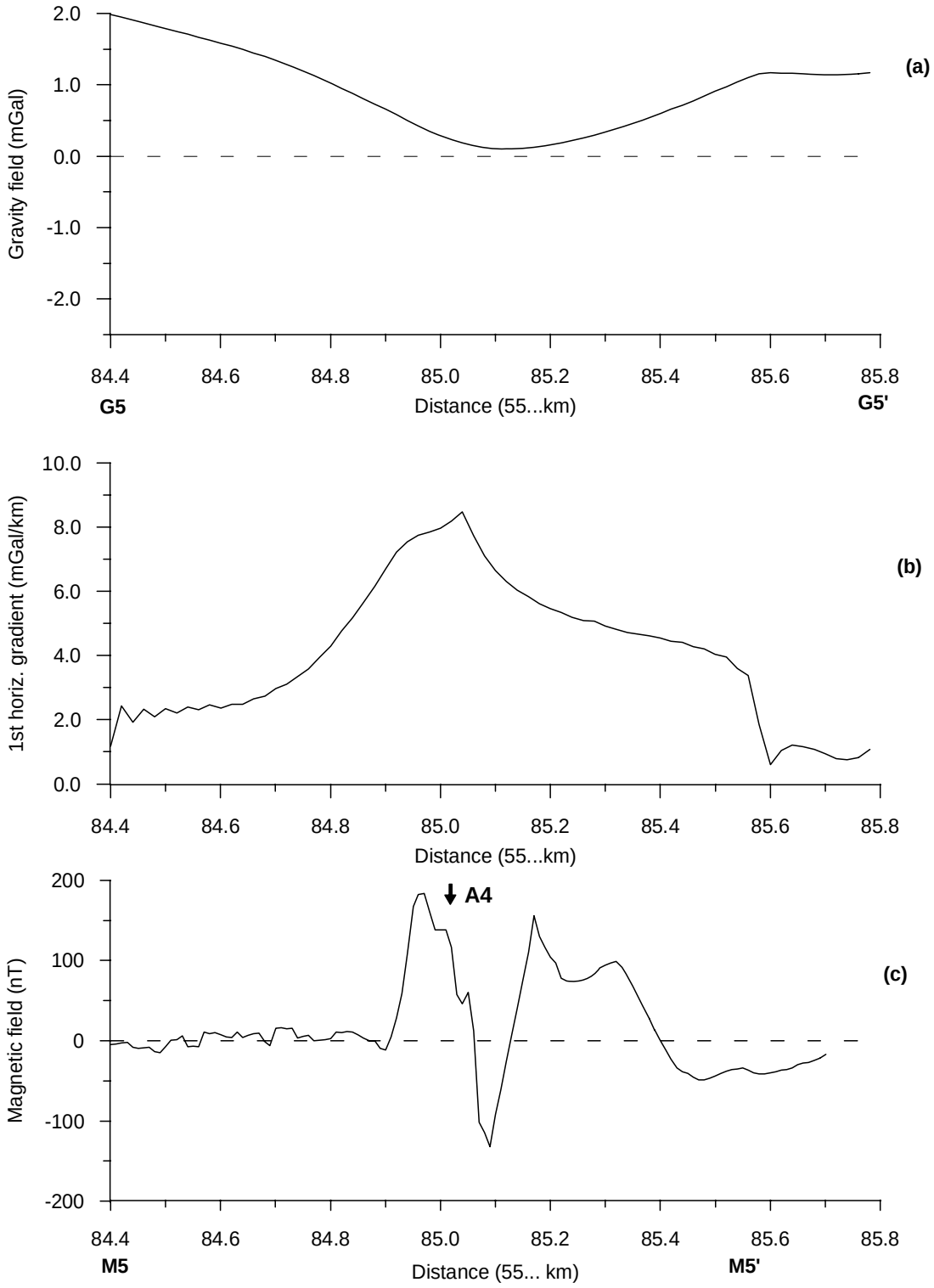

Fig. 7.13 SN-profiles of the observed gravity anomaly (a), its first horizontal derivative (b) and of the magnetic field (C). Coordinates of extremal points are (2579.06,5584.4; 2579.06,5585.8), (2579.05,5584.4; 2579.05,5585.7 km) for G5-G5' and M5-M5', respectively.

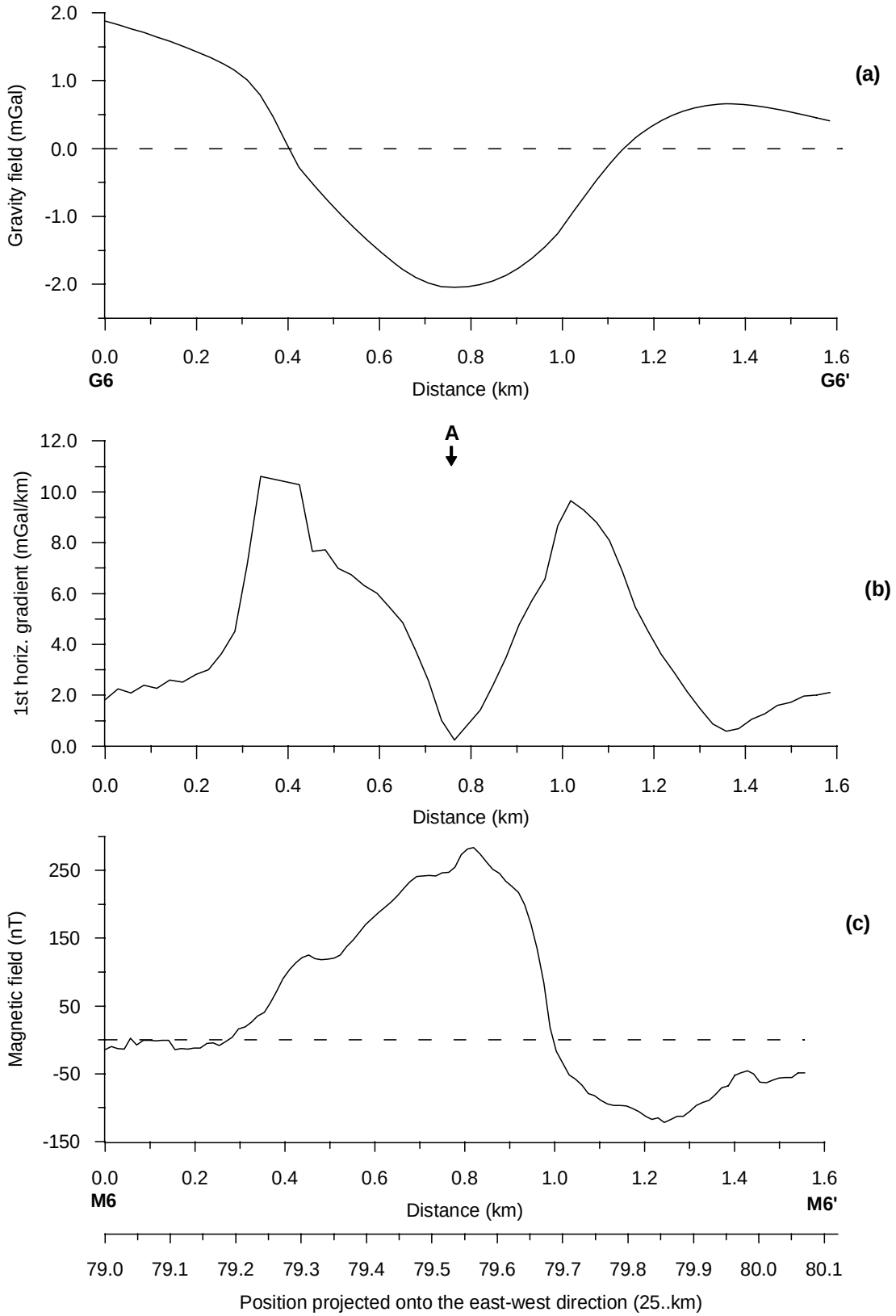

Fig. 7.14 SWNE-profiles of the gravity field (a), its first horizontal derivative (b) and of the magnetic field (c). Coordinates of extremal points are (2579.0,5584.48; 2580.12,5585.6), (2579.0,5584.5; 2579.0,5580.1 km) for G6-G6' and M6-M6', respectively.

7.3.2 Spectral analysis

The power spectrum of the gravity field is presented on Fig. 7.15a. The low frequency component indicates a deep source at an average depth of 300 m. Either the crater height is greater than that of about 200 m, theoretically expected or the density of the rocks occupying the uppermost part of the diatreme is the same as that of the sediments lying in the lower part of the crater. Considered more in detail, the spectrum of the low frequency component reveals sources at two different depths of about 190 and 350 m, respectively. However, according to Spector (1979), the slope of the low frequency component (deep source) of the power spectrum is to be treated as indicating an apparent depth, which is in excess of the true average depth to the source. The medium frequency component indicates a further source at about 115 m depth. This either corresponds to a density change within the crater sediments or to an interface between the latter and the underlying rocks which are other than sediments. Two high frequency components indicate location depths of about 28 and 13 m. Relying on the borehole profile (Fig. 7.4), the 28 and 13 m levels can be interpreted as to correspond to lithological/density changes in sediments due to juvenile and carbonate components, respectively.

The power spectrum of the magnetic field (Fig. 7.15b) defines the depth to the source of the low frequency component at about 116 m. It is not clear whether this interface, which magnetically separates the maar-diatreme filling into two main rock units, corresponds to the bottom of the crater filling or simply to a change in magnetic properties of the crater sediments. The depth to the source of the high frequency component averages 22 m; a significant intermediate depth is indicated at about 48 m. These two levels correspond to susceptibility changes (increase) in crater sediments due to intercalations of juvenile components, the amount of which varies from depth to depth (Fig. 7.4). This is demonstrated as well by the erratic/an echelon character of the high frequency component (Fig. 7.15b) as by the undulations in the susceptibility profile (Fig. 7.4). The 116 and 22 m interfaces are more or less in good agreement with those defined by the power spectrum of the gravity field. On Figures 7.16 and 7.17 are presented the low- and high-pass filtered components of the gravity and magnetic fields, respectively. On the contour maps of the high-pass filtered components appear the same anomalous zones, which were put in evidence by previous quantitative and qualitative interpretaion.

The spectral analysis establishes a change in density and magnetic properties at about 115 m depth. Is this value, which does not much differ from some of those estimated by gravity inversion, the real depth to the crater floor? Taking into account that a crater height of about 200 m should theoretically be expected and that, according to the power spectrum of the magnetic field, there is no difference in magnetic properties of the rocks lying below the 115 m level, it can be deduced that the rocks occupying the lower part of the crater might petrologically be of a same composition as those (tuffs) filling the underlying diatreme. This can be explained by the fact that a part of the ejected tuffs slumped down into the crater by erosion prior to the sedimentation process. This would indicate that the crater walls were relatively steep and the climatic conditions were favourable enough (rainy?) to enable a quick erosion process. Alternatively, an optimal content of juvenile (mafic) components in the crater sediments below the 115 m level might have led to an acquisition of density and magnetic properties similar to those of the underlying tuffs.

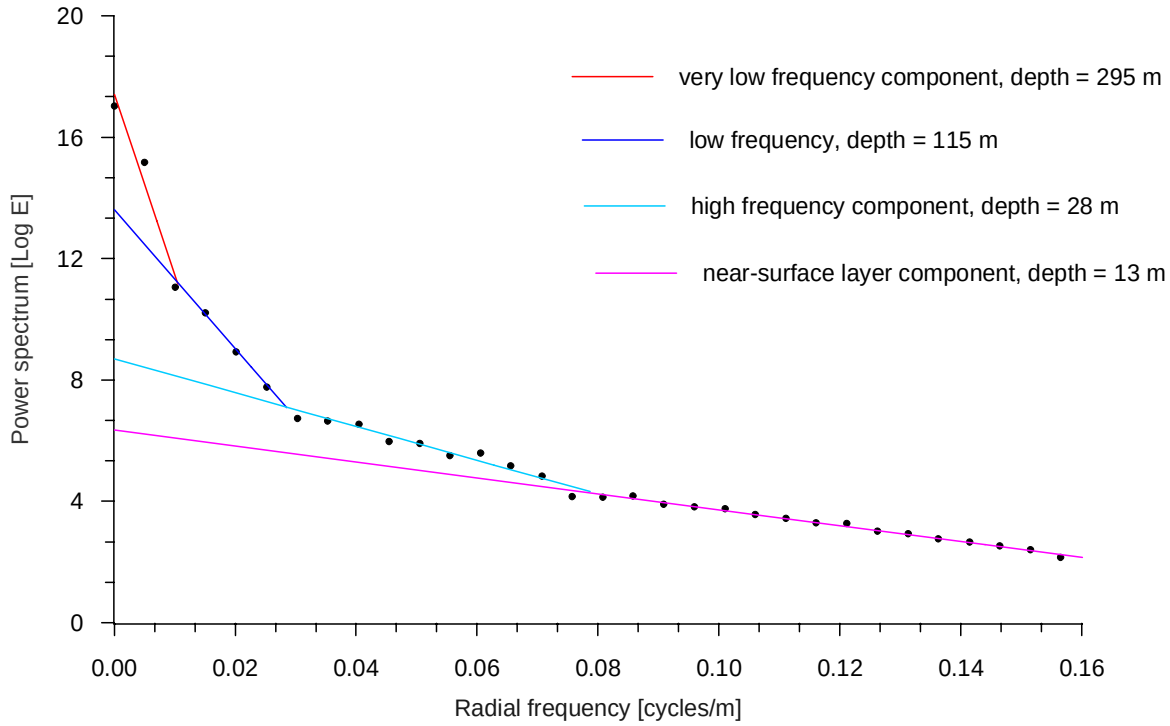

Fig. 7.15a Logarithmic power spectrum of the gravity field (Hausten-Morswiesen Maar).

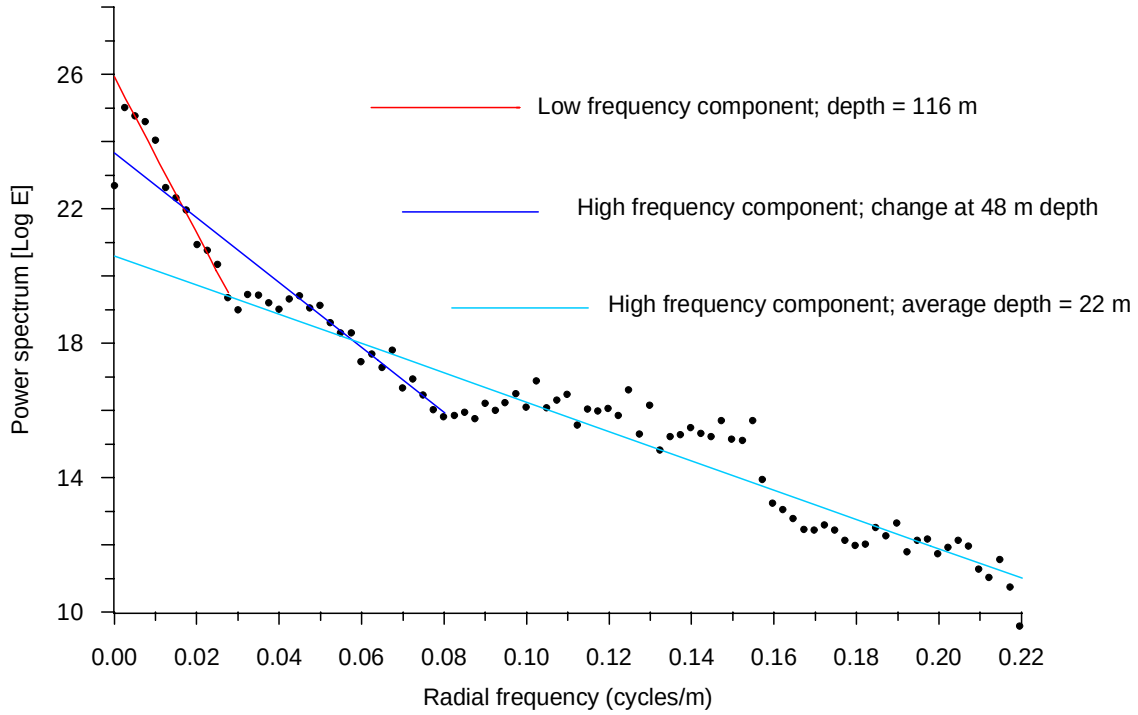

Fig. 7.15b Logarithmic power spectrum of the magnetic field (Hausten-Morswiesen Maar).

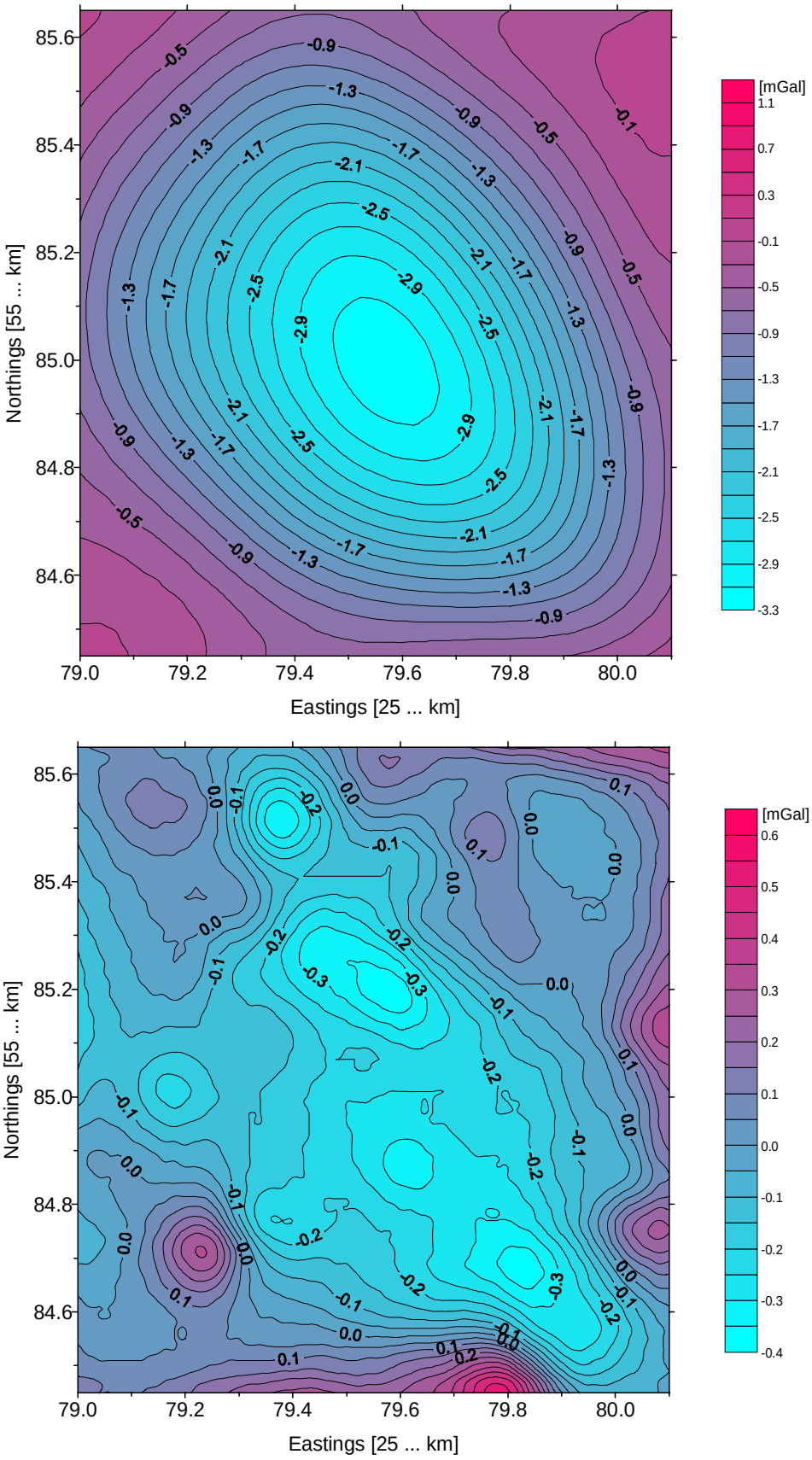

Fig. 7. 16 Low- and high-pass filtered components (respectively up and down) of the gravity anomaly of the Hausten-Morswiesen Maar.

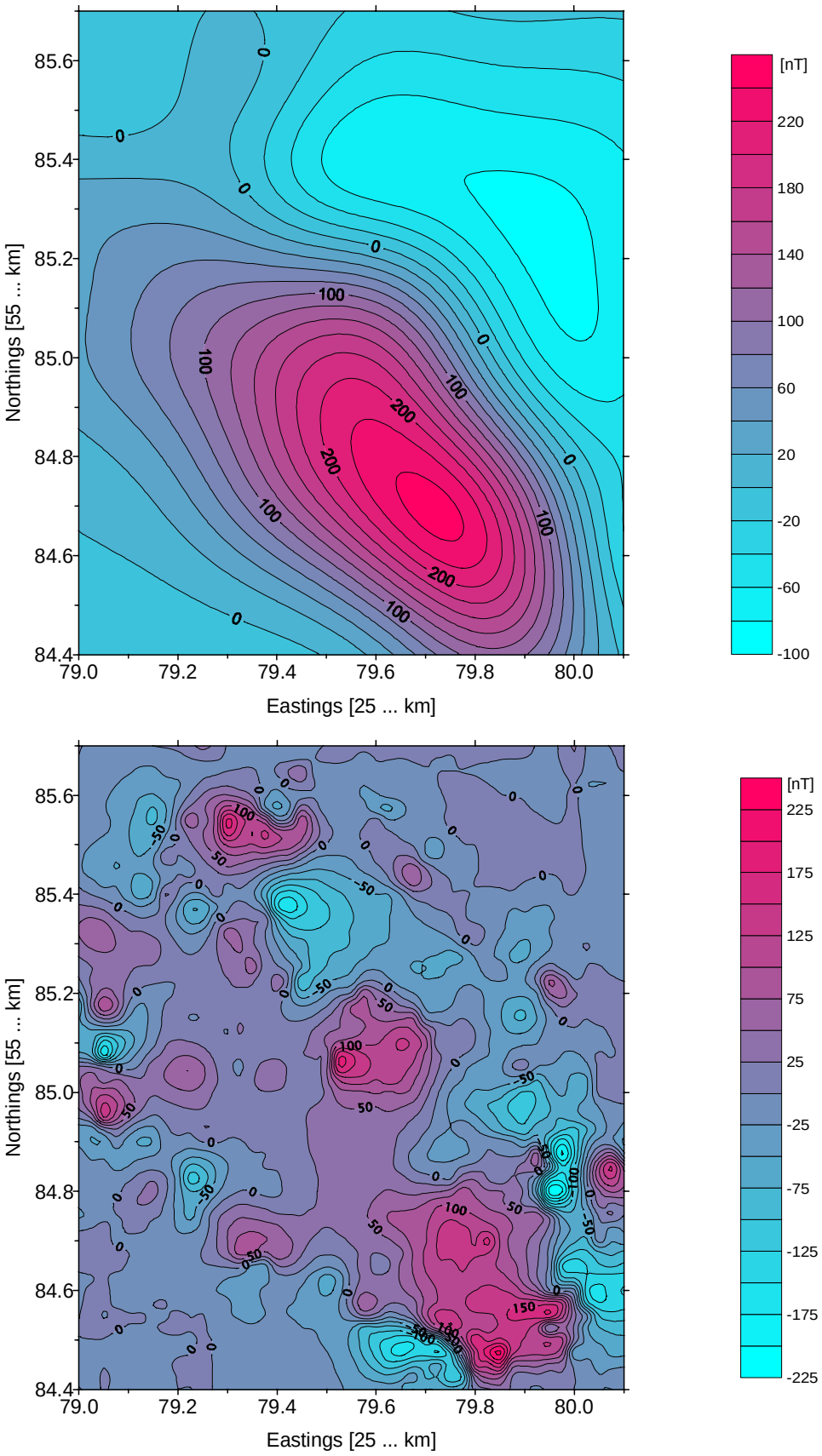

Fig. 7. 17 Low- and high-pass filtered components (respectively up and down) of the magnetic anomaly of the Hausten- Morswiesen Maar.

7.4 Investigation of the surface boundary of the maar

As already mentioned in 7.3.1, it is not clear which of the two boundaries indicated by the first horizontal derivative of the gravity field (Fig. 7.6b) corresponds to the real surface boundary of the Hausten-Morswiesen Maar. The outer boundary fairly fits that which was defined by the first vertical derivative and used for gravity inversion in 7.2. In order to get complementary information, gravity inversion has been conducted again, using the inner boundary as top contour of the model body. Parameterization was similar to that in 7.2. The results of the representative models are presented in Tables 7.6, 7.7, 7.8 and on Fig. 7.18 as well. Generally, the whole maar-diatreme structure is reduced to a single diatreme with a relatively high overall density averaging to 2.30 g/cm^3. The height of the diatreme varies around 800 m, which nearly matches the average size of the surface diameter. The dip angle of the diatreme walls (α_d) is about 82°. As can be seen on Fig. 7.18, none of the models fairly fits the observations. Though the fit of model G with both larger density and height is better than that of model F, it is clearly worse than that of model B, which was estimated by previous inversion using the outer boundary (see 7.2). In the intermediate model H, the diatreme has a height of about 780 m; the density estimate (2.342 g/cm^3) is a bit higher than that given by model G. This effect is compensated by a slight widening of the diatreme ($\alpha_d = 85°$) and by an additional underlying diatreme of much smaller size ($H_d \leq 50$ m) and less density (2.10–2.30 g/cm^3). This density is characteristic for tuffs. The computed curve for model H coincides with that of model G.

The high overall density might be explained by the fact that the density of the crater sediments is increased by the effect of the juvenile (mafic) components and nearly matches that of the underlying diatreme tuffs. The strong misfit toward the boundary areas demonstrates that the maar should have a larger surface diameter, which probably corresponds to the outer boundary, indicated by the first horizontal derivative of the gravity field and defined by the first vertical derivative as well. Otherwise, the maar-diatreme volcano might be thought of being surrounded by a mechanically weak zone, where the density of the country rocks has decreased due to a breakdown caused by repeated phreatomagmatic explosions. The width of this zone, approximated from the inner and outer average diameters of respectively 800 and 1050 m, should amount to 250–300 m. Geophysical investigations conducted by Diele (2000) on the Pulvermaar showed that the latter is surrounded by a halo of reduced density due to rocks relaxation caused by stress-waves, which originated from heavy repeated eruptions during the formation of the maar volcano. This might apply to some or all maars too.

Table 7.6 Confidence intervals and resolutions of the estimates; *model F.*

Parameter	LB	Estimate	UB	Resolution
ρ_d	2.240	2.290	2.330	0.80
H_d	600.0	690.0	780.0	0.64
α_d	78.0	79.0	81.0	0.60
D_{bd}	398.0	405.0	415.0	0.60

Table 7.7 Confidence intervals and resolutions of the estimates; *model G.*

Parameter	LB	Estimate	UB	Resolution
ρ_d	2.300	2.330	2.367	0.70
H_d	765.0	895.0	1020.0	0.67
α_d	82.4	83.5	84.3	0.56
D_{bd}	414.0	420.0	424.0	0.56

Table 7.8 Confidence intervals and resolutions of the estimates; *model* H^+.

Parameter	LB	Estimate	UB	Resolution
ρ_d	2.231	2.342	2.374	0.72
H_d	460.0	778.0	1097.0	0.66
α_d	82.3	85.4	86.8	0.60
D_{bd}	477.0	495.0	503.0	0.60

$^+$ diatreme underlain by another small vertical one: ($0 \leq H \leq 50$ m; $\rho = 2.2 \pm 0.1$ g/cm^3).

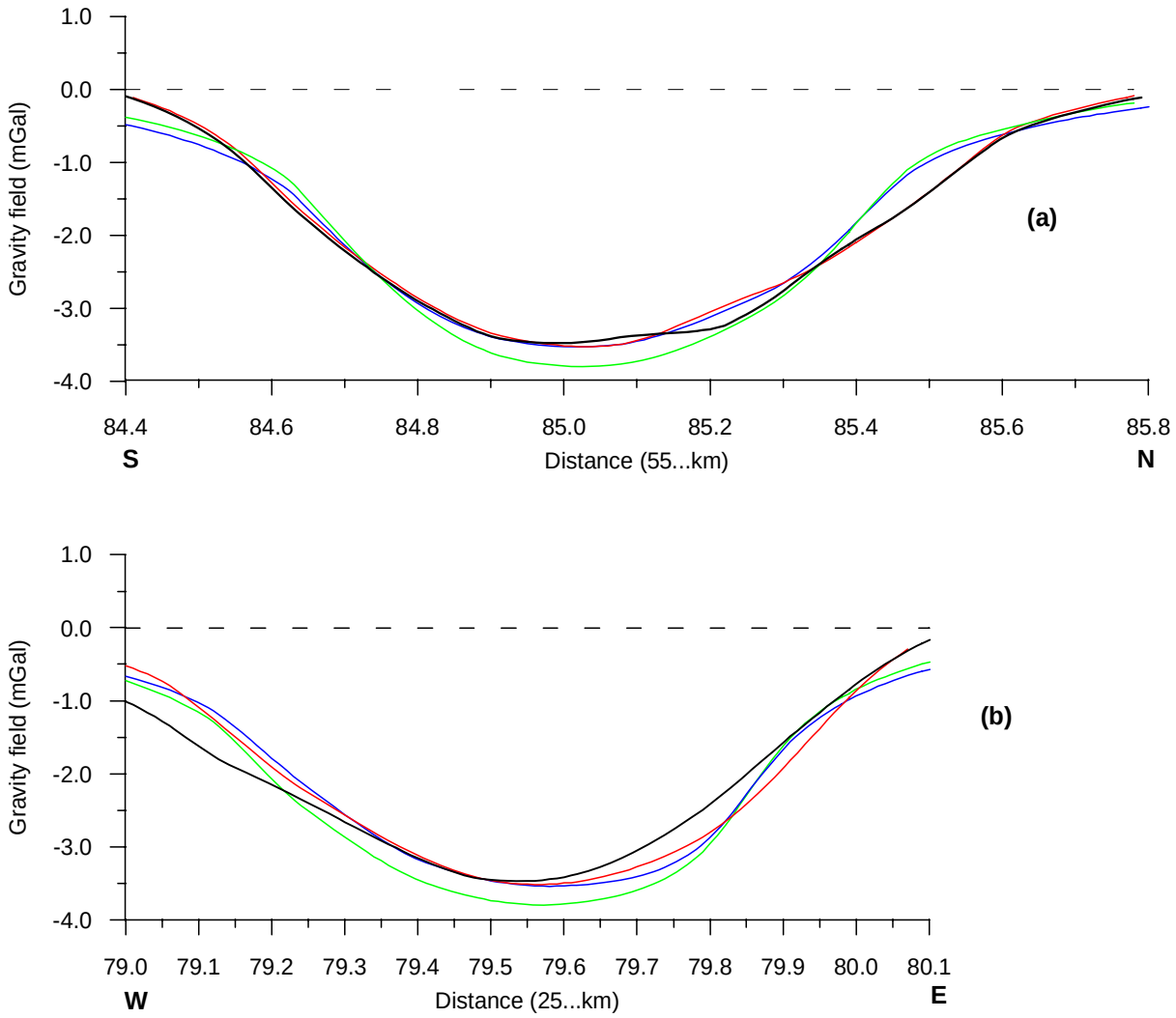

Fig. 7.18 Gravity profiles of the Hausten-Morswiesen Maar; coordinates of extremal points are (2579.54,5584.4; 2579.54, 5585.8) for (a) and (2579.0, 5580.0; 2580.1, 5580.0 km) for (b), respectively.

observed; computed; model B (from previous inversion in 7.2).

Model F; Dtm = 750 m; Hd = 690 m; Dbd = 405 m; $\alpha = 80°$; ρ = 2.290 g/cm**3

Model G; Dtm = 750 m; Hd = 895 m; Dbd = 410 m; $\alpha = 83°$; ρ = 2.330 g/cm**3

Model H; Dtm = 750 m; Hd = 780 m; Dbd = 490 m; $\alpha = 85°$; ρ = 2.342 g/cm**3

7.5 Inversion of low-pass filtered magnetic data

Since the analysis results show that the magnetic anomaly is too complicated due to effects of near-surface sources, low-pass filtered data were rather used for inversion. Some of the geometric parameters estimated by gravity inversion and by the spectral analysis served as a-priori information. The same geometric model was used as in gravity inversion. But the height of the crater and the dip angle of its walls were assigned constant values of about 250 m and 45°, respectively. Inversion has been conducted in two different procedures. In the first procedure, it has been assumed that the magnetization of the source(s) below the 100 m depth is the same and only induced. Three unknowns were parameterized: the susceptibility (χ), the height (H_d) and the bottom diameter (D_{bd}) of the diatreme. The elements of the geomagnetic field were assigned values computed by the IGRF ($F_o = 48000$ nT, I = 66°, D = −1°). In the second procedure, the magnetization was assumed total and having any direction. Its three components (J_x, J_y and J_z), together with the two geometric parameters H_d and D_{bd}, were considered as unknowns.

The major inversion results for the representative models of both procedures are shown in Tables 7.9a, 7.9b. and on Figures 7.19, 7.20, 7.21 as well. Generally, none of the models achieves a good fit, whereby the misfit is worst for models M and N in which the magnetization was assumed induced. Among the models in which the magnetization was considered total, model P yields better results (Tab. 7.9a, 7.9b). The magnetization has been estimated to about 0.73 A/m; this value corresponds to an apparent susceptibility of 19055×10^{-6} SI, which is higher than the average susceptibility (10000×10^{-6} SI) of the tuffs of the Eifel maars. Tuffs of some of the Eifel maars have high susceptibilities due to a relatively high content of mafic components (see Chapter 2). This might be valid for the Hausten-Morswiesen Maar too. Otherwise, a certain amount of a NRM, smaller than the induced component, should be contributing to the anomaly. The inclination (I) and the declination (D) of the total magnetization are respectively 59 and 9°; those of the NRM equal 46 and 20°, for an induced magnetization $I_i = 0.48$ A/m, corresponding to an assumed homogeneous susceptibility of 12570×10^{-6} SI. The estimates of the height (H_d) and the bottom diameter (D_{bd}) of the diatreme are about 500 m each. So, the total height of the maar-diatreme amounts to about 750 m. By the way, this value nearly matches that estimated by gravity inversion in 7.4.

As can be well seen on Figures 7.19, 7.20 and 7.21, even for model P, there still are strong discrepancies between the computed and the low-pass filtered anomalies. It is to be pointed out that geometric factors, such like the irregular shape of the maar and certainly the mismatch between the top contour of the model and the real surface boundary of the maar, also to some minor extent contribute to the discrepancies. Nevertheless, the results confirm those obtained so far. The anomalies of the residuum occur in those zones, which have been revealed by the preceding results. So, beside the main maar-diatreme, other smaller sources located within the latter and at its boundary are contributing to the magnetic anomaly. Taking into account that low-pass filtered data were used for inversion, the occurence of the residual anomalies indicates that the vertical extent of some or all the sources of the high-pass filtered (local) anomalies is deeper than 100 m. This especially applies to the small structure A2 at the south-eastern boundary, where the anomaly is strongest. The structure A2 might be a maar-diatreme volcano too. The

causative structure A3 in the central areas might be an intrusive body (a pipe or a dome). The shape of the low-pass filtered anomaly (Fig. 7.17) and the residual anomalies at the SE- and NWW-boundaries (Fig. 7.21) indicate that some mafic 2D-sources might be contributing to the whole magnetic effect. Such sources might be the remains of dikes, which have been destroyed by phreatomagmatic explosions or dikes which formed either during the same volcanic activity as the maar-diatreme or during the posteruptive phase due to a reactivation of the tectono-magmatic processes.

Table 7.9a Results of inversion of low-pass filtered magnetic data; estimated and derived parameters for model P.

Parameter	Value	Unit
Average diameter of the top boundary of the maar (D_{tm})	1020.0	m
Average diameter of the crater bottom (D_{bc})	530.0	m
Thickness of the upper layer of the crater sediments	100.0	m
Average height of the maar crater (H_c)	250.0	m
Average slope of the crater walls (α_c)	45.5	°
Average height of the diatreme (H_d)	510.0	m
Average diameter of the diatreme bottom (D_{bd})	510.0	m
Average slope of the diatreme (α_d)	88.0	°
X-component of the total magnetization (J_x)	0.3675	A/m
Y-component of the total magnetization (J_y)	0.0595	A/m
Z-component of the total magnetization (J_z)	0.6254	A/m
Total magnetization (J)	0.7278	A/m
Inclination of the total magnetization (I)	59.2	°
Declination of the total magnetization (D)	9.2	°
Computed apparent susceptibility (χ)	19055×10^{-6}	SI
Remanent magnetization (J_r)	0.262	A/m
X-component of the remanent magnetization (J_{xr})	0.1723	A/m
Y-component of the remanent magnetization (J_{yr})	0.0630	A/m
Z-component of the remanent magnetization (J_{zr})	0.187	A/m
Inclination of the remanent magnetization (I_r)	46.0	°
Declination of the remanent magnetization (D_r)	20.0	°
Koenigsberger ratio (Q)	0.5	–

Table 7.9b Confidence intervals and resolutions of the estimates; model P.

Parameter	LB	Estimate	UB	Resolution
J_x	0.347	0.367	0.389	0.96
J_y	0.044	0.060	0.075	0.98
J_z	0.602	0.625	0.650	0.91
H_d	357.0	513.0	668.0	0.81
D_{bd}	354.0	510.0	665.0	0.63

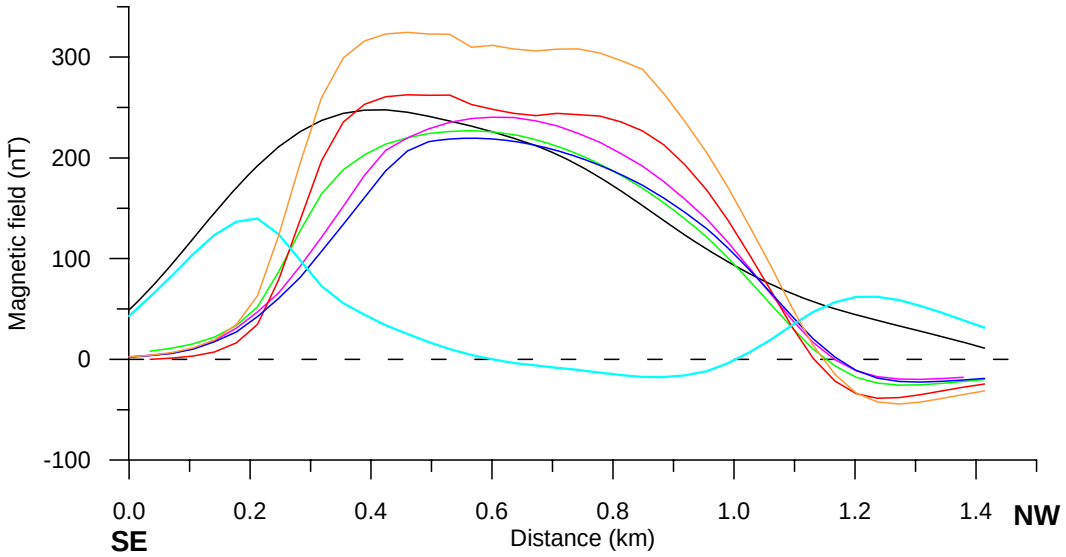

Fig. 7.19a SE-NW-profiles of the magnetic field; Hausten-Morswiesen Maar; coordinates of end points : (2580.0, 5584.4; 2579.0, 5585.4) km.

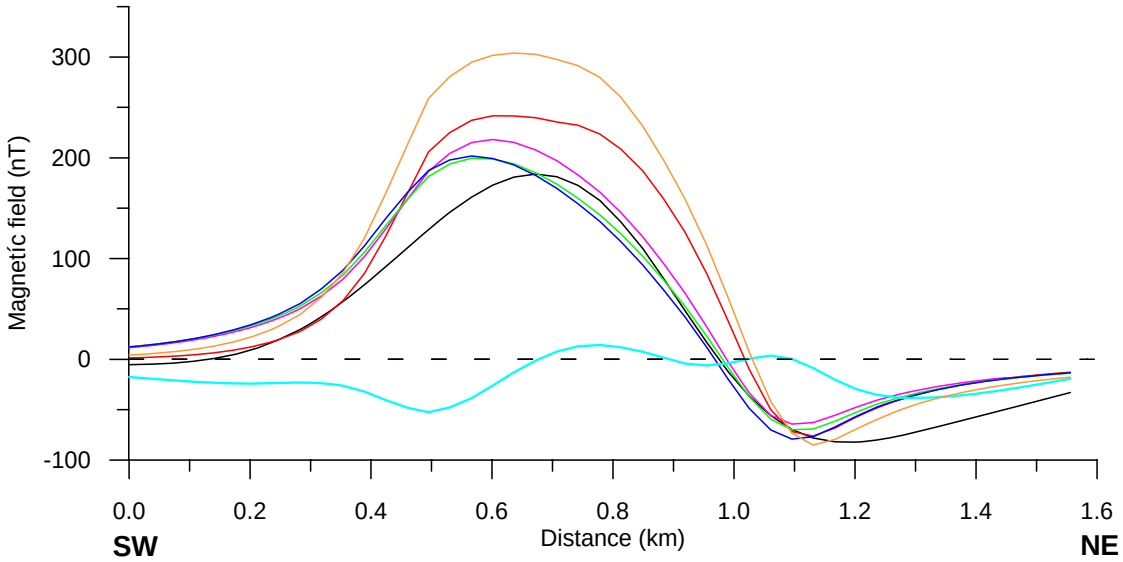

Fig. 7.19b SW-NE-profiles of the magnetic field; Hausten-Morswiesen Maar; coordinates of end points: (2579.0, 5584.5; 2580.1, 5585.6) km.

low-pass filtered — residual for model P.

M — computed : H_c = 250 m, α_c = 46°, H_d = 600 m, α_d = 81°, J_i = 1.37 A/m, I = 66°, D = -1°

N — computed : H_c = 225 m, α_c = 43°, H_d = 1140 m, α_d = 82°, J_i = 1.33 A/m, I = 66°, D = -1°

O — computed : H_c = 220 m, α_c = 42°, H_d = 485 m, α_d = 90°, J_t = 0.74 A/m, I_t = 63°, D_t = 13°

P — computed : H_c = 250 m, α_c = 46°, H_d = 515 m, α_d = 89°, J_t = 0.73 A/m, I_t = 59°, D_t = 9°

Q — computed : H_c = 220 m, α_c = 46°, H_d = 390 m, α_d = 86°, J_t = 0.75 A/m, I_t = 59°, D_t = 15°

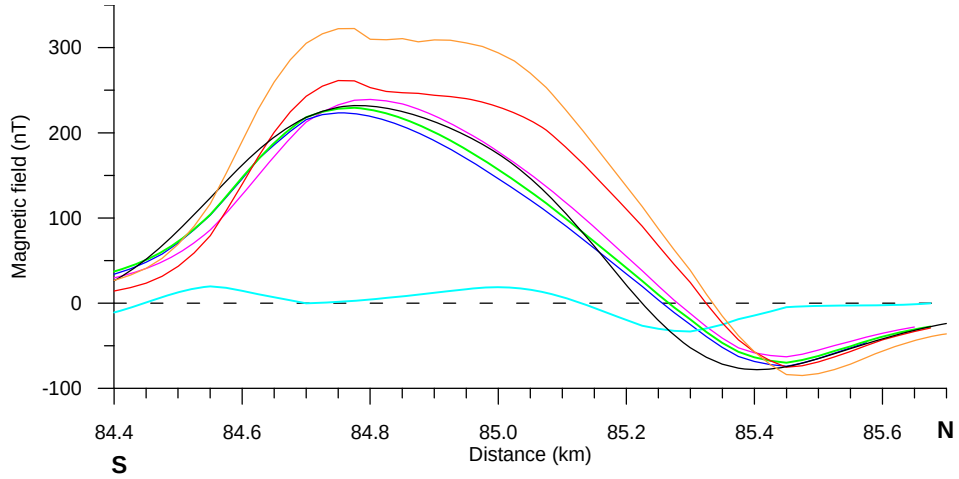

Fig. 7.20a S-N-profiles of the magnetic field; Hausten-Morswiesen Maar; coordinates of end points : (2579.55, 5584.4; 2579.55, 5585.7) km.

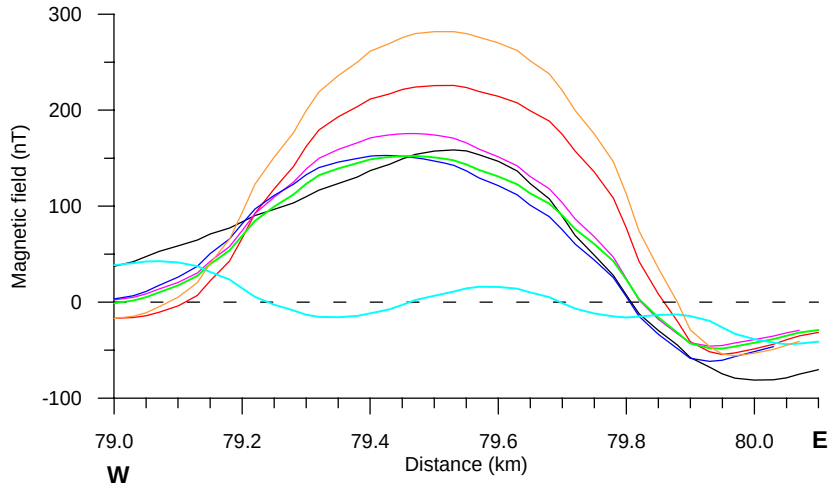

Fig. 7.20b W-E-profiles of the magnetic field; Hausten-Morswiesen Maar; coordinates of end points: 2579.0, 85.05; 2580.1, 5585.05) km.

low-pass filtered

residual for model P.

M computed : $H_c = 250$ m, $\alpha_c = 46°$, $H_d = 600$ m, $\alpha_d = 81°$, $J_i = 1.37$ A/m, I = 66°, D = -1°

N computed : $H_c = 225$ m, $\alpha_c = 43°$, $H_d = 1140$ m, $\alpha_d = 82°$, $J_i = 1.33$ A/m, I = 66°, D = -1°

O computed : $H_c = 220$ m, $\alpha_c = 42°$, $H_d = 485$ m, $\alpha_d = 90°$, $J_t = 0.74$ A/m, $I_t = 63°$, $D_t = 13°$

P computed : $H_c = 250$ m, $\alpha_c = 46°$, $H_d = 515$ m, $\alpha_d = 89°$, $J_t = 0.73$ A/m, $I_t = 59°$, $D_t = 9°$

Q computed : $H_c = 220$ m, $\alpha_c = 46°$, $H_d = 390$ m, $\alpha_d = 86°$, $J_t = 0.75$ A/m, $I_t = 59°$, $D_t = 15°$

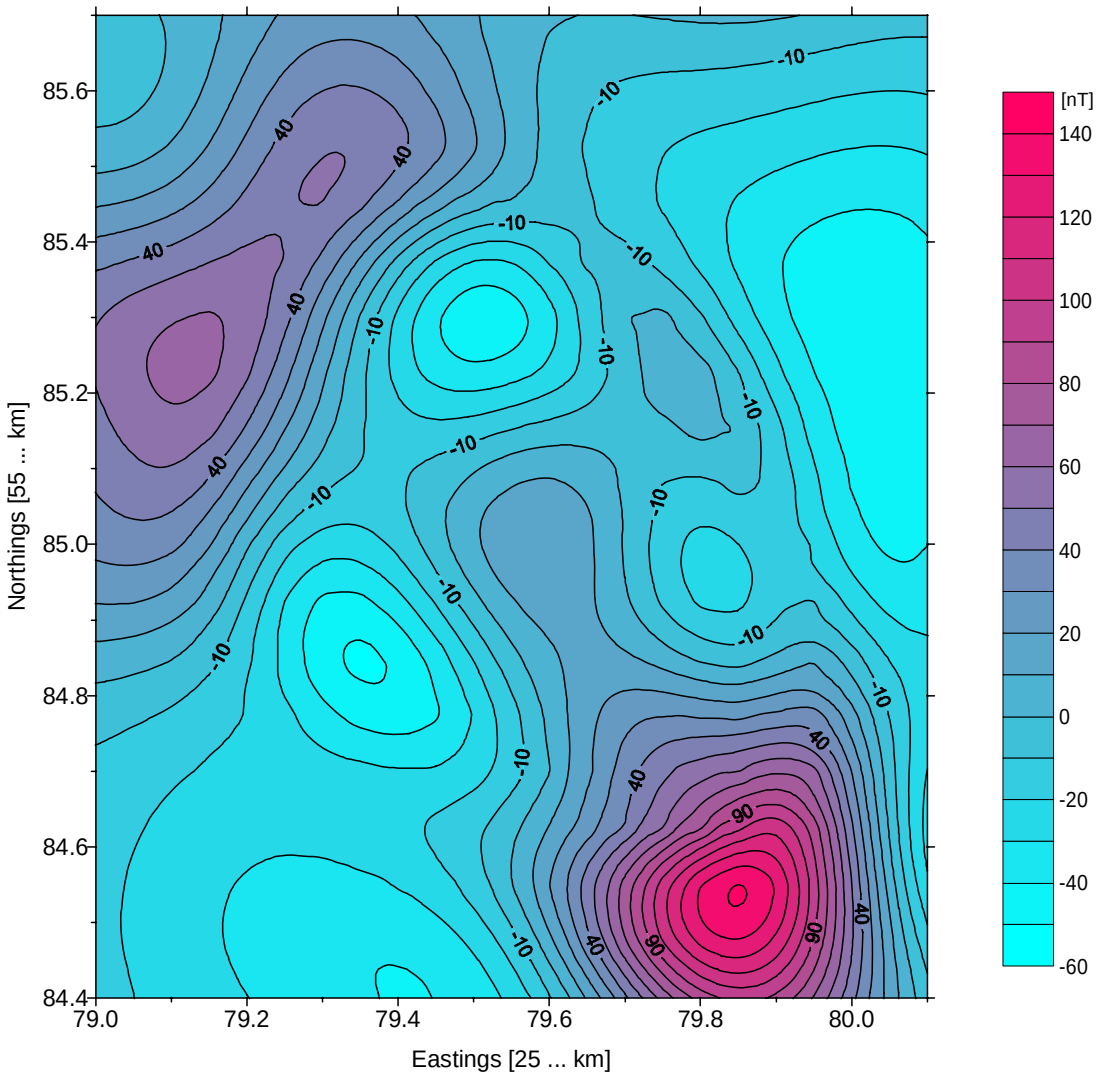

Fig. 7. 21 Residuals between the low--pass filtered and computed magnetic anomalies for model P; Hausten-Morswiesen Maar.

7.6 Synthesis of results and model of the Hausten-Morswiesen Maar

A model of the Hausten-Morswiesen Maar, derived from all interpretation results is presented in Table 7.10 and on Fig. 7.22, showing respectively the parameters and the vertical cross-section. The maar-diatreme volcano has an average top and bottom diameter of 1050 and 400 m, respectively. Its height averages 1000 m, whereby that of its crater amounts to (250± 50) m. The vertical extent of the diatreme estimated by magnetic inversion is smaller than that estimated by gravity inversion. This can be explained by the nonuniqueness in potential fields or might indicate that some of the respective major sources of the gravity and magnetic anomalies are not equivalent. Moreover, the geophysical effect decreases quicker for the magnetic than for the gravity potential as the distance increases. Accordingly, the resolution of deep masses is worse by magnetic inversion. The dip angles of the crater and diatreme walls respectively vary around 40 and 80°. There is a change in magnetic properties at about 100 m depth. Above this depth, the density varies around 2.05 g/cm^3 and below it — around 2.20 g/cm^3. But the power spectrum of the gravity field indicates further density changes at an average depth of 250 m, which probably corresponds to the crater/diatreme interface. Some models yielded a relatively high overall density of about 2.3 g/cm^3 for the maar-diatreme as a whole. The magnetization, approximated from the susceptibility profile on Fig. 7.4, is about 0.3 A/m above the 100 depth. Below this depth, the magnetization is estimated to about 0.7 A/m and is same. This indicates that the rocks of the lower part of the crater might be the same as those of the underlying diatreme. Alternatively, a high content of mafic components in crater sediments might contribute to a higher magnetization equal to that of the underlying tuffs. Some two-dimensional intrusive bodies (dykes?) are supposed to occur within the maar-diatreme volcano.

The maar-diatreme volcano is associated with other smaller structures (A1–A4), which formed within it. Concerning the geologic nature of these structures, the character of their anomalies suggests that they are small depressions with a certain similarity/relation to the main maar-diatreme. They are probably filled by tuffs — originated from either the tuff wall or the tuff rim of the maar or both — overlain by sediments. But the filling of the structure A4 at the western boundary is supposed to be predominantly made of juvenile components, which flowed into the maar crater from nearby eruption centres. The effects of these components led to an increase of both the overall density and susceptibility of the filling of the structure A4. Consequently, the density contrast to the country rocks is small and the structure A4 is better outlined in the magnetic than in the gravity field. Investigations conducted by Lorenz et al. (2003) revealed subsidence processes in some maar-diatreme volcanoes of the Gutau Volcano Group in eastern Saxony, Germany. Subsidence processes are caused by density increase in crater sediments due to water filling and compaction. Such processes might have occurred within the Hausten-Morswiesen Maar and led to the formation of the small-size basins A1–A4. These then formed much time after the phreatomagmatic event during the late phase of the posteruptive development. In case of a syngenetic formation, the structure A3 in the central area should then be a scoria cone or a mafic (basaltic?) intrusive body; otherwise it could not be detected because of the thick overlaying crater sediments.

Table 7.10 Model parameters of the Hausten-Morswiesen Maar.

Name	Diameter Top [m]	Diameter Bottom [m]	Height [m]	Density ρ [g/cm^3]	Magnetization J [A/m]	Dip angle α [°]
Maar crater Upper part	1050		100 ± 20	2.05 ± 0.10	0.3 ± 0.05	40 ± 10
Maar crater Lower part		500 ± 100	150 ± 50	2.20 ± 0.10	0.7 ± 0.05	40 ± 10
Diatreme		400 ± 100	800 ± 200[a] 500 ± 150[b]	2.25 ± 0.10	0.7 ± 0.05	80 ± 10

[a , b] respectively from gravity and magnetic inversion.

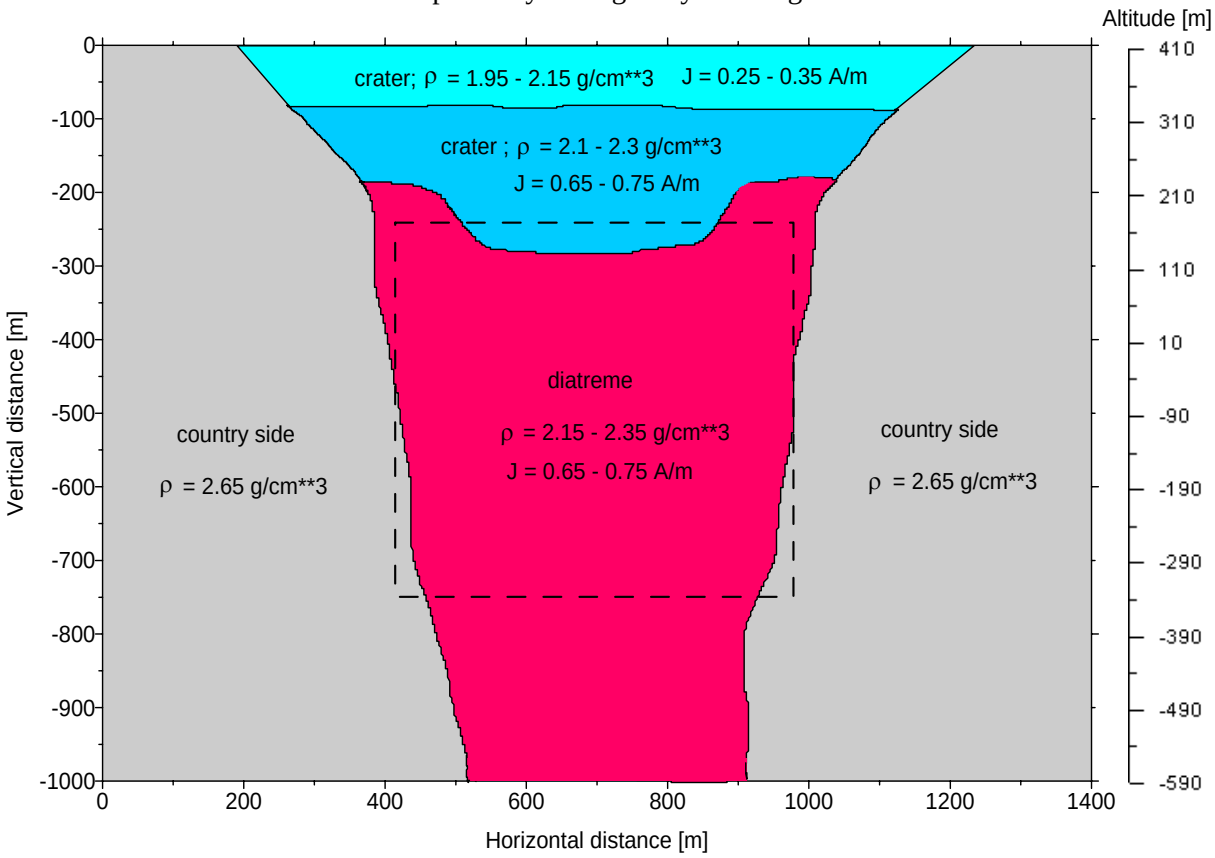

Fig. 7.22 Vertical cross-section of the model of the Hausten-Morswiesen Maar, based on interpretation results; the dashed outline shows the cross-section of the diatreme estimated by magnetic inversion.

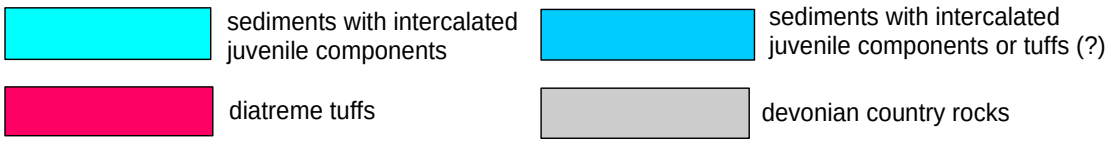

Refering to the depths of 350 and 190 m indicated by the low frequency component of the power spectrum of the gravity field, it is more likely that a major part of the crater sediments, namely those lying in the central area, subsided, while those lying in the peripheral areas did not. Considering that the 350 m apparent depth exceeds the true depth, the latter is roughly estimated to 250–300 m. This means that the sediments have undergone a subsidence of 50 to 100 m. The small structure B by Morswiesen in the Southeast is supposed to be a maar too, which formed during the same volcanic activity as the main structure A. An areal picture of the Hausten-Morswiesen Maar and its associated small structures is presented on Fig. 7.23. Since the small structures A1–A4 formed within the main maar-diatreme volcano, the dashed line corresponding to the maxima of the horizontal derivative of the gravity (Fig. 7.23) then marks the sharp contact between the top of the crater sediments and the country rocks. Indeed, the surface boundary of the crater sediments does not fit that of the maar crater, especially for relatively young maars.

The results of all interpretation methods show that the Hausten-Morswiesen Maar is a very complex structure. Thus, further investigations are required for a better knowledge. It is especially recommended to carry out detailed gravity and magnetic surveys in order to get more data, which can enhance interpretation.

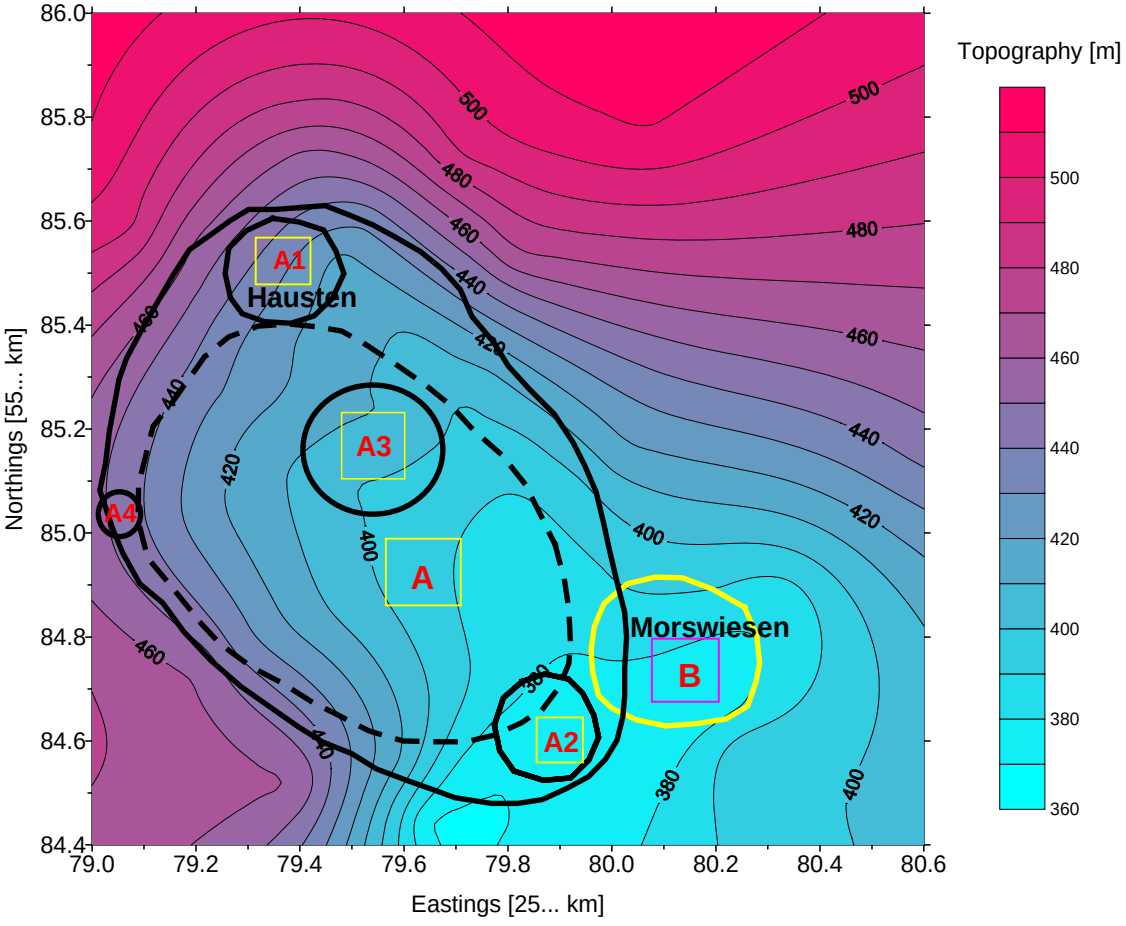

Fig. 7.23 Areal picture of the complex structure of the Hausten-Morswiesen Maar, derived from a cooperative interpretation of gravity and magnetic data. The thick black lines approximately show the boundaries of the main maar A and its associated smaller (subsidence ?) structures A1-A4; the dashed line shows the surface contact between the crater sediments and the country rocks ; the yellow line shows another small (maar?) structure B, probably also related to A.

8. Classification of maar-diatreme volcanoes

The results of qualitative and quantitative interpretation of gravity and magnetic observations, supported by theoretical modeling, showed that maar-diatremes differ from one another in vertical and horizontal dimensions, in physical properties and in geologic setting. The numerical characteristics of some Eifel maars, which have been studied in this work, are presented in Table 8.1 and on Figures 8.1, 8.2 as well. On the basis of the results, the Eifel maar-volcanoes can be classified into three main types:

I. maar-diatremes of large horizontal and vertical extent, filled up by tuffs overlain by crater sediments. The magnetic anomaly is mainly due to tuffs and generally ≤ 400 nT. The gravity anomaly, predominantly caused by light crater lake sediments, is relatively high ($-6.0 \leq \Delta g_a \leq -3.0$ mGal). This type of maar-diatremes represents the classical case, where the conditions were favourable enough for a relatively long time phreatomagmatic process leading to a widening and deepening of the maar through collapsing due to successive explosions. To this type belong the following maars: Jungferweiher, Döttingen (Tertiary, High Eifel), Kirchweil, Meerfeld (Quaternary, West Eifel) and the Hausten-Morswiesen Maar (Quaternary, East Eifel).

II. Shallow maar-diatremes of small or large horizontal extent, filled up by tuffs overlain by crater sediments. Magnetic anomalies are generally below 400 nT. Gravity anomalies have values lying between -3.0 and -2.5 mGal. For this type, the phreatomagmatic process did not last long because of a shortage either of groundwater or magma or both needed for the explosive interaction. It is likely that magmatic sills might lie on the crater floor of some maar-diatremes of this type the representatives of which are the Dehner, Pelm, am Römerhof Maars (Quaternary, West Eifel).

III. Maar-diatremes with scoria cones located within the crater; the diatreme is filled up by tuffs; the scoria cone, having its root in the diatreme, is surrounded and covered by sediments mixed with tuffs and scorias. Magnetic anomalies are relatively high (≥ 500 nT) and can even reach more than 1000 nT. Due to the relatively increased overall density of the crater filling, the density contrast is reduced, which leads to weak gravity anomalies amounting to -2.5 up to -2.0 mGal. According to Hawthorne (1973), some kimberlite pipes tend in depths to separate into discrete root-like tubular bodies which may terminate upwards as domes or "blind pipes". Since the model of kimberlite diatreme formation seems to be analogous to that of maar-diatremes (Lorenz, 1973), Hawthorne's statement could also hold for the latter. At a late stage of the phreatomagmatic process, there was no more water available to interact with the ascending magma which thus extruded in a form of a scoria cone. Examples are the Mosbruch Maar (Tertiary, High Eifel) and the Roth, Schönfeld, Brücker Maars (Quaternary, West Eifel).

Note that most of the heights and the dip angles presented in Table 8.1 have been estimated by the approximation method (Chap. 4), considering the maar-diatreme as a whole. As demonstrated by modeling results (Jungferweiher, Roth, Schönfeld and Hausten-Morswiesen Maars) the dip angles of the diatreme walls are larger and vary between 70 and 85°, which consequently leads to larger, but not necessarily, actual heights of the maar-diatremes.

Table 8.1 Numerical characteristics of some Eifel maar-diatremes derived from gravity and magnetic observations.

Maar (Type)	Gravity anomaly Δg_a $[mGal]$	Magnetic anomaly ΔF (nT)	Diameter d [m]	Height h [m]	Ratio $\lvert\Delta g_a\rvert : d$	Ratio d/h	Dip angle α [°]
Döttingen (I)	−3.6	400	1100	1250	1:305	0.9	66
Meerfeld (I)	−6.0 −4.5	150	1100	1100 600	1:183 1:244	1.0 1.83	63 48
Jungferweiher (I)	−5.5	350	1500	800 1500*	1:275	1.875 1.0	47 75*
Hausten-Morswiesen (I)	−3.5	400	1050	400 1000*	1:300	2.6 1.05	40 80*
Pelm (II)	−2.7		800	330	1:295	2.4	40
Dehner (II)	−2.5	300	750	310	1:300	2.4	40
Roth (III)	−2.0	800	800	1100	1:400	0.73	70
Schönfeld (III)	−2.5	1300	500	440 350*	1:200	1.1 1.4	60 75*

* height of maar-diatreme and dip angle of the diatreme walls estimated by modeling, otherwise by the approximation method described in Chapter 4.

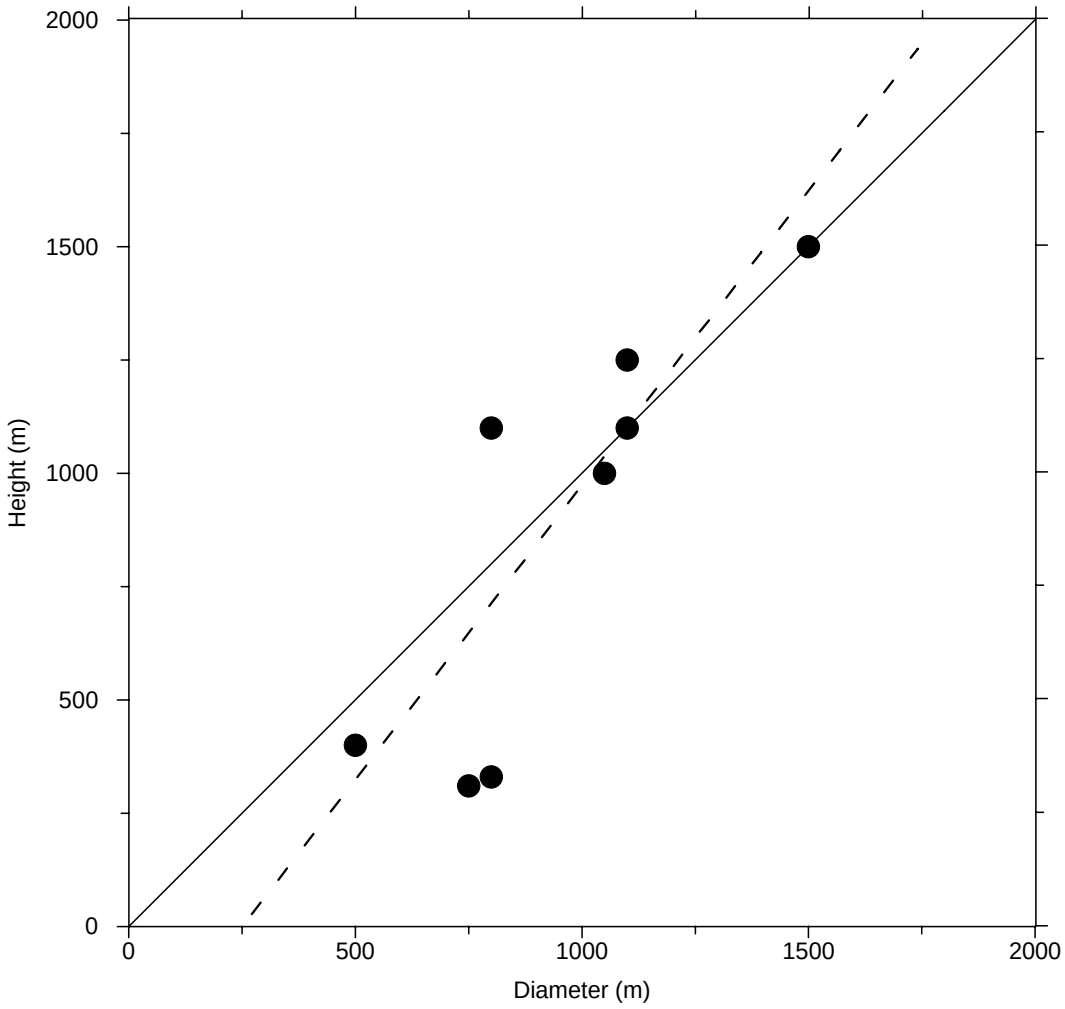

Fig. 8.1 Relationship between diameter and height for some Eifel maar-diatremes.

● corresponds to approximate present day surface diameters of the maar-diatremes

– – Regression line from data corresponding to present day surface diameters

——— straight line corresponding to a 1:1 diameter to height ratio

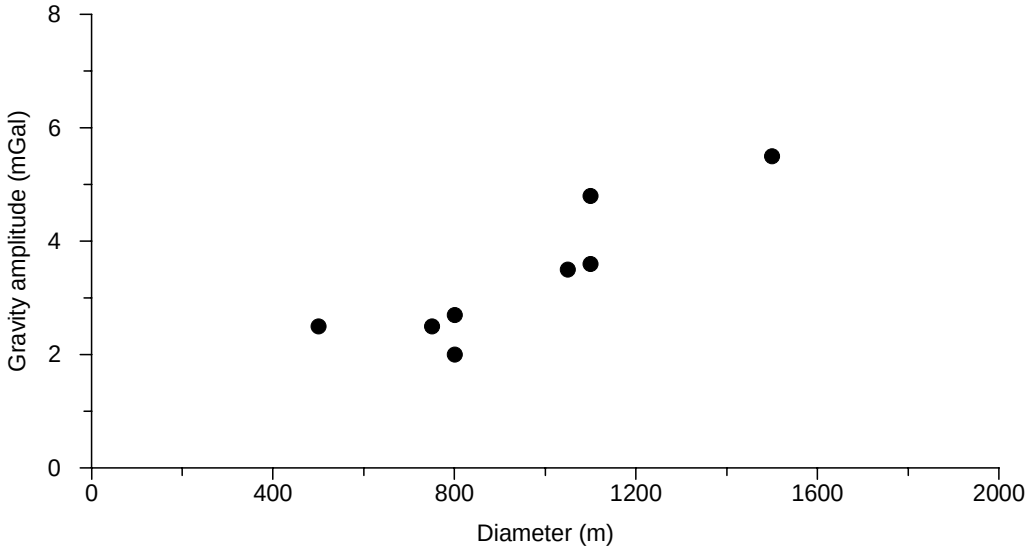

Fig. 8.2a Relationship between the diameter and the size of the gravity anomaly for some Eifel maar-volcanoes.

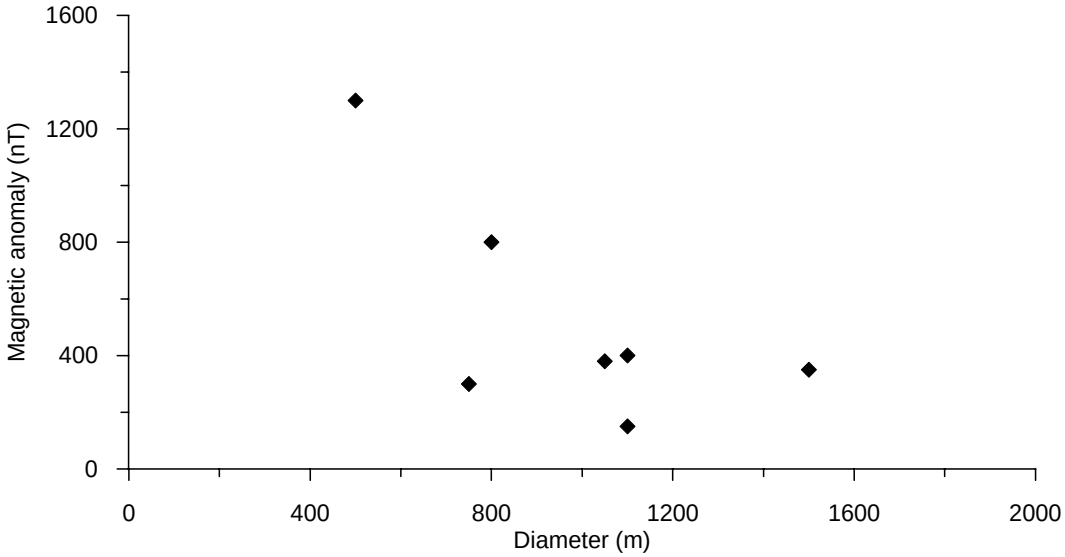

Fig. 8.2b Relationship between the diameter and the size of the magnetic anomaly for some Eifel maar-volcanoes.

9. Discussion and conclusions

Maar-diatreme volcanoes form following to phreatomagmatic processes triggered by magma/groundwater interaction. These processes are mainly controlled by geomorphological, tectonic, thermodynamic, hydraulic conditions and by the mechanical properties of the rocks as well, factors which vary from locality to locality. This leads to different relationships between the diameters and the heights of the maar-diatremes and, as a matter of fact, to different dip angles of the walls of the latter. Diatremes of maar-volcanoes are filled by tuffs, overlain by crater lake sediments. Within some maar-diatremes occur other geologic features such like scoria cones, dykes and intrusions, which affect the physical fields. Density and magnetic properties of the maar-diatreme rocks differ from a maar to another. They mainly depend on the composition but diverse factors such like the thermal, climatic and diagenetic conditions under which the rocks formed might considerably affect them. Generally, the density and the magnetization of crater sediments are smaller than those of diatreme tuffs. Concerning the magnetization, a remanent component — DRM for the sediments and a TRM for the tuffs — is sometimes present and much higher than the induced one.

The observed geophysical anomaly of a maar-volcano is a function of all the factors mentioned above and further others. So, it can not be related to only one parameter of the structure. According to Lorenz (1986), a larger diameter of the maar-diatreme would imply a greater depth of the diatreme root and a higher value of the geophysical anomaly. Generally, it is also said that the surface diameter and the height of the maar-diatreme are in the one to one ratio. As can be seen in Table 8.1, on Figures 8.1 and 8.2, contrary to the above postulates partly referring to kimberlite pipes, there exists no generalized systematics between diameter and height nor between geophysical anomaly and dimensions of the maar-diatremes. The Pelm and the Dehner Maars have diameters which are more than twice the respective heights. The magnitude of the gravity anomaly of the Schönfeld Maar is greater than that of the Roth Maar though the latter has a larger diameter. The magnetic anomaly of the Schönfeld Maar is highest though the latter is smaller than all the maar-diatremes studied. The height and/or the dip angle of the walls of each maar-diatreme has to be individually estimated. However, the graph on Fig. 8.2a shows that the gravity anomaly generally increases with the size of the diameter of the maar. Moreover, the results in Table 8.1 show that the diameter to height ratio for about 50% of the studied maar-diatremes is around 1. I assume that a 1:1 diameter to height ratio applies to maar-diatremes of Type I (Chap. 8), the extent of which, according to the theory, increases in depth as the ascending magma interacts with groundwater. If the conditions are favourable for a long time phreatomagmatic process, the height might be much larger than the surface diameter. In such a case, the height estimate by the approximation method is too inaccurate and should be considered as the minimal size. Actually, as was established in Chapter 4, the increase of the height to diameter ratio above a certain value ($h/d \geq 1$) does not bring much change in the gravity response of the maar-diatreme structure, especially for diameters less than 1000 m (normal range of maar-diatreme diameters).

Inversion results showed that physical properties most strongly affect the behaviour of the model. Thus, the maar-diatreme can not be well resolved by gravity and magnetic

inversion without a good knowledge of density and magnetic properties. This is especially valid for magnetic inversion, due to the complicated character of the magnetic field, which is defined not only by scalar but also by vector parameters involved. Even if the properties were well known, a good resolution of the diatreme would be hardly achievable since the effect of the deepest masses on the model response is very small. This is confirmed by inversion results, in which the resolution of the estimate of the diatreme height is mostly worst. Another handicap is the non-uniqueness of most geophysical inverse problems in general (Treitel and Lines, 1988) and particularly of potential field problems (Al-Chalabi, 1969), due to a covariation/correlation between different parameters.

A series of further problems impede the inversion. Maar-diatremes are outcroping, which means that measurements are made directly within the structure itsself. So, the observations are affected by all kind of inhomogeneities. Small errors in position of observation/computational points might introduce large errors in model response. Moreover, the shape of most maar-diatremes is characterized by irregularities — especially at the surface — which can not be properly accounted for, in modeling. Mathematically, the inverse problem can not be exactly solved since there always exists a null-vector space, which can not be seen. In terms of geology, this means that there are unknown geologic factors or others which affect the geophysical field but can never be seen/considered.

The choice of the model, which at best fits the observations, should be made using all available information, as well a priori as a posteriori and last not least, a good reasoning of the interpreter. The selected model should be given with probabilistic bounds. The standard deviations used to define the probability intervalls of the estimates should be adjusted for the linear dependence (covariation) of parameters.

The use of only one method can not, generally, guarantee a reliable determination of the maar parameters. The investigation of maar-diatreme volcanoes by combined gravity and magnetic methods can ensure satisfatory results. But some maar-volcanoes are very complex structures. Therefore, beside modeling, further interpretation tools such like spectral analysis, field transformations, should be used to get complementary information, which can help to better understand the nature of the structures. In some cases, due to specifc physico-geological factors, anomalies might mainly be caused by only one particular parameter and thus can not be simply related to the whole structure. For example, a high remanent magnetization or a very low density of a single section of a maar-diatreme can almost alone explain the anomaly. This is the case in the Messel Maar, where the magnetic anomaly is mainly caused by a high remanent magnetization of a 60 m thick tuff layer, lying at about 300 m depth, while the gravity anomaly is predominantly caused by very light oilshales, lying in the crater above 200 m depth (Schulz et al., 2002; Wallner et al., 2003). In such a case, gravity and magnetic methods must be assisted by other geological and geophysical techniques for a clear and complete insight into the nature of the maar-volcano. Good data sets are required to enable and ensure a reliable interpretation. Therefore, an accurate data acquisition, together with a sufficient coverage, is highly recommended.

Though the formation of the maar-diatreme volcanoes is similar to that of the kimberlite pipes, I think that they formed in different thermodynamic and hydrogeological environments. In the case of kimberlite pipes, both interacting magma and groundwater were probably supplied by deep and large reservoirs. Large amounts of magma and water

under high pressure and temperature conditions contributed to a relatively long period phreatomagmatic process, which led to large structures. It is not excluded that some volatiles might have also contributed to the process. The occurence of diamonds in kimberlite pipes supports this hypothesis. Concerning the maar-diatreme and tuff-ring-diatreme volcanoes, the phreatomagmatic process takes place due to an interaction between magma from small and shallow magma chambers (probably segregated magmas) and relatively small amounts of near-surface groundwater under low temperature and pressure conditions. This leads to shorter time eruptions and consequently to structures of smaller size in comparison with kimberlite pipes. Nevertheless, the dip angle angle of the diatreme walls is similar to that of the kimberlite pipes and varies between 70 and 85°; that of the crater walls — between 30 and 50°. As shown by combined interpretation results for the Hausten-Morswiesen Maar, subsidence processes can take place during the posteruptive development of maar-volcanoes and lead to the formation of smaller structures within the latter.

REFERENCES

Ahorner, L., 1983, Historical seismicity and present-day microearthquake activity of the Rhenish Massif, Central Europe, *in* Fuchs, K., von Gehlen, K., Mälzer, H., Murawski, H., and Semmel, A., Eds., Plateau Uplift. The Rhenish Shield — a case history: Springer-Verlag, 198–221.

Aki, K., Richards, P.G., 1980, Quantitative seismology, theory and methods, Volume 2: W.H. Freeman & Co. Al-Chalabi, M., 1971, Some studies relating to nonuniqueness in gravity and magnetic inverse problems: Geophysics, **36**, 835–855.

Al-Chalabi, M., 1992, When least-squares squares least: Geophys. Prosp. **40**, 359–378.

Alonso, M., Finn, E.J., 1968, Fundamental university physics: Addison-Wesley Pubishing Company.

Andreev, B.A., Kluschin, I. G., 1965, Geologic Interpretation of gravity anomalies (in russian): Nedra Publications, Leningrad.

Bannert, U., 1989, Gravimetrische Messungen im Vulkangebiet der Westeifel im Raum Kelberg mit Modellentwicklungen zum quartären Mosbrucher Maar: Dipl.-Arb. (unveröff.), Univ. Frankfurt a.M.

Berger, E., Brousse, R., et Causse, C., 1968, Les pipes et les diatrèmes des Causses septentrionaux: Bull. Soc. de géol. France, X, 588–600.

Bibus, E., and Semmel, A., 1977, Über die Auswirkungen quartärer Tektonik auf die altpleistozänen Mittelrhein-Terrassen: Catena, **4**, 385–408.

Böhnel, H., Reismann, N., Jäger, G., Haverkamp, U., Negendank, J.F.W., and Schmincke, H.-U., 1987, Paleomagnetic investigation of Quaternary West Eifel (Germany): indication for increased volcanic activity during geomagnetic excursion/event?: J. Geophys., **62**, 50–61.

Booth, V., 1984, Communication in science – Writing and speaking: Cambridge Univ. Press.

Bott, M.H.P., 1982, The interior of the Earth – its structure, constitution and evolution: Edward Arnold Ltd.

Büchel, G., Lorenz, V., 1982, Zum Alter des Maarvulkanismus der Westeifel: N. Jb. Geol. Paläont. Abh., **163**, no. 1, 1–22.

Büchel, G., 1984, Die Maare im Vulkanfeld der Westeifel, ihr geophysikalischer Nachweis, ihr Alter und ihre Beziehung zur Tektonik der Erdkruste: Dr. rer. nat. Diss. (unveröff.), Univ. Mainz.

Büchel, G., and Mertes, H., 1982, Die Eruptoinszentren des Westeifeler Vulkanfeldes: Z. dt. geol. Ges., **133**, 409–429.

Büchel, G., 1987, Geophysik der Eifel-Maare — Erkundung neuer Maare im Vulkanfeld der Eifel mit Hilfe geomagnetischer Untersuchungen: Mainzer geowiss. Mitt., **16**, 227–274.

Büchel, G., 1988, Geomagnetische Erkundung von Trockenmaaren im Vulkanfeld der Westeifel: Mainzer geowiss. Mitt., **17**, 357–376.

Büchel, G., Christensen, U., Jacoby, W., Ritzert, M., & Wolters, B., 1988, Gravimetrische Untersuchungen im Bereich des Kelberger Hochs (Hocheifel): Mainzer geowiss. Mitt., **17**, 377–387.

Büchel, G., 1990, Das Kelberger Hoch — Ein integriertes Modell einer tertiären Magmakammer: Habilitationsschrift, Univ. Mainz.

Büchel, G., 1991, Gutachten über die Geologie und Hydrogeologie des Maares von Haustenbach-Morswiesen. (unveröff.)

Bundesanstalt für Geowissenschaften und Rohstoffe, 1976, Karte der Anomalien der Totalintensität des erdmagnetishen Feldes in der Bundesrepublik Deutschland, 1 : 500 000.

Cipa, W., 1958, Erdmagnetische Vermessung einiger Lavaströme und Tuffschlotte in der Vorder-Eifel: Geol. Jb., **75**, 663–698.

Claerbout, J.F., and Muir, F., 1973, Robust modeling with erratic data: Geophysics, **38**, 826–844.

Clarke, G.K.C., 1969, Optimum second-derivative and downward continuation filters: Geophysics, **34**, 424–437.

Clement, C.R., 1982, A comparative study of some major kimberlite pipes in the Northern Cape and Orange Free State: Ph.D. thesis, Univ. of Cape Town.

Collins, S.J., Dodds, A.R, Johnson, B.D., 1974, Gravity profile interpretation using the Fourier Transform: Geophysics, **39**, 862–866.

Corbato, C.E., 1965, A least squares procedure for gravity interpretation: Geophysics, **30**, 228–233.

Cordell, L., and Henderson, R.G., 1968, Iterative three-dimensional solution of gravity anomaly data using a digital computer: Geophysics, **33**, 596–601.

Cox, A., Hart, R.B., 1986, Plate Tectonics — How it works: Blackwell Scientific Publications, Inc.

Crosson, R.S., 1976, Crustal structure modeling of earthquake data: 1 - Simultaneous least squares estimation of hypocenter and velocity parameters: J. Geophys. Res., **81**, no. 17, 3036–3046.

De Meyer, F., 1984, Two structural models for the werstern flank of the Brabant massif: Geophys. Prosp., **32**, 37–50.

Diele, L., 2000, Der Pulvermaar-Vulkan: Struktur und Massenbilanzen auf der Basis von geophysikalischen Messungen und Volumenkalkulation: Dr. rer. nat. Diss. (unveröff.), Univ. Würzburg.

Dortman, N.B., Ishchanyan, A. R., 1992, Magnetic properties of effusive rocks (in russian), *in* Dortman, N.B., Eds., Petrophysics, **1**, 158–165, Nedra Publications, St.-Petersburg.

Drisler, J., and Jacoby, W., 1983, Gravity anomaly and density distribution of the Rhenish Massif, *in* Fuchs, K., von Gehlen, K., Mälzer, H., Murawski, H., and Semmel, A., Eds., Plateau Uplift. The Rhenish Shield — a case history: Springer-Verlag, 366–380.

Fedi, M., Florio, G., and Rapoli, A., 1994, A method to estimate the total magnetization direction from a distortion analysis of magnetic anomalies: Geophys. Prosp., **42**, 261–274.

Franzreb-Hertel, S., 1989, Gravimetrische Untersuchungen eines Gebietes in der Hocheifel bei Kelberg: Dipl.-Arb. (unveröff.), Univ. Frankfurt a.M.

Frechen, J., 1976, Siebengebirge am Rhein, Laacher Vulkangebiet, Maargebiet der Westeifel, Vulkanologisch-petrographische Exkursionen: Samml. geol. Führer, **56**, 3. Aufl.

Frese, R.R.B., von, Hintze, W.J., Braile, L.W., and Luca, A.L., 1981, Spherical Earth gravity and magnetic anomaly modeling by Gauss-Legendre quadrature integration: J. Geophys., **49**, 234–242.

Fuchs, K., von Gehlen, K., Mälzer, H., Murawski, H., and Semmel, A., 1983, Plateau uplift. The Rhenish Shield — a case history: Springer-Verlag.

Gill, P.E., Murray, W., and Wright, M.H., 1981, Practical optimization: Academy Press Inc.

Golub, G.H., and Reinsch, C., 1970, Singular Value Decomposition and Least Squares Solutions, *in* Wilkinson, J., and Reinsch, C., Eds., Handbook for Automatic Computation, II, Linear Algebra: Springer-Verlag.

Gosselet, J., 1885, Aperçu géologique sur le terrain dévonien du Grand Duché de Luxembourg: Ann. Soc. géol. Nord, **12**, 260–300.

Grant, F.S., and West, G.F, 1965, Interpretation theory in applied geophysics: McGraw-Hill Book Co.

Grant, F.S., 1972, Review of data processing and interpretation methods in gravity and magnetics: Geophysics, **37**, 647–661.

Graybill, F.A., 1983, Matrices with applications in statistics, 2nd edition: Wadsworth, Inc.

Haverkamp, B., 1984, Paleomagnetische Messungen an den Sedimentkernen der Bohrung B4 im Meerfelder Maar: Cour. Forsch. Inst. Senckenberg, **65**, 21–28.

Hawthorne, J.B., 1975, Model of a kimberlite pipe, *in* Ahrens, L.H., Dawson, J.B., Duncan, A.R., and Erlank, A.J., Eds., Physics and Chemistry of Earth, **9**, Pergamon Press, 1–15.

Hildebrand, F.B., 1974, Introduction to numerical analysis: McGraw-Hill Book Co.

Henk, A., 1984, Zur Geologie und Geophysik des Meerfelder Maares und seiner Umgebung/Westeifel: Dipl.-Arb. (unveröff.), Univ. Mainz.

Herzog, M., Böhnel, H., Kohnen, H., and Negendank, J.F.W., 1988, Variation of magnetic properties and oxidation state of titanomagnetites within selected alkali-basalt lava flows of the Eifel-Area, Germany: J. Geophys., **62**, 180–192.

Hoerl, A.E., and Kennard, R.W., 1970_a, Ridge regression – biased estimation for nonorthogonal problems: Technometrics, **12**, no. 1, 55–67.

Hoerl, A.E., and Kennard, R.W., 1970_b, Ridge regression — application to nonorthogonal problems: Technometrics, **12**, no. 1, 69–82.

Hörrle, B., 1991, Die Genese des kesselförmig erweiterten Tales von Pelm und der topographischen Verebnungsfläche von Neunkirchen (Westeifel-Vulkanfeld): Dipl.-Arb. (unveröff.), Univ. Mainz.

Höver, J., 1987, Geologische und geophysikalische Untersuchungen am Trautzberger Maar/ Westeifel: Dipl.-Arb. (unveröff.), Univ. Frankfurt a.M.

Huckenholz, H.G., 1983, Tertiary volcanism of the Hocheifel area, *in* Fuchs, K., von Gehlen, K., Mälzer, H., Murawski, H., and Semmel, A., Eds., Plateau Uplift. The Rhenish Shield — a case history: Springer-Verlag, 121–128.

Hunsche, U., 1973, Geomagnetische, geoelektrische und magnetotellurische Messungen im

Rahmen einer Exkursion zum Mosenberg und zum Meerfelder Maar in der Westeifel: Gamma, **22**.

IAGA Division I, Working Group 1, D.R. Barraclough, Chairman, 1984, International Geomagnetic Reference Field Revision 1987: Geophysics, **53**, 576–578.

Jackson, D.D., 1972, Interpretation of inaccurate, insufficient and inconsistent data: Geophys. J. R. Astr. Soc., **28**, 97–109.

Jacoby, W.R., 1967, On the calculation of the gravity effect of arbitrarily shaped three dimensional masses with digital computers: Zeits. f. Geophys. **33**, 163–166.

Jacoby, W.R., 1970, Gravity diagrams for thickness determination of exposed rock bodies: Geophysics, **35**, 471–475.

Jödicke, H., Untiedt, J., Olgemann, W., Schulte, L., and Wagenitz, V., 1983, Electrical conductivity structure of the crust and upper mantle beneath the Rhenish Massif, *in* Fuchs, K., von Gehlen, K., Mälzer, H., Murawski, H., and Semmel, A., Eds., Plateau Uplift. The Rhenish Shield — a case history: Springer-Verlag, 288–302.

Klein, A., Jacoby, W.R., Smilde, P.,1997, Mining-induced crustal deformation in Northwest Germany: modeling the rheological structure of the lithosphere: Earth Planet. Sci. Lett., **147**, 107–123.

Knapp, G., 1978, Erläuterungen zur Geologischen karte der nördlichen Eifel 1:100 000, 2. Aufl.

Kohnen, H., K., et al., 1976, Geophysikalische Untersuchungen am Lavastrom des Horngrabens in der Westeifel, N.Jb. Geol. Paläont. Mh., 21–30, Stuttgart.

Kopecký, L., Pišová, J., Pokorný, L., 1967, Pyrope-bearing diatremes of the Ceské Středohoři Mountains: Sbornik geologických věd, geologie, řada G. sv., **12**, 118–124.

Korn, G.A., Korn, T.M., 1968, Mathematical handbook for scientists and engineers: McGraw-Hill Book Co.

Krumbein, W.C., Graybill, F.A., 1965, An introduction to statistical models in geology: McGraw-Hill Book Co.

Ku, C.C., Telford, W.M., and Lim, S.H., The use of linear filtering in gravity problems: Geophysics, **36**, 1174–1203.

Ku, C.C., 1977, A direct computation of gravity and magnetic anomalies caused by 2- and 3-dimensional bodies of arbitrary shape and arbitrary magnetic polarization by equivalent-point method and a simplified cubic spline: Geophysics, **42**, 610–622.

Lawson, C. L., and Hanson, R. J., 1974, Solving least squares problems: Prentice-Hall, Inc.

Ledoux, H., 1987, Geologische Karte von Nordrhein-Westfalen 1:100 000, Blatt C 5506 Bonn: Geol. L.-A. Nordrhein-Westfalen.

Lines, L.R., and Treitel, S., 1984, A review of least squares inversion and its applications to geophysical problems: Geophys. Prosp. **32**, 159–186.

Lines, L.R., Schultz, A.K., and Treitel, S., 1988, Cooperative inversion of geophysical data: Geophysics, **53**, 8–20.

Lippolt, H.J., 1983, Distribution of volcanic activity in space and time, *in* Fuchs, K., von Gehlen, K., Mälzer, H., Murawski, H., and Semmel, A., Eds., Plateau Uplift. The Rhenish Shield — a case history: Springer-Verlag, 112–120.

Litinsky, V.A., 1989, Concept of effective density — key to gravity depth determinations for sedimentary basins: Geophysics, **54**, 1474–1482.

Löhnertz, W., 1978, Zur Alterstellung der tiefliegenden fluviatilen Tertiärablagerungen der SE-Eifel (Rheinisches Schiefergebirge): N. Jb. Geol. Paläont. Abh., **156**, 179–206.

Logatschev, A.A., Sacharov, V.P., 1979, Magnetic prospecting (in russian): Nedra Publications, Leningrad.

Lorenz, V., 1973, On the formation of maars: Bull. Volcanol., Tome xxxvii-2, 183–204.

Lorenz, V., 1975, Formation of phreatomagmatic maar-diatreme volcanoes and its relevance to kimberlite diatremes, *in* Ahrens, L.H., Dawson, J.B., Duncan, A.R., and Erlank, A.J., Eds., Physics and Chemistry of Earth, **9**, Pergamon Press, 17–27.

Lorenz, V., and Büchel, G., 1980_b, Zur Vulkanologie der Maare und Schlackenkegel der Westeifel: Mitt. Pollichia, **68**, 29–100.

Lorenz, V., and Büchel, G., 1980_a, Die Kesseltäler der vulkanischen Westeifel; Nachweis ihrer Maargenese: Mainzer geowiss. Mitt., **8**, 173–191.

Lorenz, V., 1982, Maare and Schlakenkegel der Westeifel: Spektrum der Wissenschaft, **2**, 26–37.

Lorenz, V., 1985, Maars and diatremes of phreatomagmatic origin — a review: Trans. geol. Soc. S. Afr., **88**, 459–470.

Lorenz, V., 1986, On the growth of maars and diatremes and its relevance to the formation of tuff-rings: Bull. Volcanol., **48**, 265–274.

Lorenz, V., Suhr, P., and Goth, K., 2003, Maar-Diatrem-Vulkanismus — Ursachen und Folgen. Die Guttauer Vulkangruppe in Ostsachsen als Beispiel für die komplexen Zusammenhänge: Z. geol. Wiss. **31**, (4–6): 267–312.

Mälzer, H., Hein, G., and Zippert, K., 1983, Height changes in the Rhenish Massif: determination and analysis, *in* Fuchs, K., von Gehlen, K., Mälzer, H., Murawski, H., and Semmel, A., Eds., Plateau Uplift. The Rhenish Shield — a case history: Springer-Verlag, 260–275.

McGrath, P.H., 1991, Terrestrial magnetism, its terminolgy, and manifestations from an interpreter's point of view, *in* Notes for Canadian Geophysical Union, short course. Interpretation of gravity and magnetic anomalies for non-specialists, 189–253.

Marquardt, D.W., 1963, An algorithm for least squares estimation of nonlinear parameters, J. Soc. Ind. Appl. Math., **11**, 431–441.

Marquardt, D.W.,1970, Generalized inverses, ridge regression, biased linear estimation, and nonlinear estimation: Technometrics, **12**, no. 3, 591–612.

Mechie, J., Prodehl, C., and Fuchs, K., 1983, The long-range seismic refraction experiment in the Rhenish Massif, *in* Fuchs, K., von Gehlen, K., Mälzer, H., Murawski, H., and Semmel, A., Eds., Plateau Uplift. The Rhenish Shield — a case history: Springer-Verlag, 260–275.

Meissner, R., Springer, M., Murawski, H., Bartelsen, H., Flüh, E.R., and Dürschner, H., 1983, Combined seismic reflection-refraction investigations in the Rhenish Massif and their relation to recent tectonic movements, *in* Fuchs, K., von Gehlen, K., Mälzer, H., Murawski, H., and Semmel, A., Eds., Plateau Uplift. The Rhenish Shield — a case history: Springer-Verlag, 276–287.

Menke, W., 1984, Geophysical data Analysis — Discrete inverse theory: Academy Press Inc.

Merchant, M.J., 1981, Fortran 77 — Language and style: Wadsworth, Inc.

Mertes, H., 1983, Aufbau und Genese des Westeifeler Vulkanfeldes: Bochumer geol. u. geotech. Arb., **9**, Bochum.

Mertes, H., and Schmincke, H.-U., 1983, Age distribution of volcanoes in the West-Eifel: N. Jb. Geol. Paläont. Abh., **166**, 260–293.

Meyer, W., 1958, Geologie der Siegener Schichten zwischen Ahr und Nette (Osteifel): Z. dt. geol. Ges., **109**, 452–462.

Meyer, W., 1988, Geologie der Eifel, 2. ergänzte Aufl., Stuttgart (Schweitzerbart).

Meyer, W., and Pahl, A., 1960, Zur Geologie der Siegener Schichten in der Osteifel und im Westerwald: Z. dt. geol. Ges., **112**, 278–291.

Müller-Sohnius, D., Horn, P., and Huckenholz, H.G., 1989, Kalium-Argon-Datierungen an tertiären Vulkaniten der Hocheifel (BRD): Chem. Erde, **49**, 119–136.

Murawski, H., 1964, Die Nord-Süd Zone der Eifel und ihre nördliche Fortsetzung: Publ. serv. Géol. Luxembourg, **14**, 285–308.

Murawski, H. et al., 1983, Regional tectonic setting and geological structure of the Rhenish Massif, *in* Fuchs, K., von Gehlen, K., Mälzer, H., Murawski, H., and Semmel, A., Eds., Plateau Uplift. The Rhenish Shield — a case history: Springer-Verlag, 9–38.

Negendank, J., Irion, G., and Linden, J., 1982, Ein eozänes Maar bei Eckfeld nordöstlich Manderscheid (SW-Eifel): Mainzer geowiss. M itt., **11**, 157–172.

Odegard, M.E., and Berg, J.W., 1965, Gravity interpretation using the Fourier integral: Geophysics, **30**, 424–438.

Oldenburg, D.W., 1974, The inversion and interpretation of gravity anomalies: Geophysics, **39**, 526–536.

Parker, R.L., 1974, Best bounds on density and depth from gravity data: Geophysics, **39**, 644–649

Pilkington, M., and Crossley, D.J., 1986, Determination of crustal interface topography from potential fields: Geophysics, **51**, 1277–1284.

Pirrung, B.M., 1992, Geologische und geophysikalische Untersuchungen am tertiären "Eckfelder Maar", Südwesteifel: Mainzer Naturw. Archiv, **30**, 3–21.

Pirrung, B.M., 1997, Zur Genese der tertiären Seesedimente von Eckfeld (Eifel), Enspel (Westerwald), Messel (Sprendlinger Horst) und Siblos (Rhön): geologische und geophysikalishe Untersuchungen: Dr. rer. nat. Diss. (unveröff.), Univ. Jena.

Piskunov, N.S., 1978, Differential and integral calculus, Vol. I and II (in russian): Science Publications, Moscow.

Press, W.H., Flannery, B.P., Teukolsky, S.A., Vetterling, W.T., 1986, Numerical recipes — The art of scientific computing: Cambridge Univ. Press.

Raikes, K., and Bonjer, K.-P., 1983, Large-scale mantle heterogeneity beneath the Rhenish Massif and its vicinity from teleseismic P-residuals measurements, *in* Fuchs, K., von Gehlen, K., Mälzer, H., Murawski, H., and Semmel, A., Eds., Plateau Uplift. The Rhenish Shield — a case history: Springer-Verlag, 315–331.

Reid, A.B., Allsop, J.M., Granser, H., Millett, A.J., and Somerton, I.W., 1990, Magnetic interpretation in three dimensions using Euler deconvolution: Geophysics, **55**, 80–

91.

Ritter, J.J.R., Jordan, M., Christensen, U.R. and Achauer, U., 2001, A mantle plume below the Eifel volcanic fields, Germany: Earth Planet. Sci. Lett., **186**, 7–14.

Robinson, E.A., 1981, Least squares regression analysis in terms of linear algebra: Goose Pond Press.

Roest, W.R., Verhoef, J., and Pilkington, M., 1992, Magnetic interpretation using the 3-D analytic signal: Geophysics, **57**, 116–125.

Roest, W.R., and Pilkington, M., 1993, Identifying remanent magnetization effects in magnetic data: Geophysics, **58**, 653–659.

Sheriff, R.E., 1984, Encyclopedic Dictionnary of Exploration Geophysics, 2*nd* Edition: Soc. Expl. Geophys.

Schmincke, H.-U., Lorenz, V., and Seck, H.A., 1983, The Quaternary Eifel Volcanic Fields, *in* Fuchs, K., von Gehlen, K., Mälzer, H., Murawski, H., and Semmel, A., Eds., Plateau Uplift. The Rhenish Shield — a case history: Springer-Verlag, 139–151.

Schmincke, H.-U., 1986, Vulkanismus

Schulz, R., Harms, F.-J., Felder, M., 2002, Die Forschungsbohrung Messel 2001: Ein Beitrag zur Entschlüsselung des Genese einer Ölschieferlagerstätte, Z. Angew. Geol., **4**, 9–17.

Silva, J.B.C., 1986, Reduction to the pole as an inverse problem and its application to low-latitude anomalies: Geophysics, **51**, 369–382.

Smilde, P., 1997, Verwendung und Bewertung von a-priori Information bei potentiell singulären Inversionsproblemen am Beispiel der gravimetrischen Bestimmung von Dichteverteilungen: Dr. rer. nat. Diss. (unveröff.), Univ. Mainz.

Smith, F.B., and Shanno, D.F., 1971, An improved Marquardt procedure for nonlinear regressions: Technometrics, **13**, 64–74.

Sonne, V., and Weiler, H., 1984, Die detritischen alttertiären (oligozänen) Faunen- und Florenelemente in den Sedimenten des Meerfelder Maares: Cour. Forsch. Inst. Senckenberg, **65**, 87–95.

Spector, A., and Parker, W., 1979, Computer compilation and interpretation of geophysical data, *in* Hood, P.J., Eds., Geophysics and Geochemistry in the search for metallic ores: Geol. Surv. of Canada, Econ. Geol. Report 31, 527–544.

Stachel, T., und Büchel, G., 1989, Das Döttinger Maar: Fallstudie eines großen tertiären(?) Tuffschlotes im Vulkanfeld der Hocheifel: Z. dt. geol. Ges., **140**, 35–51.

Stewart, G.W., 1973, Introduction to matrix computation: Academic Press Inc.

Talwani, M., and Ewing, M., 1960, Rapid computation of gravitational attraction of three-dimensional bodies of arbitrary shape: Geophysics, **25**, no. 1, 203–225.

Talwani, M., 1965, Computation with the help of a digital computer of magnetic anomalies caused by bodies of arbitrary shape: Geophysics, **30**, 797–817.

Tarantola, A., and Valette, B., 1982, Generalized nonlinear inverse problems solved using the least squares criterion: Am. Geophys. Union, Rev. of Geophys. and Space Physics, **20**, no. 2, 219–232.

Tarantola, A., 1987, Inverse problem theory — Methods for data fitting and model parameter estimation: Elsevier Science Publ. Co, Inc.

Telford, W.M., Geldart, L.P., Sheriff, R.E., Keys, D.A., 1990, Applied geophysics: Cambridge Univ. Press.

Treitel, S., and Lines, L.R., 1988, Geophysical examples of inversion (with a grain of salt): The Leading Edge of Exploration, **7**, no. 11, 32–35.

Voll, G., 1983, Crustal xenoliths and their evidence for crustal structure underneath the Eifel volcanic district, *in* Fuchs, K., von Gehlen, K., Mälzer, H., Murawski, H., and Semmel, A., Eds., Plateau Uplift. The Rhenish Shield — a case history: Springer-Verlag, 336–342.

Wallner, H., Jacoby, W., Sebazungu, E., 2003, Geophysikalische Untersuchungen der Messel-Störungszone und der Ölschieferbecken auf dem Sprendlinger Horst zur Erforschung der Beckengenese, DFG-Abschlussbericht, Mainz.

Wood, C.A., Maars, *in* Green, J., Eds., Volcanoes and volcanology: Ser. Earth Sci. **16**

Woolsey, T.S., McCallum, M.E., and Schumm, S.A., 1975, Modeling of diatreme emplacement by fluidization, *in* Ahrens, L.H., Dawson, J.B., Duncan, A.R., and Erlank, A.J., Eds., Physics and Chemistry of Earth, **9**, Pergamon Press, 29–42.

Wörner, G., Schmincke, H.-U., and Schreyer, W., 1982, Crustal xenoliths from the Quaternary Wehr volcano (East Eifel): N. Jb. Miner. Abh., **144**, 29–55.

Worthington, M.H., 1984, An Introduction to geophysical tomography: First Break, **2**, no. 11, 20–26.